



THE UNIVERSITY *of* EDINBURGH

This thesis has been submitted in fulfilment of the requirements for a postgraduate degree (e. g. PhD, MPhil, DClinPsychol) at the University of Edinburgh. Please note the following terms and conditions of use:

- This work is protected by copyright and other intellectual property rights, which are retained by the thesis author, unless otherwise stated.
- A copy can be downloaded for personal non-commercial research or study, without prior permission or charge.
- This thesis cannot be reproduced or quoted extensively from without first obtaining permission in writing from the author.
- The content must not be changed in any way or sold commercially in any format or medium without the formal permission of the author.
- When referring to this work, full bibliographic details including the author, title, awarding institution and date of the thesis must be given.

**OPTIMISATION, EVALUATION AND APPLICATION OF
CEREBROVASCULAR REACTIVITY MEASUREMENT
USING MAGNETIC RESONANCE IMAGING IN
PATIENTS WITH CEREBRAL SMALL VESSEL
DISEASE**

Emilie Sleight



**THE UNIVERSITY
of EDINBURGH**

Doctor in Philosophy

The University of Edinburgh

2023

Declaration

I declare:

- (a) that the thesis has been composed by myself,
- (b) that the work is my own except where clearly stated otherwise,
- (c) that, as I have been a member of a research group, I have made a substantial contribution to the work, such contribution being clearly indicated,
- (d) that the work has not been submitted for any other degree or professional qualification except as specified, and
- (e) that any included publications are my own work, except where indicated throughout the thesis and summarised and clearly identified on the declarations page of the thesis.

Emilie Sleight, 03/03/2023

Abstract

Small vessel disease (SVD) is a common cause of strokes and dementia. Currently, there are no treatments; therefore, developing and validating early biomarkers of disease progression and treatment response is important for future drug trials. Though SVD pathogenesis is not well understood, findings from previous studies suggest that blood-brain barrier dysfunction and impaired cerebrovascular reactivity (CVR) contribute to the disease. The latter can be measured in vivo using a vasoactive stimulus in parallel with magnetic resonance imaging (MRI) techniques sensitive to blood flow, such as blood oxygen level dependent (BOLD) contrast, and has frequently been assessed in patients with steno-occlusive diseases. However, it is unclear if the technique is reliable when investigating cerebrovascular health in deep structures of the brain where SVD is prevalent. Therefore, this thesis aimed to assess and optimise the reliability of CVR measurements and deepen our understanding of its role in SVD pathogenesis.

A systematic review was performed to provide a detailed overview of CVR MRI methodologies and clinical applications, including SVD, present in the literature, which identified several acquisition and analysis methods, a need for greater standardisation and lack of data on reliability. Specifically in SVD research, there was limited application of CVR MRI in SVD populations, little optimisation and reliability assessment of CVR in deep brain structures relevant to SVD, such as in white and subcortical grey matter. Following those findings, the effects of voxel- and region-based analysis approaches on reliability of CVR estimates were investigated using simulations and test-retest data from healthy volunteers. Voxel-based CVR magnitude estimates in tissues with high noise levels were prone to bias, whereas biases in region-based estimates were independent of noise level, but consistently underestimated CVR magnitude relative to the ground-truth mean. Furthermore, the test-retest study confirmed the repeatability of CVR

estimates from a BOLD-CVR experiment with fixed inhaled stimulus, although a systematic, but small, bias was detected due to habituation to the gas challenge. The data from healthy volunteers were further used to conduct a proof-of-concept and investigate the feasibility of extracting cerebral pulsatility from BOLD-CVR data. Small-to-moderate correlations with pulsatility from phase-contrast MRI were found depending on the regions considered. CVR pulsatility was also computed in a small cohort of SVD patients: it was higher than in healthy volunteers, but no associations were found with SVD burden. It was concluded that further optimisation and validation of the technique is needed before being suitable for clinical research. Following the optimisation of the CVR MRI technique, relationships between CVR and SVD neuroimaging features, cognition, stroke severity and outcome were investigated cross-sectionally and longitudinally in a cohort of patients with mild stroke. In the cross-sectional analysis, CVR impairment in normal-appearing and damaged tissues was associated with worse SVD burden and cognition deficit. Furthermore, the longitudinal analysis showed that baseline CVR impairment predicted worsening of white matter hyperintensity and perivascular space volumes after one year.

In conclusion, assessment of CVR in the brain and its deeper structures was successfully conducted in healthy volunteers and patients with SVD using MRI. However, this required appropriate optimisation of processing strategy as the latter can affect accuracy of CVR parameters and inter-study comparability. Importantly, applying the technique in a cohort of SVD patients led to the findings that CVR impairment was related to worse SVD burden and is a potential marker of SVD severity and progression.

Lay summary

Small vessel disease is a condition arising from small blood vessels lying deep in the brain being damaged. They are too small to be imaged individually in a living brain with current technology. The disease is a high burden to society as it occurs with normal ageing, there are no treatments for it and it causes strokes and dementia, which are leading causes of death worldwide. Research using advanced medical imaging can help us to understand what is going wrong in the brain tissue in this condition and find ways to monitor the disease in order to test new treatments. Amongst other things, blood vessels may not be increasing their size enough when the brain needs more oxygen and nutrients to function. This “reactivity” property can be measured using a specific brain imaging technique that uses magnetic resonance imaging (MRI). The challenge of measuring reactivity in small vessel disease is that the signal coming from small blood vessels is low and hard to detect. The aim of this thesis was to find the best way to measure and analyse the reactivity of those small blood vessels in order to understand its role in small vessel disease.

To do this, I read papers from all the previous studies that used this specific technique. I was then able to give an overview of the different aspects and challenges to consider when applying the technique and found that it was unclear which method was most suitable to analyse data from patients with small vessel disease. Therefore, I created a computer program, which allowed me to compare the different methods and select the most accurate one in the context of small vessel disease. Then, I looked at extracting the variation of blood flow in the brain between heartbeats, also known as pulsatility of the blood, using the same data acquired to measure reactivity. This is usually done using a different type of brain scan, which increases the overall scan duration. I was able to detect pulsatility in some parts of the brain, but concluded that the technique should be further validated before being used in clinical

research. Finally, I searched for links between the blood vessels not reacting properly and other abnormalities related to small vessel disease. I found that patients with blood vessels that were less reactive had a more severe state of disease, which worsened even more after one year.

To conclude, the work described in this thesis demonstrated that measuring the reactivity of small blood vessels in the brain is possible if the technique is carefully optimised for such measurements. The loss of reactivity from the blood vessels seems to contribute to small vessel disease. Further research and technical improvement will help to determine its exact role in the development and progression of the disease.

Acknowledgments

I owe a great deal of thanks to my primary supervisor Dr Michael J. Thrippleton for his invaluable support and whose critical thinking was essential to this thesis. I am grateful to my secondary supervisors: Prof Joanna M. Wardlaw – whose passion for small vessel disease research has been a great source of inspiration – Prof Ian Marshall and Dr Michael S. Stringer who provided me with precious guidance and encouragement throughout this work.

I would also like to thank patients, healthy volunteers and all my colleagues without whom this project would not have been feasible, namely Dr Dominic Job for helping out on server issues, Dr Francesca M. Chappell for her advice on statistics, Dr Joana Leitão for her input regarding physiological recordings, Dr Lucy Kershaw for being a caring thesis committee member, Dr Bradley MacIntosh (University of Toronto) for discussions regarding BOLD pulsatility, and the radiographers for their help with the healthy volunteer and MSS3 studies. I would also like to thank my office mates – Verónica, Angela, Bastien, Beth, Cameron, Al, Una, Fabian, Sam, Laura, José, to name but a few – and a warm thanks to Carmen for patiently explaining to me some clinical terms.

I am very grateful to the University of Edinburgh College of Medicine and Veterinary Medicine, the UK Dementia Research Institute and the Medical Research Council for their generous financial support and giving me this invaluable PhD experience.

Last but not least, I would like to thank my family and friends whose support was crucial to this PhD. I can't thank them enough for always checking-up on me and encouraging me. A special thanks to Yasmin for the unforgettable runs, which provided me with a good work-life balance. Thank you to Manuel for his unwavering love and support. I am thankful to my parents and my brother who encouraged me throughout my life and always believed in my abilities.

Publications related to this thesis

Peer-reviewed journal articles

- 1 **Sleight, E.**, Stringer, M. S., Marshall, I., Wardlaw, J. M., Thrippleton, M. J. (2021). Cerebrovascular reactivity measurement using magnetic resonance imaging: a systematic review. *Frontiers in Physiology*, 12:643468.

Author's contribution: performed the search, analysed the data, and prepared the manuscript

Contribution by others: MJT, JMW, MSS, and IM contributed to the work by discussing the eligibility and data extraction of some papers and by reviewing the manuscript.

- 2 **Sleight, E.**, Stringer, M. S., Mitchell, I., Murphy, M., Marshall, I., Wardlaw, J. M., Thrippleton, M. J. (2023). Cerebrovascular reactivity measurements using 3T BOLD MRI and a fixed inhaled CO₂ gas challenge: repeatability and impact of processing strategy. *Frontiers in Physiology*, 14:1070233.

Author's contribution: designed the study, acquired, processed and analysed the CVR data, created and analysed the simulations and prepared the manuscript.

Contribution by others: MJT, MS, IMa and JMW contributed to the work by participating in the study design and discussing the interpretation of the results. IMi and MM participated in the acquisition of the CVR data.

Journal articles submitted for peer-review or in preparation

- 1 **Sleight, E.**, Stringer, M. S., Clancy, U., Arteaga, C., Jaime Garcia, D., Hewins, W., Jochems, A. C. C., Hamilton, O. K. L., Manning, C., Morgan, A. G., Penman, R., Cheng, Y., Liu, X., Zhang, J., Hamilton, I., Jardine, C., Brown, R., Sakka, E., Kampaite, A., Wiseman, S., Valdes-Hernandez, M., Chappell, F. M., Doubal, F. N., Marshall, I., Thrippleton, M. J., Wardlaw, J.

M.. Cerebrovascular reactivity in patients with small vessel disease: a cross-sectional study. Status: submitted in peer-reviewed journal.

Author's contribution: prepared the manuscript, contributed to data collection and processing, and did the formal analysis and interpretation of data.

Contribution by others: JMW, UC, MJT, IM and FND designed the study. UC, CA, DJG and WH participated in patient recruitment. MSS, UC, CA, DJG, WH, ACCJ, OKLH, CM, AGM, RP, YC, XL, JZ, IH, CJ, RB, ESa, AK, SW, MV-H, FMC and JMW contributed to data collection and/or processing. MSS, CM, AGM, MV-H, FMC, IM, MJT and JMW contributed to data analysis and interpretation. JMW, MSS, IM, and MJT supervised the project.

- 2 **Sleight, E.**, Stringer, M. S., Clancy, U., Arteaga, C., Jaime Garcia, D., Hewins, W., Jochems, A. C. C., Hamilton, O. K. L., Manning, C., Morgan, A. G., Penman, R., Hamilton, I., Jardine, C., Brown, R., Wiseman, S., Valdes-Hernandez, M., Chappell, F. M., Doubal, F. N., Marshall, I., Thrippleton, M. J., Wardlaw, J. M.. Impaired cerebrovascular reactivity in patients with small vessel disease: a longitudinal study. Status: in preparation for submission.

Author's contribution: prepared the manuscript, contributed to data collection and processing, and did the formal analysis and interpretation of data.

Contribution by others: JMW, UC, MJT, IM and FND designed the study. UC, CA, DJG and WH participated in patient recruitment. MSS, UC, CA, DJG, WH, ACCJ, OKLH, CM, AGM, RP, IH, CJ, RB, SW, MV-H, FMC and JMW contributed to data collection and/or processing. MSS, CM, AGM, MV-H, FMC, IM, MJT and JMW contributed to data analysis and interpretation. JMW, MSS, IM, and MJT supervised the project.

Conference abstracts

1. **Sleight, E.**, Stringer, M. S., Clancy, U., Arteaga, C., Garcia, D. J., Hewins, W., Jochems, A. C. C., Penman, R., Cheng, Y., Liu, D., Zhang, J., Hamilton, I., Jardine, C., Brown, R., Sakka, E., Kampaite, A., Wiseman, S., Valdes-Hernandez, M., Chappell, F., Doubal, F., Marshall, I., Thrippleton, M. J., Wardlaw, J. M. (2023). Cerebrovascular reactivity is a predictor of small vessel disease severity after one year in patients with mild stroke. ISMRM Annual Scientific Meeting 2023, Toronto, Canada.
2. **Sleight, E.**, Stringer, M. S., Clancy, U., Arteaga, C., Garcia, D. J., Hewins, W., Chappell, F. M., Jochems, A. C. C., Hamilton, I., Jardine, C., Brown, R., Sakka, E., Wiseman, S., Valdes-Hernandez, M., Kampaite, A., Doubal, F. N., Marshall, I., Thrippleton, M. J., Wardlaw, J. M. (2022). Relationship between cerebrovascular reactivity and small vessel disease neuroimaging features. SINAPSE Annual Scientific Meeting 2022, Glasgow, UK.
3. **Sleight, E.**, Stringer, M. S., Murphy, M., Mitchell, I., Marshall, I., Wardlaw, J. M., Thrippleton, M. J. (2022). Repeatability of the BOLD-CVR experiment at 3T with fixed inspired CO₂ concentration gas stimulus. ISMRM Annual Scientific Meeting 2022, London, UK.
4. **Sleight, E.**, Stringer, M. S., Clancy, U., Arteaga, C., Garcia, D. J., Hewins, W., Chappell, F. M., Jochems, A. C. C., Hamilton, I., Jardine, C., Brown, R., Sakka, E., Wiseman, S., Valdes-Hernandez, M., Kampaite, A., Doubal, F. N., Marshall, I., Thrippleton, M. J., Wardlaw, J. M. (2022). Relationship between cerebrovascular reactivity and small vessel disease neuroimaging features. European Stroke Organisation Conference 2022, Lyon, France.
5. **Sleight, E.**, Stringer, M. S., Clancy, U., Chappell, F. M., Garcia, D. J., Hewins, W., Wisemen, S., Sakka, E., Valdes-Hernandez, M., Doubal, F. N., Marshall, I., Thrippleton, M. J., Wardlaw, J. M. (2021).

Relationship between cerebrovascular reactivity at baseline and longitudinal change in white matter hyperintensities burden in patients with SVD. European Stroke Organisation Conference 2021, Virtual.

Table of Contents

Declaration	III
Abstract	V
Lay summary.....	VII
Acknowledgments	IX
Publications related to this thesis.....	XI
List of abbreviations.....	XXI
List of figures	XXVII
List of tables.....	XXXI
1 Introduction	1
1.1 Cerebral small vessel disease	1
1.1.1 Clinical manifestations and risk factors	2
1.1.2 Neuroimaging features	3
1.1.3 Proposed pathogenesis and vascular dysfunction	5
1.2 Magnetic resonance imaging	7
1.2.1 Principles of nuclear magnetic resonance.....	7
1.2.2 How to get an image from an MRI scanner?	10
1.2.3 Using MRI to measure CVR.....	15
1.2.4 Characteristics of CVR response	20
1.3 Challenges of CVR MRI in cerebral SVD.....	22
1.4 Aims and outline of the thesis	23
2 Cerebrovascular reactivity measurement using magnetic resonance imaging: a systematic review	25
2.1 Introduction	25
2.1.1 Vasodilatory stimulus	25
2.1.2 Signal acquisition	26
2.1.3 Processing method	27
2.1.4 Aims of the review.....	27
2.2 Materials and methods.....	28
2.2.1 Search strategy.....	28
2.2.2 Eligibility criteria	28

2.2.3 Data extraction	29
2.3 Results	29
2.3.1 Search results	29
2.3.2 Population characteristics.....	30
2.3.3 Pathologies.....	32
2.3.4 MRI technique	33
2.3.5 Vasodilatory stimulus.....	34
2.3.6 CVR data processing methods	41
2.3.7 Repeatability, reproducibility and accuracy of CVR measurements	46
2.3.8 The relationship between BOLD response and PaCO ₂	46
2.3.9 Potential confounders of CVR analysis.....	52
2.3.10 CVR definition and units	52
2.4 Discussion	54
2.4.1 Reporting standards	54
2.4.2 Clinical populations.....	54
2.4.3 Acquisition	55
2.4.4 Processing Methods	56
2.4.5 Validation	56
2.4.6 Definition and interpretation of CVR	57
2.4.7 Definition and interpretation of CVR delay	58
2.4.8 Implications for future research.....	58
2.4.9 Strengths and Weaknesses.....	60
2.5 Conclusion.....	60
2.6 Update of the review and discussion with respect to the thesis.....	61
3 Cerebrovascular reactivity measurements using 3T BOLD MRI and a fixed inhaled CO₂ gas challenge: repeatability and impact of processing strategy.....	65
3.1 Introduction.....	65
3.2 Materials and methods	67
3.2.1 Simulations	67
3.2.2 Participants	68
3.2.3 Magnetic resonance imaging.....	68
3.2.4 Vasodilatory stimulus	69
3.2.5 Data processing	70

3.2.6	Regions of interest.....	71
3.2.7	Statistics.....	72
3.3	Results.....	72
3.3.1	Simulations.....	72
3.3.2	MRI experiments	75
3.3.3	CVR and physiological parameters.....	76
3.3.4	Comparison of ROI- and voxel-based analysis in vivo	83
3.4	Discussion	83
3.4.1	Simulations.....	84
3.4.2	In vivo findings.....	85
3.4.3	Implications	86
3.4.4	Strengths and limitations	88
3.4.5	Conclusion.....	89
3.5	Conclusion with respect to the thesis.....	89
4	Cerebral pulsatility measurement using BOLD-CVR MRI	91
4.1	Introduction	91
4.2	Methods.....	92
4.2.1	Participants.....	92
4.2.2	MRI acquisition	92
4.2.3	Data processing.....	93
4.2.4	Statistics.....	100
4.3	Results.....	100
4.3.1	Participants.....	100
4.3.2	Cerebral pulsatility in healthy volunteers.....	101
4.3.3	Cerebral pulsatility in SVD patients.....	115
4.4	Discussion	116
4.4.1	Cerebral pulsatility in healthy volunteers.....	120
4.4.2	Cerebral pulsatility in SVD patients.....	122
4.4.3	Future directions.....	123
4.4.4	Limitations	124
4.5	Conclusion	125
5	The Mild Stroke Study 3.....	127
5.1	Introduction	127

5.2	Methods.....	128
5.2.1	Participants	128
5.2.2	Study design	129
5.2.3	Data collection.....	130
5.2.4	MRI data processing	135
5.3	Results	138
5.3.1	General results.....	138
5.3.2	CVR results.....	138
5.4	Discussion and conclusion	142
6	Cerebrovascular reactivity in patients with small vessel disease: cross-sectional analysis	143
6.1	Introduction.....	143
6.2	Methods.....	144
6.3	Results	145
6.3.1	Population characteristics	145
6.3.2	WMH.....	152
6.3.3	Lacunes and cerebral microbleeds.....	152
6.3.4	Brain atrophy.....	152
6.3.5	PVS.....	153
6.3.6	SVD burden	153
6.3.7	NIHSS, mRS and cognition	153
6.4	Discussion	153
7	Cerebrovascular reactivity in patients with small vessel disease: longitudinal analysis	157
7.1	Introduction.....	157
7.2	Methods.....	157
7.3	Results	158
7.3.1	Population characteristics	158
7.3.2	WMH.....	159
7.3.3	Lacunes and cerebral microbleeds.....	159
7.3.4	Brain volume	165
7.3.5	PVS volumes	166
7.3.6	Visual scores.....	167

7.4	Discussion	168
8	Discussion and conclusion	171
8.1	CVR MRI methodology	171
8.1.1	Summary of findings.....	171
8.1.2	Contributions to the CVR MRI field	173
8.1.3	Limitations	174
8.2	Cerebrovascular reactivity in patients with small vessel disease ..	175
8.2.1	Summary of findings.....	175
8.2.2	Contributions to the SVD clinical field	175
8.2.3	Limitations	177
8.3	Conclusion	177
	Bibliography	179
	Appendix	217

List of abbreviations

ACZ: acetazolamide

ASL: arterial spin labelling

BBB: blood-brain barrier

BG: basal ganglia

BH: breath-hold

BOLD: blood oxygen level dependent

CADASIL: cerebral autosomal dominant arteriopathy with subcortical infarcts and leukoencephalopathy

CBF: cerebral blood flow

CBV: cerebral blood volume

CC: correlation coefficient

CGM: cortical grey matter

CMRO₂: cerebral metabolic rate of oxygen

CNR: contrast-to-noise ratio

CO₂: carbon dioxide

CPAP: continuous positive airway pressure

CSF: cerebral spinal fluid

CSO: centrum semiovale

CT: computed tomography

CV: coefficient of variation

CVR: cerebrovascular reactivity

DCE: dynamic contrast-enhanced

DE: dual-echo

DSC: dynamic susceptibility contrast

dMRI: diffusion MRI

DWI: diffusion-weighted imaging

EtCO₂: end-tidal carbon dioxide

EtO₂: end-tidal oxygen

EPI: echo-planar imaging

PVS: perivascular space

FID: free induction decay

fMRI: functional magnetic resonance imaging

FOV: field-of-view

GLM: general linear model

GM: grey matter

GRE: gradient-echo

HC: healthy control

HIV: human immunodeficiency viruses

HRF: haemodynamic response function

ICC: intraclass coefficient of variation

ICV: intracranial volume

IQR: interquartile range

IR: inversion recovery

MAP: mean arterial pressure

MCA: middle cerebral artery

MELAS: mitochondrial encephalomyopathy, lactic acidosis and stroke-like episodes

MoCA: Montreal cognitive assessment

MR: magnetic resonance

MRI: magnetic resonance imaging

mRS: modified Rankin scale

NA: not applicable

NAWM: normal-appearing white matter

NIHSS: National Institutes of Health stroke scale

NMR: nuclear magnetic resonance

OSA: obstructive sleep apnoea

O₂: dioxygen

PaCO₂: arterial carbon dioxide partial pressure

PC: phase-contrast

pCASL: pseudo continuous arterial spin labelling

pH: potential of hydrogen

PET: positron emission tomography

PI: pulsatility index

PLD: post-labelling delay

PVS: perivascular space

qT1: quantitative T₁

RF: radiofrequency

RI: repeatability index

RMS: root mean square

ROI: region of interest

RS: resting-state

SE: spin-echo

SGM: subcortical grey matter

SMS: simultaneous multi-slice

SOD: steno-occlusive disease

SPECT: single-photon emission computed tomography

SSS: superior sagittal sinus

STD: standard deviation

SVD: small vessel disease

SWI: susceptibility-weighted imaging

TCD: transcranial Doppler ultrasound

tCNR: temporal contrast-to-noise ratio

TE: echo time

TIA: transient ischaemic attack

TR: repetition time

T1W: T₁-weighted

T2W: T₂-weighted

T2-FLAIR: T₂-weighted fluid-attenuated inversion recovery

VASO: vascular space occupancy

VRF: vascular risk factor

WB: whole brain

WM: white matter

WMH: white matter hyperintensity

2D: two-dimensional

3D: three-dimensional

List of figures

- 1-1. SVD lesions observed on brain MRI
- 1-2. Formation of the net proton magnetisation M_0 and its behaviour in an NMR experiment
- 1-3. Longitudinal and transverse relaxation of the net magnetisation M
- 1-4. Magnetic field gradient produced along the z-axis
- 1-5. Dephasing of spins due to a linear magnetic field gradients
- 1-6. Dephasing of spins due to the phase and frequency encoding
- 1-7. Spin-warp pulse sequence and k-space trajectory
- 1-8. EPI pulse sequence and k-space trajectory
- 1-9. Paradigm designs
- 2-1. Flow diagram of the literature search
- 2-2. Distribution of the MRI sequences used in studies with the associated year of publication of the paper
- 2-3. Distribution of the stimuli with the associated MRI sequence and paradigm types with associated total duration of the CVR experiment
- 2-4. Bar chart showing the number of studies that apply different pre-processing steps
- 2-5. Distribution of the CVR processing and delay computation methods with the associated year of publication of the paper
- 3-1. Mean BOLD time series in SGM modelled using shifted EtCO₂ and linear drift term
- 3-2. Simulations showing the effect of tCNR on the estimation of CVR magnitude and delay corresponding to all subcortical and cortical GM, and NAWM voxels
- 3-3. Simulations showing the impact of the delay constraint and assumption of fixed delay at a voxel tCNR of 0.1 on the estimation of CVR magnitude and delay in NAWM
- 3-4. Maps of CVR magnitude and delay from one representative participant obtained from scan 1 and 2

- 3-5. Comparison of CVR magnitudes and delays between scans
- 3-6. Violin distribution of CVR magnitude and delay in SGM and NAWM as a function of the scan and the processing method: ROI-based versus voxel-based analysis
- 4-1. Preparation of BOLD data for pulsatility extraction
- 4-2. BOLD waveform formation
- 4-3. Segmentation of MCA in the right hemisphere of one of the healthy volunteers corresponding to voxels showing high pulsatility on the PI map
- 4-4. Pulsatility maps in one of the healthy volunteers as a function of the order of the Fourier series
- 4-5. Comparison of pulsatility measurements between BOLD-CVR and PC MRI in healthy volunteers
- 4-6. Comparison between pulsatility maps with and without respiration correction using RETROICOR
- 4-7. Mean BOLD waveform along the normalised cardiac cycle in different brain regions of one of the healthy volunteers
- 4-8. Pulsatility in regions corresponding to blood vessels in healthy volunteers
- 4-9. Pulsatility in tissues supplied by MCA in healthy volunteers
- 4-10. Pulsatility in the air and CO₂ blocks in different brain regions of healthy volunteers
- 4-11. Pulsatility difference between healthy volunteers and SVD patients different brain regions
- 5-1. Study protocol from pre-visit assessment to one year follow-up
- 5-2. Flowchart of the CVR MRI experiment
- 5-3. Flow chart showing patient recruitment and CVR data acquisition and processing for baseline visit
- 5-4. CVR magnitude and delay in MSS3 patients as a function of the region-of-interest
- 6-1. Flow diagram showing data exclusion process from cross-sectional analyses

- 6-2. Standardised regression coefficients from cross-sectional analysis between SVD features and CVR in SGM, NAWM and WMH
- 6-3. Cross-sectional relationships between adjusted CVR, SVD features and cognition
- 7-1. Flow diagram showing the dataset exclusion process for the longitudinal analysis
- 7-2. Standardised regression coefficients from longitudinal analysis between SVD quantitative features after one year (corrected for values at baseline) and baseline CVR in SGM, NAWM and WMH
- 7-3. Longitudinal relationships between baseline CVR and adjusted SVD quantitative features after one year
- 7-4. One year change in WMH and BG PVS volumes as a function of CVR quintile
- 7-5. Change in total Fazekas scores after one year
- A2-1. Distributions of CVR magnitudes and delays in CGM, CGM and NAWM in the cohort-averaged parameter map
- A2-2. Comparison of CVR magnitudes between scans using Bland-Altman plots in subcortical GM, cortical GM, GM and NAWM
- A2-3. Comparison of CVR delays between scans using Bland-Altman statistics in subcortical GM, cortical GM, GM and NAWM
- A2-4. Difference in CVR magnitude and in physiological parameters between scans

List of tables

- 2-6. Pathologies in which CVR was investigated
- 2-7. Median values and ranges of MRI parameters at 3T found in the literature
- 2-8. Mean/median CVR values at 3T in healthy volunteers as a function of the age range
- 2-9. Comparison of CVR values measured using MRI versus alternative imaging modalities
- 2-10. Findings of repeatability of CVR estimates
- 3-1. Mean and standard deviation across subjects of CVR magnitudes and delays in SGM, CGM, GM and NAWM computed for each scan with ROI- and voxel-based processing
- 3-2. Inter-scan coefficients of variation for CVR magnitude and delay in SGM, CGM, GM and NAWM as a function of the analysis type
- 3-3. Mean and standard deviation of the physiological variables
- 4-1. Population characteristics for the pulsatility analysis
- 4-2. Differences between orders of the Fourier series fit to extract CVR pulsatility in healthy volunteers
- 4-3. Differences between analysis to extract CVR pulsatility in healthy volunteers
- 4-4. Coefficients from linear regression between pulsatility measurement from BOLD-CVR MRI and PC MRI in healthy volunteers
- 4-5. Linear regression between cerebral pulsatility and EtCO₂
- 4-6. Inter-block pulsatility differences in different brain regions of healthy subjects
- 4-7. Linear regression between cerebral pulsatility and SVD burden
- 5-1. MRI sequence parameters of the MSS3 study
- 5-2. Regional mean values and inter-regional differences in CVR magnitude and delay
- 6-1. Population characteristics of cross-sectional analysis

- 6-2. Cross-sectional analyses
- 7-1. Population characteristics of longitudinal analysis
- 7-2. Longitudinal analyses with quantitative SVD features
- 7-3. Longitudinal analyses with SVD visual ratings
- A2-1. Mean and standard deviation across subjects of CVR magnitudes and delays in SGM, CGM, GM and NAWM computed for each delay constraint and each scan with ROI- and voxel-based processing
- A3-1. Regression coefficients from univariate cross-sectional analysis
- A3-2. Cross-sectional linear regression between CVR and WMH volume, adjusted for age, sex and vascular risk factors
- A3-3. Cross-sectional linear regression between CVR and periventricular Fazekas score, adjusted for age, sex and vascular risk factors
- A3-4. Cross-sectional linear regression between CVR and deep white matter Fazekas score, adjusted for age, sex and vascular risk factors
- A3-5. Cross-sectional linear regression between CVR and total Fazekas score, adjusted for age, sex and vascular risk factors
- A3-6. Cross-sectional linear regression between CVR and number of lacunes, adjusted for age, sex and vascular risk factors
- A3-7. Cross-sectional linear regression between CVR and number of microbleeds, adjusted for age, sex and vascular risk factors
- A3-8. Cross-sectional linear regression between CVR and deep atrophy score, adjusted for age, sex and vascular risk factors
- A3-9. Cross-sectional linear regression between CVR and superficial atrophy score, adjusted for age, sex and vascular risk factors
- A3-10. Cross-sectional linear regression between CVR and total atrophy score, adjusted for age, sex and vascular risk factors
- A3-11. Cross-sectional linear regression between CVR and brain volume, adjusted for age, sex and vascular risk factors
- A3-12. Cross-sectional linear regression between CVR and BG PVS score, adjusted for age, sex and vascular risk factors

- A3-13. Cross-sectional linear regression between CVR and CSO PVS score, adjusted for age, sex and vascular risk factors
- A3-14. Cross-sectional linear regression between CVR and total PVS score, adjusted for age, sex and vascular risk factors
- A3-15. Cross-sectional linear regression between CVR and BG PVS volume, adjusted for age, sex and vascular risk factors
- A3-16. Cross-sectional linear regression between CVR and CSO PVS volume, adjusted for age, sex and vascular risk factors
- A3-17. Cross-sectional linear regression between CVR and total PVS volume, adjusted for age, sex and vascular risk factors
- A3-18. Cross-sectional linear regression between CVR and SVD score, adjusted for age, sex and vascular risk factors
- A3-19. Cross-sectional linear regression between CVR and NIHSS, adjusted for age, sex and vascular risk factors
- A3-20. Cross-sectional linear regression between CVR and mRS, adjusted for age, sex and vascular risk factors
- A3-21. Cross-sectional linear regression between CVR and MoCA, adjusted for age, sex and vascular risk factors
- A3-22. Regression coefficients from cross-sectional analysis after adjusting for WMH volume
- A3-23. Regression coefficients from cross-sectional analysis after adjusting for EtCO₂ baseline
- A3-24. Regression coefficients from cross-sectional analysis after excluding datasets with high motion during BOLD-CVR scan
- A3-25. Regression coefficients from cross-sectional analysis after excluding datasets with short hypercapnic paradigm
- A3-26. Regression coefficients from cross-sectional analysis after excluding datasets where masks contain low number of voxels in mean BOLD space

- A3-27. Regression coefficients from cross-sectional analysis after excluding datasets with structural images of poorer quality
- A4-1. Regression coefficients from univariate longitudinal analysis
- A4-2. Longitudinal linear regression between WMH volume at one-year follow-up and baseline CVR, adjusted for WMH volume at baseline, age, sex and vascular risk factors
- A4-3. Longitudinal linear regression between number of lacunes at one-year follow-up and baseline CVR, adjusted for number of lacunes at baseline, age, sex and vascular risk factors
- A4-4. Longitudinal linear regression between number of microbleeds at one-year follow-up and baseline CVR, adjusted for number of microbleeds at baseline, age, sex and vascular risk factors
- A4-5. Longitudinal linear regression between brain volume at one-year follow-up and baseline CVR, adjusted for brain volume at baseline, age, sex and vascular risk factors
- A4-6. Longitudinal linear regression between BG PVS volume at one-year follow-up and baseline CVR, adjusted for BG PVS volume at baseline, age, sex and vascular risk factors
- A4-7. Longitudinal linear regression between CSO PVS volume at one-year follow-up and baseline CVR, adjusted for CSO PVS volume at baseline, age, sex and vascular risk factors
- A4-8. Longitudinal linear regression between total PVS volume at one-year follow-up and baseline CVR, adjusted for total PVS volume at baseline, age, sex and vascular risk factors
- A4-9. Regression coefficients after adjusting for WMH volume at baseline
- A4-10. Regression coefficients after adjusting for EtCO₂ baseline
- A4-11. Regression coefficients after excluding datasets with high motion during BOLD-CVR scan
- A4-12. Regression coefficients after excluding datasets with short hypercapnic paradigm

- A4-13. Regression coefficients after excluding datasets where masks contain low number of voxels in mean BOLD space
- A4-14. Regression coefficients after excluding datasets with structural images of poorer quality

1 Introduction

1.1 Cerebral small vessel disease

Cerebral small vessel disease (SVD) refers to a range of clinical symptoms and neuroimaging findings that are thought to arise from the dysfunction of small perforating arteries, capillaries and venules in the brain and is currently lacking treatment.¹⁻³ It contributes to most vascular dementias and a third of patients with Alzheimer's disease also exhibit SVD features.^{4,5} Overall, SVD contributes to more than 50% of dementias.^{4,5} Furthermore, SVD causes 20% of strokes worldwide including 25% of ischaemic and most haemorrhagic strokes.² SVD increases the probability of stroke recurrence, limits independence and increases the risk of mortality after stroke.^{6,7} In 2015, the cost of dementia to society in England was estimated at £24.2 billion;⁸ while prevalence of vascular dementia/Alzheimer's disease doubles every 5.3/4.3 years respectively.⁹ The care of patients with strokes in England, Wales and Northern Ireland was estimated at £1.7 billion at one year and £3.6 billion at five years after stroke.¹⁰ In cases where no stroke or dementia have been diagnosed, SVD still causes symptoms and disability.^{7,11,12} Therefore, SVD represents a huge economic burden to society.

Sporadic (i.e. non-familial) SVD is a consequence of ageing and of different comorbidities.⁷ Thus, sporadic SVD typically manifests in mid to late life.⁷ The most common familial form of SVD is known as cerebral autosomal dominant arteriopathy with subcortical infarcts and leukoencephalopathy (CADASIL). However, the scope of this thesis is limited to the sporadic form of SVD.

Due to limited spatial resolution of standard clinical neuroimaging techniques, it is not possible to observe directly the dysfunction of small blood vessels in vivo. Consequently, SVD refers to the range of clinical manifestations and associated changes in brain tissues.¹¹

1.1.1 Clinical manifestations and risk factors

A wide range of clinical manifestations have been noted in patients with SVD. Those are associated with diverse risk factors that can be separated into vascular, lifestyle and lifetime risk factors. The different clinical manifestations and risk factors are given below.

Clinical manifestations

SVD is often accompanied by lacunar ischaemic stroke, intracerebral haemorrhage and cognitive decline.⁷ Other clinical manifestations of the disease are:^{7,11}

- gait and balance dysfunction^{13,14}
- neuropsychiatric symptoms such as delirium, apathy, fatigue¹²
- urinary symptoms.^{15,16}

More subtle symptoms, including delusion, emotional lability, subjective memory complaints and depression, have also been seen in SVD patients, though their association to SVD is not yet established.⁷ In some cases, SVD develops without the patient or their relatives noticing any manifestations of the disease.¹⁷ This so-called “silent” SVD is instead detected incidentally on brain images. In those patients, symptoms may not appear, potentially due to the relatively small size or precise location of the lesions.⁷

Vascular risk factors

SVD has vascular risk factors (VRFs) common to stroke and other cardiovascular conditions that include:

- age^{7,18,19}
- hypertension defined as blood pressure greater than 140/90 mmHg^{7,18–22}
- hypercholesterolaemia^{20,21}
- diabetes mellitus type 1 and 2.^{7,21–23}

Previous studies showed that those VRFs are independently associated with the progression of white matter hyperintensities²⁰ and overall SVD burden.¹⁸ Therefore, their contribution needs to be taken into account when investigating the pathogenesis of SVD.

Life-related risk factors

Lifestyle and lifetime risk factors of SVD are:

- excessive alcohol intake^{7,21}
- smoking^{7,18,20–22}
- high dietary sodium intake defined as more than 5 g per day^{7,21,24,25}
- lack of physical exercise^{21,26}
- lower cognitive abilities and lower educational attainment.^{7,27}

Including sex as a risk factor is still debatable as it might reflect age or recruitment bias.^{7,28} Research suggests that sleep disorders such as obstructive sleep apnoea might also be a risk factor of SVD.^{7,21,29} Genetics is also a risk factor of SVD as a family history of stroke increases the risk of developing SVD.³⁰

1.1.2 Neuroimaging features

Since the early 1980s, magnetic resonance imaging (MRI) has been used as an additional tool to computed tomography (CT) in routine clinical brain imaging with scans including T_1 -weighted (T1W), T_2 -weighted (T2W), T_2 -weighted fluid-attenuated inversion recovery (T2-FLAIR) and diffusion-weighted imaging (DWI). SVD is characterised by multiple neuroimaging features that can be observed on MRI images. As such, standards for reporting vascular changes on neuroimaging (STRIVE criteria) were developed by the Centres of Excellence in Neurodegeneration to develop definitions and define imaging standards for research into SVD.³¹ SVD features include recent small subcortical infarcts, white matter hyperintensities (WMH), lacunes, microbleeds, enlarged perivascular spaces (PVS) and brain atrophy (Figure 1-1). This section gives a brief description of each one of these SVD lesions.

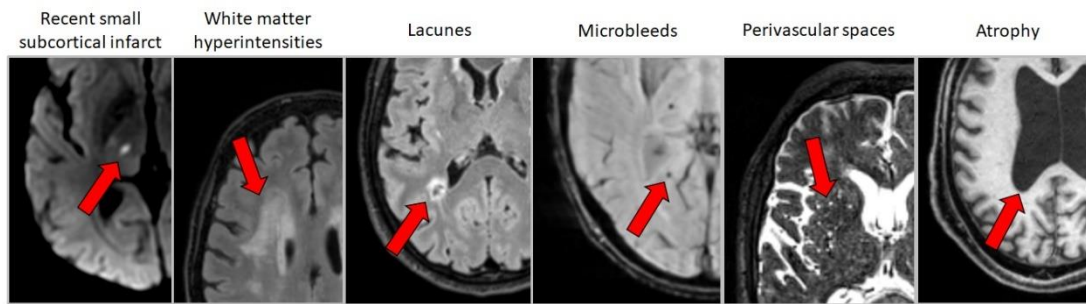


Figure 1-1: SVD lesions observed on brain MRI. The images came from SVD patients from the Mild Stroke Study 3 (see Chapter 5).

Recent small subcortical infarcts are lesions a few weeks old in territories of perforating arterioles.³¹ They cause 25% of ischaemic strokes, but some of them are silent, therefore not accompanied by lacunar stroke syndromes.^{7,17} Recent small subcortical infarcts appear hyperintense on DWI and can evolve into T2W hyperintensities or lacunar cavities.³¹

WMH are lesions of presumed vascular origin with variable size that arise from demyelination and increased interstitial fluid.² They are hyperintense on T2W images such as T2-FLAIR MRI.³¹ WMH are commonly seen in the elderly^{7,18,19} and higher WMH burden is associated with increased SVD severity and VRFs.^{18,20} Increased WMH volumes predict an increased risk of stroke, dementia and death.⁶ Though WMH gradually worsen, some have been found to improve.^{32,33}

Lacunes are old, small subcortical infarcts or small deep haemorrhages that are filled with fluid. They are hypointense on T2-FLAIR images and usually have a hyperintense rim around them.³¹ They are commonly seen in elderly people and are associated with increased risk of stroke, gait disturbance and dementia.^{34–36}

Microbleeds are small haemorrhages that are hypointense on T_2^* -weighted or susceptibility-weighted images (SWI).³¹ Their association with cognitive impairment has been shown in previous studies.³⁷

PVS are fluid-filled spaces around the blood vessels that are part of the drainage system of the brain. Depending on the position of the MRI slice with respect to the blood vessels, surrounding enlarged PVS are either round or linear. They appear hyperintense on T2W MRI and hypointense on T1W or T2-FLAIR MRI.³¹ They are associated with increasing age,³⁸ WMH,³⁹ lacunes⁴⁰ and cognitive decline.⁴¹

Brain atrophy corresponds to the decrease of brain volume due to tissue loss.³¹ This tissue loss arises from neuronal loss, cortical thinning and enlarged cerebral spinal fluid (CSF) spaces. Brain atrophy is associated with SVD severity and cognitive decline.⁴²

1.1.3 Proposed pathogenesis and vascular dysfunction

In the 1950s, Fisher gave the first description of abnormalities of small arterioles (40–200 μm) in 20 deceased patients.^{43–46} Those abnormalities consisted of changes in the organisation of the arterial walls that led to narrowing or occlusion of the small perforating arteries. Fisher hypothesised that the lesions were caused by the deposition of material on the arterial walls, known as lipohyalinosis (deposition of lipids on the arterial walls), and/or atherosclerosis (formation of plaques in larger perforating arteries, i.e. 200–800 μm).⁴⁴ Such mechanisms reduce the arrival of blood flow in tissues and would contribute to the presence of lacunar infarcts and WMH. Since then, the understanding of the disease has deepened and clinical imaging techniques have developed allowing the detection of other features of the disease such as enlarged PVS.^{47,48} Furthermore, SVD features are not only seen close to arterioles, but are globally present in the brain of SVD patients. Consequently, other mechanisms have been proposed to revise Fisher's hypothesis such as inflammation,⁴⁹ oligodendrocyte apoptosis,⁵⁰ endothelial dysfunction⁵¹ and blood-brain barrier (BBB) impairment.⁴⁵ Hereafter, pathogenesis due to endothelial dysfunction and/or BBB impairment is described.

BBB refers to cells forming the wall of the blood vessels including endothelial cells joined together by tight junctions, basement membrane, pericytes, smooth muscle cells and astrocyte end-feet.^{2,52} Its role is to maintain the interstitial milieu by regulating brain oxygenation and metabolite transport, repairing myelin, clearing waste and ensuring interstitial fluid balance.⁵²

The precise sequence in which endothelial dysfunction occurs is unknown.² Initially, endothelial dysfunction could be induced by plasmin components or physical factors like elevated blood pressure.⁴⁵ This can then result in BBB breakdown and leakage of substances (e.g. proteins, inflammatory markers, blood cells, fluids) through the vessel walls.^{2,45} Consequently, this can lead to increased interstitial fluid and damage to the surrounding tissues as well as further damage to the vessel walls.^{2,45,53} There are many plausible consequences that can be stated at this stage: inflammation, thickening and stiffening of vessel walls, impaired vasodilation (or cerebrovascular reactivity, CVR) and impaired oxygen and nutrient transport.^{2,11} Tissue injury could propagate further away from the sites of BBB breakdown due to the increased interstitial fluid around vessels. Indeed, this would elongate the diffusion path of the nutrients in order to reach neurons.² Interestingly, dysfunction of the glymphatic system is also linked to SVD through enlarged PVS.^{39,53} Following BBB breakdown, inflammation and dysfunction of pericytes could lead to an accumulation of inflammatory cells in PVS, thereby altering fluid clearance and brain waste removal.⁵³ The temporal relationship between enlarged PVS formation and vascular impairment also needs clarification.

The pathogenesis of BBB breakdown can explain more SVD features than Fisher's hypothesis and much of the evidence supports this mechanism.^{2,45} Increased BBB leakage is associated with increasing age,^{45,54,55} diagnosis of dementia,^{45,55–57} higher WMH burden,^{45,55,58–60} patients with lacunar versus cortical stroke^{61,62} and with more PVS.⁶² In a small study including patients who developed vascular dementia, plasma proteins were found around perforating arteries, supporting the theory of BBB leakage.⁶³ Animal models of oedema-related lesions showed similarities with SVD tissue damage

supporting the theory that increased interstitial fluid due to BBB leakage could induce neuronal damage.⁶⁴ Other preclinical studies showed that oedema could also account for arterial wall disorganisation or the lipohyalinosis observed by Fisher.⁶⁵ Furthermore, in rodents with sporadic SVD, endothelial cell dysfunction blocked the maturation of oligodendrocyte precursor cells that is essential for the production and repair of myelin.⁶⁶ In patients with SVD, BBB leakage can be found in normal-appearing white matter (NAWM)^{67,68} and increases with proximity to WMH.⁶⁹

As mentioned previously, impaired vasodilation, or CVR, would be another manifestation of vascular dysfunction reflecting the inability to match tissue blood supply to demand. In patients with WMH and in SVD patients with minor stroke, impaired CVR is associated with older age,^{70,71} hypertension,^{70,72} lacunar versus non-lacunar stroke,² higher WMH burden^{72–74} and increased intracranial cerebral pulsatility.⁷⁵ Reduced CVR might also predict progression from NAWM to WMH.⁷⁶ However, the relationship between CVR and other SVD features has not been investigated and the order in which vascular dysfunctions (BBB dysfunction, CVR, intracranial pulsatility) occur is unknown.

1.2 Magnetic resonance imaging

1.2.1 Principles of nuclear magnetic resonance

Magnetic field and magnetic moment of nuclei

Nuclear magnetic resonance (NMR) relies on the magnetic properties of nuclei. Some nuclei such as that of protons (^1H) have a non-zero intrinsic spin angular momentum \mathbf{J} which provides them with a magnetic moment $\boldsymbol{\mu}$ proportional to \mathbf{J} . The proportionality constant is known as the gyromagnetic ratio γ . Protons have the largest gyromagnetic ratio ($\gamma = 42.58 \text{ MHz/T}$) and are abundant in biological tissues. Thus, most of MRI is based on protons such as the MRI techniques considered in this thesis.

In NMR, a strong magnetic field \mathbf{B}_0 is created along the z-axis using a superconducting magnet. When placed in this magnetic field, the magnetic moment of a proton will tend to align itself with the magnetic field like a bar magnet would. However, due to its spin angular momentum, the proton will also experience a torque perpendicular to its magnetic moment $\boldsymbol{\mu}$ and to the magnetic field \mathbf{B}_0 . The resulting movement is precession analogous to a gyroscope. The frequency of this precession, known as the Larmor frequency, is given by:

$$\omega = \gamma B_0 \quad (1.2-1)$$

The \mathbf{B}_0 field splits the energy level of a proton into two, each energy level corresponding to a different magnetic state (Figure 1-2(A)). In the low energy state, the magnetic moment of the proton is aligned with the magnetic field \mathbf{B}_0 (i.e. spin-up state), whereas in the high energy state, it is aligned against \mathbf{B}_0 (i.e. spin-down state). At room temperature, protons have thermal energy. This implies that not all the protons are in the low energy state, but a significant proportion are in the high energy state (Figure 1-2(A)). The total magnetisation \mathbf{M}_0 aligned with \mathbf{B}_0 results from the slightly higher number of protons in the lower energy state. Increasing the magnetic field strength B_0 increases the proportion of protons in the low energy state and therefore M_0 .

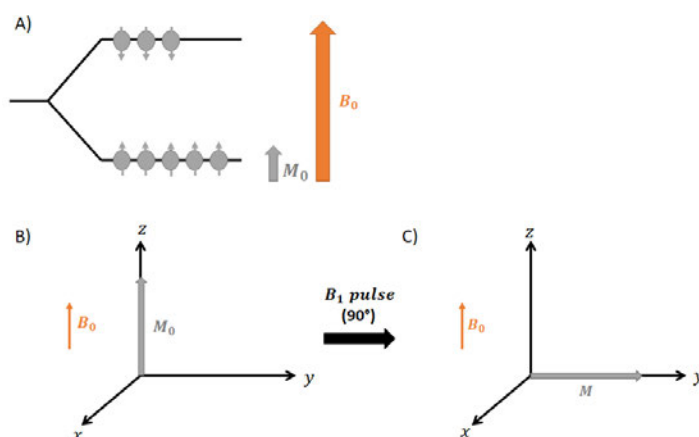


Figure 1-2: Formation of the net proton magnetisation M_0 and its behaviour in an NMR experiment. (A) Energy levels of the protons split into two due to the

magnetic field \mathbf{B}_0 . (B) Net magnetisation \mathbf{M}_0 of the protons in the \mathbf{B}_0 field. (C) Net magnetisation \mathbf{M} after a 90° pulse induced by the \mathbf{B}_1 field.

Magnetic resonance and relaxation mechanisms

The precession of the protons due to \mathbf{B}_0 can be detected when the spins are flipped away from \mathbf{B}_0 and is most detectable when the nuclei are precessing in the plane transverse to \mathbf{B}_0 . For this reason, a transverse oscillating magnetic field \mathbf{B}_1 is induced by an electromagnetic coil. By tuning the frequency of oscillation to the Larmor frequency of the protons, resonance is achieved and can be used to flip the net magnetisation \mathbf{M}_0 away from \mathbf{B}_0 (Figure 1-2(B) and (C)). After applying the \mathbf{B}_1 field for a short time interval, also known as a \mathbf{B}_1 or radio-frequency (RF) pulse, two relaxation processes occur (Figure 1-3). First, the precessing spins gradually return to their thermal equilibrium state in which the net magnetisation \mathbf{M} is aligned to \mathbf{B}_0 by exchanging energy with the surrounding thermal pool. This is also known as T_1 , spin-lattice or longitudinal relaxation. Another type of relaxation arises when the precessing spins lose phase coherence between each other due to local magnetic field inhomogeneities resulting in decreasing net magnetisation in the transverse plane called T_2 , spin-spin or transverse relaxation. However, imperfection of the \mathbf{B}_0 field itself can also cause local inhomogeneities resulting in transverse relaxation with a smaller time constant T_2^* . Fortunately, if needed, those static field inhomogeneities can be corrected for by shimming the \mathbf{B}_0 field or their effects on transverse magnetisation cancelled using a spin-echo (SE) sequence.

Mathematically, the relaxation of the net magnetisation can be described by the Bloch equations introduced in 1946:

$$\begin{aligned}\frac{dM_x(t)}{dt} &= \gamma(\mathbf{M}(t) \times \mathbf{B}(t))_x - \frac{M_x(t)}{T_2} \\ \frac{dM_y(t)}{dt} &= \gamma(\mathbf{M}(t) \times \mathbf{B}(t))_y - \frac{M_y(t)}{T_2}\end{aligned}\tag{1.2-2}$$

$$\frac{dM_z(t)}{dt} = \gamma(\mathbf{M}(t) \times \mathbf{B}(t))_z - \frac{M_z(t) - M_0}{T_1}$$

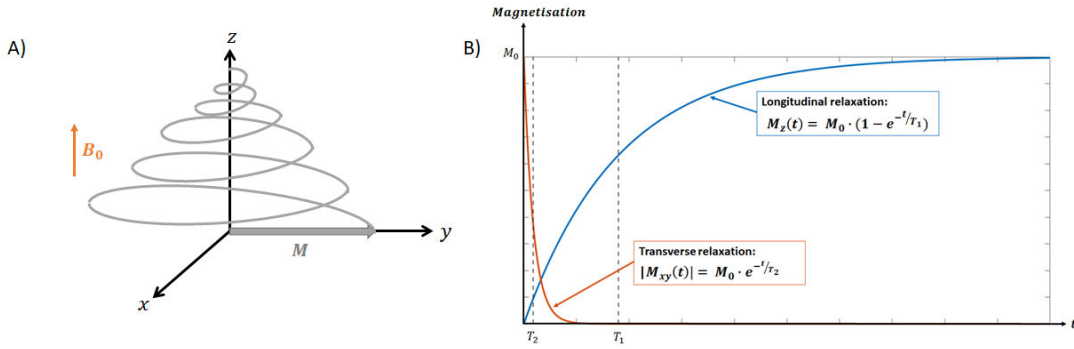


Figure 1-3: Longitudinal and transverse relaxation of the net magnetisation \mathbf{M} .

(A) Trajectory of the net magnetisation in the magnetic field \mathbf{B}_0 after an RF pulse of 90°. (B) Behaviour of the amplitude of the transverse and longitudinal magnetisations after a 90° RF pulse.

Free induction decay

According to Lenz's law, variations in the net magnetisation vector \mathbf{M} across time due to precession produce an electric current in the transverse plane. Therefore, after the \mathbf{B}_1 pulse, an MRI receive coil can be used to measure this electric current. This electrical signal is a decreasing oscillation called the free induction decay (FID). As mentioned previously, the amplitude decrease of the oscillations is due to transverse relaxation; therefore, the envelope of the FID is a decreasing exponential with characteristic time corresponding to the transverse relaxation.

1.2.2 How to get an image from an MRI scanner?

Magnetic field gradients

In proton MRI, one is interested in finding the local density of protons. In order to do so, magnetic field gradients along the three orthogonal direction x , y and z are used ($\mathbf{G}=(G_x, G_y, G_z)$). The principle of a gradient along z is shown in Figure 1-4: by producing currents in two different coils but in opposite directions, one can induce two opposing magnetic fields. Those magnetic

fields are vectorially added to the B_0 field, producing a linearly increasing field along the z-axis. The same principle applies to the other directions x and y.

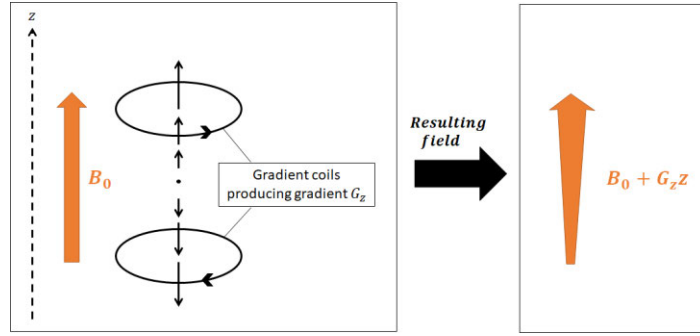


Figure 1-4: Magnetic field gradient produced along the z-axis. Gradient coils are used to produce a magnetic field that varies linearly with the position along the z-axis (G_z).

As the Larmor frequency defined in Equation (1.2-1) depends on the magnetic field, one has now a precession frequency that depends on the spatial position \mathbf{r} of the protons:

$$\omega(\mathbf{r}) = \gamma(B_0 + \mathbf{G} \cdot \mathbf{r}) \quad (1.2-3)$$

After applying an RF pulse, the signal from the transverse magnetisation at time t , $s(t)$, is given by:

$$s(\mathbf{G}, t) = \int \rho(\mathbf{r}) e^{i\omega(\mathbf{r})t} d\mathbf{r} = \int \rho(\mathbf{r}) e^{i\gamma(B_0 + \mathbf{G} \cdot \mathbf{r})t} d\mathbf{r} \quad (1.2-4)$$

where $\rho(\mathbf{r})$ the density of protons at position \mathbf{r} . To reduce required digitisation rate, removal of the carrier frequency (i.e. Larmor frequency) is performed. One keeps only the phase difference with respect to the Larmor frequency in a step called phase sensitive detection. The signal stored is therefore:

$$S(\mathbf{G}, t) = \int \rho(\mathbf{r}) e^{i\gamma \mathbf{G} \cdot \mathbf{r} t} d\mathbf{r} \quad (1.2-5)$$

Spatial frequency space or k-space

Due to the applied gradient field, the phase angle at time t , $\theta(t)$, depends linearly on the position \mathbf{r} .

$$\theta(t) = \omega(\mathbf{r}) \cdot t = (\gamma B_0 + \gamma \mathbf{G} \cdot \mathbf{r}) \cdot t \quad (1.2-6)$$

Figure 1-5 illustrates the dephasing of the spins initially in phase. Applying a linear gradient along one direction results in dephasing with the shape of an helix with a wavelength λ that becomes shorter the longer the time the gradient is applied and with a higher gradient amplitude. For a constant gradient, we define the wavevector $\mathbf{k}=(k_x, k_y, k_z)$ as:

$$\mathbf{k} = \frac{2\pi}{\lambda} = \gamma \mathbf{G} t \quad (1.2-7)$$

The signal $S(t)$ from the transverse magnetisation in Equation (1.2-5) can be rewritten as:

$$S(\mathbf{k}) = \int \rho(\mathbf{r}) e^{i\mathbf{k} \cdot \mathbf{r}} d\mathbf{r} \quad (1.2-8)$$

Taking the Fourier transform of $S(\mathbf{k})$, one can recover $\rho(\mathbf{r})$. Therefore, to get a map of the proton density, one needs to sample k-space by modifying the amplitude of the gradients applied and/or waiting for k to vary with time (Equation (1.2-7)).

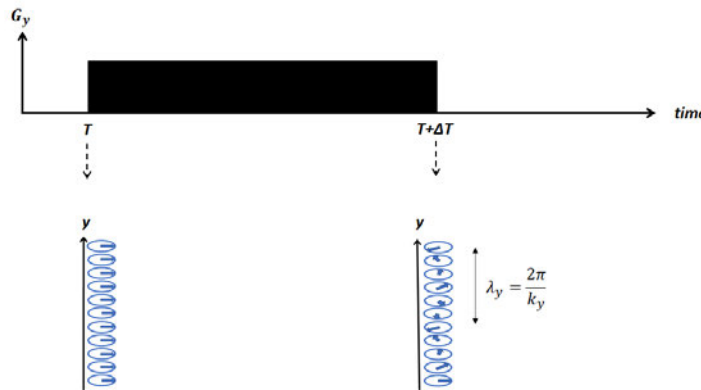


Figure 1-5: Dephasing of spins due to a linear magnetic field gradients. The spins are initially in phase assuming the gradient G_y is applied after an RF pulse. After applying the gradient for a duration ΔT , the dephasing of the spins follows the shape of a helix with wavelength λ_y .

Slice selection

For spatial frequency encoding, first, one uses slice selection with one of the gradients, for example along the z-axis. One selects a range of z-values by exciting a range of frequencies. In order to do so, the \mathbf{B}_1 pulse is oscillating at the frequency of the centre of the slice ω_{RF} and its envelope shape (e.g. a sinc function) is varied to control the profile and thickness of the slice. Once the slice has been selected, the gradient is reversed such that the spins in the selected slice are in phase.

Phase and frequency encoding

The spatial encoding of the two-dimensional (2D) slice is done in two steps: phase and frequency encoding (Figure 1-6). During phase encoding, one applies a gradient in one direction; usually along the y-axis. The spins are dephasing due to their different precession frequencies. Once the gradient is switched off, the spins precess again at the Larmor frequency, but with a phase that varies linearly along y, as shown in Figure 1-5 and Figure 1-6. The phase difference with respect to the Larmor frequency of the voxels at position y is $e^{i\gamma G_y t y} = e^{ik_y y}$.

The frequency encoding step is similar to the phase encoding step, but, this time, a gradient is applied along the orthogonal direction, which in our example is x. We acquire the transverse signal as the gradient is on to sample k-space along k_x :

$$S(\mathbf{k}) = \iint \rho(\mathbf{r}) e^{ik_x x} e^{ik_y y} dx dy \quad (1.2-9)$$

As mentioned previously, one can recover the proton density at position \mathbf{r} by taking the 2D Fourier transform of $S(\mathbf{k})$.

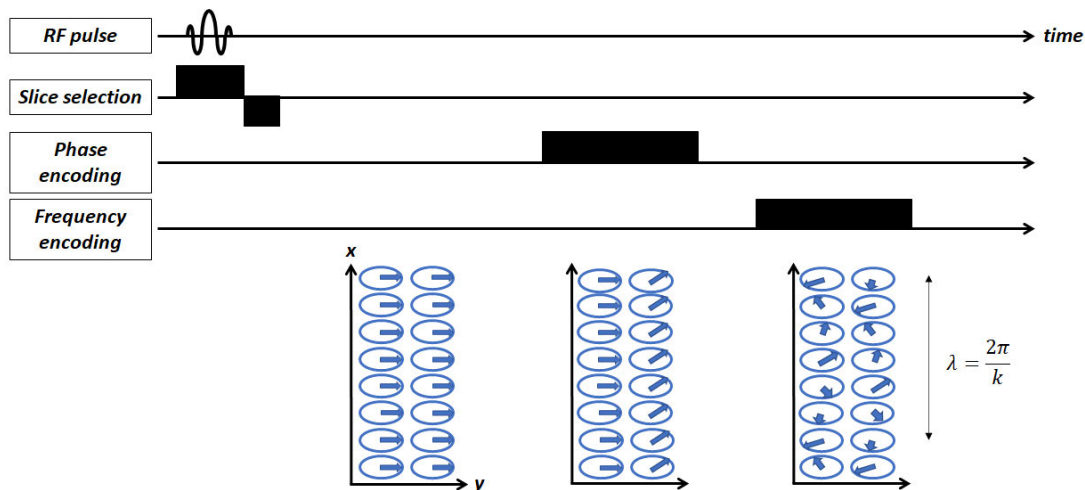


Figure 1-6: Dephasing of spins due to the phase and frequency encoding. The phase encoding step results in spins precessing at the Larmor frequency but with a phase varying along the y-axis. The frequency encoding step results in spins precessing at a frequency that varies linearly along the x-axis, while keeping the phase difference acquired during phase encoding.

To illustrate the sampling process of k -space, the spin-warp pulse sequence is given in Figure 1-7. For a given value of the gradient G_y during the phase encoding step, one moves along the k_y axis of k -space (Equation (1.2-7)). During the frequency encoding step, k_x is sampled for the specific value of k_y . Sampling multiple points in k -space is required prior to taking the Fourier transform of the transverse signal which is achieved by repeating the sequence after a certain repetition time (TR) but with a different amplitude of G_y .

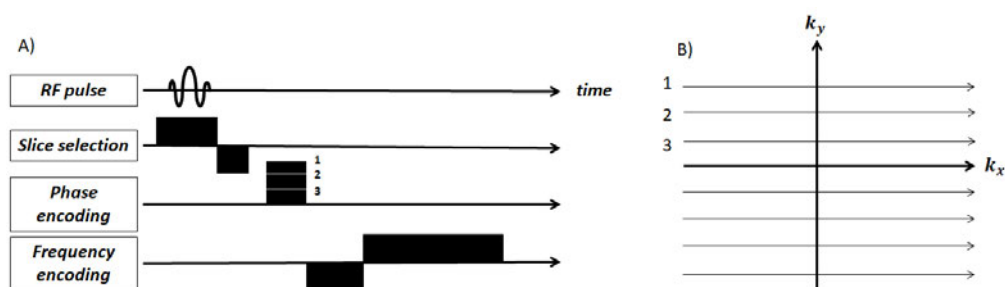


Figure 1-7: Spin-warp pulse sequence and k -space trajectory. (A) Spin-warp sequence with, in order, the application of the RF pulse, slice selection gradient G_z ,

phase encoding gradient G_y and frequency encoding gradient G_x . (B) The associated k -space trajectory where k_y is varied at each repetition by changing the amplitude of the phase encoding gradient G_y as shown in A.

2D echo-planar imaging sequence

The 2D echo-planar imaging (EPI) technique (Figure 1-8) is a fast implementation of the spin-warp sequence (Figure 1-7). Instead of repeating the pulse sequence, the entire 2D k -space is sampled at once. One first moves to one corner of k -space. In-between each k_x line acquisition, k_y is slightly altered to move along the k_y -axis and G_x is reversed to change the direction of acquisition along the k_x -axis. This sequence is used when a fast volume acquisition is needed; for example, to gain in temporal resolution when one is interested in the temporal evolution of the MRI signals.

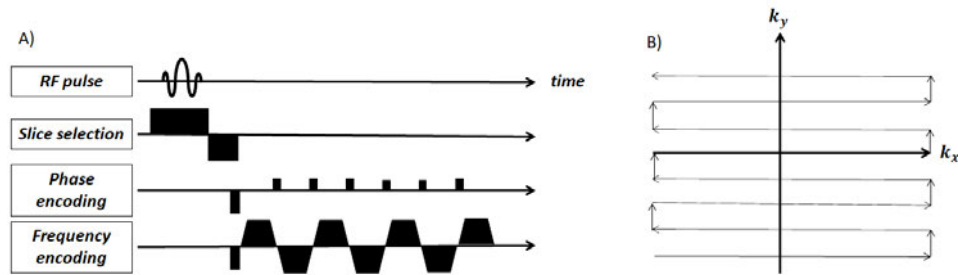


Figure 1-8: EPI pulse sequence and k -space trajectory. (A) EPI sequence with, in order, the application of the RF pulse, slice selection gradient G_z and the simultaneous phase encoding gradient G_y and frequency encoding gradient G_x . (B) The associated k -space trajectory where k_y is slightly altered after acquiring the k_x line by applying the phase encoding gradient G_y .

1.2.3 Using MRI to measure CVR

This part of the thesis gives an overview of different MRI modalities, vasodilatory stimuli and related paradigms that can be used to measure CVR. A more extensive comparison between techniques and experimental setups as well as their prevalence in the literature are given in Chapter 2.

Common MRI techniques to measure CVR: BOLD and ASL

There are different MRI techniques that can be used to assess CVR by measuring cerebral blood flow (CBF) or cerebral blood volume (CBV). Hereafter, the two most common techniques are described: blood oxygen level dependent (BOLD) and arterial spin labelling (ASL).

BOLD MRI is a technique that arises from the change in concentration of deoxyhaemoglobin. Haemoglobin is a protein that carries oxygen throughout the body via the blood vessels. Upon oxygen consumption, oxyhaemoglobin becomes deoxyhaemoglobin accompanied by a change in conformation and in magnetic properties: deoxyhaemoglobin is paramagnetic as opposed to the diamagnetic oxyhaemoglobin. This change in magnetic properties causes dephasing of the protons in the surroundings of the vessels, thereby reducing T_2^* . This effect propagates in the surrounding tissues, which gives the blooming appearance to BOLD images.

Models of the BOLD signal change relative to baseline in terms of CBV or CBF and the deoxyhaemoglobin concentration [dHb] have been developed, of which the model from Davis et al., 1998 and Hoge et al., 1999 is the most widely used:^{77,78}

$$\frac{\Delta BOLD}{BOLD_0} = M \left(1 - \left(\frac{CBF}{CBF_0} \right)^\alpha \left(\frac{[dHb]}{[dHb]_0} \right)^\beta \right) = M \left(1 - \left(\frac{CBV}{CBV_0} \right) \left(\frac{[dHb]}{[dHb]_0} \right)^\beta \right) \quad (1.2-10)$$

Subscript “0” represents baseline values. M is a coefficient corresponding to the BOLD signal change when all the deoxyhaemoglobin is eliminated from a voxel, i.e. the maximal BOLD signal change. The constant β depends on the vessel size and geometry and on the magnetic field strength and the constant α comes from the power law:⁷⁹

$$\left(\frac{CBV}{CBV_0} \right) = \left(\frac{CBF}{CBF_0} \right)^\alpha \quad (1.2-11)$$

Therefore, the BOLD signal originates from a vascular contrast dependent on CBV, CBF and on the concentration of deoxyhaemoglobin in the blood. The

latter also depends on oxygen consumption and arterial oxygen content. This contributes to the complexity of analysing and understanding BOLD data.

During hypercapnia, one usually assumes constant oxygen consumption, though this hypothesis is still under debate today.⁸⁰ This results in the baseline-normalised deoxyhaemoglobin concentration being inversely proportional to the baseline-normalised CBF.⁷⁸ Equation (1.2-10) can be simplified as follows:⁷⁸

$$\frac{\Delta BOLD}{BOLD_0} = M \left(1 - \left(\frac{CBF}{CBF_0} \right)^{\alpha-\beta} \right) \quad (1.2-12)$$

As $\alpha < \beta$,⁷⁸ it implies that increased baseline-normalised CBF induced by vasodilation leads to an increase in the measured BOLD relative intensity.

Aside from measuring CVR, BOLD MRI is commonly used to measure functional activity: due to the increase in oxygen consumption and CBF during brain activity, the local changes in haemoglobin conformation modify the BOLD intensity (Equation (1.2-10)). The change in BOLD signal due to neuronal activity depends, among others, on the stimulus and B_0 -field strength (e.g. 1-5% for a motor task at clinical field strengths)⁸¹. This branch of MRI is called functional MRI (fMRI) but is not the focus of this thesis.

Another MRI technique used to measure CVR is ASL, which assesses tissue perfusion. An image of the brain area of interest is acquired as a control image. Another step consists of tagging water protons in a slab that is upstream from the region-of-interest (ROI). This is done by inverting the magnetisation of the protons in this slab. Then the tagged protons flow in the brain area of interest on the time scale of a few seconds. By imaging the brain area of interest after tagging the water protons and subtracting it from the control image, one gets a perfusion-weighted image, although this results in keeping only 1-2% of the original signal. One of the downsides of ASL is the signal loss downstream due to T_1 -relaxation, affecting particularly areas that are far down the vasculature from the inversion slab. Furthermore, ASL is less sensitive than BOLD

because the T_2^* effect of the latter extends throughout the tissues surrounding blood vessels. Therefore, BOLD is often used for a CVR experiment instead of ASL.

Vasodilatory stimulus

Vasodilation is a process by which CBF is regulated and can be induced by natural variations of arterial carbon dioxide (CO_2) partial pressure (PaCO_2).⁸² When CO_2 crosses the BBB, it triggers intracellular and extracellular acidosis, thereby relaxing the smooth muscle cells.⁸³ Those cells are lining the arterial blood vessels and control for their diameter; therefore, vasodilation results from their relaxation.

Vasodilation can also be triggered by an exogenous stimulus, such as manipulation of PaCO_2 ,⁸⁴ which is the stimulus considered in this thesis. As PaCO_2 is not readily available in vivo, the end-tidal CO_2 (EtCO_2), i.e. the maximal exhaled CO_2 partial pressure, is often used as its surrogate.⁸³ There are different ways of achieving exogenous manipulation of PaCO_2 . First, one can voluntarily modulate the breathing pattern using techniques such as breath-holding, hyperventilation or paced-breathing.^{85,86} Though this technique is non-invasive, it relies on patient compliance. Another way is the administration of CO_2 -enriched gas.⁸⁴ This can be done by using a gas with fixed concentration of CO_2 (typically 5-6%), rebreathing the exhaled air or by targeting EtCO_2 levels. The latter can be achieved manually or using a device (for example, RespirAct™, Thornhill Research Inc., Toronto, Canada),⁸⁷ that alters the concentration of CO_2 in the inhaled gas. Using an EtCO_2 -targeting device ensures consistent EtCO_2 change across participants, but requires a more expensive and specialist equipment. Another exogenous stimulus that does not require modulation of PaCO_2 is the injection of acetazolamide (ACZ),⁸⁴ which is a carbonic anhydrase inhibitor that causes acidosis.⁸⁸ However, the onset and ending of the induced effect is slow compared to EtCO_2 -manipulating stimuli.

Paradigm

CVR measurements from natural CO₂ variation do not require any paradigm as they are part of a resting-state experiment. However, when using a vasodilatory stimulus, one needs to consider paradigm design.

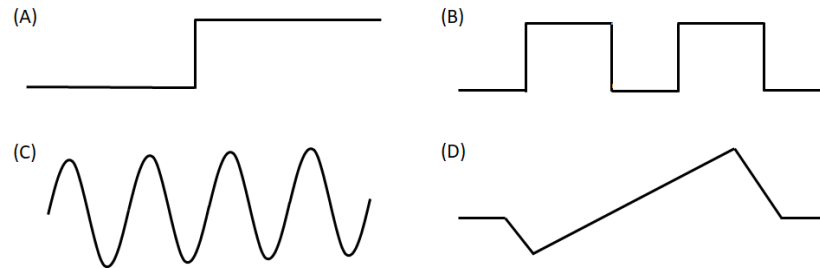


Figure 1-9. Paradigm designs. (A) Step, (B) block, (C) sinusoidal and (D) ramp paradigms.

The simplest way is a step paradigm (Figure 1-9(A)): MRI volumes are acquired during a baseline period where no stimulus is applied, then during the stimulus-on period. This paradigm design can be used with an EtCO₂-modulating stimulus or with injection of ACZ.⁸⁹ However, the technique can be sensitive to low frequency artefacts such as signal drift.

Another popular and simple type of paradigm is the block paradigm (Figure 1-9(B)), which is also commonly used in fMRI studies. Periods of stimulus on and off are repeated in an alternating manner.^{83,90} Such repetitions make the method more robust against noise in the data. As the transitions between off and on stimulus are short, a block paradigm can be used to assess the vasodilation response by investigating the response time and shape of the MRI response, also known as the haemodynamic response function (HRF).⁹¹ This type of paradigm can also be used to investigate the dynamics of the MRI signal when returning to baseline post-stimulus.⁹²

Studies have also used a sinusoidal paradigm (Figure 1-9(C)) to administer a hypercapnic gas, in which the EtCO₂ levels are generally oscillating between hypo- and hypercapnia around the normocapnia level.⁹³ This method is used to further process the data using Fourier analysis, but requires a device, such as RespirAct, that can precisely control the EtCO₂ levels.

The final paradigm to mention is the ramp paradigm (Figure 1-9(D)), in which the stimulus is decreased or increased in a slow manner to allow the MRI response to follow the change in EtCO₂.^{94,95} In this case, each EtCO₂ value has a related MRI signal intensity. This technique requires the use of a device that targets the EtCO₂ levels and is used to investigate the entire range of vasoconstriction and vasodilation and to investigate the shape of the MRI signal intensity versus EtCO₂ curve.

Furthermore, it is possible to combine different paradigms in one MRI experiment. A popular choice is to combine a block and a ramp stimulus to extract information related to the dynamics of the MRI response to an abrupt stimulus and information related to the shape and range of the MRI intensity versus EtCO₂ curve.⁹²

1.2.4 Characteristics of CVR response

Definition of CVR magnitude

Using BOLD MRI, CVR magnitude is commonly defined as the relative change in BOLD signal with respect to the change in EtCO₂ and is reported in %/mmHg:⁸³

$$CVR = \frac{\Delta BOLD}{BOLD_0 \cdot \Delta EtCO_2} \times 100 \quad (1.2-13)$$

BOLD₀ is the baseline intensity of the BOLD signal and Δ represents absolute change in the related parameter. However, this definition assumes that the BOLD response to a change in EtCO₂ is linear.

Previous studies have investigated the BOLD response at different EtCO₂ levels by progressively modulating the EtCO₂ levels using a ramp paradigm and allowing the BOLD response to reach stability.^{94,95} They have shown that, in healthy participants, the BOLD response to EtCO₂ is linear in a limited range that includes the subjects' resting EtCO₂ level. Indeed, the MRI response saturates at high hypercapnic stimulus strength either due to the limited

capacity of the blood vessels to dilate further, or due to saturation of the MRI contrast.⁹⁴ A similar phenomenon applies to vasoconstriction.

Dynamics of the CVR response

The BOLD response to a CO₂ challenge is a dynamic process and depends on multiple factors. When a subject is breathing a CO₂-enriched stimulus, CO₂ arrives in the blood through the alveoli of the lungs and travels to the cerebral blood vessels. First, the BOLD response depends on the blood arrival time which can differ between tissues and in cerebrovascular diseases.⁹⁶ Blood arrival time can also be affected by the steal phenomenon or redistribution of blood flow due to competing blood vessels.⁹⁷ Secondly, in the brain, CO₂ crosses the BBB to trigger vasodilation through the relaxation of smooth muscle cells. This process depends on the CO₂ diffusion rate and sensitivity, remaining dilation capacity,^{98,99} BBB permeability and health of the cells surrounding the blood vessel.

Previous studies have investigated ways to measure the dynamics of the CVR response. Blood arrival times were measured using ASL or BOLD during hyper- or hypoxia.^{96,97} Vasodilation response times can be investigated by modelling the BOLD signal using an HRF. When using a linear model between the BOLD signal and shifted EtCO₂ profile (which is equivalent to modelling the BOLD signal as the convolution between the EtCO₂ signal and a delayed delta HRF), the BOLD signal is assumed to be a scaled, potentially delayed, version of the EtCO₂ signal - vasodilation is assumed instantaneous, thus neglecting the vasodilation response time. However, some studies have modelled the BOLD signal as the convolution between the EtCO₂ and an exponential or double-gamma HRF, allowing the shape of the MRI response to differ from the EtCO₂ profile to model slower processes during vasodilation/vasoconstriction.^{91,100}

1.3 Challenges of CVR MRI in cerebral SVD

Since the end of the 20th century, CVR MRI has been developing as a technique to assess the health of cerebral blood vessels, though it has mostly been used to investigate cerebral steno-occlusive pathologies such as Moyamoya disease or carotid stenosis/occlusion. CVR images at clinical field strengths (1.5 – 3T) have a spatial resolution of a few millimetres, which is lower than the resolution needed to observe individual small vessels and their dilation or constriction. This implies that the signal in individual voxels arise from the underlying group of blood vessels. Despite this intrinsic limitation, there is growing interest in applying the technique to SVD research given that vascular dysfunction contributes to SVD pathogenesis. However, the technique has several challenges that need consideration:

- Literature on the CVR experiment presents a wide range of methodologies from MRI acquisition and use of vasodilatory stimulus to data processing, with a lack of consensus regarding their use. Therefore, there is a need to summarise information about this diversity. This would help the community to define a harmonised CVR methodology, which might depend on the pathology investigated.
- Moreover, there is a need to address the diversity in processing methods. Comparisons on the basis of repeatability and reliability are missing, but are essential for greater consensus between studies. Especially, processing methods to extract CVR might be prone to errors when MRI signals have a low temporal contrast-to-noise ratio (tCNR), for example in white matter (WM) tissues, which are less perfused. This is problematic for SVD research, where WMH lesions appear in the WM of SVD patients and blood vessels in such tissues are of interest. Therefore, it is important to understand which processing methods reduce the impact of noise on CVR measurements.

1.4 Aims and outline of the thesis

This thesis aims to:

- i. provide a summary of the diversity of CVR methodologies in order to facilitate translation towards harmonisation of the technique
- ii. compare robustness of region- versus voxel-based processing methods against noise and investigate the reliability of delay-correction methods
- iii. exploit CVR data and show that extracting cerebral pulsatility, another vascular parameter that is of interest in cerebrovascular pathologies, in parallel with CVR estimates is feasible
- iv. investigate the relationship between CVR and SVD features in cross-sectional and longitudinal settings in order to help improve our understanding of SVD pathogenesis.

The thesis is divided into 8 chapters including the current introduction chapter. Hereafter, the content and aims of each chapter are given.

Chapter 2 contains an overview of the multiple CVR MRI acquisition and processing strategies that exist in the literature. A systematic review was performed for studies that measured CVR in humans using MRI.

Chapter 3 assesses repeatability and reliability of CVR measurements based on healthy volunteer data and simulations to optimise aspects of the processing strategy for SVD research.

Chapter 4 provides a proof-of-concept that cerebral pulsatility can be extracted from BOLD-CVR data in healthy volunteers and SVD patients.

Chapter 5 describes the design of an SVD longitudinal study aiming at investigating the relationships between vascular dysfunction, SVD features and disease progression.

Chapter 6 investigates the cross-sectional relationships between CVR and radiological features characterising the SVD burden in the study cohort described in chapter 5.

Chapter 7 focuses on relationships between CVR and progression of radiological SVD features over a period of one year.

Chapter 8 provides a summary of findings and highlights the contributions of this thesis to the fields of SVD and MRI research. It also specifies the limitations of the work and lists potential directions for future research.

2 Cerebrovascular reactivity measurement using magnetic resonance imaging: a systematic review

The aim of this chapter is to provide comprehensive description of how CVR has been measured using MRI in the existing literature and identify potential gaps in the application of the technique in clinical populations. To this end, a systematic review was conducted, peer-reviewed and published in *Frontiers in Physiology* in February 2021.¹⁰¹ I performed the search, analysed the data and wrote the paper. I acknowledge that Dr Michael J. Thrippleton, Dr Michael S. Stringer, Prof Ian Marshall and Prof Joanna M. Wardlaw also contributed to the work by discussing the eligibility and data extraction of some papers and by reviewing the manuscript. All co-authors accepted the publication of the paper in this thesis.

The content of this chapter is based mainly on this published review article. At the end of the chapter, a short update of the review is provided.

2.1 Introduction

CVR reflects the ability of the blood vessels to dilate in order to match tissue blood supply to increased demand and can be investigated by measuring the change in CBF or CBV that vasodilation induces. It is a valuable tool for assessing vascular health in pathologies, including steno-occlusive diseases,¹⁰² while more subtle CVR impairments have been found in Alzheimer's disease¹⁰³ and cerebral small vessel disease.² The measurement of CVR relies on three key elements: the vasodilatory stimulus, the signal acquisition and the processing method.

2.1.1 Vasodilatory stimulus

Vasodilation occurs naturally as a mechanism of CBF auto-regulation, but can also be triggered by exogenous stimuli inducing extracellular and intracellular acidosis. The resulting decrease in potential of hydrogen (pH) relaxes smooth

muscle cells lining the arteries and arterioles, thereby increasing their diameter. Common stimuli include changes in PaCO_2 induced by voluntary modulations of the breathing pattern, including breath-holding, hyperventilation and paced breathing^{83,85,86} or by inhalation of CO_2 -enriched gas.^{83,84} As PaCO_2 cannot easily be measured in vivo, EtCO_2 , the most recent end-tidal CO_2 partial pressure, is often used as a surrogate and can be measured by recording the CO_2 level in the exhaled gas using a gas monitor. Several approaches exist to manipulate PaCO_2 : inhalation of gas with fixed CO_2 concentration (e.g. CO_2 -enriched air or carbogen), rebreathing the exhaled gas, EtCO_2 targeting manually or using a computer-controlled device.⁸⁴ Vasodilation can be induced without modulating the composition of the inhaled gas or breathing pattern by injection of ACZ, a carbonic anhydrase inhibitor that causes acidosis.⁸⁸

2.1.2 Signal acquisition

Several imaging methods can assess haemodynamic changes induced by the vasodilatory stimulus. Positron emission tomography (PET), single-photon emission computed tomography (SPECT)¹⁰⁴ and CT¹⁰⁵ have all been used to measure CVR, but involve ionising radiation and have low temporal resolution. TCD is a practical alternative, but has a limited field of view that allows blood velocity measurements only in parts of single large vessels, which do not necessarily reflect local changes in tissue blood supply.^{106,107} MRI is a non-invasive, non-ionising technique which allows CVR mapping using contrasts related to CBF and/or CBV. ASL and phase-contrast (PC) MRI measure CBF in tissue and large vessels respectively,^{108,109} while vascular space occupancy (VASO) MRI measures CBV.¹¹⁰ Dynamic susceptibility contrast (DSC) MRI measures both CBF and CBV¹¹¹ by monitoring the T_2 or T_2^* -weighted signal following intravenous injection of a gadolinium-based contrast agent. BOLD imaging, using a T_2 or T_2^* -weighted sequence, can also measure CVR due to its sensitivity to a combination of CBF and CBV.

2.1.3 Processing method

The signal change due to the vasodilatory stimulus must be converted into a quantitative or semi-quantitative measurement of CVR using one of several methods. Pre-versus-post-stimulus subtraction of the MRI signal relies on the computation of the absolute or relative signal difference before and after the stimulus has been applied.^{112,113} Often, the pre- and post-values are calculated by taking the average of the MRI volumes acquired during each period respectively, discarding volumes that are acquired during the transition period. Linear regression is a method that investigates the linear relationship between the dependent variable (in this case the MRI signal or derived CBF) and independent variables (e.g. EtCO₂, to reflect the vasodilatory stimulus; time, to model a linear signal drift),^{83,114} allowing the MRI time course to be modelled using multiple predictors simultaneously. Cross-correlation quantifies the similarity between two signals (e.g. the MRI signal and EtCO₂) as a function of their relative time delay¹¹⁵ and has been used as a measure of CVR. Nonlinear fitting involves modelling the MRI signal as a nonlinear function.^{116,117} It requires some initial estimate of the CVR and other parameters such as CVR delay, and can be more challenging to implement than linear regression, but has the advantage that any models can be used to fit the MRI signal. Some models (e.g. calibrated fMRI models) also allow quantitative estimation of CVR and other parameters that can be of interest such as cerebral metabolic rate of oxygen (CMRO₂). Frequency-based analysis includes transfer function¹¹⁸ and Fourier⁹³ analyses. In both methods, the signals of interest (e.g. the MRI signal and EtCO₂) are transformed into the frequency domain. The magnitude of the signal at the stimulus frequency is then defined as the CVR. Finally, the standard deviation of the MRI signal^{119,120} can be computed as a metric of CBF change due to natural vasodilation and vasoconstriction.

2.1.4 Aims of the review

Since many combinations of the above stimuli, imaging methods and analysis techniques are possible, there are potentially many different ways to measure

CVR in vivo, resulting in a high degree of methodological diversity in the literature. Previous reviews described common CVR MRI experiments^{83,84,86,121,122} or CVR data analysis.¹²³ However, as far as we are aware, there are no systematic reviews detailing the breadth of CVR MRI acquisition techniques, processing methods and applications that have been presented and used in the literature.

We conducted a systematic literature review of papers reporting the use of CVR MRI techniques. We present an overview of the different aspects of the CVR MRI experiment reported and applied in the literature, describing the most common methods and clinical research applications. We classified and systematically analysed reports of the MRI techniques, vasodilatory stimuli, data processing methods and study populations. Based on these findings we identified recent practices, trends, technical findings and evidence from clinical studies to inform future application and standardisation of CVR MRI protocols.

2.2 Materials and methods

2.2.1 Search strategy

We systematically reviewed the EMBASE and MEDLINE databases from 1980, until June 2020 using Ovid. The search strategy combined terms relating to: “Cerebrovascular reactivity”, “MRI”, “BOLD”, “ASL”, “PC”, “hypercapnia”, “acetazolamide” and “CO₂”. We manually added relevant articles from the authors’ libraries. The search was not constrained to English-language literature. Full details of the search strategy are provided in the appendix (Appendix A1).

2.2.2 Eligibility criteria

We included all studies that investigated changes in cerebral blood flow or cerebral blood volume using MRI due to vasodilation or vasoconstriction in humans. We excluded reviews, conference abstracts, editors’ notes and case reports (single-subject studies focussed on methodological aspects of CVR

were included). We removed studies that did not investigate induced vasodilation in the brain or used another imaging modality (e.g. CT, PET) to measure CVR. Studies that measured the change in the BOLD signal in response to a functional task and hypercapnia but did not compute a CVR metric were also excluded.

2.2.3 Data extraction

One author (E.S.) screened the titles and abstracts of all potentially eligible publications to exclude duplicates and assess eligibility against the inclusion criteria before reading the full text of the remaining articles to determine eligibility. Eligibility and data extraction were discussed with other authors where queries around inclusion or exclusion, or data extraction arose.

We extracted population characteristics, including pathology, sample size, age and gender. We recorded MRI acquisition parameters including magnetic field strength, type of pulse sequence and sequence parameters (e.g. TR, TE, spatial resolution, field-of-view). We recorded the type of vasodilatory stimulus, measurement of EtCO₂ and/or end-tidal O₂ (EtO₂), stimulus paradigm and, where available, information on tolerability, number and reason for any excluded or failed scans. Finally, we extracted information on the pre-processing steps, delay correction/computation methods and CVR processing methods applied, reported grey and white matter CVR values in healthy volunteers and relevant findings.

2.3 Results

2.3.1 Search results

We identified 732 articles, 176 of which were removed as duplicates (Figure 2-1). Of the remaining 556 papers, 317 were excluded on review of the title and abstract due to a lack of analysable data or insufficient detail (n=192: conference abstracts (n=131), reviews (n=34), and case reports and notes to the editor (n=27)), inaccessibility (n=1), only reporting rodent studies (n=2),

using other modalities (e.g. PET, TCD, CT, SPECT) (n=71) and not measuring CVR (n=51). After full text review an additional 14 papers were removed because they used other imaging modalities to measure CVR (n=6) or did not measure CVR (n=8). Additionally, 24 articles were added from the authors' libraries. We included 235 papers in the review. Summary data extracted from each study is included in the online supplementary material: <https://www.frontiersin.org/articles/10.3389/fphys.2021.643468/full#supplementary-material>.

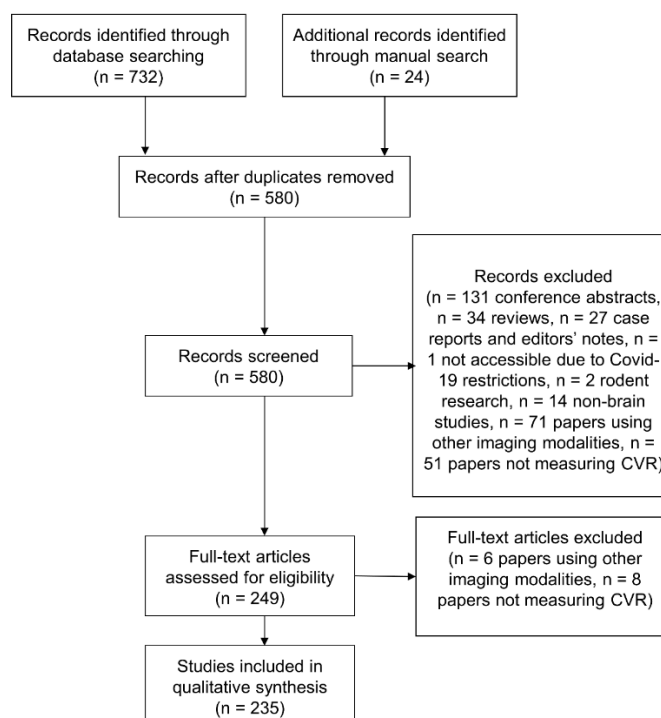


Figure 2-1: Flow diagram of the literature search.

2.3.2 Population characteristics

The studies included 5369 unique participants. 36 subjects were excluded before CVR due to contraindication to MRI (n=6) or ACZ (n=3), claustrophobia in the MRI scanner (n=5), too large to fit in the MRI scanner (n=1), anxiety during pre-testing of the stimulus (n=1) and intolerance of the stimulus (n=20). The remaining 5333 unique participants who had a CVR scan comprised 2394 patients and 2939 healthy participants. All studies reported a sample size, with

a mean sample size of 35 (median: 19, range: 1-536). Forty-five studies had fewer than 10 subjects whereas 9 included more than 100 subjects. Twelve papers did not report any age information, a further 18 papers reported only the age range. The mean age, computed as the mean of the mean or median ages, was 44.3 (1.4-92) years. The median gender distribution was 43% females and 57% males, excluding the 18 studies not reporting gender distribution.

The total number of scans including longitudinal scans was 7437. The number of scans excluded from analyses is 518/7437 (7%), not including scans that were selected from a database for being of good quality. Per study, the mean percentage of datasets excluded from analysis was 6% (range: 0-38%). Scans were excluded for one or more reasons: incomplete dataset (28/518, 5%), subject's discomfort (79/518, 15%), irregular breathing (3/518, 1%), non-compliance (38/518, 7%), technical issues (67/518, 13%), pre-processing issues (5/518, 1%), poor data quality (40/518, 8%), motion artefacts (183/518, 35%), outlier CVR values (13/518, 3%), non-CVR related (75/518, 14%, e.g. post-operative stroke, resolution of stenosis, hematoma, issue with therapeutic intervention) and no reasons reported (2/518, 0.3%).

Information on tolerability of the CVR experiment ranged from information regarding subject withdrawal to subjective rating of tolerability and was reported in 51/235 (22%) studies (1162/5333 unique subjects). Overall, the CVR experiment in these 51 studies was mostly described as well-tolerated. One article studied the tolerability of 434 CVR (294 subjects) scans acquired with EtCO₂ targeting BOLD MRI and concluded that it was well tolerated.¹²⁴ Six studies reported subjective tolerability: the experiment was rated as tolerable to very tolerable with minimal discomfort on average in each study. Twenty-three studies detailed complaints of discomfort: 11 studies reported no complaints or adverse effects whereas 12 did. These 12 studies (618 subjects) reported one hundred and twenty complaints transient to the CVR scan: respiratory symptoms due to gas inhalation such as breathing resistance and shortness of breath (n=77), anxiety and/or claustrophobia (n=16), dizziness

and/or headache (n=10), narrowness of head coil with gas apparatus (n=4), tachycardia (n=3), paraesthesia (n=3), chest tightness (n=1), conjunctive erythema (n=1), tremor (n=1), hand weakness (n=1), nausea, confusion and blurred vision (n=1) and no details of the complaints (n=2). No long-lasting symptoms were reported and no studies using acetazolamide injection detailed complaints or adverse effects. In 17 studies, 79 scans were defined as intolerable by the subject due to: anxiety (n=21), claustrophobia (n=16), discomfort related to gas apparatus in the scanner (n=9), position in the head coil (n=2) and no details (n=31).

2.3.3 Pathologies

Cerebral steno-occlusive diseases (e.g. Moyamoya disease, carotid stenosis/occlusion) were the most commonly investigated diseases (72/235 studies, 31%), followed by dementia and cognitive impairments (9/235, 4%), normal ageing (8/235, 3%), small vessel disease (7/235, 3%), sport-related concussions (7/235, 3%), obstructive sleep apnoea (5/235, 2%), stroke (5/235, 2%; one of which also investigated CVR in steno-occlusive disease), traumatic brain injury (4/235, 2%), tumours (4/235, 2%), diabetes with or without hypertension (3/235, 1%), and miscellaneous (18/235, 8%). Of the 142 articles reporting CVR measurements in pathology (referred to in Table 2-1), 70 studies assessed CVR to investigate pathophysiology, 48 studies explored the technical feasibility of a methodology to detect CVR impairment, 13 studies investigated the effect of a therapeutic intervention on CVR (surgical intervention for steno-occlusive diseases such as revascularisation, candesartan therapy for diabetes, bariatric surgery for obese subjects, haemodialysis for end-stage renal disease, therapeutic continuous positive airway pressure for obstructive sleep apnoea), six studies investigated the progression of pathologies, and five studies looked at the effect of CVR on fMRI BOLD activation. Relative to healthy controls, CVR was lower in patients in most of the pathologies^{99,110,114,125–127} and CVR delays were longer in steno-occlusive diseases, small vessel disease and dementia.^{114,118,128–130}

2.3.4 MRI technique

The number of CVR MRI studies that were conducted at 3T is 178/235 (74%), with the remainder acquired at: 1.5T (47/235, 20%), 7T (9/235, 4%), 2T (2/235, 1%) and a combination of 1.5 and 3T (3/235, 1%). Studies used one or more MRI techniques to acquire CVR data (Figure 2-2): BOLD (155/235, 66%), ASL (41/235, 17%), dual-echo providing simultaneous ASL and BOLD data (27/235, 11%), PC (12/235, 5%), DSC (11/235, 5%) and VASO (3/235, 1%). In recent publications, BOLD, ASL and dual-echo ASL/BOLD are the most common MRI techniques. Summary MRI parameters for the BOLD gradient-echo echo-planar imaging (GRE-EPI), pseudo continuous ASL (pCASL) and dual-echo ASL/BOLD GRE-EPI techniques at 3T are given in Table 2-2.

Three studies (n=18) found BOLD-derived CVR values were lower at lower magnetic field strengths,^{131–133} two of which (n=9) reported a linear relationship between BOLD-derived CVR and the field strength.^{131,132} In one study (n=16), ASL-derived CVR did not differ at different field strengths.¹³⁴ One study (n=8) reported longer post-labelling delay results in lower baseline CBF and ASL-CVR measurements.¹³⁵ Use of EPI with parallel imaging compared to spiral imaging, reduced signal loss due to susceptibility-induced magnetic field gradients in BOLD-CVR measurements without affecting sensitivity, which was defined as the CVR t-statistic (n=5).¹³⁶ Furthermore, one study (n=5) showed that using simultaneous multi-slice acceleration of factor 2 and 3, can reduce scan duration by at least a half compared to conventional EPI while maintaining the CVR sensitivity.¹³⁷ Compared to single-echo ASL or BOLD EPI, a multi-echo (four echoes) EPI acquisition followed by T_2^* fitting of the signal decay had higher inter-scan repeatability of breath-hold CVR analysed across voxels, CVR sensitivity and test-retest reliability analysed using the intra-class correlation coefficient (n=14).¹³⁸

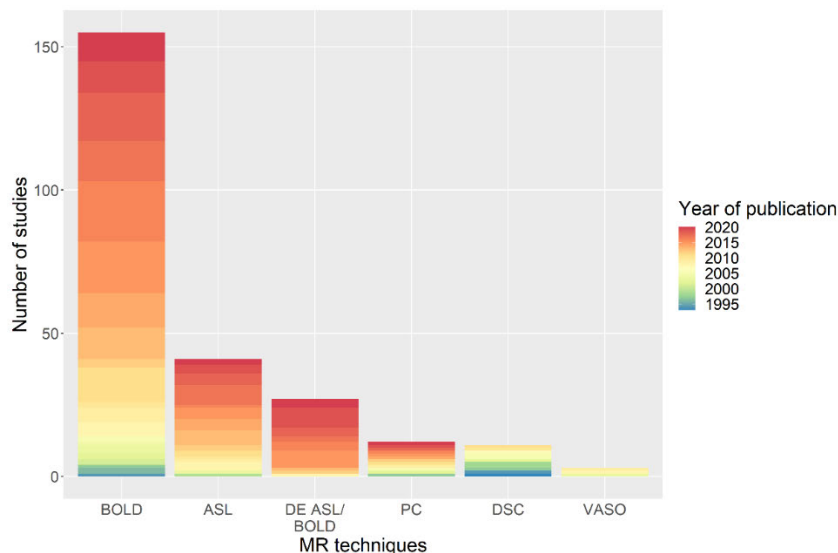


Figure 2-2: Distribution of the MRI sequences used in studies with the associated year of publication of the paper. (BOLD = blood-oxygen-level-dependent, ASL = arterial spin-labelling, DE = dual-echo, PC = phase-contrast, DSC = dynamic susceptibility contrast, VASO = vascular space occupancy)

2.3.5 Vasodilatory stimulus

To induce vasodilation, several stimuli were employed in the literature (Figure 2-3A): EtCO₂ targeting manually or using a computer-controlled device such as RespirAct (81/235 studies, 34%), fixed inspired gas administration (69/235, 29%), breathing modulations (52/235, 22%), ACZ injection with median dose of 1 g (29/235, 12%), rebreathing (10/235, 4%), resting-state haemodynamic fluctuations (8/235, 3%) and not reported (1/235, 0.4%). Three different fixed inspired gases were identified: CO₂-enriched (67%), O₂-enriched (i.e. hyperoxia, 10%), and CO₂- and O₂-enriched air (i.e. carbogen, 23%). In some studies, these gas compositions were alternated during the same paradigm with or without intermittent normal air periods using the fixed inspired gas, EtCO₂ targeting methods: alternating hypercapnia and hyperoxia (15/235, 6%), alternating CO₂-enriched air and carbogen (1/235, 0.4%). For fixed inspired CO₂ paradigms, the median percentage of inhaled CO₂ was 5% (range: 2-10%). While the combination of MRI sequence and stimulus generally varied across studies DSC-MRI was used only with ACZ injection.

Table 2-1: Pathologies in which CVR was investigated. “Mean age” was computed by taking the average across studies of the reported mean/median age of the patients. (CPAP = continuous positive airway pressure, MELAS = Mitochondrial encephalomyopathy, lactic acidosis and stroke-like episodes, HIV = Human immunodeficiency viruses, NA = not applicable, OSA = obstructive sleep apnoea)

Pathology	Number of studies	Number of patients/controls	Mean age of patients/controls	Findings
Cerebral steno-occlusive diseases ^{82,89,91,98,102,110–113,115,116,118,124,127,128,139–195}	72	1786/ 541	51.4/ 44.9	<ul style="list-style-type: none"> - Lower CVR than healthy controls^{82,98,150,156,165,177} - Longer delays than healthy controls^{118,128,156,179} - Increased CVR^{157,170,183} and smaller delays¹⁵⁷ after surgical intervention
Dementia and cognitive impairment ^{74,99,130,196–201}	9	770/ 125	60.5/ 68.1	<ul style="list-style-type: none"> - Lower CVR than healthy controls^{74,198} - Longer delays than healthy controls¹³⁰ - Higher CVR deficit versus healthy controls associated with higher leukoaraiosis⁷⁴ and hypertension²⁰¹ - Lower CVR in the bilateral frontal cortices of Alzheimer’s patients compared to patients with vascular dementia²⁰⁰
Normal ageing ^{71,95,202–207}	8	NA/374	Range: [20, 90]	<ul style="list-style-type: none"> - Lower CVR at older ages^{95,202–207} - Greater WM CVR and shorter delay with increasing age⁷¹

Small vessel disease ^{72,114,129,208-211}	7	272/54	67.4/ 45.7	<ul style="list-style-type: none"> - Lower CVR with increased WMH burden^{72,208} and compared to healthy controls^{114,129,208,209} - Longer delays than healthy controls^{114,129,210} - Reduced WM CVR associated with higher WMH volumes, basal ganglia PVS and higher venous pulsatility and lower foramen magnum CSF stroke volume⁷² - Lower baseline CVR associated with progression of WMH but not microbleeds or lacunar infarcts²⁰⁸ - Lower CVR associated with increased number of vascular risk factors such as hypertension, diabetes, hypercholesterolemia²⁰⁹, lower fractional anisotropy, lower CBF and CBV and higher mean diffusivity²¹¹ - Lower CVR and longer delays in NAWM that progressed into WMH²¹⁰
Sport-related concussions ²¹²⁻²¹⁸	7	113/ 128	18.6/ 21.2	<ul style="list-style-type: none"> - Lower CVR in the default mode network at mid-season and one month post-season compared to pre-season baseline. Decrease in CBF occurred only one month after season²¹⁸ - Longitudinal reduction in CVR during season compared to pre-season baseline was associated with prolonged accumulation to high magnitude acceleration events²¹⁴ - Predominant increase in CVR compared to baseline during the recovery phase but remains mostly altered despite clinical recovery²¹⁵

				<ul style="list-style-type: none"> - Higher CVR in clinically recovered patients with history of concussions than in athletes without^{216,217}
Obstructive sleep apnoea ^{219–223}	5	125/55	50.6/ 44.5	<ul style="list-style-type: none"> - Greater CVR than in healthy controls measured using ASL with BH, BOLD with BH²²³ and BOLD with EtCO₂ targeting²²¹. - ASL response to fixed CO₂ enriched air reduced in patients with OSA compared to healthy controls, whereas BOLD response to fixed CO₂ enriched air or BH did not show group differences²²². - Reduced CVR in the motor areas controlling the upper airway musculature compared to healthy controls²¹⁹. - No change in CVR upon CPAP withdrawal²²⁰
Stroke ^{125,224–226}	5	135/ 102	58.7/ 51.0	<ul style="list-style-type: none"> - Lower CVR in impaired tissue and compared to healthy controls^{125,225,226} - Higher CVR with increasing distance from lesion¹¹¹ - Reduced CVR associated with peri-infarct T2 hyperintensities, greater infarct volume and worse outcomes²²⁶
Traumatic brain injury ^{126,227–229}	4	90/77	32.2/ 31.8	<ul style="list-style-type: none"> - Lower CVR than healthy controls in one study²²⁸ - No difference in CVR between patients and healthy controls in one study²²⁹ - Lower GM CVR with more concussion symptoms¹²⁶

Gliomas ^{230–233}	4	50/12	43.9/ not reported	- Lower CVR on ipsilateral side for low and high grade gliomas
Diabetes ^{234–236}	3	103/32	67.5/ 61.8	<p>- Lower CVR in diabetic hypertensive patients than in only hypertensive patients^{234,235}</p> <p>- Higher CVR in bilateral prefrontal lobe in one study²³⁶</p> <p>- Increased CVR after candesartan therapy²³⁴</p>

Pathologies investigated in two studies:

- Cardia index and coronary artery disease^{237,238}
- Sickle cell disease^{239,240}
- Multiple sclerosis^{241,242}
- Obesity^{243,244}
- Brain arteriovenous malformation and cerebral proliferative angiopathy^{245,246}
- Parkinson's disease^{247,248}

Pathologies investigated in one study:

- End-stage renal disease²⁴⁹
- Bipolar disorder²⁵⁰
- Late-life depression²⁵¹
- Late-onset epilepsy²⁵²
- HIV²⁵³
- Aneurysmal subarachnoid haemorrhage²⁵⁴
- MELAS²⁵⁵

Table 2-2: Median values and ranges of MRI parameters at 3T found in the literature. (PLD = post-labelling delay, TR = repetition time, TE = echo time, FOV = field-of-view, GRE = gradient-echo, EPI = echo-planar imaging, SMS = simultaneous multi-slice)

MRI technique	Number of studies	TR [ms]	TE [ms]	Flip angle [°]	Spatial resolution [mm]	3D FOV [mm]	PLD [ms]	Label duration [ms]	GRAPPA/SENSE (number of studies)	SMS (number of studies)
BOLD GRE-EPI	118	2000 [66.4, 3000]	30 [20, 50]	85 [40, 90]	3.44x3.44x4 [1.72x1.72x2, 4x4x8]	225x220x126 [192x150x18, 256x256x195]	-	-	2 [1.8, 3] (14)	3 [2, 6] (2)
pCASL GRE-EPI	16	4000 [3000, 4500]	14 [10, 20]	90 [90, 90]	3x3x6 [3x3x4, 7x7x7]	240x240x119 [220x220x54, 240x240x135]	1525 [900, 2000]	1650 [1500, 1650]	2.5 [2, 2.5] (8)	(0)
Dual-echo pCASL/ BOLD GRE-EPI	22	4000 [3000, 4500]	TE ₁ = 10 [8.4, 16], TE ₂ = 30 [25, 47]	90 [90, 90]	3.44x3.44x5 [3x3x3.9, 4.5x4.5x7]	240x240x116.1 [192x192x87, 256x256x132]	1220 [600, 1868]	1650 [1200, 2000]	2 [2, 2.3] (10)	(0)

Block design paradigms were most common (212/235 studies, 90%) with a median stimulus plateau duration of 1 minute. The median total experiment duration was 9 min (Figure 2-3B). One study did not specify the type of paradigm, and 12 further studies did not report the duration of the CVR experiment.

Removing studies that used ACZ stimulus, 160/207 studies measured EtCO₂ (77%) of which 21 did not report the targeted or achieved EtCO₂ variation (14%), 80 studies also measured EtO₂ (39%). The median EtCO₂ change induced by the stimulus was 9 mmHg (range: 2.2-28 mmHg). Seventy-five studies reported mean baseline EtCO₂ at rest (47%), with a median value of 39 mmHg (range: 31.2-43.4 mmHg). 21% of the studies that used EtCO₂ targeting controlled the baseline EtCO₂ (40 mmHg for all studies) instead of using the individual EtCO₂ value when breathing normal air.

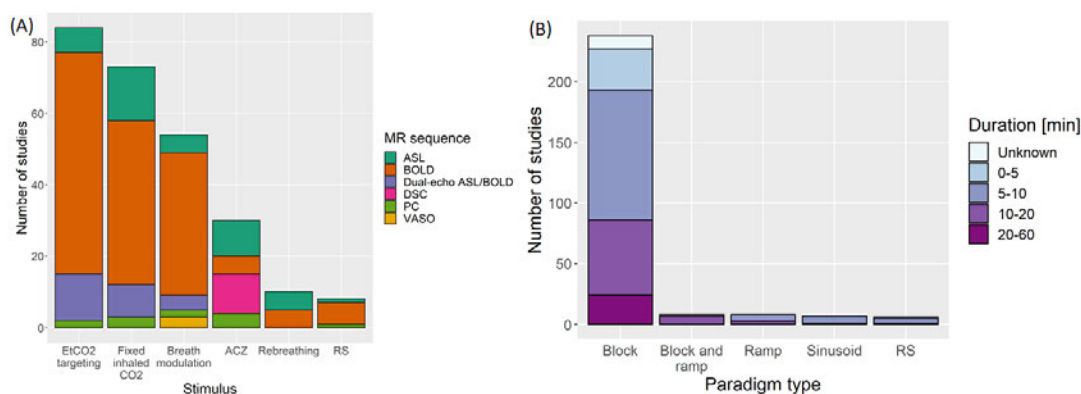


Figure 2-3: Distribution of the A) stimuli with the associated MRI sequence and B) paradigm types with associated total duration of the CVR experiment. In A, the “breath modulation” stimulus includes breath-holding, paced breathing and hyperventilation stimuli. (ACZ = acetazolamide injection, RS = resting-state, BOLD = blood oxygen-level dependent, ASL = arterial spin-labelling, PC = phase contrast, DSC = dynamic susceptibility contrast, VASO = vascular space occupancy)

One study (n=4) found BOLD response to EtCO₂ is 60 times higher than to EtO₂, but demonstrated that during hypercapnic BOLD-CVR experiments, EtO₂ should be controlled if the change in EtCO₂ is small compared to the change in EtO₂.²⁵⁶ One study (n=9) demonstrated that carbogen should not be

used with BOLD or ASL to measure CVR due to a lack of correlation between both MRI techniques as opposed to CVR measurements using CO₂-enriched air with BOLD or ASL.²⁵⁷ Another study (n=20) found that, for a gas challenge, an effect of at least 2 mmHg EtCO₂ change is required to detect haemodynamic impairment using BOLD at 3T.¹⁶⁵ RS-BOLD was found to give CVR results that were associated with fixed-inspired CO₂ BOLD (n=48)⁸² and RespirAct BOLD (n=13)²⁵⁸ measurements. One study (n=8) reported differences in response amplitude and onset time depending on whether BH was performed before and after expiration.²⁵⁹ For BOLD-BH, one study (n=6) demonstrated that the fraction activation volume saturated for breath-hold durations of 20 s and above; thus recommended using breath-hold durations of 20 s to give sufficient sensitivity to BOLD signal changes to detect impaired CVR.²⁶⁰

2.3.6 CVR data processing methods

Common pre-processing steps that were reported (Figure 2-4) were sequence-dependent and included motion correction (167/235 studies, 71%), spatial smoothing (107/235, 46%), registration of functional volumes to MNI or subject space (96/235, 41%), ROI or whole brain delay correction (93/235, 40%), drift removal/modelling (79/235, 34%), voxel-wise delay correction (62/235, 26%) and discarding transient MRI volumes to consider only those where steady-state signal was reached (42/235, 18%). Only 3% of papers corrected for sampling line delay. Slice-time correction was used in 51 of 180 BOLD/DE-BOLD studies. Eroding the edges of the ROIs can reduce vascular contamination of CVR due to larger responses to CO₂ in blood vessels than in tissues.¹¹⁴ T₁ correction was recommended for ASL-CVR data involving the use of carbogen or other hyperoxic gas because of changes in the longitudinal relaxation time during hyperoxia (n=24).²⁶¹ The most common software packages used for pre-processing and/or CVR analysis were Statistical Parametric Mapping (SPM, 89/235 studies, 38%), in-house Matlab (The Mathworks, Natick, MA, United States) software (90/235, 38%), FMRIB Software Library (FSL, 65/235, 28%) and Analysis of Functional NeuroImages

(AFNI, 54, 23%) (some studies used more than one package in combination). Only one in-house Matlab script (for pre-processing BOLD and EtCO₂ data) reported to be publicly available.²⁶²

Of the six classes of CVR calculation methods identified, linear regression is the most common method overall (149/235 studies, 63%) and in recent publications. However, several newer methods are under development including frequency-based analysis.¹¹⁸ The main reference signal used to compute linear regression or cross-correlation is the EtCO₂ (89/235 studies, 38%). An HRF was incorporated in the MRI signal model in 14% of the studies (32/235), with the single or double gamma function being the most common choice (22/235 studies, 9%). A relatively new method to find an appropriate regressor is RIPTiDe (Regressor Interpolation at Progressive Time Delays), which derives the reference signal from the MRI data by iteratively applying principal component analysis on aligned MRI time courses until convergence of the regressor.^{90,115} Twenty-one studies did not clearly describe the CVR processing method, of which two included no information, these were excluded from the summary of CVR processing method (Figure 2-5A).

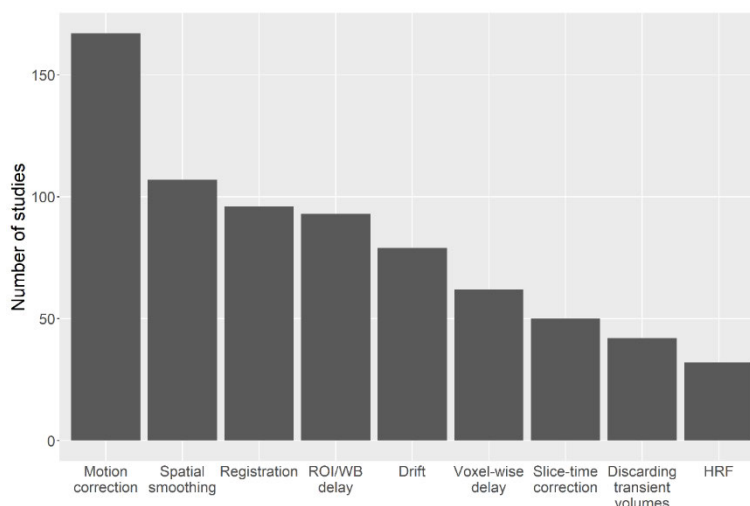


Figure 2-4: Bar chart showing the number of studies that apply different pre-processing steps. (ROI = region-of-interest, WB = whole brain, HRF = haemodynamic response function)

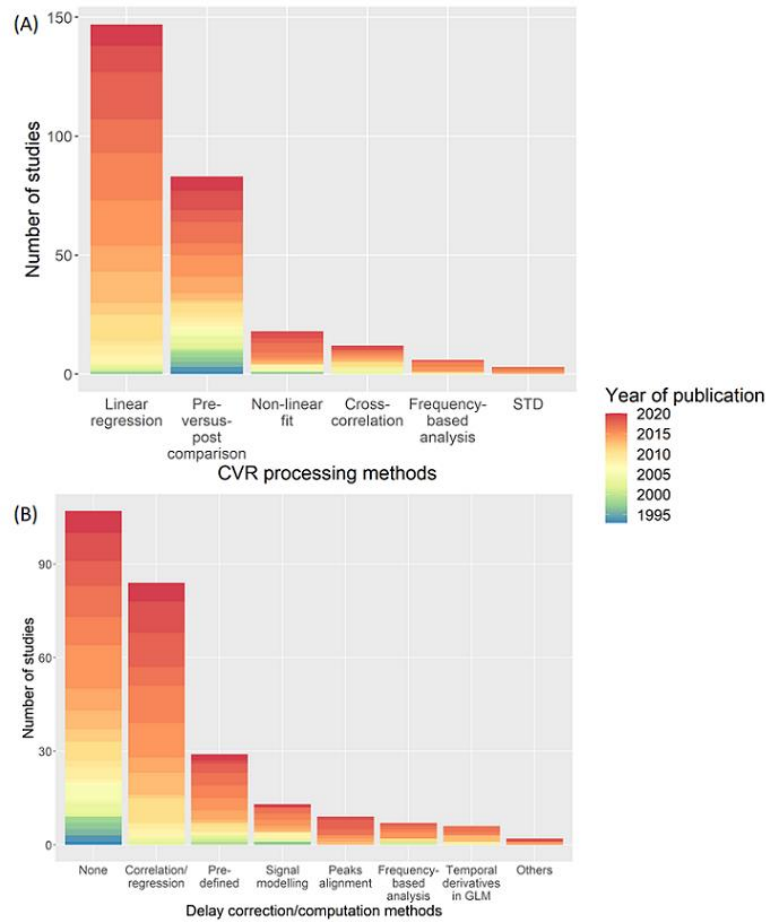


Figure 2-5: Distribution of the (A) CVR processing and (B) delay computation methods with the associated year of publication of the paper. The category “Others” in (B) includes deconvolution to find the HRF between the EtCO₂ and the MRI signal, and GLM with two (“fast” and “slow”) regressors. (STD = standard deviation of MRI signal, HRF = haemodynamic response function, GLM = general linear model)

Dynamic aspects of CVR (e.g. lung-to-brain delay, response time) were computed in 128/235 studies (54%) using different methods (Figure 2-5B), however, some studies used different MRI techniques and multiple associated delay processing methods. Fourteen of the delay computation methods were not clearly described and 8 of which could not be included in Figure 2-5B. Cross-correlation- and linear regression-based methods can be used to compute CVR delay by determining the time shift that gives the best correlation between the BOLD signal and a reference signal (e.g. EtCO₂). The most

common delay computation methods are cross-correlation- or, equivalently, linear regression-based approaches (84/128 studies, 66%) and pre-defined delay, e.g. from literature, voxel examination, (29/128, 23%). The delay between two signals can be found using linear regression or cross-correlation by determining the time shift giving the best correlation between these two signals. As with CVR computation, delay computation is an evolving area and new methods are arising including obtaining the delay directly from the HRF between the BOLD signal and EtCO₂.¹²⁹ One study corrected the hypercapnic delay for delay due to the vasculature (i.e. the delay it takes for the blood and CO₂ to travel from the lungs to the brain tissues) by using the BOLD delay from a hyperoxia challenge as a surrogate of vasculature delay and assuming no vasodilation due to hyperoxia.⁹⁷ This correction can distinguish between delay due to vasculature and delay due to vasodilation.

CVR values in whole brain, grey and white matter of healthy volunteers are summarised in Table 2-3. The associated processing methods were linear regression (72/104, 69%), pre-versus-post stimulus value comparison (17/104 values, 16%), non-linear signal modelling (13/104, 13%) and frequency-based analysis (2/104, 2%). CVR in grey matter (GM) was higher than CVR in WM. Moreover, measuring WM CVR using ASL is not common, probably due to the fact that ASL suffers from low contrast-to-noise ratio (CNR).⁸³

Table 2-3: Mean/median CVR values at 3T in healthy volunteers as a function of the age range (in the square brackets are the minimum and maximum values and in the round brackets is the number of values and number of subjects used to compute the mean). The associated processing methods were linear regression, pre-versus-post stimulus value comparison, non-linear signal modelling and frequency-based analysis.

Age range	Whole brain		Grey matter		White matter	
	%BOLD signal change/mmHg	%CBF/mmHg	%BOLD signal change/mmHg	%CBF/mmHg	%BOLD signal change/mmHg	%CBF/mmHg
< 30	0.19/0.18 [0.14, 0.24] (6 studies, 94 subjects)	4.5 (1 study, 16 subjects)	0.35/0.26 [0.05, 1.80] (17 studies, 294 subjects)	3.69/3.6 [1.9, 6.6] (7 studies, 124 subjects)	0.12/0.12 [0.03, 0.29] (12 studies, 236 subjects)	1.1 (1 study, 18 subjects)
30-50	0.22/0.22 [0.11, 0.28] (15 studies, 169 subjects)	4.64 (1 study, 16 subjects)	0.26/0.26 [0.14, 0.44] (10 studies, 127 subjects)	3.60/3.28 [2.40, 5.11] (3 studies, 45 subjects)	0.12/0.13 [0.08, 0.18] (8 studies, 101 subjects)	-
> 50	0.21/0.21 [0.15, 0.31] (6 studies, 120 subjects)	3.58/3.4 [2.2, 5.30] (4 studies, 279 subjects)	0.36/0.36 [0.13, 1.30] (6 studies, 124 subjects)	2.12/2.13 [2.10, 2.15] (2 studies, 21 subjects)	0.13/0.12 [0.05, 0.33] (5 studies, 117 subjects)	-

2.3.7 Repeatability, reproducibility and accuracy of CVR measurements

CVR values determined using MRI were generally found to be similar or well-correlated with those obtained using other imaging modalities such as PET, SPECT or TCD (Table 2-4: 10 studies, 193 subjects). Within- and between-day repeatability of MRI was studied mostly in healthy participants and in some stroke and steno-occlusive patients (Table 2-5: 14 studies, 191 subjects). The reported coefficients of variation show that CVR measurements are less repeatable between- than within-days^{263,264} and less repeatable in WM than in GM due to lower CNR in WM.^{114,263}

CVR MRI measurements were also compared between MRI techniques. BOLD-CVR and ASL-CVR were well-correlated using fixed CO₂ concentration (n=127)^{191,257,265} and computer-controlled EtCO₂ using RespirAct (n=13).²⁶⁶ One study found no correlation between BOLD-CVR and ASL-CVR using carbogen (n=9).²⁵⁷ Using acetazolamide DSC-CVR correlated well with BOLD-CVR (n=16),¹¹³ but there was a lack of agreement between DSC-CVR and PC MRI (n=8).²⁶⁷

2.3.8 The relationship between BOLD response and PaCO₂

The healthy BOLD signal response to CO₂ was found to be sigmoidal in two studies (n=18).^{94,268} The sigmoid model of the BOLD response to CO₂ was used in a further three studies (n=65).^{92,95,165} In four studies, vasodilatory resistance to CO₂ was modelled using the BOLD response.^{98,99,139,190} The relationship between resistance and CO₂ was assumed sigmoidal due to the limited ability of the blood vessels to constrict and dilate (n=141). One study (n=32) suggested that steal phenomenon associated with some pathologies could alter the sigmoid relationship between CO₂ and vasodilatory resistance.¹³⁹

Table 2-4: Comparison of CVR values measured using MRI versus alternative imaging modalities. (TCD = transcranial Doppler ultrasound, BH = breath-hold, BOLD = blood oxygen level-dependent, ACZ = acetazolamide, SPECT = single photon emission computed tomography, CC = correlation coefficient, CV = coefficient of variation, RI = repeatability index, GM = grey matter, DSC = dynamic susceptibility contrast, MCA = middle carotid artery, ICC = intraclass CC, HC=healthy controls, SOD=steno-occlusive disease)

References	MRI technique	Comparator	Population	Results
Ziyeh et al., 2005 ¹¹⁶	BOLD; fixed inhaled CO ₂	TCD; fixed inhaled CO ₂	20 SOD	Pearson CC for signal change in MCA territory: $r=0.71$
Fierstra et al., 2018 ¹⁸⁷	BOLD; EtCO ₂ targeting	PET; ACZ	16 SOD, 10 HC	- Pearson CC for CVR difference unaffected vs affected hemisphere: $r^2=0.47$ - Pearson CC for CVR difference unaffected vs affected hemisphere in MCA territory: $r^2=0.61$
Herrera et al., 2016 ¹⁴⁹	BOLD; BH	TCD; BH	15 SOD, 7 HC	Cohen's kappa coefficient for the visual classification of normal or impaired CVR in the ipsilateral lentiform nucleus between the two methods: Overall, $\kappa=0.54$; Controls, $\kappa=0.69$; Patients, $\kappa=0.43$
Shiino et al., 2003 ¹⁶⁶	BOLD; BH	SPECT; ACZ	10 SOD, 17 HC	- Linear correlation between mean whole brain %BOLD change with mean whole brain change in CBF from SPECT: $r=0.70$
Hauser et al., 2019 ¹⁶⁹	BOLD; BH	PET; ACZ	20 SOD	- Spearman CC for maps: $r=0.90$ - Pearson CC for relative signal change in vascular territories relative to cerebellum: $r=0.71$

Heijtel et al., 2014 ²⁶⁹	ASL; fixed inhaled CO ₂	PET; fixed inhaled CO ₂	16 HC	<ul style="list-style-type: none"> - Pearson CC for GM CBF: $r^2=0.30$ for baseline, $r^2=0.12$ for hypercapnia - GM CVR [%/mmHg]: 2.82 for ASL vs. 2.50 for PET - Inter-modality RI: 22.9% for baseline, 30.3% for hypercapnia
Uchihashi et al., 2011 ¹⁵³	ASL; ACZ	SPECT; ACZ	20 SOD	<ul style="list-style-type: none"> - Spearman rank CC of mean relative CVR in frontal and temporal lobes: $r=0.88$ - Accuracy: mean difference in CVR of frontal and temporal lobes: 1.3%
Kim et al., 2011; ¹⁶⁰ Ma et al., 2007 ¹⁸¹	DSC; ACZ	SPECT; ACZ	17 ¹⁶⁰ and 12 ¹⁸¹ SOD	<p>Wilcoxon signed rank test on percent change in mean relative CBF in GM MCA territory¹⁶⁰:</p> <ul style="list-style-type: none"> - normal side: 0.76-0.18 - lesion side: 0.38-0.67 <p>Association between detection of CVR impairment with SPECT and reduced DSC-CVR¹⁸¹</p>
Grandin et al., 2005 ²⁷⁰	DSC; ACZ	PET; ACZ	13 HC	<ul style="list-style-type: none"> - Inter-modality correlation (coefficient of determination) in individual subjects: r^2 between 0.70 and 0.84 - Mean difference in CBF and CBV: 8.2 ml/min/100g and 2.09 ml/100g at rest, 5.7 ml/min/100g and 2,45 ml/100g after ACZ

Table 2-5: Findings of repeatability of CVR estimates. (BH = breath-hold, BOLD = blood oxygen level-dependent, ACZ = acetazolamide, CC = correlation coefficient, CV = coefficient of variation, GM = grey matter, DSC = dynamic susceptibility contrast, ICC = intraclass CC, HC=healthy controls, SOD=steno-occlusive disease, STD=standard deviation, RI = repeatability index)

References	MRI technique	Repeatability	Population	Results
Thrippleton et al. 2018 ¹¹⁴	BOLD; fixed inhaled CO ₂	Within-day repeatability	15 HC	<ul style="list-style-type: none"> - Inter-session CV of GM CVR: 7.9-15.4% for a 3 min & 11.7-70.2% for a 1 min challenge - Inter-session CV of WM CVR: 16.1-24.4% for a 3 min & 27.5-141.0% for a 1 min challenge
Sobczyk et al., 2016; ¹⁹⁵ Dengel et al., 2017; ²⁶⁴ Leung et al., 2016 ²⁷¹	BOLD; EtCO ₂ targeting	Within- ^{264,271} and between-day repeatability ^{195,264,271} & within-day consecutive intra-scan repeatability ²⁶⁴	15, ¹⁹⁵ 11 ²⁶⁴ and 10 ²⁷¹ HC	<ul style="list-style-type: none"> - Within-day intra-scan ICC of GM CVR²⁶⁴: 0.84 - Within-day intra-scan CV of GM CVR²⁶⁴: 5.70% - Within-day inter-scan ICC CVR in GM: 0.78,²⁶⁴ 0.86;²⁷¹ WM: 0.90²⁷¹ - Within-day inter-scan CV of GM CVR:²⁶⁴ 6.62% - Between-day ICC CVR in GM: 0.69,²⁶⁴ 0.78;²⁷¹ WM: 0.72²⁷¹ - Between-day CV CVR in GM: 7.87%,²⁶⁴ 7.3%¹⁹⁵ WM: 10.3%¹⁹⁵

Dlamini et al., 2018; ¹⁴⁵ Peng et al., 2020; ¹³³ Bright and Murphy, 2013 ²⁷²	BOLD; BH	Within-day, ^{133,145} between-day, ¹³³ inter-regressors ²⁷² and intra-subject ²⁷² repeatability	20 SOD. ¹⁴⁵ 9, ¹³³ 12 ²⁷² HC	<ul style="list-style-type: none"> - Within-day ICC of whole brain CVR: 0.7,¹⁴⁵ >0.4¹³³ - Within-day CV of positive GM CVR: 9.1%,¹⁴⁵ <33%¹³³ - Within-day CV of negative GM CVR :¹⁴⁵ 22.5% - Inter-regressor ICC of GM CVR²⁷²: <0.4 for ramp regressor and 0.82 for EtCO₂ regressor - Intra-subject ICC of GM CVR:²⁷² 1.03% for EtCO₂ regressor
Sousa et al., 2014 ²⁷³	BOLD; paced deep breathing	Test-retest and inter-subject repeatability	9 HC	<ul style="list-style-type: none"> - Inter-subject CV of GM CVR: 20% - Intra-subject CV of GM CVR: 8% - Intra-subject ICC of GM CVR: 1.04
Kassner et al., 2010 ²⁶³	BOLD; EtCO ₂ forcing	Within, between-day and inter-subject repeatability	19 HC	<ul style="list-style-type: none"> - ICC of GM CVR: 0.92 within-day, 0.81 between-day - ICC of WM CVR: 0.88 within-day, 0.66 between-day - CV of GM CVR: 4.2% within-day, 6.8% between-day, 20% inter-subject - CV of WM CVR: 6.3% within-day, 9.9% between-day, 21.8% inter-subject

Liu et al., 2017; ⁸² Taneja et al., 2019 ¹¹¹	Resting-state BOLD	Within-day ⁸² and between-day ¹¹¹ repeatability	6 stroke ¹¹¹ , 10 HC ⁸²	<p>- Within-day ICC:⁸² 0.91</p> <p>- Between-day correlation of lesion CVR:¹¹¹ $r^2=0.91$</p> <p>- Between-day correlation of contralateral-to-lesion CVR:¹¹¹ $r^2=0.79$</p>
Heijtel et al., 2014 ²⁶⁹	ASL; fixed inhaled CO ₂	Within- and between-day repeatability	16 HC	<p>- Within-day RI: 18.2%; Between-day RI: 25.1% for baseline CBF, 24.8% for hypercapnia CBF</p> <p>- CV of inter-subject variability: 12.9% for baseline CBF, 15.6% for hypercapnia CBF</p>
Merola et al., 2018 ²⁷⁴	Dual-echo ASL/BOLD; fixed inhaled CO ₂	Within- and between-day repeatability	26 HC	<p>- Correlation with coefficient of determination of GM CVR variability: 0.57 for within-day inter-scan, 0.41 for within-day inter-session, 0.02 for between-day</p> <p>- CV of inter-subject variability of GM CVR: 17.5% for within-day, 25% for between-day</p> <p>- CV of intra-subject variability for GM CVR: 9.5% for within-day inter-scan, 12.5% for within-day inter-session,</p>

				17.5% between-day
Grandin et al., 2005 ²⁷⁰	DSC; ACZ	Inter-scan repeatability	13 HC	<ul style="list-style-type: none"> - Repeatability using the STD of the mean difference in CBF between scans: 22.4% - Repeatability using the STD of the mean difference in CBV between scans: 18.2%

2.3.9 Potential confounders of CVR analysis

When analysing CVR measurements, baseline MRI signal or EtCO₂ values,⁹⁵ and negative CVR clusters can lead to misinterpretation of CVR data.^{93,275} Higher baseline EtCO₂ was associated with lower CVR (n=291).^{276–278} Baseline CBF and CBV were lower with age (n=81),^{204,239,279} by contrast one study suggested age-related differences in baseline CBF may result from differences in baseline EtCO₂ (n=46).²⁰²

Negative CVR clusters correspond to MRI responses anti-correlated to the stimulus. In some cases this might simply reflect long CVR delays if latter are not appropriately modelled. Negative CVR could also reflect the steal phenomenon, where tissues with high CVR ‘steal’ blood flow from other regions due to flow redistribution.^{91,139,142,166,170,173,174,177,178,275,280} However, they usually appear in the deep WM,²⁷⁵ near and in the ventricles.⁹³ Therefore, others have suggested that they may result from low CNR in the WM tissues leading to spurious CVR values,⁹³ or shrinkage of the CSF space due to vasodilation.^{281–283} The latter effect can be diminished by shortening TE.²⁸³

2.3.10 CVR definition and units

CVR was defined differently across studies and was reported in several units: relative change in BOLD signal divided by absolute change in EtCO₂ with

%/mmHg units (110/235, 47%), relative change in CBF divided by absolute change in EtCO₂ with %/mmHg units (36/235, 15%), relative change in BOLD signal with % units (50/235, 21%), relative change in BOLD signal divided by relative change in total haemoglobin concentration ([Hb]) with %/[Hb] units (1/235, 0.4%), relative change in BOLD signal divided by breath-by-breath O₂-CO₂ exchange ratio with % units (1/235, 0.4%), relative change in BOLD signal divided by relative change in EtCO₂ with % units (1/235, 0.4%), relative change in BOLD signal during one period of breath-hold with %/s units (1/235, 0.4%), relative change in CBF with units % (27/235, 11%), relative change in CBF during one period of breath-hold with %/s units (1/235, 0.4%), absolute change in CBF with ml.100g⁻¹.min⁻¹ units (5/235, 2%), absolute change in CBF divided by the change in EtCO₂ with ml.100g⁻¹.min⁻¹mmHg⁻¹ units (2/235, 1%), absolute change in CBF divided by mean arterial pressure divided by change in EtCO₂ with ml/min/mmHg² (1/235, 0.4%), mean arterial pressure divided by change in CBF with mmHg.ml⁻¹.min.100g units (1/235, 0.4%), relative change in CBV with % units (n=13), absolute change in CBV with ml.100g⁻¹ units (1/235, 0.4%), absolute change in BOLD signal divided by change in EtCO₂ a.u./mmHg (2/235, 1%), relative change in T_2^* with % units (1/235, 0.4%), absolute change in T_2^* divided by change in EtCO₂ with ms/mmHg units (1/235, 0.4%), absolute change in R_2^* divided by change in EtCO₂ with s⁻¹/mmHg (1/235, 0.4%). A further nine CVR definitions had no units because CVR was defined as the correlation coefficient between two time courses (7/235, 3%) and two were defined as the absolute change in BOLD signal divided by the standard deviation of the baseline BOLD signal (1/235, 0.4%) or by the absolute change in mean cerebellum BOLD signal (1/235, 0.4%). One article described different resistance sigmoid parameters associated with CVR such as resting reserve or amplitude, i.e. extend of vascular resistance from resting EtCO₂ state to maximum vasodilation and extend of vascular resistance from maximum vasoconstriction to maximum vasodilation, respectively. Both resting reserve and amplitude are resistance parameters in mmHg/nL/s.

2.4 Discussion

We identified 235 papers using MRI to measure CVR including 5333 subjects, which covered several different acquisition and analysis methods. Stimuli, paradigm and duration, sequences used for acquisition and processing methods varied considerably. We found several papers, which investigated specific aspects of the CVR MRI experiment such as processing methods or reproducibility of CVR measurement, but sample sizes were often low, and validation studies remain limited. Reporting was also inconsistent.

2.4.1 Reporting standards

Most papers included sufficient detail on the acquisition of CVR data (222/235, 94%). Only 22% of studies (51/235) reported CVR tolerability, less than half of which (23/235, 10%) reported presence or absence of discomfort complaints which may affect suitability for some patient populations. Processing (214/235, 91%) including delay computation methods (114/128, 89%) were well reported, though only 54% (128/235) accounted for delay.

2.4.2 Clinical populations

CVR was measured in several pathologies including steno-occlusive diseases, stroke, small vessel disease, brain injuries and dementia. Patients generally had lower CVR compared to healthy participants,^{99,110,114,125–127} though in obstructive sleep apnoea findings were mixed. Delays were longer in steno-occlusive, small vessel disease and dementia patients than in healthy controls, but were not reported in other pathologies. CVR metrics have been associated with cerebrovascular dysfunction, disease severity, and response to interventions (including revascularisation surgery for steno-occlusive diseases). CVR is therefore a promising biomarker of haemodynamic impairment and changes with broad applicability.

2.4.3 Acquisition

Most CVR studies used a 3T scanner (178/235, 74%) and 2D GRE-EPI BOLD sequence (118/235, 50%) for acquisition. While several different sequences can measure CVR, all have limitations. BOLD signal results from a complex interaction between CBF, CBV, haemoglobin concentration, oxygen extraction fraction, CMRO₂ and arterial O₂ partial pressure.⁸³ Changes in any of these parameters can alter the BOLD signal; however, there is evidence that CBV and CBF change together during hypercapnia^{284,285} and that BOLD-CVR is well-correlated with ASL-CVR.^{102,257,265} Cerebral metabolic rate of oxygen consumption might change during hypercapnia; however it is thought that these changes are small for low levels of CO₂ stimulus.²⁸⁵ ASL allows direct measurement of CBF and is also widely used (41/235, 17%), but suffers from low CNR;⁸³ differences in labelling duration and efficiency, and bolus arrival time can also potentially affect CVR estimation. Calibrated fMRI (9/235, 4%) using dual-echo BOLD/ASL allows simultaneous quantification of CVR and cerebral metabolism parameters (e.g. rate of oxygen consumption and oxygen extraction fraction).^{117,274,286,287} However, calibrated fMRI models depend on the initialisation values of model parameters, model assumptions such as the oxygen metabolism not being altered during hypercapnia and hyperoxia stimuli,²⁸⁸ and are more complex to implement. PC MRI (12/235, 5%) measures CVR at the large-vessel level and generally provides limited spatial coverage; although 4D phase-contrast flow imaging^{207,289} is developing rapidly, the long scan duration currently limits applicability for measuring CVR in patients. Several different paradigms were used, which varied in duration and number of repetitions. EtCO₂ targeting (81/235, 34%) and fixed CO₂-inhalation (69/235, 29%) are the most widely used vasodilatory stimuli with a block paradigm (212/235, 90%) with a median paradigm duration of 9 min. Fixed CO₂-inhalation is easier to set up than EtCO₂ targeting but the change in EtCO₂ associated with a specific inspired CO₂ concentration may vary between subjects. EtCO₂ targeting allows precise control over the EtCO₂ and paradigm but requires expensive, specialist equipment. 75% of respiratory

challenge studies (160/207) measured ETCO_2 . However, in patients with lung diseases, using EtCO_2 is not a direct surrogate for PaCO_2 because lung regions could be emptied sequentially rather than in parallel during exhalation.⁸⁵

2.4.4 Processing Methods

CVR was mainly computed using linear regression (149/235, 63%). Few studies described why a particular processing method or regressor was used, and comparisons between different methods are lacking.²⁹⁰ 40% of the studies (93/235) calculated a whole brain or single ROI delay that was applied to all voxels. While this method may be relatively robust against noise, delay is known to vary between and within tissue types.^{114,129} However, only 26% of studies (62/235) accounted for voxel-wise delays. An HRF between the stimulus and MRI signal was used in only 14% of the studies (32/235). This might be because the CVR HRF is unknown and may vary between stimuli, paradigms and pathologies.^{91,210} Assuming a non-delta-function HRF allowed delay and steady-state CVR to be investigated in parallel,^{91,115} but can be more complex to implement and computationally demanding.

2.4.5 Validation

CVR measurements and detection of CVR impairment using MRI and other imaging modalities (e.g. BOLD-CVR to TCD-CVR,¹¹⁶ BOLD-CVR to SPECT-CVR,¹⁶⁶ DSC-CVR to PET-CVR²⁷⁰) were well-correlated, validating the CVR MRI experiment. Furthermore, biological validation such as results from studies comparing CVR in patients with steno-occlusive diseases and healthy controls, also supports use of CVR as a biomarker.^{116,144,146,152,153} Preclinical CVR imaging is also a fast-growing field which has been applied in preclinical models of stroke, cancer and Alzheimer's disease.^{291–293} Preclinical CVR studies predominantly follow similar approaches to human studies but involve additional considerations such as the effect of anaesthetic agents on resting CBF.²⁹⁴ Isolated vessel preparations,^{295,296} laser speckle imaging²⁹⁷ and multiphoton microscopy^{298,299} can also assess CVR preclinically and may help

improve understanding of how impaired vasoreactivity develops and further direct validation of CVR MRI as a clinical biomarker of cerebrovascular health.²⁹⁴ CVR measurements using MRI techniques showed lower repeatability between-days than within-days.^{264,274} CVR measurements were also less repeatable in WM than in GM due to a lower CNR.^{114,263} Studies with higher sample sizes and investigating reproducibility in different pathologies would be helpful to further validate the CVR MRI experiment.

2.4.6 Definition and interpretation of CVR

The definition and units of CVR vary across studies depending on choice of sequence, stimulus, paradigm and analysis methods. However, CVR is most commonly reported as the relative change in BOLD signal (110/235, 47%) or CBF (36/235, 15%) per unit change in EtCO₂ as %/mmHg.

Several aspects influence CVR values beyond the vasodilatory capacity of vessels, which must be considered in interpreting the results. The CVR steal phenomenon has been proposed as a systemic mechanism governing the cerebrovascular system by prioritising blood supply to specific regions and potentially leading to local deficits elsewhere. Low or negative CVR values may also result from low CNR or blood vessel dilation near the ventricles shrinking the CSF space and artificially decreasing the BOLD signal due to differences in CSF and blood signal intensities.^{281–283} Excluding voxels that contain CSF or using a shorter TE (e.g. 21 ms for a TR of 1500 ms at 3T) can reduce negative artefacts in CVR data.²⁸³ Other physiological factors can affect the MRI signal, including resting CBF and oxygen extraction fraction. Finally, as blood vessels have a limited vasodilation capacity, the linearity of the MRI response to the vasodilatory stimulus has a restricted range. Indeed, the shape of the MRI response to the stimulus and baseline parameters including resting CBF and EtCO₂ can influence CVR values.^{94,95,277,278} Despite some gaps in current knowledge, CVR has a proven validity and utility in several diseases as described above.

2.4.7 Definition and interpretation of CVR delay

Delay in the MRI response to a stimulus can lead to inaccurate CVR values if it is not accounted for, and could give further information on vascular health. Voxel-wise or ROI delay should be favoured as opposed to whole brain delay to better account for differences in tissue response and distance from blood vessels. Artificially high or low delay values can be obtained when the noise level is high, i.e. low CNR. Definitions of delay were inconsistent in distinguishing between lung-to-brain delay and duration of the vasodilation process.⁷¹ For example, one study computed the lung-to-brain delay, assuming instantaneous MRI response, as the shift in the EtCO₂ that gives the lowest residual when regressed against the MRI time course: the delay in GM and WM were approximately 15 and 35 seconds respectively.⁷¹ Another study computed the response time using a mono-exponential fit of the MRI signal: they found response time constants between a few seconds in GM up to 100 seconds in WM.⁹¹

2.4.8 Implications for future research

Harmonisation of the CVR MRI experiment

Variability in the implementation of CVR experiments, including the choice of sequence and MRI parameters, such as TR and TE for BOLD MRI and post-labelling delay for ASL MRI,¹³⁵ cause heterogeneity in the CVR values, making it challenging to interpret findings across studies and conduct meta-analyses. CVR measurements are highly dependent on MRI sequence (e.g., BOLD, ASL, PC and DSC), since each measures a different quantity as an estimate or surrogate of CBF, which are not directly comparable.²⁶⁵

Harmonisation of acquisition and processing methods would allow more uniform definitions of CVR, delay and HRF, enhancing inter-study comparability, although specific techniques may be better suited to some pathologies and patient groups. Such efforts may also find consensus on the optimal paradigm duration to ensure that CO₂ reaches the ROI and the MRI response reaches the steady state. As many groups have developed in-house

software to process CVR data, making these publicly available, as a step towards development of validated, community-driven open-source software, would also promote reproducibility and harmonisation.

While little consensus currently exists, our review reveals evidence of convergence in some aspects of the CVR MRI experiment: the use of BOLD at 3T with a block paradigm for the acquisition and definition of CVR as the relative change in BOLD signal per unit change in mmHg (%/mmHg). Early attempts to establish a framework for reaching consensus have recently been initiated.²⁹⁰ Further work is needed to reach consensus regarding signal processing and CO₂ delivery methods. CVR is also highly dependent on the image analysis methods used, including the erosion of ROIs to avoid signal contamination from neighbouring tissues, or ROI versus voxel-wise analysis.

Considerations for future studies

Detailed reporting of methods and results is essential for interpretation and inter-study comparison of CVR data. Future publications should give sufficient detail to allow processing to be reproduced and, where possible, authors should release their software in version controlled open-source repositories. Results should preferably be reported in relative signal units to allow inter-study comparisons. Accurate recording and reporting of tolerability and reasons for excluding CVR scans is also important to facilitate clinical translation.

Nonlinearity due to the limited vasodilation capacity of the blood vessels, is a consideration when interpreting CVR values. In this case, CVR reflects both the maximum response as well as the sensitivity to CO₂. Research is needed to identify the aspects of the CVR response (e.g. maximum response, MRI response versus EtCO₂ slope) that are most sensitive and specific in key pathologies. Accounting for voxel-wise lung-to-brain delay would allow direct comparison of the BOLD signal and EtCO₂ and should improve the accuracy of CVR values. Drift in the MRI signal can be significant and should be controlled for during signal processing.⁸³

Finally, there are age-related changes in CVR values: CVR is lower with increasing age in GM and WM.^{71,204,300} Statistical analyses should account for such key covariates, which requires larger sample sizes or matched study design. CVR is also associated with vascular risk factors including hypertension, diabetes, hypercholesterolemia and smoking.^{72,201,209,211}

2.4.9 Strengths and Weaknesses

This review included foreign language papers (5/236), though one such paper was inaccessible. Most but not all of the required information was obtained during the data extraction. This might have added a bias to the results of this review: for example, description of the CVR processing and delay computation methods were not clear in 9% and 11% of the studies, respectively. Furthermore, the sample size of many studies was low (mean sample size: 35, 45/235 studies ≤ 10 participants), particularly in studies investigating repeatability and reproducibility of CVR values (mean: 16). This review was also restricted to human studies; therefore it does not provide a detailed description of preclinical CVR methods, although the main processing techniques are similar. Moreover, the mean age across studies could have been computed using the mean of the reported mean or median age across studies weighted by the associated number of subjects in order to take into account the sample size of each study. Finally, the administration of a particular stimulus could have been investigated as a function of the number of research groups using it instead of the number of studies, as the current findings could be biased by the number of publications from single groups.

2.5 Conclusion

To our knowledge, this is the first systematic review to summarise and describe the diverse acquisition and analysis techniques used to measure CVR using MRI, and their applications in health and disease. While CVR MRI is a relatively new and evolving technique we identified applications in several clinical populations including steno-occlusive and small vessel disease,

highlighting the value of CVR measurements in medical research. However, acquisition techniques, analysis methods and definitions of CVR all varied substantially. Future work should target consensus recommendations to facilitate more reliable and harmonised CVR measurement for use in clinical research and trials of new therapies.

2.6 Update of the review and discussion with respect to the thesis

The systematic review contributed to the thesis by giving an extensive description of CVR MRI experiments existing in the literature and highlighting the gaps in the field. For example, the review revealed lack of consensus in the processing strategy of CVR data, such as the use of a delay correction method, and lack of information regarding the HRF to a CO₂ challenge. Hereafter, an overview of the research undertaken globally and presented after the publication of the systematic review is given. This overview was not based on a systematic search of the literature.

CVR was further assessed as an indicator of cerebrovascular health in multiple pathologies such as steno-occlusive diseases,^{301–303} SVD,^{304,305} cognitive impairment,³⁰⁶ traumatic brain injury,³⁰⁷ sickle cell disease³⁰⁸ and Huntington's disease.³⁰⁹

Multiple papers focussed on optimising CVR experiments. Some papers focused on improving the CVR experiment without gas challenge.^{138,310–312} One study showed that correcting for partial volume effect resulted in increased CVR magnitude and faster response in GM with an opposite result in WM; however, they did not comment on the partial volume effect in cortical versus subcortical GM.³¹³ Another study created a library of HRFs where each function was convolved with the EtCO₂ to find the one that best modelled the BOLD response to hypercapnia in order to allow for dispersion in the response.¹⁰⁰ The error of this fitting procedure was lower than with the traditional method with an instantaneous HRF. However, one limitation of such

a processing method is that the library might not include all possible HRFs, especially in pathologies where the HRF might be different to those in healthy tissues. Another study investigated CVR delay: vein architecture could modulate the delay in the BOLD response.³¹⁴ In deep WM tissues, venous blood drains into larger periventricular veins and can delocalise the CVR response. A similar effect has been observed in cortical fMRI studies where there is a contribution from venous drainage to the GM BOLD signal.³¹⁵ The distribution of medullary veins can therefore impact WM signal dispersion. This effect is important when using BOLD at 3T, a contrast that is particularly sensitive to large veins.

Further research was undertaken to validate the technique. To this end, one study found good inter-rater reliability based on five different raters that used a cloud-based pipeline to process CVR data from healthy volunteers.³¹⁶ The same study found good between-days (mean of 9 days) test-retest and inter-scanner (Philips Achieva versus Siemens Prisma 3T scanners) reliability. Another study investigated the creation and use of CVR atlases across different sites. The use of an atlas can help interpret CVR maps by taking into account normal variations in CVR due to age and tissue type.¹⁴¹ They obtained two atlases, each created based on datasets from a different scanner located at a different site (Siemens MAGNETOM Skyra Fit versus GE Signa 3T scanners) and found no significant differences between GM and WM of those atlases, thereby confirming the use of a single atlas across multiple sites.³¹⁷

Finally, a published review paper describes the “lessons” learned over the last two decades regarding CVR experiments and gives advice on how to conduct a CVR experiment and on the pitfalls to avoid or take into account.³¹⁸ For example, in order to measure vasodilation response time induced by a change in PaCO₂, the time taken for the PaCO₂ to reach steady state should be shorter than the vasodilation response time in fastest responding tissues.

In conclusion, there is persistent interest in using CVR MRI experiments to assess cerebrovascular health. Several studies have been conducted to

optimise the experiment and to understand the pathological information that can be extracted from CVR metrics, as well as attempting to quantify CVR in different clinical populations. However, some aspects of CVR development need further attention: comparison between processing methods, better understanding of CVR delay. The next chapter will address the use of ROI- versus voxel-based analysis as well as the use of variable versus fixed CVR delay.

3 Cerebrovascular reactivity measurements using 3T BOLD MRI and a fixed inhaled CO₂ gas challenge: repeatability and impact of processing strategy

The systematic review conducted in Chapter 2 showed a high diversity of methods to process CVR data. More specifically, CVR parameters have been computed using voxel- or ROI-based analyses. In addition, there were inter-study differences in CVR delay computation using variable delay, fixed delay or no delay correction. However, no work has compared the different processing strategies. In order to move towards harmonisation of the CVR MRI experiment, it is important to understand which methods are more accurate, precise, repeatable or robust against noise in the data. The work presented in this chapter addresses this issue and has been published with supplementary material in the *Frontiers in Physiology* in February 2023.³¹⁹ I designed the study, acquired, processed, and analysed the CVR data, created and analysed the simulations and wrote the paper. Dr Michael J. Thrippleton, Dr Michael S. Stringer, Prof Ian Marshall and Prof Joanna M. Wardlaw contributed to the study design and we discussed the interpretation of the results together. Isla Mitchell and Maddy Murphy participated in the data acquisition. All six of them reviewed the final manuscript and accepted its publication in this thesis.

3.1 Introduction

CVR reflects the ability of the cerebral blood vessels to dilate in response to a vasoactive stimulus. Investigating CVR impairment in cerebral tissues is of particular interest in patients with cerebrovascular diseases.^{72,157} This can be achieved in vivo using MRI.⁸³ Typically, a hypercapnic stimulus is used to trigger vasodilation and induce changes in vascular parameters, including CBF, which can be detected using vascular-sensitive MRI techniques.^{109,320,321} The CVR MRI technique is well-correlated with other imaging modalities such as TCD and PET.^{116,269} BOLD MRI is most widely used along with EtCO₂

recording, with CVR magnitude typically defined as the percent change in the BOLD signal due to the hypercapnic challenge divided by the change in EtCO₂ to account for the magnitude of the stimulus.¹⁰¹ As CVR reflects a dynamic process, CVR delay, which comprises CO₂ travel time between the lungs and the brain tissues and vasodilation response time, is often included as a variable in the signal model to avoid underestimation of CVR magnitude.⁸³ An HRF has been proposed as a means to separate travel to vasodilation response time,^{91,100} though this is not commonly used in the literature.¹⁰¹

Previous studies have found good repeatability of CVR magnitude measured with a hypercapnic BOLD experiment,^{114,263,264,271,274,278} though it is lower in NAWM than in GM.^{114,263,271} However, the studies did not report on inter-scan differences in physiological variables such as blood pressure, respiration and heart rates. Indeed, CVR is a momentary measurement affected by the underlying physiology: changes in respiration rate can alter the arterial CO₂ partial pressure⁸⁵ and studies have reported increased heart rate during hypercapnia.^{79,322} Repeatability of the CVR delay has only been reported for 1.5T MRI,¹¹⁴ whereas CVR experiments are typically performed at 3T.¹¹⁴ Furthermore, CVR data analysis methods differed across studies.^{90,94,115,179,272} First, various CVR delay computation methods were present across the literature: some studies used an estimated constant^{263,264,271,278} and others a variable CVR delay.¹¹⁴ It is unknown how robust the estimation of CVR delay is against noise and its impact on the reliability of CVR magnitude estimates. While voxel-^{263,271,278} and ROI-based^{114,264} analyses were applied, there is little evidence to indicate which analysis is more appropriate.

In this work, we aimed to determine (i) the within-day test-retest repeatability of CVR magnitude and delay with a 3T BOLD MRI experiment using a fixed inhaled CO₂ stimulus while measuring blood pressure, heart and respiration rates; (ii) the impact of noise on accuracy and precision of CVR magnitude and delay measurements; (iii) the impact of using variable versus fixed or zero delay; (iv) the impact of extracting CVR magnitude and delay using voxel-based versus ROI-based analysis.

3.2 Materials and methods

3.2.1 Simulations

Simulations were conducted using MATLAB (version R2018b, MathWorks, Inc., MA, United States) to investigate the effect of noise and processing methods on CVR estimates. We simulated the EtCO₂ trace as a block paradigm without noise ranging from 40 (normocapnia) to 50 mmHg (hypercapnia). Timings of the paradigm replicated the in vivo stimulus (see section 3.2.4). The BOLD voxel time courses were generated by scaling and shifting the EtCO₂ trace according to the given CVR magnitude and delay, respectively. BOLD signals had a temporal resolution of TR = 1 s. Values for the true median, mean and standard deviation of CVR magnitude and delay in ROIs were extracted from the healthy volunteers' data acquired in this study by averaging CVR maps across subjects (see Appendix A2.1).

The number of signals simulated for each ROI was set to the median number of voxels per ROI in a healthy volunteer dataset, described below, namely: 1247 in subcortical GM (SGM), 656 in cortical GM (CGM) and 11748 in NAWM. For each voxel, we added random Gaussian noise with a standard deviation equal to the hypercapnia-induced change in BOLD signal divided by the pre-defined tCNR. The true CVR magnitudes and delays were sampled according to distributions of CVR magnitudes and delays extracted from the healthy volunteer data of this study (see Appendix A2.1, Figure A2-1). We therefore used distributions with a median/mean \pm STD of 0.25/0.27 \pm 0.13, 0.25/0.30 \pm 0.21 and 0.10/0.11 \pm 0.07 %/mmHg for true CVR magnitude and 8/10 \pm 8, 15/20 \pm 16 and 27/29 \pm 13 s for CVR delay in SGM, CGM and NAWM respectively.

For different values of tCNR and analysis type (voxel- and ROI-based), we simulated 1000 repetitions (N voxels per repetition) of the same experiment. We computed the mean and standard deviation of CVR magnitude and delay estimates across the repetitions.

For the voxel-based analysis, we performed multiple linear regression between each simulated BOLD time courses and time-shifted EtCO₂ (see section 3.2.5). For the ROI-based analysis, we applied linear regression to the mean BOLD signal of the ROI.

To investigate the effect of the delay constraint, we repeated simulations using four delay ranges: -31 to 93, 0 to 58, -93 to 93, -31 to 124 seconds. We also simulated CVR magnitude estimation assuming a fixed delay, based on three previous approaches reported in the literature: (i) a global delay defined as the delay calculated from the averaged BOLD signal across GM and NAWM voxels, (ii) a GM delay calculated from the averaged BOLD signal across GM voxels and (iii) a delay of zero seconds corresponding to no delay correction.

3.2.2 Participants

Healthy volunteers were recruited for two CVR scans. The study was conducted under Research Ethics Committee approval (ref. 14/HV/0001) and according to the principles expressed in the Declaration of Helsinki. All volunteers gave written informed consent. Exclusion criteria consisted of contraindication to MRI, migraine, hypertension, anxiety disorders, panic attacks, respiratory and cardiovascular illnesses and known family history of subarachnoid haemorrhage, intracranial aneurysm or arteriovenous malformation.

3.2.3 Magnetic resonance imaging

All images were acquired using a 3T MRI scanner (MAGNETOM Prisma, Siemens Healthcare GmbH, Erlangen, Germany) with a 32-channel receive head coil. Each participant underwent two 13.5-minute CVR scans, each acquired using axial 2D single-shot gradient-echo echo-planar imaging (GRE-EPI; TR/TE = 1550/30 ms, 67° flip angle, 23.5×23.5 cm² FOV, 94×94 acquisition matrix, 50×2.5 mm slices, 2.5 mm³ isotropic resolution, multiband acceleration factor 2, in-plane GRAPPA acceleration factor 2, 5 dummy scans) during a hypercapnic challenge. We discarded the first minute of the scanning

(39 volumes) to obtain the same paradigm as in clinical studies on small vessel disease.¹¹⁴ Structural imaging sequences consisted of sagittal T1W 3-dimensional (3D) inversion recovery (IR) spoiled GRE (TR/TE = 2500/4.37 ms, 7° flip angle, 25.6×25.6×19.2 cm³ FOV, 256×256×192 acquisition matrix size, 1.0 mm³ isotropic resolution, GRAPPA acceleration factor 3 in anterior-posterior phase-encoding direction) and axial T2W 3D RARE (TR/TE = 3200/408 ms, 24.0×24.0×15.8 cm³ FOV, 256×256×176 acquisition matrix size, 0.9 mm³ isotropic resolution, GRAPPA acceleration factor 2 in phase- and partition-encoding directions).

The scanning session took place between 11 am and 4 pm. Structural images were acquired after the first CVR scan, followed by a short break when the subject came out of the scanner room before the second CVR scan.

3.2.4 Vasodilatory stimulus

The hypercapnic challenge used an established method which consisted of a block paradigm alternating between 2 minutes of medical air and 3 minutes of fixed inhaled CO₂ stimulus for a duration of 12 minutes.¹¹⁴ Actually, the first air block was 3 minutes long, but, for the analyses, we did not consider the data acquired during the first minute. The hypercapnic gas contained 6% CO₂, 21% O₂ and 73% N₂, while the medical air contained 21% O₂ and 79% N₂ (BOC Special Products, United Kingdom). Expired CO₂ and oxygen (O₂) concentration waveforms were measured with a sampling frequency of 20 Hz using CD-3A CO₂ and S-3A Oxygen sensors (AEI Technologies, Pittsburgh, United States) respectively, calibrated prior to each CVR scan. We recorded peripheral oxygen saturation, blood pressure pre- and post-CVR, heart rate and respiration rate using an MR conditional patient monitor with a sampling frequency of 1 Hz (MR400 and IP5; Philips, United Kingdom).

After each CVR scan, we asked participants to rate the tolerability of the scan (scale: 1 = very tolerable, 2 = tolerable, 3 = not very tolerable, 4 = intolerable) and recorded any reports of discomfort and possible hypercapnia symptoms.

3.2.5 Data processing

The CO₂ and O₂ concentrations were converted to partial pressures by multiplying them by the atmospheric pressure (i.e. 760 mmHg). The resulting waveforms were converted into EtCO₂ and EtO₂ traces using in-house MATLAB code, which identifies the signal peaks or troughs, as previously described.¹¹⁴

DICOM files were converted into NIFTI format.³²³ BOLD images were realigned to each participant's mean BOLD image using SPM12.³²⁴

For the ROI-based analysis, we computed the mean BOLD signal-time course in each ROI and performed multiple linear regression between the mean BOLD time course, the time-shifted EtCO₂ course and a vector comprising the volume numbers to account for a linear signal drift in MATLAB (Figure 3-1). Unless otherwise mentioned, we allowed time shifts ranging from -31 to 93 seconds, both multiples of TR, for the EtCO₂ profile allowing for long responses in damaged tissues¹¹⁴ and for negative delays in individual voxels or ROIs due to noise in the BOLD signals. This delay range was used previously.^{114,304} The optimal time shift was taken from the model with lowest sum of squared residuals. CVR magnitude (%/mmHg) was computed as the regression coefficient associated with the time-shifted EtCO₂ term divided by the mean BOLD baseline signal and multiplied by 100, where the mean BOLD baseline was defined as the mean intensity of the mean BOLD signal over the first 30 volumes (overlapping medical air inhalation). CVR delay was defined as the optimal time shift plus 4 seconds to account for the sampling line delay. The latter was calculated prior to the study as the average time across 5 repetitions for an abrupt CO₂ concentration change at the distal sampling point to be reported by the sensor. In the voxel-based analysis, the same multiple linear regression process was applied to the BOLD time course of each voxel within the ROI and the resulting CVR magnitude and delay estimates were averaged across the ROI.

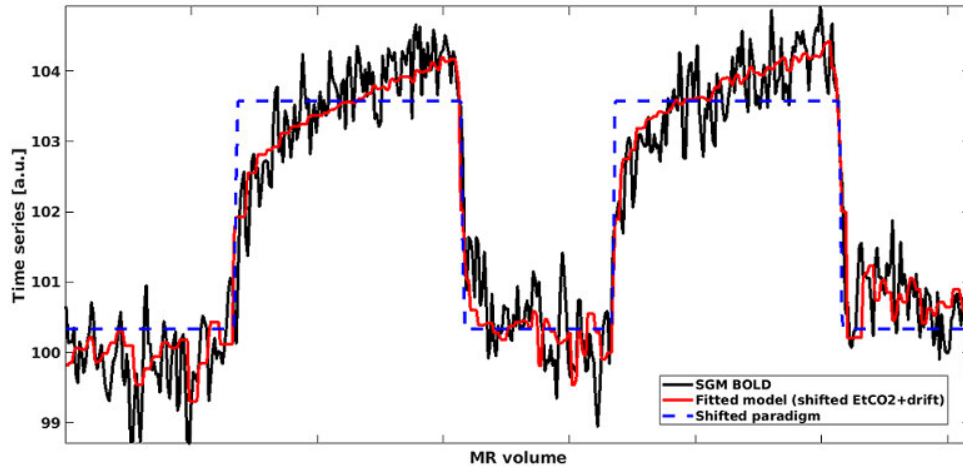


Figure 3-1: Mean BOLD time series in SGM (black) modelled using shifted EtCO₂ and linear drift term (red). The shifted rescaled paradigm is shown in blue: high values correspond to hypercapnia periods whereas low values correspond to normocapnia periods.

For each analysis, we investigated the dependence of CVR estimates on the range of allowed delay values, i.e. delay constraint. In practice, delay constraint is limited by the amount of EtCO₂ data recorded before and after the MRI acquisition. We reprocessed the data with a higher upper bound (from -31 to 124 seconds instead of -31 to 93 seconds).

We defined tCNR in vivo as the difference in mean BOLD intensity during hypercapnia and during normocapnia, excluding a one minute transition period at the start of a new block to allow for the BOLD response to stabilise, divided by the standard deviation of the BOLD baseline signal. For each ROI, we computed the tCNR of the mean BOLD signal time course as well as the mean tCNR for voxels within the ROI.

3.2.6 Regions of interest

We used FSL FAST³²⁵ and FIRST³²⁶ (FMRIB Analysis Group, Oxford, United Kingdom) to segment CGM, SGM (formed of the thalamus, putamen, pallidum and caudate nucleus) and NAWM in native T1W space based on the MNI-152 template.^{327,328} To reduce partial volume effects, all ROIs were eroded using a box kernel with a width of 3 voxels centred on the target voxel. The linear affine

transformation between the T1W and mean BOLD spaces was calculated using FLIRT^{329,330} and applied to transform each ROI into the mean BOLD space. We then applied a threshold of 50% to obtain binary masks in the mean BOLD space.

3.2.7 Statistics

CVR magnitude, CVR delay and physiological parameters were reported as mean \pm standard deviation. We investigated inter-scan, inter-block and inter-analysis differences using Bland-Altman statistics including the 95% confidence intervals for the mean difference reported in square brackets. We defined the inter-scan difference of a parameter as the parameter at scan 2 minus the parameter at scan 1. The inter-block difference in a parameter was defined as the mean value during the CO₂ blocks minus that during the air blocks. The inter-analysis difference of a parameter was defined as the value from the ROI-based analysis minus that from the voxel-based analysis. Furthermore, we computed the inter-scan CV for CVR magnitudes and delays as the standard deviation of the differences in paired measurements (i.e. one pair for each participant) divided by the mean of the pair-averaged values. The impact of physiological parameters was assessed using a linear regression model with the inter-scan difference in CVR magnitude as outcome, the inter-scan differences in baseline EtCO₂ and EtCO₂ change as independent variables and without an intercept, as described previously.²⁷⁸

3.3 Results

3.3.1 Simulations

Simulations were performed using openly-accessible MATLAB scripts (<https://doi.org/10.7488/ds/3503>), which can also be used to process in vivo CVR data. At high tCNR, CVR parameters estimated from the simulated data using voxel-based analysis converged to the ground-truth mean values (Figure 3-2). However, at lower tCNR, random error increased and a positive bias was

observed for both CVR magnitude and CVR delay for the voxel-based analysis. CVR magnitudes derived from ROI-based analysis had a similar precision to those from voxel-based analysis, but were always lower than the true CVR magnitude (Figure 3-2). CVR delays from ROI-based analysis converged to the ground-truth median values at high tCNR; at low tCNR, they remained accurate but were less precise.

To investigate the origins of the biases in the voxel-based analysis, we simulated NAWM CVR estimates using different delay constraints at a low tCNR of 0.1 (Figure 3-3). CVR estimates from ROI-based analysis were independent of the delay constraint. However, CVR estimates from voxel-based analysis depended on the centre of the delay constraint.

When CVR magnitude was estimated with a fixed delay, estimates from ROI- and voxel-based analyses were similar (Figure 3-3), but large systematic errors were observed (5 – 32%). The closer the fixed delay was to the mean delay in the ROI, the lower the relative error in CVR magnitude. For example, using a fixed delay obtained by fitting the mean GM signal resulted in large relative errors in NAWM CVR (>20%).

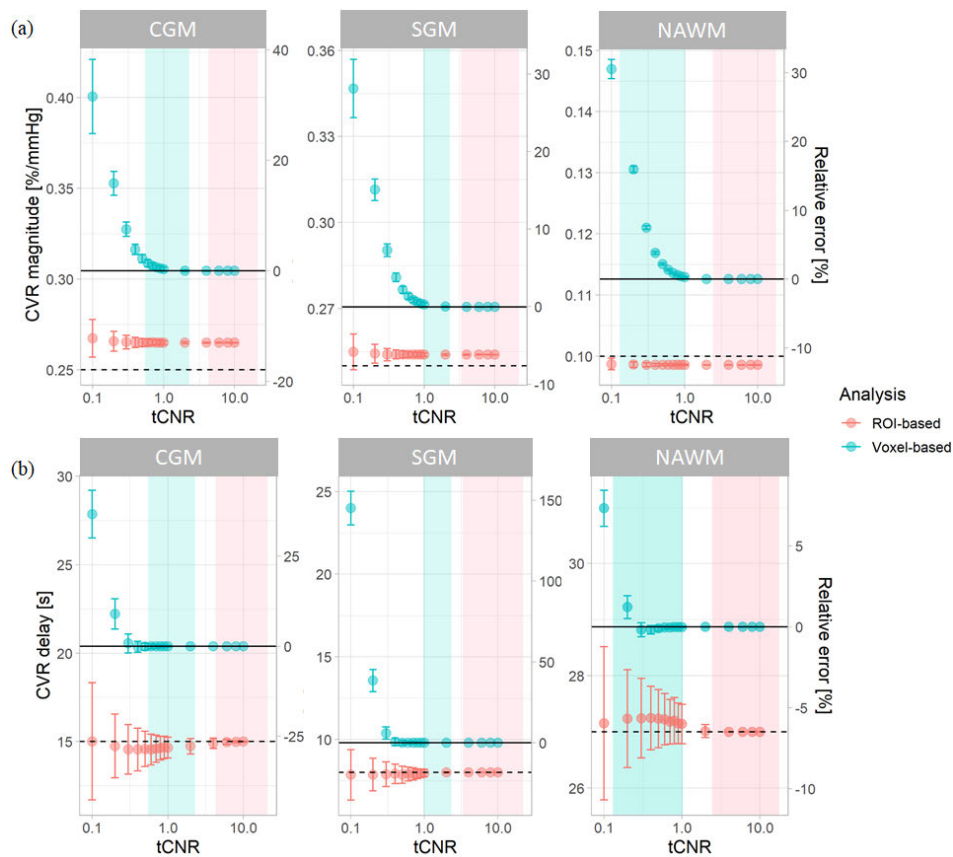


Figure 3-2: Simulations showing the effect of $tCNR$ on the estimation of CVR magnitude (a) and delay (b) corresponding to all subcortical and cortical GM, and NAWM voxels. Data points and error bars indicate the mean \pm the standard deviation of the estimates across 1000 simulations. Simulations were performed for both ROI- (pink) and voxel-based (blue) analyses. $tCNR$ on the x-axis represents the $tCNR$ in voxels. The range of $tCNR$ values in the in vivo data are represented by the shaded areas in blue for $tCNR$ in voxels and in pink for $tCNR$ of mean BOLD signals. The delay constraint was from -31 to 93 seconds, corresponding to the delay constraint used to process real data. Horizontal solid and dashed lines represent the ground-truth mean and median values, respectively. The relative errors were computed with respect to the ground-truth mean values.

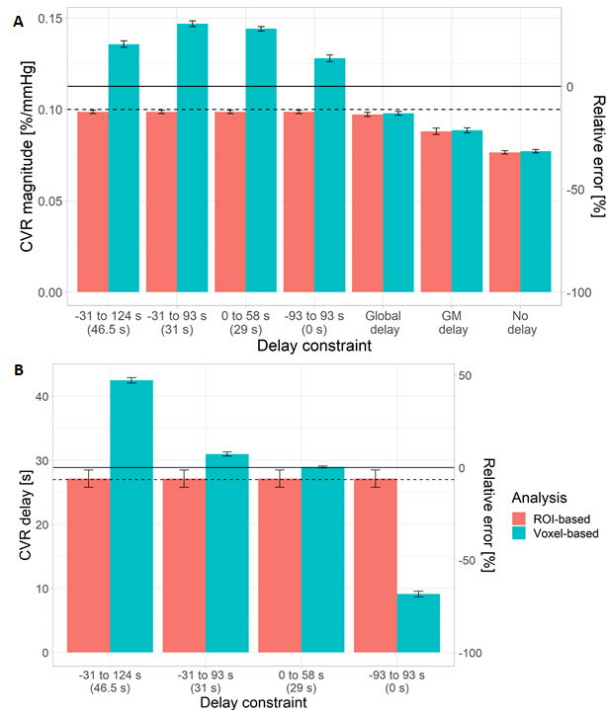


Figure 3-3: Simulations showing the impact of the delay constraint and assumption of fixed delay at a voxel $tCNR$ of 0.1 on the estimation of CVR magnitude (a) and delay (b) in NAWM. The bars and error bars correspond to the mean and standard deviation respectively of the CVR estimates across 1000 repetitions for the voxel- (blue) and ROI-based (pink) analyses. Horizontal solid and dashed lines represent the ground-truth mean and median values, respectively. The relative errors were computed with respect to the ground-truth mean values. The central values for each delay constraint are shown in parentheses.

3.3.2 MRI experiments

Raw data acquired for this work were made openly accessible (<https://doi.org/10.7488/ds/3492>). We recruited 15 healthy volunteers (age: 28.1 ± 5.5 years, female: 53%) who all underwent the two CVR scans with a median time of 31.5 minutes between the starts of the scans. One participant did not complete the first CVR scan, but sufficient data was collected (4.2/12 minutes) to include in the analysis. Data from another subject were excluded from the analysis due to severe motion artefacts during scan 1. Overall, the scans were well-tolerated (scan 1: 4/15 very tolerable, 10/15 tolerable, 1/15

intolerable; scan 2: 7/15 very tolerable, 8/15 tolerable). Symptoms reported by the subjects per scan were: 26/30 dyspnoea, 9/30 dry mouth, 8/30 dizziness or headache, 6/30 tingling sensations, 6/30 anxiety, 6/30 sensation of accelerated heart rate and 3/30 claustrophobia. Subjects reported mask discomfort in 3/30 scans and noticed a difference between the two inhaled gases in 27/30 scans.

3.3.3 CVR and physiological parameters

CVR magnitude and delay measurements at the two scans are shown in Table 3-1 and displayed in Figure 3-4, Figure 3-5, Figure 3-6 and Supplementary Figures A2-2, A2-3. CVR magnitude was higher in GM than in NAWM (scan 1 difference: 0.19 [0.17, 0.21] %/mmHg for ROI-based analysis, 0.20 [0.17, 0.22] %/mmHg for voxel-based analysis), while CVR delay was shorter (-25.3 [-31.3, -19.3] s for ROI-based analysis, -21.8 [-23.7, -20.0] s for voxel-based analysis; Table 3-1). Inter-scan CVs ranged from 7.48 to 14.91 % for CVR magnitude and from 12.49 to 50.00 % for CVR delay (Table 3-2). CVR magnitude was systematically lower at scan 2 than scan 1 (difference in GM: -0.01 [-0.03, -0.00] %/mmHg corresponding to -4 % change for ROI-based analysis, -0.02 [-0.03, -0.00] %/mmHg corresponding to -7% for voxel-based analysis; Figure 3-5, Figure 3-6, Table 3-1, Figure A2-2).

Physiological variables and baseline BOLD signals measured at both scans are given in Table 3-3. EtCO₂ (Table 3-3, Figure A2-4) and EtO₂ (Table 3-3) changes were greater in scan 2 than in scan 1 (+1.0 [0.4, 1.5] mmHg for EtCO₂, +1.6 [0.4, 2.8] mmHg for EtO₂) but the baseline values were similar. In a linear model, reduced CVR magnitude was associated with increased EtCO₂ change in SGM (-0.012 [-0.021, -0.003] %/mmHg²) and NAWM (-0.006 [-0.010, -0.002] %/mmHg²), and increased baseline EtCO₂ in GM (-0.013 [-0.023, -0.004] %/mmHg²). Mean heart rate was lower at scan 2 than at scan 1 (difference: -5.5 [-8.6, -2.4] bpm; Table 3-3). Heart rate was lower during the CO₂ block than during the air block in scan 1 but did not change between blocks in scan 2.

The respiration rate did not differ between scans and blocks nor were there differences in mean arterial pressure pre- and post-CVR scan (Table 3-3).

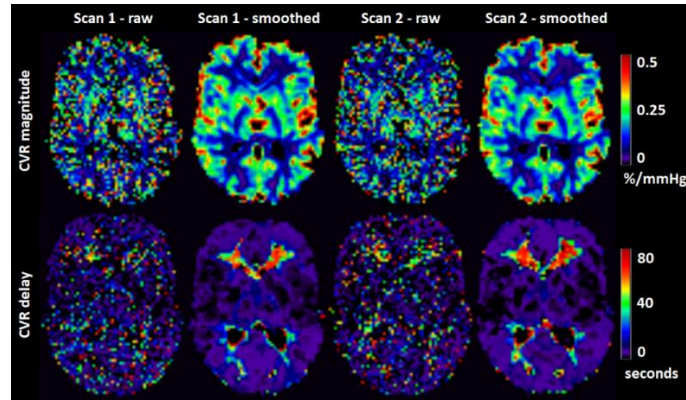


Figure 3-4: Maps of CVR magnitude and delay from one representative participant obtained from scan 1 and 2. The smoothed maps were obtained after spatially smoothing the BOLD volumes using a Gaussian filter with full width at half maximum of 4 mm and are shown here for visual purposes only.

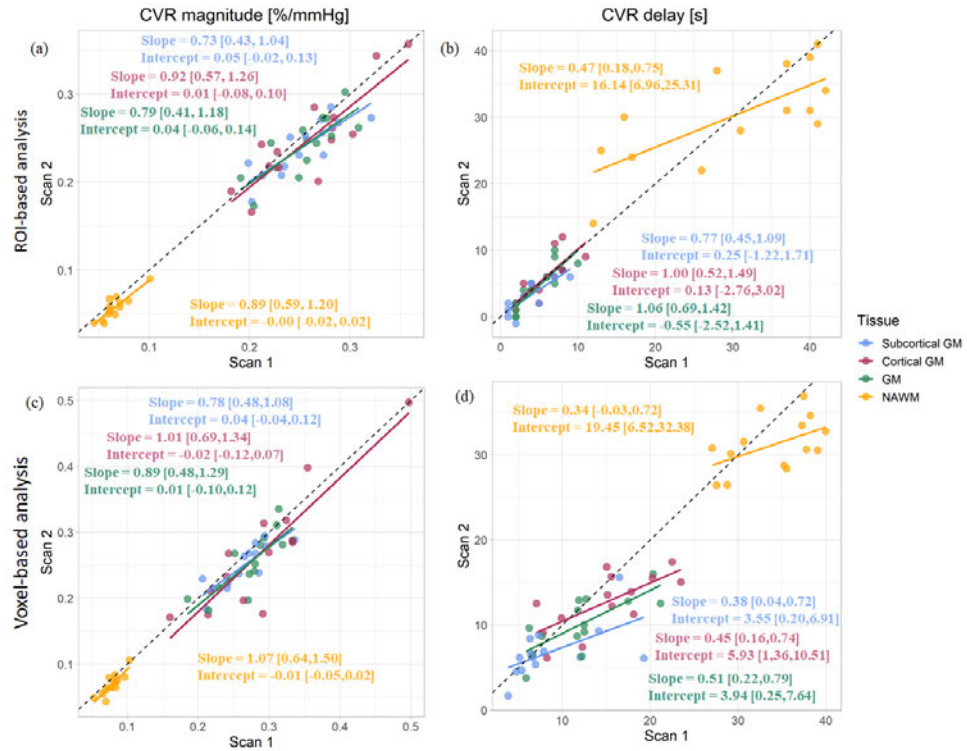


Figure 3-5: Comparison of CVR magnitudes (a,c) and delays (b,d) between scans. Estimates were computed in subcortical GM, cortical GM, GM and NAWM from the ROI-based (a,b) and voxel-based analysis (c,d).

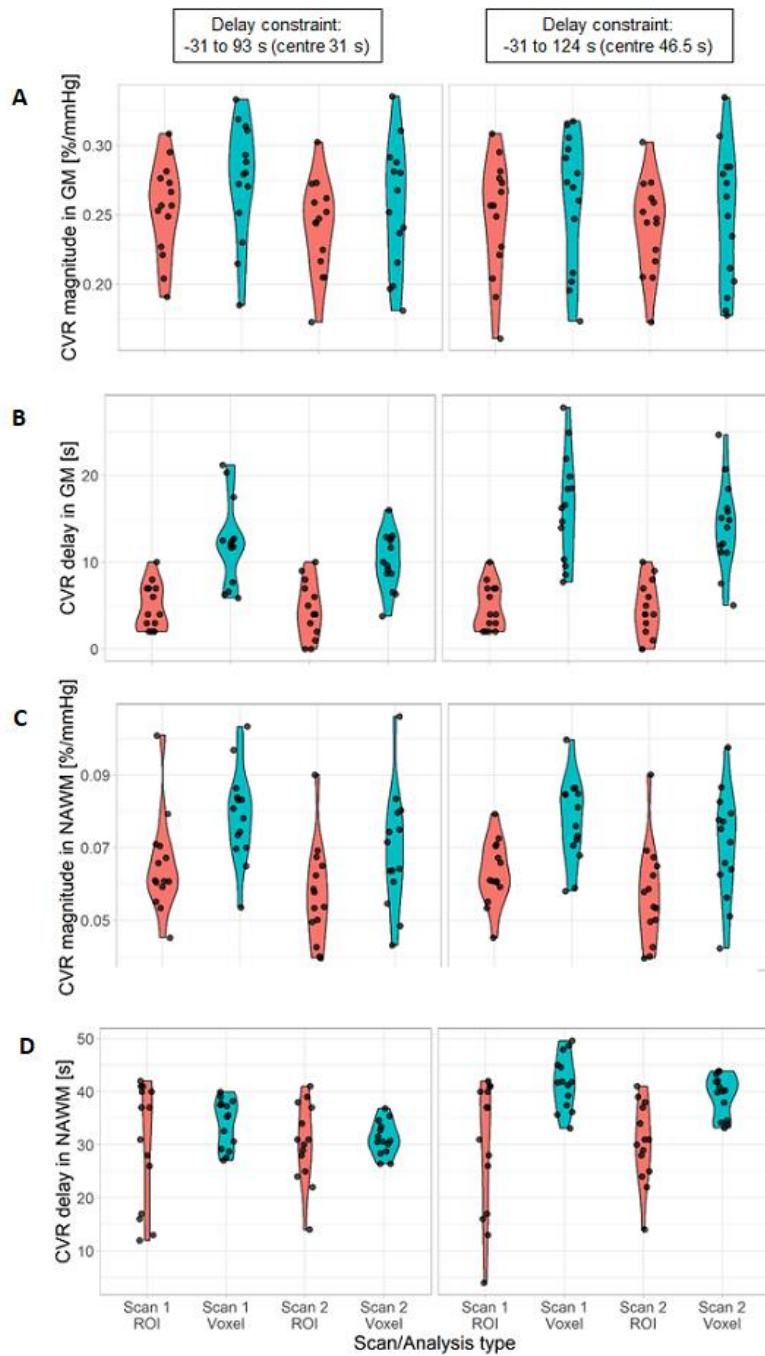


Figure 3-6: Violin distribution of CVR magnitude (A,C) and delay (B,D) in SGM (A,B) and NAWM (C,D) as a function of the scan and the processing method: ROI-based (red) versus voxel-based analysis (blue). The analysis was performed with two different delay constraints: -31 to 93 s (first column) and -31 to 124 s (second column).

Table 3-1: Mean and standard deviation across subjects of CVR magnitudes and delays in SGM, CGM, GM and NAWM computed for each scan with ROI- and voxel-based processing. Mean \pm standard deviation of the inter-scan and inter-analysis differences are reported with the 95% confidence intervals in square brackets.

ROI		Scan 1			Scan 2			Inter-scan difference (scan 2 – scan 1)	
Analysis type	Voxel	ROI	ROI-voxel difference	Voxel	ROI	ROI-voxel difference	Voxel	ROI	Voxel
CVR magnitude [%/mmHg]	SGM	0.26 \pm 0.03	0.25 \pm 0.04	-0.011 \pm 0.004 [-0.014, -0.008]	0.25 \pm 0.03	0.24 \pm 0.03	-0.010 \pm 0.003 [-0.012, -0.008]	-0.01 \pm 0.02 [-0.03, -0.00]	-0.01 \pm 0.02 [-0.02, -0.00]
	CGM	0.29 \pm 0.08	0.26 \pm 0.05	-0.030 \pm 0.036 [-0.051, -0.010]	0.27 \pm 0.09	0.25 \pm 0.05	-0.022 \pm 0.043 [-0.047, 0.003]	-0.02 \pm 0.04 [-0.04, 0.01]	-0.01 \pm 0.03 [-0.03, 0.01]
	GM	0.27 \pm 0.04	0.25 \pm 0.03	-0.020 \pm 0.013 [-0.027, -0.013]	0.26 \pm 0.05	0.24 \pm 0.03	-0.014 \pm 0.017 [-0.024, -0.004]	-0.02 \pm 0.03 [-0.03, -0.00]	-0.01 \pm 0.02 [-0.03, -0.00]
	NAWM	0.08 \pm 0.01	0.07 \pm 0.01	-0.014 \pm 0.005 [-0.016, -0.011]	0.07 \pm 0.02	0.06 \pm 0.01	-0.012 \pm 0.003 [-0.014, -0.010]	-0.010 \pm 0.009 [-0.015, -0.004]	-0.008 \pm 0.007 [-0.012, -0.004]
CVR delay [s]	SGM	8.8 \pm 4.8	3.9 \pm 2.6	-4.9 \pm 4.3 [-7.4, -2.4]	6.9 \pm 3.2	3.2 \pm 2.4	-3.7 \pm 2.1 [-4.9, -2.5]	-1.9 \pm 3.9 [-4.1, 0.4]	-0.6 \pm 1.4 [-1.5, 0.2]

CGM	14.9 ± 5.3	5.4 ± 2.6	-9.6 ± 5.1 [-12.5, -6.6]	12.7 ± 3.4	5.5 ± 3.3	-7.2 ± 3.2 [-9.0, -5.3]	-2.3 ± 3.8 [-4.5, -0.1]	0.1 ± 2.0 [-1.0, 1.3]
GM	12.2 ± 4.8	4.8 ± 2.7	-7.4 ± 4.3 [-9.9, -4.9]	10.1 ± 3.3	4.5 ± 3.2	-5.6 ± 1.9 [-6.8, -4.5]	-2.1 ± 3.2 [-3.9, -0.2]	-0.3 ± 1.5 [-1.2, 0.6]
NAWM	34.0 ± 4.6	30.1 ± 11.4	-4.0 ± 10.1 [-9.8, 1.9]	31.2 ± 3.2	30.2 ± 7.4	-1.0 ± 7.2 [-5.1, 3.2]	-2.8 ± 4.1 [-5.2, -0.5]	0.1 ± 8.0 [-4.5, 4.7]

Table 3-2: Inter-scan coefficients of variation for CVR magnitude and delay in SGM, CGM, GM and NAWM as a function of the analysis type.

Analysis type	Inter-scan CV for CVR magnitude [%]		Inter-scan CV for CVR delay [%]	
	Voxel	ROI	Voxel	ROI
SGM	7.48	7.95	50.00	40.92
CGM	14.91	10.98	27.66	37.44
GM	10.34	8.82	28.87	33.18
NAWM	11.75	10.79	12.49	26.44

Abbreviations: CVR: cerebrovascular reactivity, CV: coefficient of variation, ROI: region-of-interest, GM: grey matter, SGM: subcortical GM, CGM: cortical GM, NAWM: normal-appearing white matter.

Table 3-3: Mean and standard deviation of the physiological variables. The mean and standard deviation of inter-scan and inter-block differences are reported, together with the 95% confidence intervals.

	ROI/ Block	Scan 1	Scan 2	Inter-scan difference (scan 2 – scan 1)
BOLD baseline [a.u.]	SGM	340.1 ± 53.1	340.4 ± 50.7	0.4 ± 34.9 [-13.2, 13.9]
	CGM	328.9 ± 53.5	328.1 ± 49.2	-0.9 ± 35.3 [-14.6, 12.8]
	GM	336.4 ± 53.1	336.3 ± 49.3	-0.1 ± 35.3 [-13.8, 13.6]
	NAWM	295.4 ± 43.3	296.0 ± 39.9	0.6 ± 29.2 [-10.7, 11.9]
EtCO ₂ baseline [mmHg]	-	38.0 ± 3.8	37.7 ± 3.0	-0.3 ± 1.3 [-1.1, 0.4]
EtCO ₂ change [mmHg]	-	12.7 ± 1.6	13.6 ± 1.3	1.0 ± 1.0 [0.4, 1.5]

Chapter 3. Reliability of CVR measurements

EtO ₂ baseline [mmHg]	-	122.8 ± 5.4	122.9 ± 4.2	0.1 ± 3.4 [-1.9, 2.1]
EtO ₂ change [mmHg]	-	14.0 ± 3.1	15.6 ± 2.4	1.6 ± 2.1 [0.4, 2.8]
MAP pre-CVR scan [mmHg]	-	84.7 ± 7.7	85.8 ± 9.4	1.14 ± 8.28 [-3.64, 5.93]
MAP post-CVR scan [mmHg]	-	78.6 ± 8.4	78.8 ± 9.2	0.14 ± 5.32 [-2.93, 3.21]
Difference in MAP (post-CVR – pre-CVR) [mmHg]	-	-6.02 ± 5.76	-7.02 ± 6.58	-1.00 ± 8.76 [-6.06, 4.06]
Heart rate [bpm]	Air	71.6 ± 13.0	65.5 ± 13.7	-6.1 ± 5.2 [-9.1, -3.1]
	CO ₂	70.1 ± 13.1	65.4 ± 13.6	-4.6 ± 5.8 [-8.0, -1.3]
	All	70.9 ± 13.0	65.5 ± 13.6	-5.5 ± 5.4 [-8.6, -2.4]
Respiration rate [breaths per minute]	Air	12.3 ± 3.6	12.4 ± 3.6	0.1 ± 1.0 [-0.5, 0.6]
	CO ₂	12.4 ± 3.5	12.5 ± 3.5	0.1 ± 1.3 [-0.6, 0.9]
	All	12.4 ± 3.5	12.4 ± 3.5	0.1 ± 1.0 [-0.5, 0.7]
Inter-block difference in heart rate [bpm] (CO ₂ – Air)	-	-1.5 ± 2.3 [-2.8, -0.2]	-0.1 ± 1.9 [-1.2, 1.0]	-
Inter-block difference in respiration rate [breaths per minute] (CO ₂ – Air)	-	0.1 ± 0.9 [-0.4, 0.6]	0.0 ± 0.9 [-0.5, 0.6]	-

3.3.4 Comparison of ROI- and voxel-based analysis in vivo

CVR magnitude was lower and CVR delay shorter in the ROI-based versus voxel-based analysis (e.g. difference for scan 1: -0.020 [-0.027, -0.013] %/mmHg for GM CVR magnitude, -7.4 [-9.9, -4.9] s for GM CVR delay; Table 3-1). Nevertheless, CVR magnitude had a good test-retest repeatability (CV: 7.48–14.91 %) in all ROIs independent of analysis type (Figure 3-5, Table 3-1, Table 3-2). The repeatability of CVR delay in GM structures was good (28.87 % for the voxel-based analysis, 33.18 % for the ROI-based analysis; Figure 3-5, Table 3-1, Table 3-2). CV for CVR delay in NAWM from the voxel-based analysis was 12.49 %, compared to 26.44 % in the ROI-based analysis (Table 3-2), and its distribution was tightly centred around 33 seconds (Figure 3-6).

Increasing the upper delay constraint resulted in a delay range with a higher mid-point (46.5 s for the -31 to 124 s range vs. 31 s for the -31 to 93 s range). CVR delays from the voxel-based analysis were extended (difference for scan 1: +4.1 [2.7, 5.4] s in GM) whereas CVR delays from the ROI-based analysis did not change (Figure 3-6, Table A2-1). CVR magnitudes from the voxel-based analysis were lower (difference for scan 1: -0.015 [-0.027, -0.003] %/mmHg in GM; Figure 3-6, Table A2-1); CVR magnitudes estimated using ROI analysis were not affected.

3.4 Discussion

In this work, we found through simulations that 3T BOLD CVR magnitude values determined using voxel-based analysis rapidly lost accuracy and precision at low tCNR. ROI-based analysis estimated CVR delay accurately but underestimated CVR magnitude due to averaging BOLD signals across voxels with a distribution of ground-truth values. Fitting data with a variable delay parameter was found to be essential to obtain accurate CVR magnitude estimates, however estimates from voxel-based analysis can be strongly dependent on the delay constraints. The 3T BOLD-CVR experiment using a

fixed inspired CO₂ stimulus showed good within-day repeatability, though CVR delay estimates were less repeatable than CVR magnitude estimates. However, we noted small systematic differences in CVR magnitude between the two scans.

3.4.1 Simulations

Simulation results showed that, for ROI-based analysis, the accuracy of CVR magnitude estimates did not depend on tCNR, but there was a consistent underestimation with respect to the ground-truth mean (6-26 % depending on the ROI) due to signal averaging over voxels with a distribution of ground-truth CVR delay. On the other hand, CVR magnitude estimates were closer to the ground-truth median, although without converging towards it at high tCNR. Moreover, CVR delay estimates from ROI-based analysis were close to the ground-truth median value, independent of tCNR, reflecting the asymmetry of the CVR delay distribution. For voxel-based analysis, CVR magnitude and delay were accurate with respect to the ground-truth mean values at high tCNR. However, substantial bias with respect to the ground-truth mean CVR magnitude and delay values were found at low tCNR. Additional simulations showed that the choice of delay constraints had a strong impact on the accuracy of both parameters at low tCNR. This can be explained by the distribution of the CVR delay estimates being dominated by the delay constraints at low tCNR. Regarding precision, this was similar for CVR magnitude estimates using both methods. For CVR delay estimates, precision was higher for voxel-based analysis, however this may reflect the estimates being determined by the constraints rather than the intrinsic precision. Additional simulations explored the practice, reported in the literature, of fitting the CVR signal without a delay, or with a delay obtained by fitting the mean signal in GM or across the whole brain. This resulted in substantial systematic errors (2 – 24%) in CVR magnitude, irrespective of whether voxel- or ROI-based analysis was used, though precision was increased.

3.4.2 In vivo findings

In our group of healthy volunteers, we found GM CVR magnitudes (range: 0.19 – 0.24 %/mmHg) within the range of reported values from previous repeatability studies,^{114,263,271} though one study using an EtCO₂ targeting stimulus reported GM CVR magnitude of 0.43 %/mmHg.²⁶⁴ In our study, NAWM CVR magnitudes were lower than in GM (0.06 – 0.08 versus 0.19 – 0.24 %/mmHg) these values were also in good agreement with the literature,^{114,263} except for one study that reported NAWM CVR magnitude of 0.15 %/mmHg, but scanned adolescents, used an EtCO₂ targeting stimulus and processed the data using a voxel-based analysis with fixed global delay.²⁷¹ CVR delays were shorter in GM than in NAWM (3.2 – 14.9 s versus 30.1 – 34.0 s), agreeing with results from a previous repeatability study at 1.5T.¹¹⁴ Our results also provide further evidence for the good repeatability of the CVR experiment using an fixed inhaled stimulus: CVs for CVR magnitude repeatability were low (range including all ROIs: 7.48 – 14.91 %), similar to reported literature values using the same technique and processing method,¹¹⁴ but higher than studies using an EtCO₂ targeting stimulus.^{263,264} CVs for CVR delay repeatability (12.49 – 50.00 %) were similar to previously reported values at 1.5T.¹¹⁴

When comparing analysis approaches, we found systematically higher CVR magnitudes and longer CVR delays in all tissues for the voxel-based analysis, which was consistent with simulations. Indeed, simulations showed that processing methods are intrinsically dependent on the ground-truth distributions and differences in CVR estimates obtained from voxel- and ROI-based analyses can arise from asymmetry in those distributions. This finding, confirmed here in simulations and in data from healthy volunteers, can limit inter-study comparisons. Repeatability of CVR magnitude measurements was similar for both methods, however the repeatability for CVR delay in NAWM computed using a voxel-based analysis was higher than for ROI-based analysis. We showed that these effects were related to the delay constraint and high noise level in the voxel-wise BOLD signals. These findings are

consistent with our simulation results and show that CVR estimates from voxel-based analysis are likely to be unreliable.

Surprisingly, average CVR magnitude was slightly lower at the second scan. Such a bias was only reported in one previous repeatability study, which found that a reduction in CVR magnitude between scans was associated with higher baseline EtCO₂ and greater EtCO₂ change in the second scan.²⁷⁸ In the present study, EtCO₂ change was also significantly greater in the second scan compared to the first scan, but baseline EtCO₂ was unchanged. Greater EtCO₂ change was also associated with reduction in CVR magnitude. Therefore, we speculate that the non-linearity of the (approximately sigmoidal)⁹⁴ BOLD response to EtCO₂ combined with the greater EtCO₂ change explained the reduced CVR estimates based on a linear model at the second scan. The reason for the greater EtCO₂ change at the second scan is not known; based on the inter-scan reduction in heart rate, we speculate that habituation to the CVR experiment could be a contributing factor. This could impact studies where CVR scans are repeated within the same day, for example to investigate instantaneous effects of a specific treatment on CVR. On the other hand, this might be a short-term effect that would not affect longitudinal studies of CVR, but further work is needed to confirm this.

3.4.3 Implications

Our findings have some implications for future studies. First, using devices targeting specific values of and changes in EtCO₂ could be beneficial in reducing the impact of variable EtCO₂ change and baseline EtCO₂.⁸⁴ Familiarising the participants with the gas challenge prior to the CVR scan is essential to avoid anxiety and to minimise differences in baseline physiological state between repeated CVR measurements. Measuring blood pressure, heart and respiration rates during the CVR scan provides an indication of the extent of these effects.

The dynamic aspect of the CVR response should be taken into account. Estimating CVR delay provides additional physiological information, and is

known to differ between tissues^{71,114} and diseases.^{114,129} However, the interpretation of CVR delay should take into account possible steal effects through the redistribution of blood flow from blood vessels that have more reactivity^{92,139} and venous architecture in the WM that contributes to delayed WM responses.³¹⁴ A recent systematic review showed that, though correcting for CVR delay is becoming more common, consensus regarding the delay extraction method is still missing.¹⁰¹ We found that variable delays should be used when modelling the signal, since fitting with a fixed delay may result in large biases. Delay constraints are needed to restrict delays to realistic values. However, to allow variable delays, one should ensure sufficient EtCO₂ recording before and after the CVR scan. We expect that the findings of this study would also be applicable in analyses where bulk alignment of the EtCO₂ with the mean whole-brain or mean GM BOLD signal is used as a pre-processing step followed by voxel- or ROI-based analysis of CVR delay and magnitude.

Potential asymmetry in the distributions of ground-truth parameters should be considered. Using the median instead of mean estimates across ROIs in a voxel-based analysis could be more representative of the underlying distribution.

It is important to achieve sufficiently high tCNR to ensure accurate voxel-based mapping of CVR parameters. If this cannot be achieved then it may be advantageous to use an ROI-based analysis. However, intra-regional heterogeneity of the CVR parameters will be missed using this method, and the CVR magnitude estimates may not reflect the true mean values of non-uniform distribution. Moreover, any processing method that uses a voxel-based analysis to determine CVR delay will be subject to the bias at low tCNR found in this study (e.g. determining CVR delay for each voxel in order to realign the MRI signal before averaging). Analysis of data using different delay constraints may help verify that the estimates are not biased in this way. In our healthy volunteer cohort, analysis using different constraints did affect the

results, implying that an ROI-based analysis could be more accurate in this context.

3.4.4 Strengths and limitations

A strength of this work is that we used simulations to compare different analysis types, tCNR levels and fitting constraints. As such, we could predict estimation errors based on known ground-truth values. Furthermore, this is the first study to objectively compare multiple analysis approaches that have been commonly reported in the literature. Lastly, our in vivo repeatability MRI dataset and simulation code have been made publicly accessible to allow other researchers to test and compare their processing methods; it is hoped that this will facilitate objective comparison of methods and development of consensus-based harmonisation in the field.

There are some limitations in this study. First, findings from this study might not be applicable to CVR MRI experiments where EtCO₂ trace is not available. Furthermore, we did not investigate the effect of pre-processing methods such as spatial smoothing. However, we expect those to have an impact on the accuracy, precision and specificity of CVR estimates which should be investigated in future work. The comparison between CVR estimates from scan 1 and 2 involved linear regressions, where the estimates from scan 1 were used to predict the estimates from scan 2. A limitation of this is that it assumes that the variable used as predictor has no noise. However, CVR estimates from both scans are expected to have equal variance. Other methods could have been used to take into account the variability in the predictor, such as a χ^2 fit or orthogonal regression.^{331,332} Regarding the simulations, we did not account for a non-instantaneous impulse response function.⁹¹ Research is on-going to determine and validate the HRF underlying the BOLD-CVR signal.^{91,100} This could be addressed in future work. Moreover, the simulated noise was assumed to be independent in each voxel. For in vivo data, some noise components are temporally and spatially correlated due to phenomena such as physiological noise and patient motion. Future work could

benefit from the development of a realistic four-dimensional digital reference object for CVR. Moreover, previous work showed that noise distribution in MRI data with low tCNR is governed by a Rician distribution.³³³ However, in this work, a Gaussian distribution was used to add noise to the simulated CVR-BOLD data, which could have underestimated the true noise power. We also assumed no correlation between ground-truth CVR magnitude and delay within each tissue, since the relationship is not known. Furthermore, while our simulations incorporated non-uniform distributions of ground-truth CVR magnitude and delay within tissues, these were based on average measurements from our relatively small healthy volunteer cohort, which are themselves subject to the limitations addressed in this work. Future simulation work could incorporate improved estimates of ground-truth CVR parameter distributions. This limitation may affect the quantitative results but is unlikely to affect our conclusions.

3.4.5 Conclusion

In conclusion, we have shown that CVR measurement using 3T BOLD MRI with a fixed inhaled CO₂ concentration stimulus has good within-day repeatability in healthy volunteers, supporting its application in clinical studies and trials. We addressed the long-standing question of whether ROI- or voxel-based analysis is more accurate, predicting more robust estimation with the ROI-based approach, though underestimating CVR estimates with respect to the means of the ground-truth distribution. Voxel-based analysis should be applied and interpreted with caution. Finally, we found that accurately modelling the CVR delay is key for reducing errors in CVR magnitude estimates.

3.5 Conclusion with respect to the thesis

The work done in this chapter investigated the repeatability of the BOLD-CVR experiment using a fixed inhaled CO₂ stimulus and the accuracy and precision of different CVR data processing strategies. Experimental set-up and

processing strategies showed good repeatability, though results suggested that habituation to the gas challenge could affect the CVR effect. This effect can be mitigated by familiarising participants to the gas challenge prior to the scan. Recording blood pressure, heart and respiration rates could provide an indication of the extent of this effect. It is therefore important to monitor those parameters and to familiarise participants to the gas challenge prior to the scan. Furthermore, the work showed that ROI-based analysis with variable delay is better suited for SVD research than voxel-based analysis as low-perfusion brain regions such as WMH can have low tCNR levels.

4 Cerebral pulsatility measurement using BOLD-CVR MRI

This chapter is based on a technique to extract pulsatility from BOLD data developed at the University of Toronto by Dr Bradley MacIntosh and his group. Bradley provided me with their source code, which they used in previous studies.^{334,335} I further developed and adapted the code for BOLD-CVR data using MATLAB. Bradley also contributed to this work through discussions regarding the technique and data interpretation. I designed the study with the help of Dr Michael J. Thrippleton, Dr Michael S. Stringer, Prof Ian Marshall and Prof Joanna M. Wardlaw. I recruited healthy volunteers and acquired MRI data with the help of radiographers supervised by Maddy Murphy and Isla Mitchell. I processed and analysed the CVR data. I further acknowledge that Dr Joana Leitão from the University of Edinburgh provided me with a dataset from a healthy volunteer acquired at the University of Geneva as well as a code to filter the cardiac pulse and respiration signals and to identify their peaks. I would also like to thank Dr Alasdair G. Morgan for processing the PC data.

4.1 Introduction

Arterial stiffness is linked to ageing³³⁶ and brain-related diseases such as SVD, Alzheimer's disease and cognitive decline.^{75,337} It is thought that arterial stiffness results in the propagation of excessive pulsatility into the small blood vessels inducing downstream damage.² Studies have linked increased blood pulsatility in arteries and veins to SVD burden^{75,338,339} and one study found that increased arterial pulsatility was preceded by SVD lesions such as WMH and enlarged PVS.³⁴⁰

Cerebral pulsatility can be assessed by measuring blood flow using TCD or PC MRI. However, they are restricted to large cerebral blood vessels. Another technique of vascular origin is the BOLD MRI contrast. It is generated by the

presence of deoxyhaemoglobin in the blood which itself depends on vascular parameters such as CBF, and on brain metabolism and functional activity. Previous studies have used BOLD MRI to generate pulsatility maps³³⁴ and to assess cerebral pulsatility in the insular cortex, which was associated with pulsatility in the middle cerebral artery (MCA) measured using TCD.³³⁵

Previous studies used resting-state BOLD MRI to assess pulsatility. BOLD MRI is also used to assess CVR; therefore, the same scan could potentially be used to assess cerebral pulsatility. Moreover, as shown in previous studies, BOLD pulsatility contrast arose mostly from large blood vessels or from highly perfused regions. Cerebral pulsatility was not assessed in brain tissues of potential interest for SVD research such as NAWM or WMH.

This work aimed to: i) measure pulsatility using BOLD-CVR data in cerebral blood vessels of healthy subjects and compare it to PC pulsatility; ii) assess the feasibility of measuring BOLD-CVR pulsatility in tissues of potential interest for SVD research; iii) measure BOLD-CVR pulsatility in patients with SVD.

4.2 Methods

4.2.1 Participants

Datasets used in this analysis came from the healthy volunteer study mentioned in Chapter 3 and from the SVD study³⁴¹ described in Chapter 5. One additional dataset was provided by Dr Joana Leitão. It was acquired at the University of Geneva as part of a larger experiment on multisensory threat generalisation run by Maria Ploumitsakou, Prof Patrik Vuilleumier and Dr Joana Leitão in 2021.

4.2.2 MRI acquisition

Healthy volunteers and SVD patients underwent at least one 3T CVR scan as described in Chapters 3 and 5, respectively. Briefly, during the BOLD MRI (2D GRE-EPI readout) acquisition, participants had a hypercapnic challenge alternating between 2 minutes of medical air and 3 minutes of 6% CO₂-

enriched air. Healthy volunteers had a first medical air baseline of 3 minutes instead of 2. During the CVR scans, the expired CO₂ concentration waveform was recorded with a sampling frequency of 20 Hz. Cardiac pulse and respiration signals were recorded using a pulse oximeter at the finger and bellows respectively (Siemens Healthcare, Erlangen, Germany) with a sampling frequency of 400 Hz. Each participant also had a PC scan of the carotids (TR/TE = 19.60/5.82 ms, 1.0x1.0x5.0 mm resolution, venc = 70 cm/s) and sinuses (TR/TE = 21.70/6.59 ms, 0.7x0.7x5.0 mm resolution, venc = 50 cm/s).³⁴¹ Structural images (T1W, T2W) were also acquired.

The dataset acquired in Geneva was an fMRI dataset acquired at 3T (TrioTim, Siemens Healthcare GmbH, Erlangen, Germany) using a 2D EPI sequence (TR/TE = 1300/31.6 ms, flip angle: 64°, slice thickness: 2.5 mm, multiband acceleration factor 3). During the MRI acquisition, the participant had to categorise auditory (pure tones at four different frequencies) and visual (four different shades of blue) stimuli. Cardiac pulse and respiration were recorded with a sampling frequency of 500 Hz and 62.5 Hz respectively using an MP150 BIOPAC acquisition system coupled with the Acqknowledge Software (BIOPAC Systems, Goleta, CA; Acqknowledge version 4.2 for PC/Windows). Cardiac pulse was measured using a TSD2000-MRI plethysmograph attached at the finger and respiration was measured with a TSD160A-MRI respiratory belt.

4.2.3 Data processing

All data were processed using MATLAB (version R2018b).

Physiological recordings

The CO₂ waveform was converted into an EtCO₂ signal (see Chapter 3).

The cardiac pulse was first comb-pass filtered with a cut-off frequency of 13.8 Hz (corresponding to the number of slices divided by the multiband factor divided by TR) to remove artifacts associated with multiband BOLD sequences. The signal was then band-pass filtered between 1–40 Hz to

suppress noise. Identification of peaks was done using the MATLAB function 'findpeaks' followed by manual editing. During manual editing, spurious cardiac cycles were also identified. Data points acquired during those cycles were removed from the analysis. Then, each time point of the cardiac pulse was normalised according to its position in the cardiac cycle. Hereafter, those normalised cardiac time points are referred to as normalised cardiac positions.

For the fMRI dataset, the respiration data were also processed using a band-pass filter between 0.05–1 Hz.

BOLD-CVR data

DICOM files were converted into NIFTI format.³²³

BOLD-CVR data were processed voxel-wise using the same CVR data processing pipeline as previously including pre-processing steps (see Chapter 3). Briefly, multiple linear regressions between the BOLD time course, time-shifted EtCO₂ profile and a vector comprising the volume numbers to account for a linear signal drift were undertaken. Time shifts allowed for the EtCO₂ profile ranged from -31 to 93 s. This procedure was used to: i) detrend the BOLD time course by subtracting the term associated with linear drift from the BOLD signal; ii) extract the time delay defined as the time shift resulting in lowest sum of squared residuals.

Using the extracted time delay, each BOLD time point could be noted as being part of either an air block, a CO₂ block or a transition period defined as the one minute period from the start of an air or CO₂ block, and could be separated accordingly (Figure 4-1). Time points within transition periods were not considered for the analysis. The one-minute transition period resulted from a compromise between measuring enough BOLD time points to sample the cardiac cycle and taking into account the dispersion of the BOLD response to hypercapnia.⁹¹

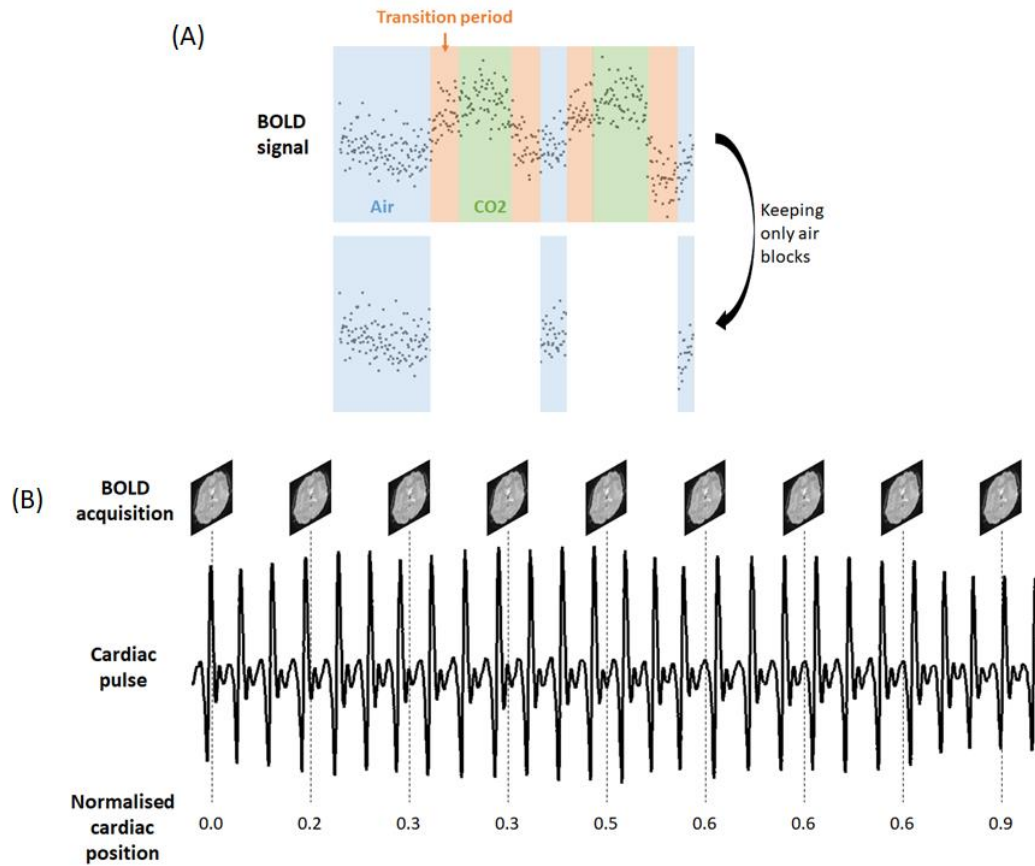


Figure 4-1. Preparation of BOLD data for pulsatility extraction. (A) Identification and separation of air (blue) and CO₂ (green) blocks and 1-min transition (orange). The example illustrated here shows extraction of air blocks. periods. (B) Sorting of BOLD timepoints according to the cardiac position.

For each voxel, the BOLD time points were associated with the closest normalised cardiac positions taking into account that each brain slice was acquired at a different time (Figure 4-1, Figure 4-2). The resulting BOLD waveforms were sampled differently across slices due to the differences in slice time acquisition. Therefore, the normalised cardiac cycle was divided into bins corresponding to a resolution of 0.002 along the cardiac cycle, and the median of BOLD values in each bin was taken (Figure 4-2). This procedure resulted in: i) the possibility of averaging the waveforms within a region; ii) comparable waveforms from the voxel- and ROI-based analysis; iii) reducing the effect of noise.

For the ROI-based analysis, an additional processing step was conducted (Figure 4-2). The voxel-wise BOLD waveforms in a ROI were not in phase given that the cardiac contribution to the BOLD signal differed across voxels due to cardiac wave propagation. Therefore, the Fourier series fitted to the BOLD waveforms were aligned with respect to their maximum value at the expense of losing robustness against noise (that is, the maximum of the Fourier series could be sensitive to an abrupt signal change due to noise). Moreover, the mean BOLD intensity was subtracted from the corresponding BOLD waveform. Hereafter, the aligned BOLD waveforms within the ROI were averaged and the average of the voxel-wise mean BOLD intensities computed previously was re-added to rescale the mean BOLD waveform.

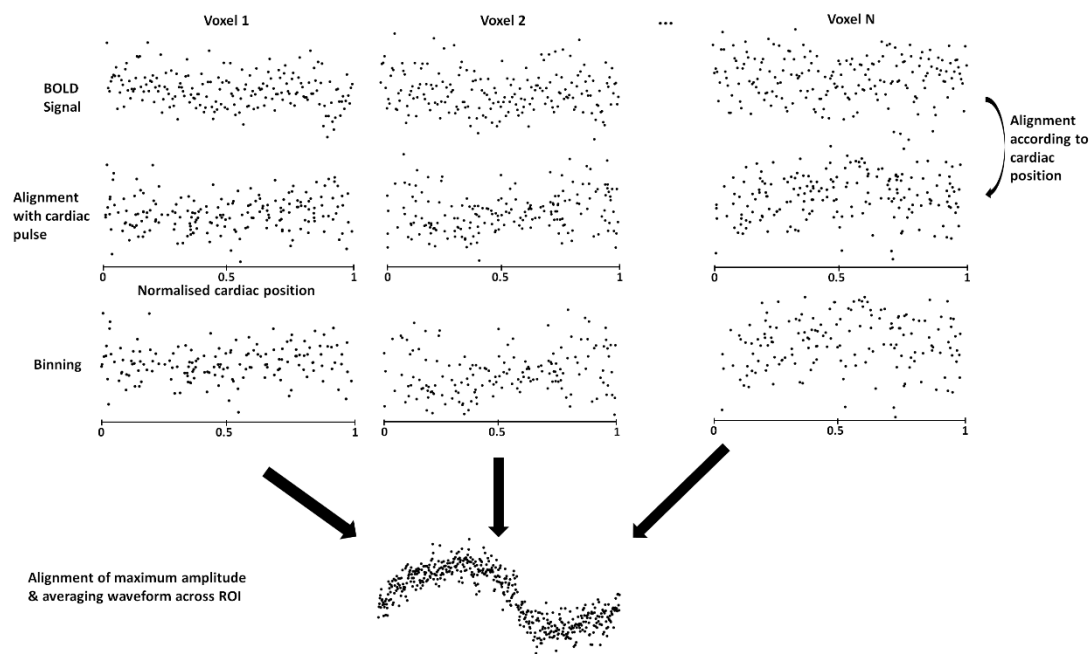


Figure 4-2. BOLD waveform formation. The BOLD signal in each voxel is sorted according to the normalised cardiac position, then binned. For ROI-based analysis, the binned signals are aligned according to the maximum amplitude of the fitted Fourier series and averaged across the voxels to form the mean BOLD waveform of the ROI.

For both the ROI- and voxel-based analysis, Fourier series were used to model the BOLD waveforms:

$$f(t) = a_0 + \sum_{i=1}^n (a_i \cos(it) + b_i \sin(it)) \quad (5-1)$$

The coefficients a_0 , a_i and b_i , $i=1, \dots, n$, were estimated by the fit. n corresponds to the order of the Fourier series that was set to 1, 2 and 3 in this work.

Two coefficients were used to measure cerebral pulsatility. First, we used Gosling's pulsatility index (PI) that is common in the literature when measuring pulsatility with PC MRI.^{72,75,338} PI was adapted for BOLD-CVR pulsatility and defined as:

$$BOLD-CVR PI = \frac{w_{max} - w_{min}}{w_{mean}} \quad (5-2)$$

Here, w designates the BOLD waveform along the normalised cardiac cycle with w_{max} being the maximum, w_{min} the minimum and w_{mean} the mean value of the waveform. A second coefficient was used to compare results with a previous study: the root mean square (RMS) of the coefficients of the Fourier series: a_i , b_i , $i=1, \dots, n$.³³⁵ This reflects the amount of oscillations in the BOLD waveform compared to a flat signal. Normalisation of the coefficient to the signal intensity was not applied here to replicate the methodology from Atwi et al., 2019.³³⁵

CNR of the mean BOLD waveform in a ROI was defined as the amplitude of the waveform divided by the standard deviation of noise in the waveform. The latter was obtained by subtracting the fitted 1st order Fourier series from the BOLD waveform and taking the standard deviation of the remaining signal. Only CNR using the 1st order Fourier series fit was used because the metric was helped estimating noise level in the BOLD waveforms and was not used for quantitative analysis.

Regions of interest for BOLD-CVR pulsatility

BOLD-CVR pulsatility was analysed in different brain regions. The T2W and BOLD-CVR PI obtained from the 1st order Fourier series and air block data were used to localise the MCA and superior sagittal sinus (SSS) regions.

Masks were manually drawn in those regions where PI was higher or equal to 0.1, which corresponded to highly pulsatile voxels (Figure 4-3).

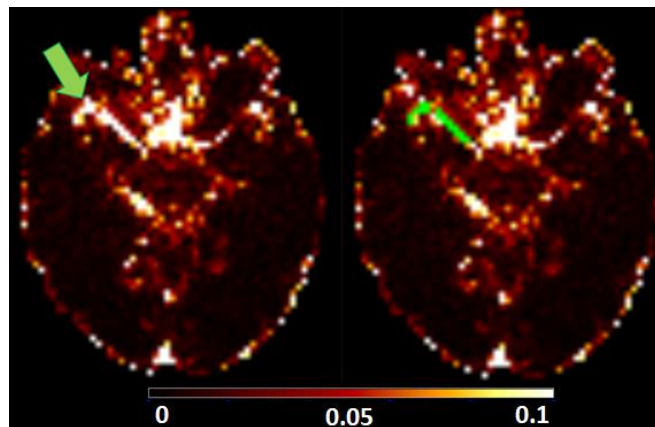


Figure 4-3. Segmentation of MCA in the right hemisphere of one of the healthy volunteers corresponding to voxels showing high pulsatility on the PI map. The map without segmentation is shown on the left and the mask is overlapped on the map on the right.

Using T1W images, ROIs were drawn manually in the internal capsule, in the centrum semiovale (CSO) NAWM and in the cortical GM next to the CSO NAWM region, designated hereafter as CSO cortical GM. In healthy volunteers, FSL FIRST³²⁶ and FLIRT^{329,330} were used to segment putamen, insular cortex and hippocampus in native T1W space based on the MNI-152 template.^{327,328} In SVD patients, the insular cortex was segmented in the same way, but putamen and hippocampus were segmented using an in-house processing pipeline that combines FreeSurfer and FSL outputs. The three types of mask were then eroded using a box kernel with a width of 3 voxels centred on the target voxel and registered to BOLD space using FSL FLIRT.

As this was a pilot study, for all subjects, only regions in the right hemisphere were considered except for SSS.

fMRI data

The fMRI dataset was received as a NIFTI image and was used to investigate the effect of respiration correction on pulsatility maps. To this end, two images

were considered: the raw BOLD image and the BOLD image where RETROICOR correction was applied using the filtered respiration signal.³⁴² In this correction, a low order Fourier series is created based on the extracted phase of the respiration trace. The model is then used to regress out the respiration contribution from the BOLD signal. Both raw and respiration-corrected images were realigned to the respective mean BOLD images using SPM12.³²⁴ BOLD volumes acquired during the tasks were discarded. Hereafter, extraction of BOLD pulsatility from both images was the same as for the BOLD-CVR data: sorting the BOLD timepoints according to the normalised cardiac position, fitting the BOLD waveform with a Fourier series and computing the BOLD-CVR PI and RMS coefficients on a voxel-wise basis. The relative error of the pulsatility maps without respiration correction with respect to the corrected maps was investigated.

PC data

Regions were drawn manually around the internal carotid and vertebral arteries and around the SSS. Background phase correction was undertaken by subtracting the mean velocity from a background ROI as described previously.⁷⁵ Flow (ml/min) from the internal carotid arteries and vertebral arteries from both sides were added together to get the total arterial flow.

Gosling's equation was used to define PI as: $PC\ PI = \frac{Flow_{max} - Flow_{min}}{Flow_{mean}}$.

SVD neuro-imaging features

WMH masks were segmented as described in Chapter 5. WMH volumes were defined as percentage of intracranial volume (%ICV) and were log-transformed to the base-10.

WMH were visually scored using the Fazekas scale³⁴³ and summing periventricular and deep WMH scores to give an overall Fazekas score from 0 to 6. Total SVD features were also visually scored from 0 to 4 by combining WMH, lacunes, microbleeds and PVS scores as done previously.¹⁸

4.2.4 Statistics

Values were reported as mean \pm standard deviation. Inter-analysis and inter-block differences were calculated using Bland-Altman statistics and were accompanied by 95% confidence intervals in square brackets. Linear regressions were used to model 1) BOLD-CVR pulsatility as a function of PC PI; 2) the effect of EtCO₂ baseline on pulsatility during the air blocks; 3) the effect of EtCO₂ baseline and EtCO₂ change on the change in pulsatility between blocks. Differences in pulsatility between the healthy and SVD groups was analysed using a Wilcoxon rank sum test (significance level: $p < 0.05$). The relationship between BOLD-CVR pulsatility in SVD patients and SVD burden (WMH volume, Fazekas score, SVD score) was investigated using linear models adjusted for age. Regression coefficients were reported with 95% confidence intervals and p-values.

4.3 Results

4.3.1 Participants

From 15 healthy volunteers recruited in the study, 9 had a complete recording of the cardiac pulse during the CVR scan (median age [interquartile range (IQR)]: 27.0 [23.0, 30.0]; Table 4-1). 20 datasets from SVD patients with complete cardiac pulse recording were selected based on the quality of the cardiac pulse trace assessed visually (median age: 63.3 [55.1, 70.2], median SVD score: 1 [0, 1]; Table 4-1). Of those datasets with complete cardiac pulse recordings, one SVD patient had a good respiration signal and 3 respiration recordings failed to capture the full respiration motion of the abdomen (1 from SVD patient and 2 from healthy volunteers). All the remaining respiration signals had some degree of clipping, i.e. cut-off of low and/or high signal intensities.

The participant who underwent the fMRI acquisition in Geneva was a 23 years old male.

Table 4-1: Population characteristics for the pulsatility analysis. Variables are reported as median with IQR in square brackets, except for the number of participant, *N*, sex and diagnosis of hypertension and diabetes reported as number (%).

	Healthy volunteers median [IQR]	SVD patients median [IQR]
N	9	20
Age	27.0 [23.0, 30.0]	63.3 [55.1, 70.2]
Female	7 (78 %)	5 (25 %)
Systolic blood pressure [mmHg]	116 [112, 120]	149 [141, 158]
Diagnosis of hypertension	-	15 (75 %)
Diagnosis of diabetes	-	9 (45 %)
WMH volume [ml]	-	6.57 [4.54, 12.23]
SVD score	-	1 [0, 1]

4.3.2 Cerebral pulsatility in healthy volunteers

Optimisation and comparison with pulsatility from PC MRI

The optimisation of pulsatility measurements was conducted based on:

- the order of the Fourier series fit: 1 to 3
- the analysis type: ROI- versus voxel-based
- the pulsatility coefficient: PI versus RMS.

Figure 4-4 shows a visual comparison of pulsatility maps for different orders of the Fourier series. The maps had a high blood vessel contrast and pulsatility was observed in CSF. As the order of the Fourier series increased, the PI map became more noisy, but the opposite was true for RMS map. This was confirmed by Table 4-2, which showed that the mean and standard deviation of PI in the MCA and SSS regions increased with the order, though this was only significant for the voxel-based analysis (difference between order 3 and 1: +0.0488 [0.0382, 0.0593] in MCA). On the other hand, RMS in those regions decreased with the order (difference between order 3 and 1 for voxel-based analysis: -3.81 [-5.58, -2.04]). Inter-analysis differences in MCA and SSS

regions of healthy volunteers showed higher PI and RMS in the voxel- compared to ROI-based analysis (difference for PI in MCA, order 1: -0.0206 [-0.0346, -0.0065]; Table 4-3), suggesting that voxel-based analysis could be more sensitive to noise.

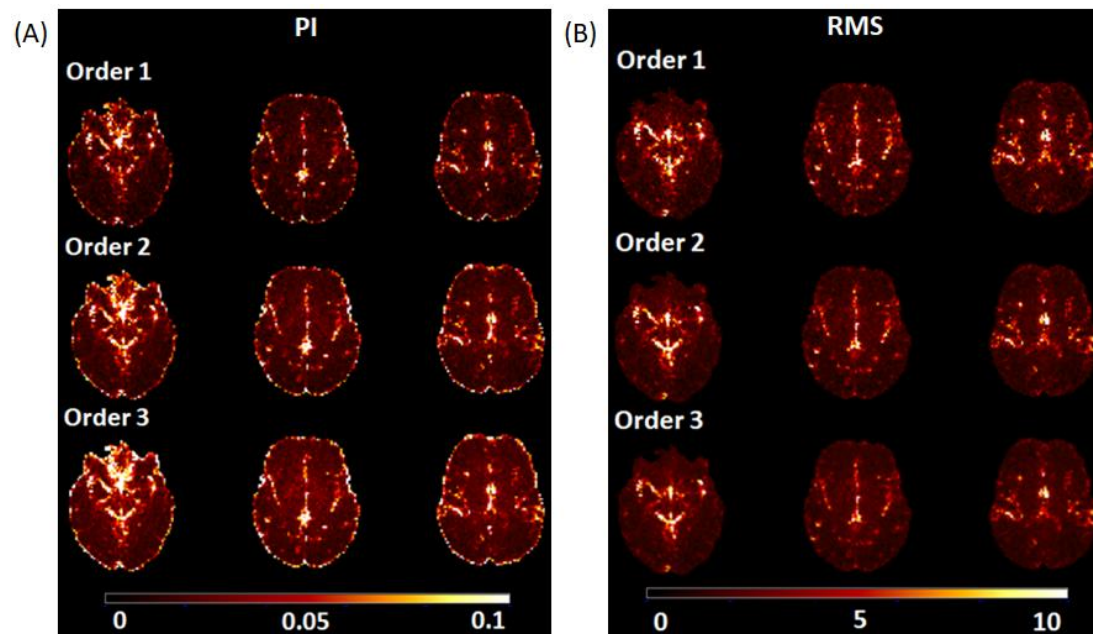


Figure 4-4: Pulsatility maps in one of the healthy volunteers as a function of the order of the Fourier series. Two types of pulsatility maps are shown: (A) PI map and (B) RMS map. The PI map appeared more noisy with increasing order of the Fourier series. The opposite was true for the RMS map.

BOLD-CVR pulsatility coefficients in the MCA and SSS regions were respectively compared to arterial and SSS PI from PC MRI for different orders of the Fourier series and the two types of analysis using linear regressions (Table 4-4). SSS pulsatility measurements between techniques were associated (regression coefficient for ROI-based PI, order 1: $B = 0.272$ [0.080, 0.463]; Table 4-4, Figure 4-5). On the other hand, MCA BOLD-CVR pulsatility increased with PC pulsatility though not significantly (Table 4-4; Figure 4-4).

Following the optimisation and comparison of BOLD-CVR pulsatility measurements with PC pulsatility, the next analyses in this chapter used coefficients from the ROI-based analysis: PI coefficients from Fourier series of order 1 and RMS coefficients from Fourier series of order 3.

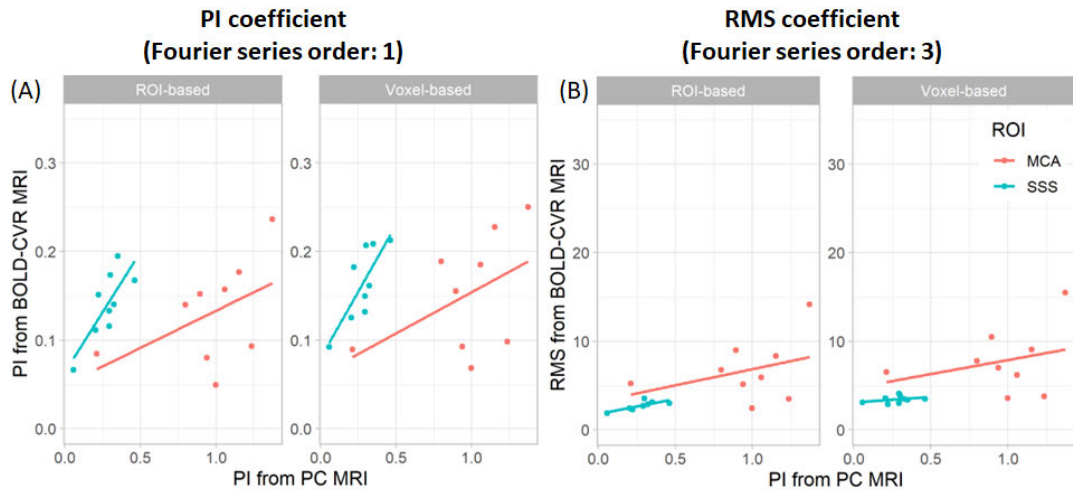


Figure 4-5: Comparison of pulsatility measurements between BOLD-CVR and PC MRI in healthy volunteers. Pulsatility from PC MRI was extracted in the arteries and SSS and was compared to the pulsatility from BOLD-CVR in the MCA (pink) and SSS regions (blue) respectively. Pulsatility from BOLD-CVR was extracted using PI with Fourier series of order 1 and using RMS using Fourier series of order 3 for different analyses (ROI- vs voxel-based).

Respiration correction using RETROICOR

Using the fMRI dataset with complete cardiac and respiration recordings, comparison between pulsatility maps with and without respiration correction was possible (Figure 4-6). The maps did not show visual differences, though the relative error maps and distributions showed the brain tissues affected by respiration, mostly brain outer regions, which are more sensitive to motion. The median relative difference [IQR] were -3.45 [-22.89, 14.48] % for the PI map and -3.76 [-18.02, 6.66] % for the RMS map.

Table 4-2: Differences between orders of the Fourier series fit to extract CVR pulsatility in healthy volunteers. Inter-order differences (mean \pm STD) in MCA and SSS regions are given for the PI and RMS coefficients and ROI- and voxel-based analysis. The 95% confidence intervals are given in the square brackets. The PI coefficient increased with the order of the Fourier series whereas the RMS coefficient decreased.

		Inter-order difference for the voxel-based analysis			Inter-order difference for the ROI-based analysis		
Order of Fourier series		Order 2 – 1	Order 3 – 1	Order 3 – 2	Order 2 – 1	Order 3 – 1	Order 3 – 2
MCA	PI	0.0304 \pm 0.0097 [0.0230, 0.0379]	0.0488 \pm 0.0137 [0.0382, 0.0593]	0.0183 \pm 0.0086 [0.0117, 0.0249]	0.00400 \pm 0.00239 [0.00217, 0.00584]	0.000766 \pm 0.005554 [-0.003504, 0.005035]	-0.00323 \pm 0.00517 [-0.00721, 0.00074]
	RMS	-2.51 \pm 1.50 [-3.66, -1.36]	-3.81 \pm 2.30 [-5.58, -2.04]	-1.30 \pm 0.84 [-1.95, -0.65]	-3.27 \pm 1.74 [-4.61, -1.94]	-4.74 \pm 2.49 [-6.66, -2.83]	-1.47 \pm 0.76 [-2.05, -0.89]
SSS	PI	0.0483 \pm 0.0153 [0.0365, 0.0601]	0.0873 \pm 0.0299 [0.0643, 0.1103]	0.0390 \pm 0.0180 [0.0252, 0.0528]	0.00608 \pm 0.0996 [-0.00158, 0.01374]	0.00818 \pm 0.01142 [-0.00060, 0.01696]	0.00210 \pm 0.00733 [-0.00353, 0.00773]
	RMS	-0.817 \pm 0.452 [-1.165, -0.469]	-1.21 \pm 0.68 [-1.73, -0.68]	-0.388 \pm 0.245 [-0.577, -0.200]	-1.30 \pm 0.20 [-1.45, -1.14]	-1.89 \pm 0.31 [-2.13, -1.65]	-0.594 \pm 0.109 [-0.678, -0.510]

Table 4-3: Differences between analysis to extract CVR pulsatility in healthy volunteers. Differences (mean \pm STD) between ROI- and voxel-based analysis in MCA and SSS regions are reported for the PI and RMS coefficients and for different Fourier series orders. The 95% confidence intervals are given in the square brackets. Voxel-based pulsatility was always higher than ROI-based pulsatility.

		Inter-analysis difference (ROI – Voxel)		
Order of Fourier series		1	2	3
MCA	PI	-0.0206 \pm 0.0183 [-0.0346, -0.0065]	-0.0470 \pm 0.0196 [-0.0621, -0.0319]	-0.0686 \pm 0.0282 [-0.0902, -0.0469]
	RMS	-0.116 \pm 0.187 [-0.260, 0.028]	-0.878 \pm 0.462 [-1.234, -0.523]	-1.05 \pm 0.53 [-1.46, -0.64]
SSS	PI	-0.0241 \pm 0.0107 [-0.0323, -0.0159]	-0.0664 \pm 0.0204 [-0.0820, -0.0507]	-0.103 \pm 0.032 [-0.128, -0.079]
	RMS	-0.0158 \pm 0.0538 [-0.0572, 0.0256]	-0.495 \pm 0.296 [-0.723, -0.268]	-0.701 \pm 0.437 [-1.037, -0.365]

Table 4-4: Coefficients from linear regression between pulsatility measurement from BOLD-CVR MRI and PC MRI in healthy volunteers. *p*-values are reported as well as 95% confidence intervals in square brackets. For CVR data, pulsatility was extracted in MCA and SSS regions for two types of pulsatility coefficient (PI vs RMS) and for two types of analysis (voxel- vs ROI-based). CVR pulsatility in MCA region was compared with arterial PC PI and CVR pulsatility in SSS region was compared with SSS PC PI.

	Order of Fourier series	Voxel-based PI	ROI-based PI	Voxel-based RMS	ROI-based RMS
MCA	1	B= 0.0929	B= 0.0838	B= 5.83	B= 6.20
		[-0.0644, 0.2501]	[-0.0538, 0.2213]	[-9.04, 20.71]	[-8.84, 21.25]
		p= 0.205	p= 0.193	p= 0.385	p= 0.362
	2	B= 0.103	B= 0.087	B= 4.011	B= 4.436
		[-0.065, 0.271]	[-0.050, 0.223]	[-7.350, 15.372]	[-6.214, 15.086]
		p= 0.192	p= 0.176	p= 0.431	p= 0.358
SSS	3	B= 0.101	B= 0.079	B= 3.162	B= 3.653
		[-0.070, 0.272]	[-0.051, 0.210]	[-6.224, 12.547]	[-5.094, 12.401]
		p= 0.205	p= 0.195	p= 0.452	p= 0.356
	1	B= 0.302	B= 0.272	B= 5.56	B= 5.63
		[0.093, 0.510]	[0.080, 0.463]	[1.36, 9.75]	[1.78, 9.49]
		p= 0.011	p= 0.012	p= 0.017	p= 0.011
	2	B= 0.292	B= 0.288	B= 2.87	B= 4.15
		[0.082, 0.502]	[0.032, 0.544]	[-0.13, 5.87]	[1.15, 7.15]
		p= 0.013	p= 0.032	p= 0.058	p= 0.014
	3	B= 0.210	B= 0.274	B= 1.24	B= 3.37
		[-0.023, 0.443]	[0.020, 0.529]	[-1.81, 4.29]	[0.89, 5.86]
		p= 0.070	p= 0.038	p= 0.369	p= 0.015

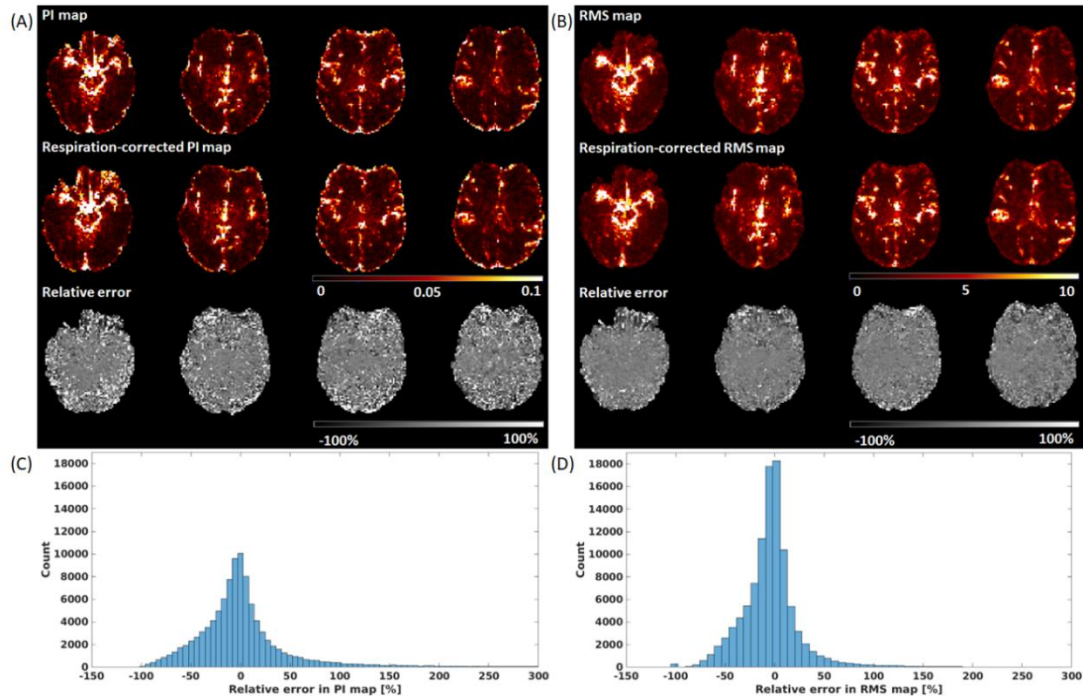


Figure 4-6: Comparison between pulsatility maps with and without respiration correction using RETROICOR. The top row shows the corrected and uncorrected (A) PI and (B) RMS maps as well as the relative error of the uncorrected map with respect to the corrected one. The bottom row shows the distribution of relative errors for the (A) PI and (D) RMS map. The x-axis was limited to the interval $[-150, 200]$ % for visual purposes.

Cerebral pulsatility in brain regions

Cerebral pulsatility in regions corresponding to cerebral blood vessels (MCA and SSS) and tissue regions supplied by the MCA (insular cortex, hippocampus, putamen, internal capsule, CSO cortical GM and CSO NAWM) were investigated. The BOLD waveforms of one healthy volunteer in those regions across the cardiac cycle are shown in Figure 4-7. In tissues that are less well perfused (e.g. CSO region) or in smaller ROIs where waveform averaging is less effective and partial volume is more prominent (e.g. hippocampus, CSO cortical GM), the amplitude of the waveforms is comparable to noise (i.e. CNR closer to 1.00).

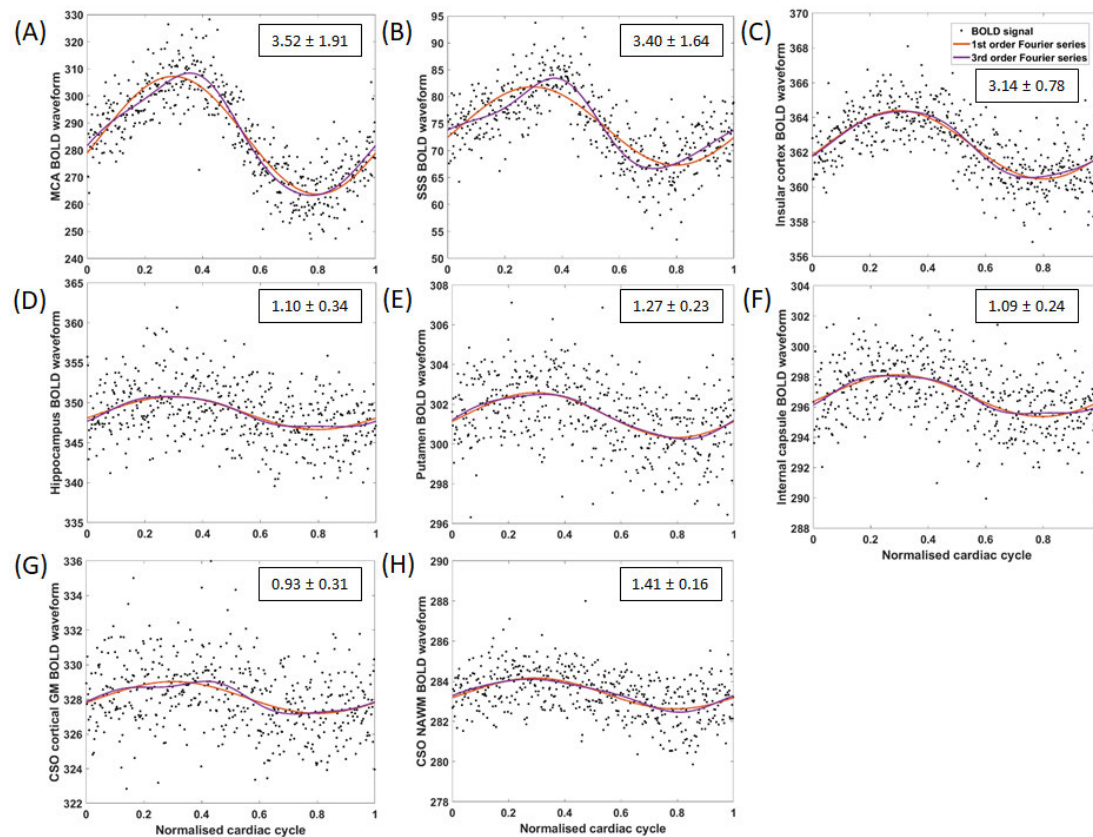


Figure 4-7: Mean BOLD waveform along the normalised cardiac cycle in different brain regions of one of the healthy volunteers. The regions considered were the (A) MCA, (B) SSS, (C) insular cortex, (D) hippocampus, (E) putamen, (F) internal capsule, (G) CSO cortical GM and (H) CSO NAWM. The fits using Fourier series of order 1 (orange) and 3 (purple) are shown. The text boxes on the upper right corner of each plot shows the mean and standard deviation of the waveform's CNR across participants. The y-axis is scaled differently on each subplot.

Pulsatility from the RMS coefficient in the MCA was higher than in the SSS, which was in agreement with the difference in pulsatility from PC MRI (Figure 4-8). This was not the case for the PI coefficient. Pulsatility decreased in tissues further downstream (Figure 4-9). There was no association found between pulsatility and EtCO₂ baseline (Table 4-5).

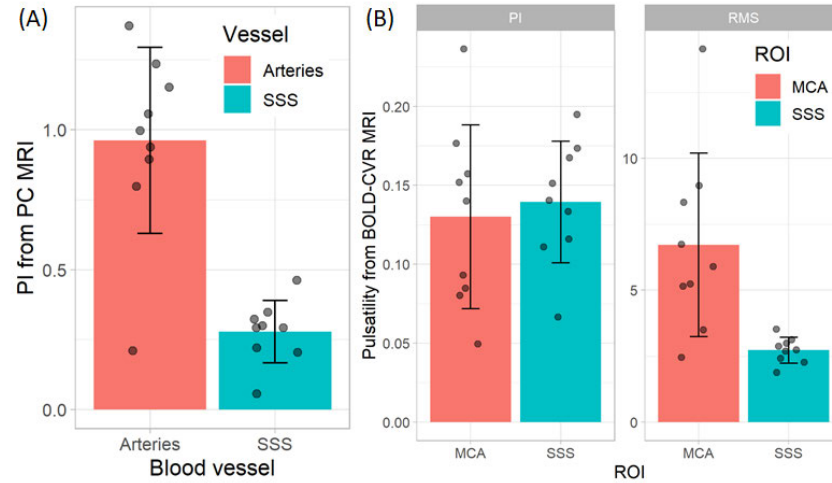


Figure 4-8: Pulsatility in regions corresponding to blood vessels in healthy volunteers. (A) Pulsatility from PC MRI in arteries (pink) and SSS (blue). (B) PI and RMS pulsatility from BOLD-CVR in MCA (pink) and SSS (blue) regions. The height of the bars corresponds to the mean pulsatility value and error bar represents the standard deviation.

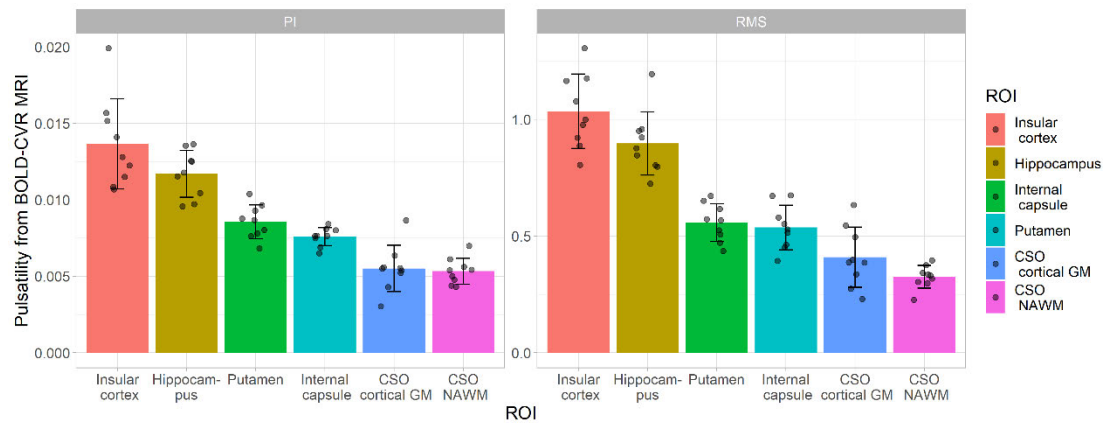


Figure 4-9: Pulsatility in tissues supplied by MCA in healthy volunteers. PI and RMS pulsatility from BOLD-CVR in the insular cortex, hippocampus, putamen, internal capsule, CSO cortical GM and CSO NAWM. The height of the bars corresponds to the mean pulsatility value and error bar represents the standard deviation.

Table 4-5: Linear regression between cerebral pulsatility and EtCO₂. Each row and column correspond to another model. The regression coefficients associated with EtCO₂ baseline and EtCO₂ change are reported along with p-values and 95% confidence intervals.

		Pulsatility during air block versus EtCO ₂ baseline	Change in pulsatility between blocks versus EtCO ₂ baseline	Change in pulsatility between blocks versus EtCO ₂ change
MCA	PI	B= 0.000702 [-0.012798, 0.014203] p= 0.906	B= 0.00275 [-0.00662, 0.01212] p= 0.510	B= -0.00668 [-0.02415, 0.01078] p= 0.396
	RMS	B= -0.00264 [-0.80848, 0.80319] p= 0.994	B= 0.122 [-0.320, 0.564] p= 0.534	B= -0.338 [-1.151, 0.474] p= 0.358
SSS	PI	B= 0.00246 [-0.00621, 0.01112] p= 0.524	B= 0.00535 [-0.00418, 0.01488] p= 0.226	B= -0.00761 [-0.02675, 0.01154] p= 0.379
	RMS	B= 0.02985 [-0.07986, 0.13956] p= 0.540	B= 0.103 [-0.232, 0.439] p= 0.490	B= -0.0848 [-0.7429, 0.5733] p= 0.769
Insular cortex	PI	B= 0.000256 [-0.000389, 0.000900] p= 0.379	B= 0.000073 [-0.000433, 0.000578] p= 0.743	B= 0.000082 [-0.000886, 0.001051] p= 0.846
	RMS	B= 0.00500 [-0.03169, 0.04169] p= 0.757	B= 0.00662 [-0.03482, 0.04806] p= 0.717	B= 0.00562 [-0.07397, 0.08521] p= 0.872
Hippocampus	PI	B= 0.000205 [-0.000098, 0.000507] p= 0.154	B= -0.000397 [-0.000766, -0.000027] p= 0.039	B= 0.000565 [-0.000270, 0.001400] p= 0.154
	RMS	B= 0.00591 [-0.02512, 0.03693] p= 0.666	B= -0.0361 [-0.0612, -0.0109] p= 0.012	B= 0.0531 [-0.0087, 0.1149] p= 0.082
Internal capsule	PI	B= 0.000042 [-0.000213, 0.000297] p= 0.710	B= -0.000087 [-0.000290, 0.000116] p= 0.346	B= 0.000147 [-0.000246, 0.000539] p= 0.406
	RMS	B= -0.00891 [-0.02568, 0.00786] p= 0.249	B= -0.00628 [-0.02057, 0.00801] p= 0.333	B= 0.0118 [-0.0155, 0.0391] p= 0.341
Putamen	PI	B= 0.000043 [-0.000089, 0.000175] p= 0.464	B= -0.000188 [-0.000446, 0.000069] p= 0.127	B= 0.000348 [-0.000148, 0.000845] p= 0.141
	RMS	B= -0.00622	B= -0.0148	B= 0.0262

		[-0.02772, 0.01527] p= 0.516	[-0.0344, 0.0048] p= 0.118	[-0.0123, 0.0647] p= 0.152
CSO cortical GM	PI	B= -0.000027 [-0.000377, 0.000323] p= 0.859	B= 0.000074 [-0.000131, 0.000279] p= 0.421	B= -0.000091 [-0.000493, 0.000311] p= 0.608
	RMS	B= -0.00579 [-0.03523, 0.02366] p= 0.656	B= 0.00338 [-0.01041, 0.01718] p= 0.580	B= 0.000345 [-0.026562, 0.027252] p= 0.977
CSO NAWM	PI	B= 0.000059 [-0.000130, 0.000248] p= 0.483	B= 0.000012 [-0.000056, 0.000081] p= 0.685	B= -0.000040 [-0.000168, 0.000088] p= 0.484
	RMS	B= -0.00207 [-0.01320, 0.00906] p= 0.673	B= -0.000232 [-0.003731, 0.003267] p= 0.880	B= -0.000161 [-0.006837, 0.006515] p= 0.956

Effect of CO₂ stimulus on cerebral pulsatility from CVR-BOLD data

Inhaling the CO₂-enriched CVR stimulus resulted in a decrease in MCA CVR-BOLD pulsatility (difference in PI: -0.0526 [-0.0847, -0.0204]; Figure 4-10, Table 4-6). There was a trend of increased pulsatility in the SSS regions and tissues which was significant in the internal capsule (difference in PI: 0.000846 [0.000125, 0.001567]; Figure 4-10, Table 4-6) and CSO NAWM (difference in PI: 0.000645 [0.000414, 0.000876]; Figure 4-10, Table 4-6). The change in pulsatility in hippocampus and putamen between the air and CO₂ blocks was higher for subjects with lower EtCO₂ baseline and higher EtCO₂ change (Table 4-5). There was no associations found between inter-block change in pulsatility, EtCO₂ baseline and EtCO₂ change in other ROIs (Table 4-5).

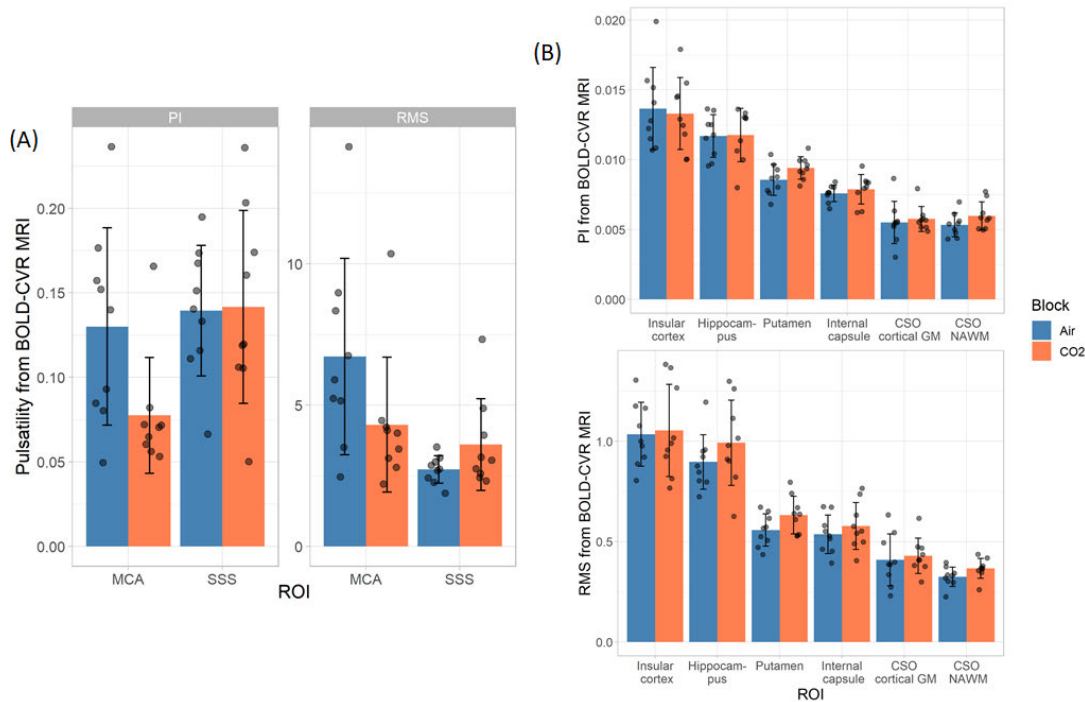


Figure 4-10: Pulsatility in the air and CO₂ blocks in different brain regions of healthy volunteers. (A) Pulsatility in the MCA and SSS regions. (B) PI and RMS pulsatility in different tissues supplied by MCA. The height of the bars corresponds to the mean pulsatility value and error bar represents the standard deviation. The air block pulsatility is shown in blue and the CO₂ block pulsatility in orange.

Table 4-6: Inter-block pulsatility differences in different brain regions of healthy subjects. Values are reported as mean \pm standard deviation for the PI and RMS coefficients. The 95% confidence intervals associated with the inter-block differences are shown in square brackets. The last two columns correspond to the inter-block differences in mean BOLD intensity and in BOLD variation during the cardiac cycle. MCA pulsatility decreased upon CO₂ inhalation whereas, in other brain regions, there is a trend in increased pulsatility in the CO₂ block.

	Air block		CO ₂ block		Inter-block difference (CO ₂ – Air)			
	CVR PI	CVR RMS	CVR PI	CVR RMS	CVR PI	CVR RMS	Mean BOLD intensity	BOLD variation
MCA	0.130 \pm 0.058	6.72 \pm 3.48	0.0775 \pm 0.0343	4.31 \pm 2.39	-0.0526 \pm 0.0418 [-0.0847, -0.0204]	-2.41 \pm 1.96 [-3.92, -0.90]	12.6 \pm 19.0 [-2.0, 27.3]	-12.0 \pm 9.9 [-19.6, -4.4]
SSS	0.139 \pm 0.039	2.73 \pm 0.49	0.142 \pm 0.057	3.61 \pm 1.62	0.00216 \pm 0.04603 [-0.03322, 0.03753]	0.881 \pm 1.501 [-0.273, 2.034]	31.4 \pm 25.3 [12.0, 50.8]	4.33 \pm 6.98 [-1.03, 9.70]
Insular cortex	0.0137 \pm 0.0030	1.04 \pm 0.16	0.0133 \pm 0.0026	1.05 \pm 0.23	-0.000359 \pm 0.002200 [-0.002050, 0.001332]	0.0191 \pm 0.1807 [-0.1198, 0.1579]	12.8 \pm 4.0 [9.7, 15.9]	0.102 \pm 0.885 [-0.578, 0.783]
Hippocampus	0.0117 \pm 0.0015	0.898 \pm 0.136	0.0118 \pm 0.0019	0.993 \pm 0.212	0.0000779 \pm 0.0022109 [-0.0016216, 0.0017773]	0.0953 \pm 0.1765 [-0.0404, 0.2310]	17.3 \pm 8.1 [11.0, 23.6]	0.273 \pm 0.869 [-0.395, 0.941]

Putamen	0.00759 ± 0.00059	0.537 ± 0.096	0.00788 ± 0.00106	0.578 ± 0.117	0.000288 ± 0.001328 [-0.000733, 0.001309]	0.0412 ± 0.1022 [-0.0374, 0.1197]	13.3 ± 4.8 [9.6, 17.0]	0.200 ± 0.519 [-0.199, 0.599]
Internal capsule	0.00855 ± 0.00111	0.558 ± 0.080	0.00940 ± 0.00080	0.633 ± 0.0942	0.000846 ± 0.000938 [0.000125, 0.001567]	0.0747 ± 0.0663 [0.0237, 0.1256]	10.1 ± 2.6 [8.1, 12.1]	0.372 ± 0.329 [0.119, 0.625]
CSO cortical GM	0.00550 ± 0.00151	0.410 ± 0.129	0.00576 ± 0.00089	0.430 ± 0.088	0.000252 ± 0.000929 [-0.000462, 0.000966]	0.0203 ± 0.0610 [-0.0265, 0.0672]	10.8 ± 3.0 [8.5, 13.1]	0.131 ± 0.331 [-0.123, 0.385]
CSO NAWM	0.00533 ± 0.00085	0.325 ± 0.049	0.00598 ± 0.00100	0.367 ± 0.050	0.000645 ± 0.000300 [0.000414, 0.000876]	0.0420 ± 0.0151 [0.0304, 0.0537]	2.13 ± 1.12 [1.27, 2.99]	0.198 ± 0.072 [0.142, 0.253]

4.3.3 Cerebral pulsatility in SVD patients

Comparison of cerebral pulsatility between SVD patients and healthy volunteers

Pulsatility measurements were compared between the healthy and SVD groups (Figure 4-11). Pulsatility in regions corresponding to blood vessels was increased in the SVD group, though only significantly so in the SSS (difference in mean values: 0.0701, $p < 0.001$, for BOLD-CVR PI; Figure 4-11). This was in agreement with the PC MRI pulsatility. In brain tissues, pulsatility was overall higher in the SVD group (e.g. difference in mean values: 0.00573, $p < 0.001$, for BOLD-CVR PI in putamen; Figure 4-11).

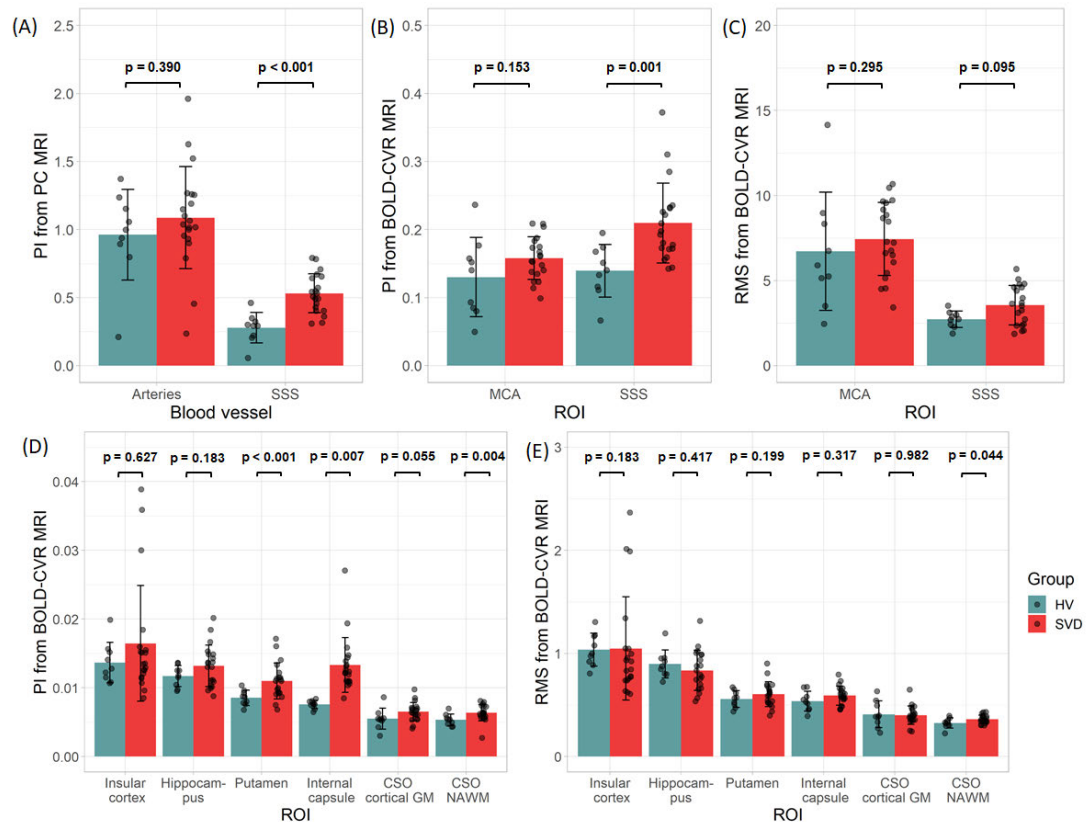


Figure 4-11: Pulsatility difference between healthy volunteers and SVD patients in different brain regions. (A) PC PI coefficient in the arteries and SSS. (B) BOLD-CVR PI coefficient in the MCA and SSS regions. (C) BOLD-CVR RMS coefficient in the MCA and SSS regions. (D) BOLD-CVR PI coefficient in different tissues supplied by MCA. (E) BOLD-CVR RMS coefficient in different tissues supplied by MCA. The height of the bars corresponds to the mean pulsatility value and error bar represents

the standard deviation. Results for the healthy group are shown in blue and results for the SVD group in orange. P-values from the Wilcoxon rank sum test are given at the top of the subplots.

Relationship between cerebral pulsatility and SVD burden

The following results were found in analyses adjusted for age. Increased arterial pulsatility from PC was associated with increased WMH volume ($B=0.539$ [0.201, 0.877] per ten-fold increase in %ICV) and higher Fazekas score ($B=0.135$ [0.012, 0.257] per score point increase; Table 4-7). Those findings were not replicated for MCA pulsatility from BOLD-CVR, though the trend was present (Table 4-7). The relationship between cerebral pulsatility and SVD burden depended on the brain regions, but most results did not reach significance (Table 4-7). Increased BOLD-CVR PI and RMS in CSO cortical GM was associated with higher Fazekas score (for PI: $B=0.000446$ [0.000015, 0.000876] per score point increase). Reduced PI in CSO NAWM was associated with increased WMH volume ($B=-0.00123$ [-0.00238, -0.00007] per ten-fold increase in %ICV) and higher Fazekas score ($B=-0.000342$ [-0.000728, -0.000045] per score point increase); though this was not replicated with the RMS coefficient.

4.4 Discussion

In this work, the feasibility of extracting cerebral pulsatility in healthy subjects using BOLD-CVR was investigated. The technique was optimised and showed moderate correlation with PC MRI. Pulsatility values and changes in pulsatility due to hypercapnia varied across brain regions, potentially reflecting the complex origin of the BOLD contrast. Cerebral pulsatility was also assessed in SVD patients, though no clear relationship between BOLD-CVR pulsatility and SVD burden were found.

Table 4-7: Linear regression between cerebral pulsatility and SVD burden. The regression coefficients associated with log10-transformed WMH volume, Fazekas score and SVD score are reported along with p-values and 95% confidence intervals. The models were adjusted for age.

ROI	MRI technique	CVR pulsatility coefficient	Log-transformed WMH volume	Fazekas score	SVD score
Arteries	PC	PI	B= 0.539 [0.201, 0.877] p= 0.004	B= 0.135 [0.012, 0.257] p= 0.033	B= 0.0249 [-0.1653, 0.2151] p= 0.786
MCA	CVR	PI	B= 0.0142 [-0.0185, 0.0469] p= 0.373	B= 0.00773 [-0.00231, 0.01776] p= 0.123	B= 0.00359 [-0.01091, 0.01809] p= 0.608
	CVR	RMS	B= 1.12 [-1.21, 3.46] p= 0.324	B= 0.425 [-0.317, 1.168] p= 0.243	B= 0.188 [-0.857, 1.233] p= 0.709
SSS	PC	PI	B= 0.00418 [-0.16319, 0.17155] p= 0.959	B= -0.000900 [-0.054812, 0.053012] p= 0.972	B= -0.0384 [-0.1088, 0.0320] p= 0.266
	CVR	PI	B= -0.0327 [-0.0940, 0.0285] p= 0.275	B= -0.00133 [-0.02179, 0.01912] p= 0.892	B= -0.00950 [-0.03681, 0.01781] p= 0.473
	CVR	RMS	B= 0.0573 [-1.3004, 1.4149] p= 0.930	B= 0.113 [-0.321, 0.547] p= 0.590	B= -0.0505 [-0.6428, 0.5419] p= 0.859

Insular cortex	CVR	PI	B= -0.00317 [-0.01292, 0.00658] p= 0.502	B= -0.000781 [-0.003940, 0.002377] p= 0.608	B= -0.00170 [-0.00592, 0.00253] p= 0.409
	CVR	RMS	B= -0.174 [-0.755, 0.406] p= 0.535	B= -0.0510 [-0.2383, 0.1363] p= 0.573	B= -0.111 [-0.361, 0.139] p= 0.363
	CVR	PI	B= 0.00167 [-0.00155, 0.00489] p= 0.289	B= 0.000516 [-0.000523, 0.002377] p= 0.309	B= -0.000595 [-0.002017, 0.000828] p= 0.390
Hippocampus	CVR	RMS	B= 0.0961 [-0.1136, 0.3057] p= 0.347	B= 0.0353 [-0.0317, 0.1023] p= 0.281	B= -0.0360 [-0.1282, 0.0562] p= 0.422
	CVR	PI	B= -0.00157 [-0.00590, 0.00277] p= 0.456	B= -0.000264 [-0.001677, 0.001149] p= 0.698	B= -0.000632 [-0.002528, 0.001265] p= 0.492
	CVR	RMS	B= 0.0168 [-0.0875, 0.1212] p= 0.738	B= 0.0156 [-0.0172, 0.0484] p= 0.330	B= 0.00516 [-0.04048, 0.05081] p= 0.814
Putamen	CVR	PI	B= 0.000320 [-0.002743, 0.003383] p= 0.828	B= 0.0000546 [-0.0009330, 0.0010423] p= 0.908	B= 0.000103 [-0.001235, 0.001442] p= 0.873
	CVR	RMS	B= 0.0141 [-0.1215, 0.1497] p= 0.829	B= 0.00668 [-0.03692, 0.05028] p= 0.750	B= 0.00660 [-0.05259, 0.06579] p= 0.817
	CVR	PI	B= -0.0000297 [-0.0014821, 0.0015415] p= 0.967	B= 0.000446 [0.000015, 0.000876] p= 0.043	B= 0.000255 [-0.000390, 0.000902] p= 0.417
CSO cortical GM	CVR	RMS	B= 0.0312 [-0.0671, 0.1295] p= 0.512	B= 0.0356 [0.0092, 0.0620] p= 0.011	B= 0.0325 [-0.0077, 0.0727] p= 0.107

CSO cortical NAWM	CVR	PI	B= -0.00123	B= -0.000342	B= 0.0000145
			[-0.00238, -0.00007]	[-0.000728, -0.000045]	[-0.0005601, 0.0005891]
			p= 0.039	p= 0.079	p= 0.958
	CVR	RMS	B= -0.0252	B= -0.00422	B= 0.00772
			[-0.0701, 0.0197]	[-0.01912, 0.01067]	[-0.01229, 0.02774]
			p= 0.253	p= 0.558	p= 0.427

4.4.1 Cerebral pulsatility in healthy volunteers

Optimisation and comparison with pulsatility from PC MRI

BOLD-CVR pulsatility measurements were optimised by visual inspection of pulsatility maps, varying the order of the Fourier fit, comparing ROI- versus voxel-based analysis and comparing BOLD-CVR pulsatility to PC pulsatility. Overall, ROI-based analyses using a Fourier series of order 1 for PI and of order 3 for RMS were more robust to noise and better correlated with pulsatility measurements from PC. This confirmed the use of the RMS coefficient from Fourier series of order 3 in a previous study.³³⁵ Associations between BOLD-CVR and PC pulsatility were investigated in arterial regions and in the SSS. Only in the SSS region were the two techniques significantly associated. This might reflect the fact that BOLD is more sensitive to venous blood, but it is important to note that the measurement location and arterial regions considered also differed: MCA was used for BOLD-CVR and the internal carotid artery along with vertebral arteries were used for PC.

Respiration correction using RETROICOR

The effect of respiration on BOLD-CVR pulsatility maps was investigated in one fMRI dataset. The difference between respiration-corrected and uncorrected pulsatility maps showed that pulsatility is affected by respiration mostly in the outer regions of the brain, which are more prone to respiration-induced motion. The median whole-brain relative error was low (3 %), but the IQR relatively big especially using the PI coefficient. Therefore, correcting for respiration, which was done in a previous study,³³⁵ could improve the correlations between BOLD-CVR and PC pulsatility measurements. This was not possible in this analysis as most of the respiration signals were clipped during the recordings. Respiration corrections such as RETROICOR need the maximum respiration amplitude related to inhalation,³⁴² which could not be obtained from the clipped signals.

Cerebral pulsatility in brain regions

Cerebral pulsatility varied across the brain and was also observed in CSF which could be explained by pulsatile blood vessels displacing surrounding CSF. From PC data, arterial pulsatility was higher than venous pulsatility which is in agreement with previous studies.³⁴⁴ This result was replicated using BOLD-CVR RMS coefficient but not using the PI coefficient. Differences between PC and BOLD pulsatility measurements could arise from BOLD contrast being affected by the vicinity of larger veins or by pulsatile motion artefacts due to the lower spatial resolution. Furthermore, this work showed that BOLD-CVR pulsatility was lower in regions further away from the main MCA branches. Extracting pulsatility in less well-perfused regions is limited by noise in the BOLD waveform. In a previous study, RMS pulsatility was measured in the insular cortex of 10 SVD patients.³³⁵ As the RMS coefficient is not normalised to the BOLD intensity, it is not comparable across scanners. Nevertheless, they found that RMS pulsatility in the insular cortex was higher than the whole brain pulsatility. This is supported by the results of this work where pulsatility in the insular cortex was higher than in the other tissue regions considered.

Effect of CO₂ stimulus on cerebral pulsatility

The effect of hypercapnia on cerebral pulsatility could be investigated using CVR data. During the CO₂ blocks, pulsatility decreased in the MCA, but did not change in the SSS. There are a few possible explanations for the decrease in MCA pulsatility. First, vasodilation increased CBF and reduced partial volume effect in the region considered, thereby increasing BOLD intensity and reducing PI. Second, there was limited dilation capacity under the pre-dilated state induced by hypercapnia which resulted in lower pulse pressure (we found lower BOLD variation across the cardiac cycle in MCA). Finally, ROIs were segmented using CVR pulsatility maps obtained from air blocks; therefore, vascular differences between normo- and hypercapnia could have emphasised partial volume effects. Another study in 10 SVD patients found increased pulsatility in MCA during hypercapnia without reporting levels of significance.³⁴⁵ The different result could come from different pre-processing

methods (example of differences: spatial smoothing, slice-time correction, respiration correction, removing scanner artefacts from cardiac pulse signal, duration of transition periods excluded from analysis). Moreover, an animal study found decreased pulsatility measured with transcranial Doppler in the basilar artery of rabbits during hypercapnia.³⁴⁶ Pulsatility in the SSS did not vary with hypercapnia. According to PC MRI, pulsatility in veins is low³⁴⁴ limiting further reduction.

Interestingly, cerebral pulsatility in tissues supplied by the MCA increased during the CO₂ blocks. Lower EtCO₂ baseline and higher EtCO₂ change could explain this change, but those associations with higher inter-block pulsatility change were not found in all tissues. Aside from intrinsic response of the vasculature to hypercapnia, there are other factors that could explain for this observation. First, as pulsatility is lower in tissues, it is more sensitive to noise. Specifically, participants are more prone to move during hypercapnia due to discomfort arising from the challenge and motion-related noise could artificially increase pulsatility. Second, increased pulsatility during hypercapnia was only significant in NAWM regions. As the BOLD response to CO₂ in those tissues is more dispersed,^{91,314} the BOLD signal intensity might not have stabilised even after excluding one-minute transition periods between blocks. This could have emphasised the difference between extrema of the BOLD waveform.

Overall, the effect of measuring pulsatility using BOLD-CVR varied across brain regions and depended on whether the ROI was purely a blood vessel, influenced also by differences between arterial and venous blood, or tissue containing blood vessels.

4.4.2 Cerebral pulsatility in SVD patients

Comparison of cerebral pulsatility between SVD patients and healthy volunteers

Cerebral BOLD-CVR pulsatility was higher in SVD patients than in healthy subjects in most brain regions. This was in agreement with PC pulsatility in the same cohorts and with previous studies.³⁴⁷ However, higher pulsatility in SVD

patients could also reflect the difference in age between the two groups as they were not age-matched.^{336,348}

Relationship between cerebral pulsatility and SVD burden

When investigating the relationship between cerebral pulsatility and SVD burden, increased arterial pulsatility from PC MRI was associated with WMH burden, with a similar trend using BOLD-CVR pulsatility. Other studies have also found such a relationship.^{75,338} The relationship between BOLD-CVR tissue pulsatility and SVD burden was heterogeneous, but CSO NAWM pulsatility was lower with increased WMH volume and Fazekas score, potentially reflecting the loss of cerebral blood vessels or viable tissue.

4.4.3 Future directions

In order for BOLD-CVR pulsatility to be used in future clinical research, the technique requires further optimisation and validation.

The CVR MRI experiment could be further optimised to allow extraction of pulsatility indices. For example, the duration of the rest and challenge periods in the paradigm of the experiment could be increased to allow sufficient sampling of the cardiac cycle and ensure stability of the BOLD signal. Optimisation of sequence parameters should also be undertaken: depending on heart rate, TR could be modified to sample more efficiently the cardiac cycle. The delimitation of transition periods between blocks in the CVR paradigm could be defined on an individual basis, taking into account the subject-specific MRI response to the stimulus. As illustrated in this work, respiration could also influence the calculation of PI, therefore future work should use respiration-correction methods.

Further work could also focus on the validation of cerebral pulsatility computation using BOLD-CVR. In this study, BOLD-CVR pulsatility was compared to PC pulsatility; however, the regions in which the techniques were compared were not identical. For example, BOLD-CVR pulsatility was extracted from the MCA territory and compared to PC pulsatility in internal

carotid and vertebral arteries. The technique could also be compared to other imaging techniques in different brain regions such as TCD³³⁵ or multiphoton microscopy in preclinical models. The technique would also benefit from preclinical research to assess its biological validity and where one can control for confounders such as respiration. Further validation would include investigating correlation with clinical variables, for example, confirming the relationship between increased BOLD-CVR pulsatility and increased blood pressure or comparing BOLD-CVR pulsatility in hypertensive and normotensive subjects. The technique should also be investigated in disease cohorts characterised by arterial stiffness such as in elderly or SVD patients.³⁴⁸ Specific conditions such as doing physical exercise or the effect of high altitude are also known to affect heart rate and blood pressure^{334,349,350} and could therefore be used to validate the technique.

4.4.4 Limitations

There are a few limitations that should be stated. First, cerebral pulsatility in tissues was not measured using another technique as comparison. TCD is not able to access such deep tissues due to the attenuation of ultrasound waves. Instead, another technique that could be considered in future work is 4D flow MRI.²⁸⁹

BOLD is an MRI contrast that depends on many parameters such as CBF, CBV, deoxyhaemoglobin concentration, haematocrit, oxygen consumption to name a few. Therefore, care should be taken when comparing BOLD pulsatility with flow pulsatility and more advanced models which better account for underlying physiological differences could be considered to measure pulsatility instead.

Small sample sizes were considered in the healthy and SVD cohorts. Therefore, it was not possible to account for vascular risk factors when investigating pulsatility in relation to SVD burden.

Last, the healthy volunteer data were used as a convenience group and were not age-matched to the SVD group: age and group were correlated with the SVD group being much older than the healthy group. As such, differences in cerebral pulsatility could reflect age differences.³⁵¹

4.5 Conclusion

This work is a proof-of-concept that cerebral pulsatility can be extracted from BOLD-CVR, which is a signal of vascular origin. Results were compared to pulsatility measurements from PC MRI data and showed small to moderate association between the two techniques. Different aspects of the technique remain to be optimised and validated for use in future clinical studies.

5 The Mild Stroke Study 3

5.1 Introduction

Due to the high prevalence of SVD in stroke² and dementia^{4,5} and lack of treatment, research is needed to deepen our understanding of SVD pathogenesis. According to previous studies, SVD is a global and dynamic disease associated with BBB breakdown,^{2,352–355} increased cerebral pulsatility^{75,339,356} and impaired CVR.^{72,74,196,357} The Mild Stroke Study 3 (MSS3: ISRCTN 12113543) is a prospective observational cohort study designed to investigate the role of vascular dysfunction in relation to the evolution of SVD. Its aims are to:

- identify factors associated with SVD lesion progression and regression
- determine the inter-relationships between parameters reflecting vascular dysfunction such as BBB leakage, CVR and cerebral pulsatility
- determine the influence of lifestyle factors on SVD vulnerability.

The study was approved by Southeast Scotland Regional Ethics Committee (reference 18/SS/0044) and NHS Lothian Research & Development (reference 2018/0084) and started in August 2018. It was designed by Prof Joanna M Wardlaw who is also the Principal Investigator of the study, Dr Fergus N Doubal and Dr Una Clancy. The study is funded by the Fondation Leducq Network for the Study of Perivascular Spaces in Small Vessel Diseases, UK Medical Research Council Dementia Research Institute, Row Fogo Charitable Trust, The Stroke Association, NHS Research Scotland, NHS Lothian Research and Development, and the University of Edinburgh.

My contribution to the study was to help with the CVR scans and administer the gas challenge to the participants. I processed and analysed the CVR data. The analyses that I carried out are detailed in Chapters 6 and 7.

5.2 Methods

5.2.1 Participants

The MSS3 recruited patients over 18 years old who presented at the Edinburgh/Lothian stroke services (e.g. stroke outpatient clinics, emergency departments, acute medical assessment units) with mild ischaemic stroke, i.e. stroke allowing them to continue their daily activities as defined by the modified Rankin Scale (mRS) of less or equal to 2 (0: no symptom of disability, 5: constant dependency, 6: death), and who were able to provide informed consent. Recruitment was performed by Dr Una Clancy, Dr Carmen Arteaga and Dr Fergus N Doubal. Exclusion criteria included pregnancy or breastfeeding, major neurological conditions, severe cardiac or respiratory diseases and MRI contraindications (e.g. pacemaker, metal implants).

The study aimed to recruit 50% patients with clinical lacunar stroke syndrome and 50% patients with non-lacunar ischaemic stroke syndromes. Strokes were defined as lacunar if a recent small subcortical infarct was visible on at least diffusion MRI (dMRI) or clinical CT images, and as cortical if patients had partial anterior circulation syndrome or posterior circulation syndrome, and if a recent cortical infarct was visible on at least dMRI or CT. Patients with no visible infarcts were still eligible to enrol in the study if no other lesions could explain their cortical stroke symptoms.

Lacunar strokes allowed for a starting point from which to track SVD disease progression. A control group formed of an age-matched population with the same high burden of vascular risk factors than the lacunar stroke syndrome group could be at high risk of developing SVD during the study if not already present at recruitment stage. Therefore, patients with non-lacunar stroke syndromes were defined as the control group as they have similar vascular risk factors and secondary prevention than patients with lacunar stroke syndrome. All participants received written and oral information regarding the study before signing the consent forms.

5.2.2 Study design

The study design is given in Figure 5-1. Patients had a pre-visit assessment where main diagnosis of index stroke was undertaken. Thereafter, they were invited for a minimum of 3 scans over a year (baseline visit, 6 months and 1 year follow-up visits). Patients with lacunar stroke syndrome or moderate-to-severe WMH burden were invited for additional visits between baseline and 6 months follow-up.

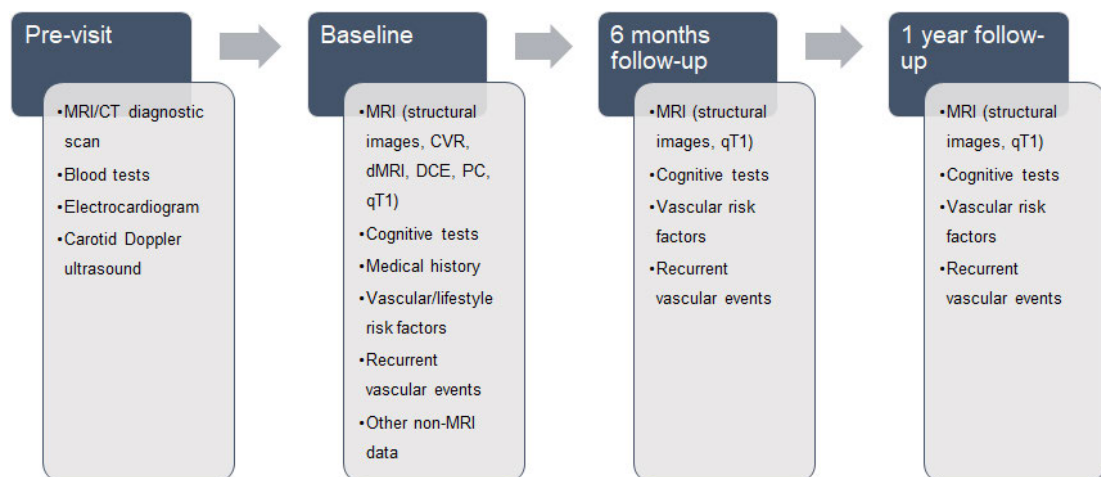


Figure 5-1. Study protocol from pre-visit assessment to one year follow-up. Stroke diagnosis was performed at pre-visit assessment. Thereafter, patients had a minimum of three visits where MRI and non-MRI data were collected.

Following the pre-visit assessment, stroke diagnosis was conducted by expert stroke physicians and neuroradiologists based on the presenting symptoms and diagnostic brain MRI or CT. An experienced neuroradiologist (Prof. Joanna M. Wardlaw) checked for acute ischaemic lesions including recent small subcortical infarcts, prior infarcts or haemorrhages, WMH, lacunes, PVS, microbleeds, siderosis and atrophy. Routine blood tests, electrocardiogram and carotid Doppler ultrasound were also conducted during the pre-visit assessment.

Within three months of index stroke, patients came for their baseline visit and underwent a structural and functional MRI scanning session. Patients also took

cognitive tests and filled questionnaires on their lifestyle (e.g. diet, sleep, fatigue, mood, demographics). We noted their medical history, the presence of vascular risk factors and any recurrent vascular events since stroke onset. Other non-MRI data were also collected such as symptoms, stroke severity, blood and urine samples and gait measurements.

During the follow-up visits, patients underwent a short MRI scanning session where structural images and quantitative T₁ (qT1) were acquired. We further collected data on changes in cognition, changes in symptoms, vascular risk factors and recurrent vascular events. The annual phone or post follow-ups consisted of questionnaires including recurrent vascular events, symptoms and cognition status.

5.2.3 Data collection

5.2.3.1 MRI data

Diagnostic scan

Patients had an MRI or CT scan as their diagnostic scan. The MRI scan was conducted on a 1.5T or 3T scanner to acquire structural images such as T1W, T2W, FLAIR, SWI and dMRI.

Baseline scans

The baseline visit included an MRI scanning session of 1.5 hours with breaks for patient comfort. We used a 3T MRI scanner (MAGNETOM Prisma, Siemens Healthcare GmbH, Erlangen, Germany) and acquired structural images (3D T1W, 3D T2W, 3D T2-FLAIR, 3D SWI, dMRI), CVR, qT1 and dynamic contrast-enhanced (DCE) MRI to measure BBB integrity, and 2D PC to measure intracranial vascular and CSF pulsatility. We also acquired ASL images in a subset of patients to measure CBF. Sequence parameters are given in Table 5-1, based on Clancy et al., 2020.³⁴¹

The CVR scan consisted of acquiring BOLD volumes using a 2D GRE-EPI sequence (Table 5-1). Patients were wearing a facemask covering mouth and

nose while lying in the MRI scanner. The scan lasted 12.5 minutes including 30 seconds of dummy scans (i.e. 14 first BOLD volumes not taken into account for data processing). During the BOLD acquisition, patients were breathing medical air (21% O₂, 79% N₂; BOC Special Products, United Kingdom) and CO₂-enriched air (6% CO₂, 21% O₂, 73% N₂) alternately for 2 minutes and 3 minutes respectively, as done previously.¹¹⁴ A medical doctor was present during the scan and we monitored peripheral oxygen saturation, blood pressure, heart rate and respiration rate using an MR conditional patient monitor (MR400 and IP5, Philips, United Kingdom; Tesla M3, MIPM, Germany; Figure 5-2). We also recorded the expired CO₂ and O₂ concentration waveforms with a sampling frequency of 20 Hz using CD-3A CO₂ and S-3A Oxygen sensors (AEI Technologies, Pittsburgh, United States) respectively, calibrated prior to each CVR scan.

The DCE MRI scan was acquired after qT1 images and lasted 21 minutes. First, three volumes were acquired without contrast agent to establish baseline signal intensity. Then, 0.1 mmol/kg body weight of gadobutrol (1 M Gadovist, Bayer AG, Leverkusen, Germany) was administered intravenously over a period of 110 to 130 seconds, followed by 20 ml saline flush. Twenty-nine DCE volumes were acquired after the injection started.

Follow-up scans

During the follow-up visits, patients had a short MRI session on a 3T scanner (MAGNETOM Prisma, Siemens Healthcare GmbH, Erlangen, Germany) consisting only of structural images (3D T1W, 3D T2W, 3D FLAIR, 3D SWI, dMRI).

Table 5-1. MRI sequence parameters of the MSS3 study. Structural scans were acquired at each visit whereas functional scans were only acquired at baseline. Multiple images were acquired for T1 mapping: one with $TI=600$ ms, one with $TI=1500$ ms and three with different flip angles (2° , 5° , 12°). R is the parallel imaging acceleration factor and MB the multiband acquisition factor. This table was based on Clancy et al., 2020.¹

MRI technique	MRI sequence	TR/TE/TI [ms]	Flip angle [°]	Spatial resolution [mm ³]	Acquisition time [min]	Other
T1W	MPRAGE (3D IR-spoiled GE)	2500/4.37/1100	7	1.0 x 1.0 x 1.0	3:45	R=3
T2W	SPACE (3D RARE)	3200/408	-	0.9 x 0.9 x 0.9	3:42	R=2x2
FLAIR	SPACE (3D RARE)	5000/388/1800	-	1.0 x 1.0 x 1.0	5:57	R=3
SWI	3D spoiled GE	28/20	9	0.6 x 0.6 x 0.3	4:02	R=2
dMRI	2D GRE-EPI	4300/74	-	2.0 x 2.0 x 2.0	11:16	R=2 MB=2
CVR	2D GRE-EPI	1550/30	67	2.5 x 2.5 x 2.5	12:30	R=2 MB=2
qT1	3D IR spoiled GRE	1040/1.82/600	5	1.2 x 1.2 x 1.2	1:55	R=2
	3D IR spoiled GRE	1940/1.82/ 1500	5	1.2 x 1.2 x 1.2	3:35	R=2
	3D IR spoiled GRE	5.4/1.82	2, 5, 12	1.2 x 1.2 x 1.2	1:36 x 3	R=2
DCE	3D spoiled GRE	3.44/1.68	15	2.0 x 2.0 x 2.0	21:08	-
PC	2D PC - carotids	19.60/5.82	12	1.0 x 1.0 x 5.0	1:39	R=2, venc=70 cm/s
	2D PC - sinus	21.70/6.59	12	0.7 x 0.7 x 5.0	2:11	R=2, venc=50 cm/s
	2D PC – subarachnoid space	25.18/8.45	12	0.8 x 0.8 x 5.0	1:55	R=2, venc=6 cm/s

ASL	3D pCASL	4350/20.98/ 500- 3030 (x12)	-	3.4 x 3.5 x 3.5	3:45	R=2
-----	----------	--------------------------------	---	-----------------	------	-----

5.2.3.2 Non-MRI data

As part of the different visits, we recorded information on the participants that were not MRI-based. This included medical history, vascular and lifestyle risk factors, symptoms and cognitive assessments, physical examination and retinal imaging.

Medical history and vascular risk factors

Medical history was recorded at baseline. This included diagnoses of diabetes mellitus, hypertension, hypercholesterolaemia, previous stroke or transient ischaemic attack (TIA), peripheral vascular disease, atrial fibrillation, ischaemic heart disease, valvular defects, heart failure and physician-diagnosed anxiety, depression or delirium. Recurrent stroke, TIA and cardiac events were documented at follow-ups.

Lifestyle risk factors

Socioeconomic risk factors were recorded at baseline such as stroke or dementia family history, age at diagnosis, alcohol consumption, smoking status, diet including salt intake, ethnicity, education, occupation, current address and retirement age. Early life risk factors were taken into account by documenting the childhood postal address, the number of persons, rooms and toilets in the property and parental occupation.

Symptoms assessment

Symptoms such as subjective memory concerns, confusional episodes, unsteadiness, falls, dizziness, headaches, fatigue, anxiety, depression and sleep were assessed at each visit. Further symptoms were also reported at baseline and after 12 months by a nominated close friend or relative by completion of the Neuropsychiatric Inventory Questionnaire, behavioural changes report since stroke, Apathy Evaluation Scale, Informant version and the Informant Questionnaire for Cognitive Decline in the Elderly.

Cognitive assessment

Cognitive assessment was conducted at each visit based on the National Institute of Neurological Disorders and Stroke-Canadian Stroke Network Vascular Cognitive Impairment Harmonization Standards. The cognitive tests included the Montreal Cognitive Assessment (MoCA), Hopkins Verbal Learning Test-revised, Controlled Oral Word Association Test, Animal Naming, Letter Digit Coding and Trailmaking A + B.

Physical examination

Stroke severity, blood pressure, gait (Timed Up and Go), manual dexterity (9-Hole Peg Test), height and weight were part of the physical examination. Blood and urine samples were collected at baseline for inflammatory and/or endothelial function markers. Stroke severity was scored according the National Institutes of Health stroke scale (NIHSS). Functional recovery was assessed through the mRS at baseline, 6 and 12 months and through the Stroke Impact Scale at 6 and 12 months.

Retinal imaging

Retinal imaging was undertaken at baseline and one-year follow-up using a Heidelberg Spectralis (Heidelberg Engineering, Franklin, MA, United States). Optical coherence tomography angiography is used to image the retina and its blood vessels. Therefore, we assessed visual acuity, retinopathy, nerve fibre layer thickness, state of the choroid, intra- and sub-retinal fluid, retinal and arteriolar widths, and branching patterns and complexity.

5.2.4 MRI data processing

All MRI images were first converted from DICOM to NIFTI format.³²³

Visual assessments

All MRI scans were assessed by an experienced neuroradiologist (Prof. Joanna M. Wardlaw). Visual assessments of SVD features were undertaken

by members of the team and checked by Prof. Joanna M. Wardlaw. They were conducted on structural images following the STRIVE criteria.³¹

Fazekas scores in periventricular and deep white matter were used to assess WMH burden ranging from 0 to 3 (high WMH burden) for each region and added together to get the overall Fazekas score from 0 to 6. We noted the presence or absence of lacunes and microbleeds along with their numbers. PVS scores were rated in the basal ganglia and in the CSO from 0 (none) to 4 (more than 40 enlarged PVS).³⁵⁸ A total PVS score was obtained by adding together the scores from the two regions. We rated superficial and deep atrophy from 0 to 6 (severe atrophy)³⁵⁹ and combined them to get the overall atrophy score. The overall SVD burden was rated using the SVD score from 0 (no SVD burden) to 4 (high SVD burden).¹⁸

Tissue segmentation and volume

Multiple segmentations were conducted by Dr Maria Valdes Hernandez after registration of all structural images to the subject's T2W image using FSL FLIRT (FMRIB Software Library, FMRIB Analysis Group, Oxford, United Kingdom).^{329,330} Those segmentations included acute stroke lesions, WMH, NAWM, SGM (formed of the thalamus, caudate head, putamen and pallidum) and PVS.

Acute stroke lesions were manually segmented on FLAIR images and checked by Prof Joanna M. Wardlaw. Other tissue segmentations were generated using an in-house processing pipeline that combines FSL³²⁵ and FreeSurfer^{360,361} outputs. All masks were then verified and corrected manually if required. PVS segmentation was conducted on T2W images following a computational method described previously.^{362,363}

For the analyses, volumes were computed based on the masks generated: intracranial, brain, WMH and PVS volumes. Brain and WMH volumes were normalised by the intracranial volume and reported as %ICV. PVS volumes were normalised to the volume of the ROI considered for PVS segmentation and reported as %ROIV.

Further mask editing was undertaken for CVR and DCE processing (Figure 5-2). To reduce partial volume effect, NAWM and SGM masks were eroded in T2W space by 1 mm in all directions. The mask of the ventricles was dilated in each direction by 5 mm to left and right directions, and 4 mm in anterior, posterior, superior and inferior directions. The dilated mask of the ventricles was then removed from the NAWM and WMH masks to remove signal contribution from large blood vessels running next to the ventricles. Contribution from overlapping large veins were also removed by manually comparing the tissue masks (NAWM, SGM and WMH) with the CVR and SWI images. Hereafter, no mask erosion was conducted.

CVR data processing

The CO₂ and O₂ waveforms were converted into EtCO₂ and EtO₂ traces using in-house MATLAB code, which identifies the signal peaks or troughs, as done previously.¹¹⁴

Regarding the CVR MRI data, BOLD images were realigned to each participant's mean BOLD image using SPM12³²⁴ (Figure 5-2). Tissue masks (NAWM, SGM, WMH) were registered to the individual's mean BOLD space by calculating the linear transform between the T2W and mean BOLD spaces using FLIRT^{329,330} (Figure 5-2). Then we applied a threshold of 50% to obtain binary masks in the mean BOLD space. Then we computed the mean BOLD signal time course in each ROI and performed multiple linear regression between the mean BOLD time course, the time-shifted EtCO₂ course and a vector comprising the volume numbers to account for a linear signal drift in MATLAB (Figure 5-2).^{114,304,319} We allowed time shifts from -31 to 93 s, all multiples of TR, for the EtCO₂ profile to allow for long and negative delays due to noise in the BOLD signal. CVR delay was defined as the optimal EtCO₂ time shift in seconds that resulted in a linear model with lowest sum of squared residuals, adding 4 seconds to take into account the sampling line delay. CVR (%/mmHg) was computed as the regression coefficient associated with the time-shifted EtCO₂ term divided by the mean BOLD baseline signal and multiplied by 100, where the mean BOLD baseline was defined as the mean

intensity of the mean BOLD signal over the first 30 volumes within the first air block.

Regional differences in CVR magnitudes and delays were computed using paired t-tests and reported as mean \pm standard deviation [95% confidence intervals].

5.3 Results

5.3.1 General results

From August 2018 to December 2021 marking the end of the recruitment period, 230 SVD patients were enrolled in the study. One patient withdrew before the baseline visit and was not considered for analysis (Figure 5-3). The median age and IQR given in square brackets of the remaining 229 patients were 67.5 [56.3, 74.4] years old and 152 (66%) were males. Out of 229, 130 (57%) had a lacunar stroke as opposed to a cortical stroke. Other population characteristics are given in Chapters 6 and 7.

5.3.2 CVR results

Up until June 2021, patients were asked to participate in/receive a CVR scan, resulting in 207 potential CVR datasets (median [IQR] age: 68.2 [57.0, 75.5] years old, 66% male and 55% with a lacunar stroke; Figure 5-3). The last 22 recruited patients had another MRI scan instead as part of a pilot project. Out of those 207 patients, 14 did not have a CVR scan (2/14 due to low oxygen saturation levels, 6/14 due to claustrophobia, 4/14 patients declined, 1/14 due to mask discomfort, 1/14 due to incidental finding of large haemorrhagic transformation). After processing the remaining datasets, 182/193 were retained for future analyses (reasons for excluding 11 datasets: 5/12 had severe visible motion artefacts and 6/12 had irregular EtCO₂ trace, probably due to poor mask seal). WMH CVR could not be computed in seven datasets because there were no remaining WMH voxels following registration and thresholding of the WMH masks in the mean BOLD space.

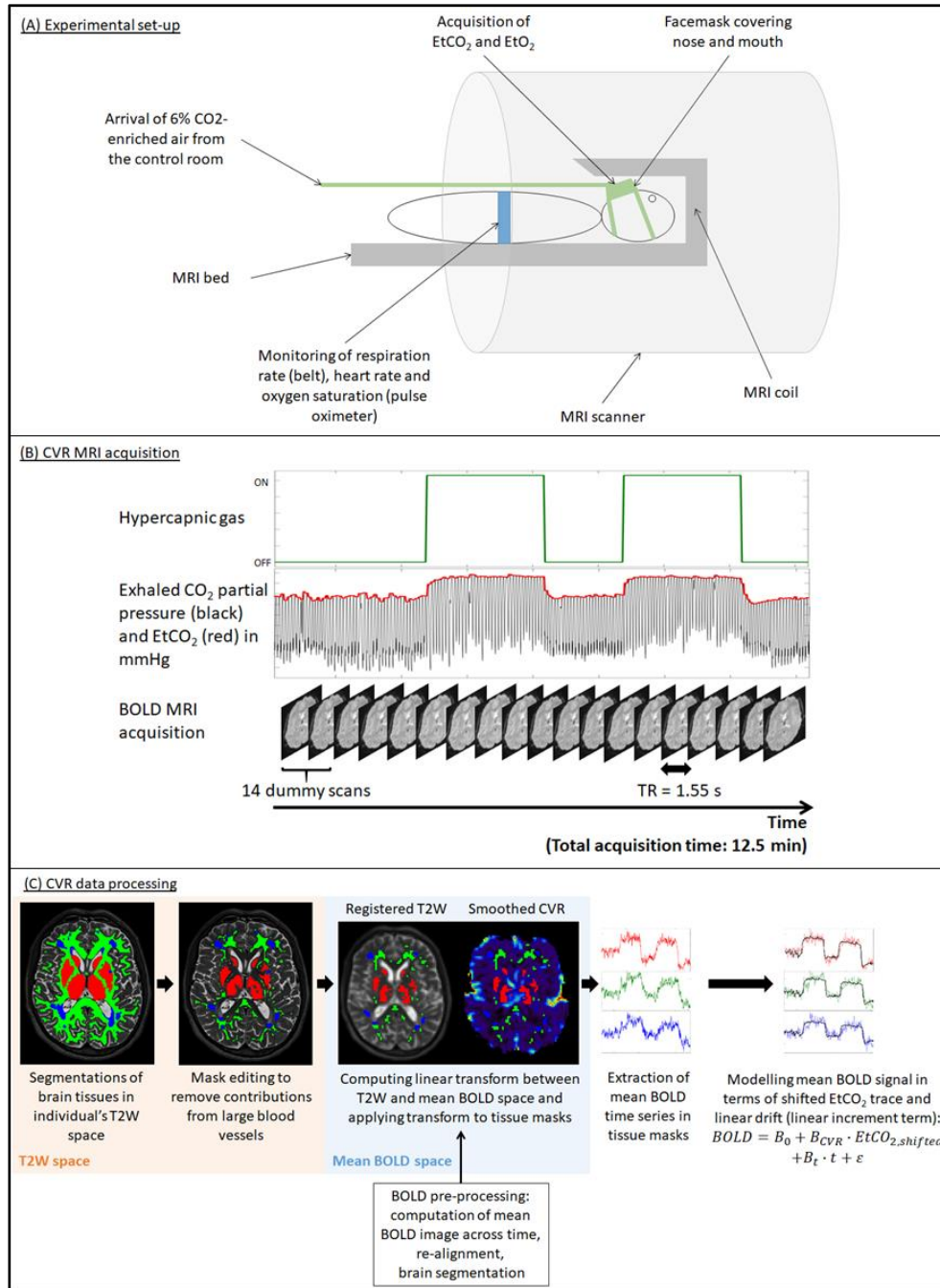


Figure 5-2. Flowchart of the CVR MRI experiment. (A) *Experimental set-up:* patient lied in the MRI scanner and breathed medical air and hypercapnic gas alternatively. (B) *Data acquisition:* during the hypercapnic challenge, exhaled CO₂ and O₂ partial pressures were measured to extract EtCO₂ and EtO₂. BOLD volumes were acquired simultaneously. (C) *Data processing:* tissue masks (red: SGM, green: NAWM, blue: WMH) were segmented in the individual's T2W space, edited to remove contributions from large blood vessels and transformed into the mean BOLD space. For each ROI,

the mean BOLD signal was computed and modelled as a function of the EtCO_2 and a linear term to extract CVR magnitude and delay.

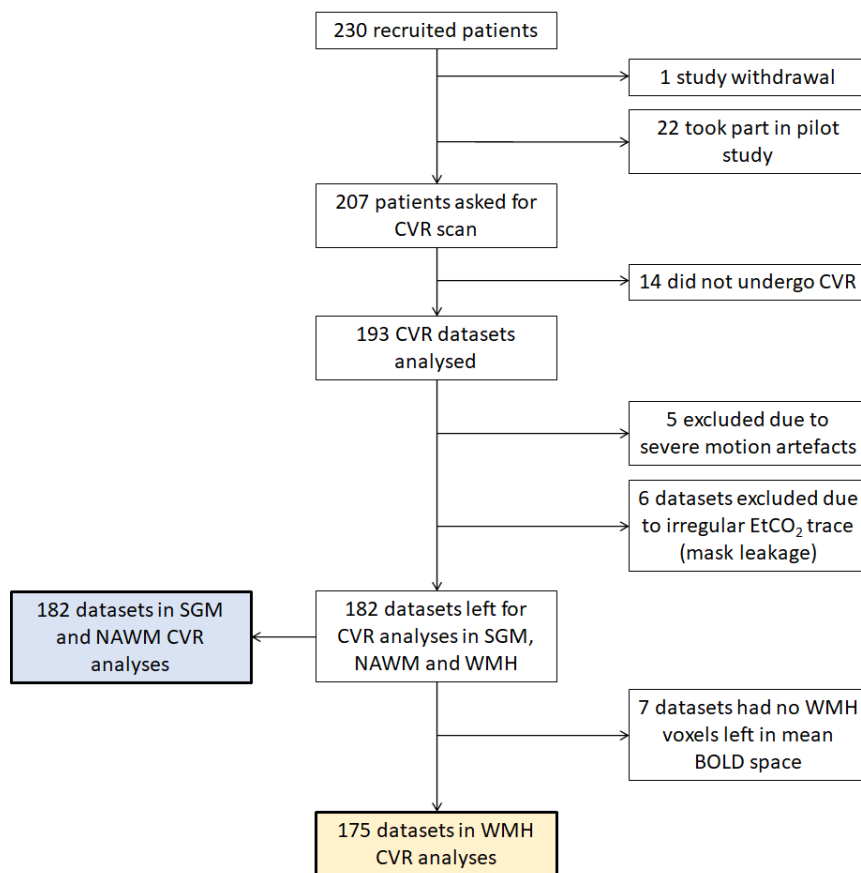


Figure 5-3. Flow chart showing patient recruitment and CVR data acquisition and processing for baseline visit.

The distribution of CVR magnitude and delay in SGM, NAWM and WMH are shown in Figure 5-4. Both CVR magnitude and delay differ between regions (Table 5-2). CVR magnitude is higher in SGM than in the white matter regions (difference in SGM versus NAWM: 0.128 ± 0.044 [0.121, 0.134] %/mmHg, $p < 0.001$) whereas CVR delay is shorter in SGM compared to white matter regions (difference in SGM versus NAWM: -32.2 ± 18.4 [-34.9, -29.5] s, $p < 0.001$). There were no differences between NAWM and WMH CVR parameters (difference in CVR magnitude: 0.002 ± 0.039 [-0.004, 0.008] %/mmHg, $p = 0.488$; difference in CVR delay: -2.4 ± 31.1 [-7.1, 2.2] s, $p = 0.300$).

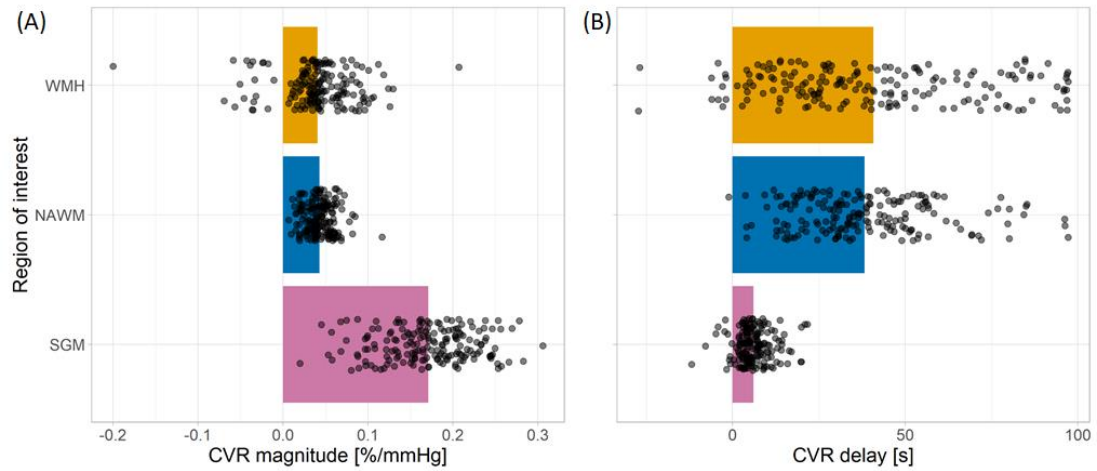


Figure 5-4. CVR magnitude and delay in MSS3 patients as a function of the region-of-interest (SGM, NAWM, WMH). Distributions and mean values are shown for (A) CVR magnitude and (B) CVR delay. The length of the bars corresponds to the mean CVR parameter in the corresponding region. Results for SGM, NAWM and WMH are shown in blue, orange and green respectively.

Table 5-2: Regional mean values and inter-regional differences in CVR magnitude and delay. Inter-regional differences were obtained using Bland-Altman statistics. Regional values are presented as $\text{mean} \pm \text{STD}$ and inter-regional differences as $\text{mean} \pm \text{STD}$ [95% confidence intervals] computed using paired *t*-test.

	Regional values			Inter-region differences		
	SGM	NAWM	WMH	SGM – NAWM	SGM – WMH	NAWM – WMH
CVR	$0.171 \pm$	$0.043 \pm$	$0.041 \pm$	$0.128 \pm$	$0.130 \pm$	$0.002 \pm$
magnitude	0.053	0.016	0.043	0.044	0.060	0.039
[%/mmHg]				[0.121, 0.134]	[0.121, 0.139]	[-0.004, 0.008]
CVR delay	$6.0 \pm$	$38.2 \pm$	$40.8 \pm$	$-32.2 \pm$	$-34.8 \pm$	$-2.4 \pm$
[s]	4.8	19.4	29.3	18.4	29.2	31.1
				[-34.9, -29.5]	[-39.2, -30.4]	[-7.1, 2.2]

5.4 Discussion and conclusion

The MSS3 study was designed to deepen our understanding of SVD by providing further insight on the connection between vascular dysfunction, imaging features and progression of the disease.

We started the study in August 2018 and finished recruiting patients in December 2021. The target sample size of the study was initially 300 patients. However, due to Covid-19, we paused recruitment for 6 months followed by a gradual resumption. Overall, this resulted in a lower sample size and delayed preliminary analyses. Nevertheless, the power of the study was high, especially when compared with previous studies investigating CVR in SVD patients.^{72,357,364}

Consistent with previous studies,^{72,114,304} we found that CVR magnitude and delay varied across regions, being respectively higher and shorter, in grey versus white matter regions. Differences in CVR delay between regions may arise from the pathology, vasculature, competitive redistribution of blood flow and regional differences in deoxyhaemoglobin concentration or in HRFs. Furthermore, we found no difference between CVR parameters in NAWM and WMH regions. In a previous studies, CVR magnitude in WMH was lower than in NAWM; however, their sample size was smaller and the patients older.^{364,365} In one of them, the cohort considered also had a higher WMH burden.³⁶⁴

In conclusion, MSS3 data can be used to understand how regional CVR is associated with SVD features and progression. Using baseline data, one can investigate the cross-sectional relationships between CVR, SVD neuroimaging features and cognition. Furthermore, one can relate baseline CVR to changes in SVD features after one year. Those cross-sectional and longitudinal analyses are the subjects of Chapters 6 and 7 respectively.

6 Cerebrovascular reactivity in patients with small vessel disease: cross-sectional analysis

This chapter contains statistical analyses carried out to investigate the cross-sectional relationships between impaired CVR, SVD neuroimaging features, cognition and stroke severity and outcome. The content of this chapter has been submitted to a peer-reviewed journal and part of it was/will be presented at conferences (ESOC 2021, ESOC 2022, SINAPSE 2022, ISMRM 2023).

6.1 Introduction

SVD is a disorder of the cerebral small vessels causing strokes³⁶⁶ and vascular dementia.^{5,9} Currently, SVD pathophysiology is unclear; no effective treatments are available.³⁶⁷ Identifying vascular dysfunctions and their relationships to disease features may help develop treatments.²

Previous cross-sectional studies have found that lower CVR in SGM and WM is associated with higher WMH burden.^{72,304,129} One study noted lower CVR in WMH compared to contralateral NAWM.³⁶⁴ Furthermore, SGM and WM CVR are associated with higher blood pressure, but not with global CBF.⁷² WM CVR is associated with enlarged PVS in the basal ganglia (BG), increased pulsatility in the venous sinuses and lower CSF stroke volume at the foramen magnum.⁷² Global CVR reduction is associated with having more microbleeds, but not with the number of lacunes.³⁵⁷ However, the sample sizes of these studies were relatively small, most of the results have not yet been replicated, and associations of CVR with clinical features such as cognitive function have not been extensively tested in SVD patients.

The aim of this chapter was to assess CVR in relation to SVD MRI features at 3T, cognitive function and stroke severity in a large cohort of SVD patients who presented with a minor non-disabling ischaemic stroke. The hypothesis was

that lower CVR in SGM, NAWM and WMH would be associated with more severe SVD imaging features, worse cognition and more severe stroke.

6.2 Methods

Patient recruitment, data collection and processing have been described in Chapter 5. In this section, the statistical methods used in the analysis are described. Analyses were conducted using R (version 3.6.1; cran.r-project.org/) with the additional packages: tidyverse, ggplot2, insight, sjPlot and car.

CVR was modelled separately for each tissue. Univariate and multivariable linear regressions were conducted using the CVR parameter of interest as outcome and SVD features, cognition or stroke severity as independent variables. In the multivariable analyses, the models were adjusted for age, sex, mean arterial pressure (MAP), smoking history (current/recent versus ex-smoker for more than one year versus never), diagnosis of hypertension, diabetes and hypercholesterolaemia. Non-collinearity between variables was checked by ensuring variable inflation factors less than 2. Model assumptions were verified: normality of residuals and heteroscedasticity. To ensure normality of residuals, WMH volumes were transformed using the logarithm to the base-10 function.

Coefficients of the linear regressions with 95% confidence intervals (CI) and p-values were reported.

Several sensitivity analyses were conducted (see Appendix A3.3): 1) adjusting for WMH volume as a proxy of SVD severity; 2) adjusting for EtCO₂ baseline; 3) excluding datasets where the mean or standard deviation of the framewise displacement during the BOLD-CVR scan were upper outliers of their respective distribution; 4) excluding datasets where the CVR scan was stopped before the end of the first CO₂ block; 5) excluding CVR data where the masks in mean BOLD space had fewer than 10 voxels.

6.3 Results

6.3.1 Population characteristics

Of 207 recruited patients, we included 182 datasets in the analysis (median age: 68.2 years old, 68% male; Table 6-1, Figure 6-1). Reasons to exclude datasets were given in Chapter 5. Of the remaining 182 datasets, 7 patients did not have WMH voxels following transformation of masks into the mean BOLD space, thus resulting in 175 datasets for WMH CVR analyses. PVS volumes could not be computed in 6/182 datasets due to noise on the T2W images. Full MoCA assessment was not available for 3/182 subjects.

CVR was similar in WMH and NAWM (mean inter-region difference [95% CI]: 0.00206 [-0.00379,0.00791] %/mmHg) and highest in SGM (SGM-NAWM CVR difference: 0.128 [0.121,0.134] %/mmHg; Table 6-1).

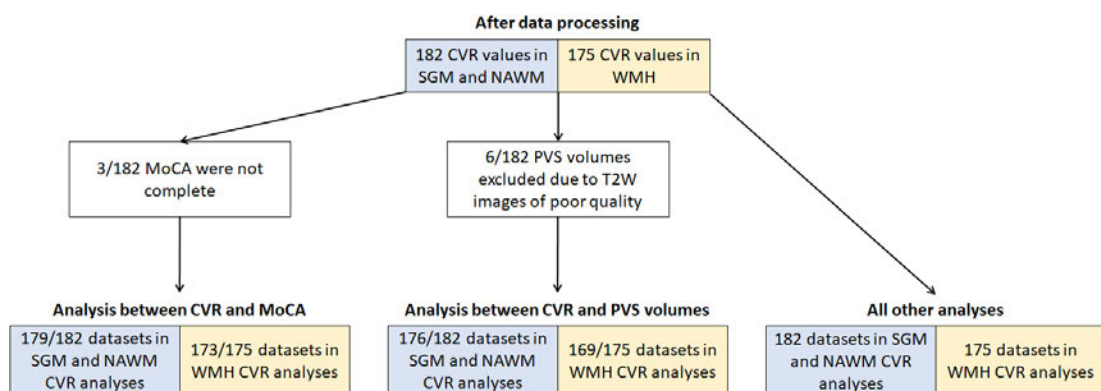


Figure 6-1. Flow diagram showing data exclusion process from cross-sectional analyses.

Table 6-1: Population characteristics of cross-sectional analysis. Non-binary variables are reported as median [IQR] and binary and smoking variables as number (%).

Variables	Analysis in SGM and NAWM	N	Analysis in WMH	N
Age [years]	68.2 [56.4, 75.4]	182	68.7 [57.2, 75.6]	175
Sex (male, female)	123 (68), 59 (32)	182	117 (67), 58 (33)	175
mRS	1 [1, 1]	182	1 [1, 1]	175
NIHSS	1 [0, 2]	182	1 [0, 2]	175
Systolic blood pressure [mmHg]	147 [136, 161]	182	147 [136, 161]	175
Diastolic blood pressure [mmHg]	85 [76, 92]	182	84 [76, 92]	175
Mean arterial pressure [mmHg]	105 [98, 114]	182	105 [98, 114]	175
Diabetes diagnosis	36 (20)	182	35 (20)	175
Hypertension diagnosis	128 (70)	182	123 (70)	175
Hypercholesterolaemia diagnosis	134 (74)	182	128 (73)	175
Smoker (current, ever, never)	30 (16), 70 (39), 82 (45)	182	29 (17), 69 (39), 77 (44)	175
Stroke type (lacunar, cortical)	77 (42), 108 (58)	182	76 (43), 99 (57)	175
WMH volume [ml]	8.09 [3.76, 18.77]	182	8.40 [4.22, 19.05]	175
WMH volume [%ICV]	0.505 [0.237, 1.144]	182	0.519 [0.269, 1.176]	175
Number of lacunes	1 [0, 3]	182	1 [0, 3]	175
Number of microbleeds	0 [0, 0]	182	0 [0, 0]	175
Deep atrophy score	3 [2, 4]	182	3 [2, 4]	175
Superficial atrophy score	3 [2, 4]	182	3 [2, 4]	175
Total atrophy score	6 [4, 8]	182	6 [4, 8]	175
Brain volume [ml]	1075 [1005, 1176]	182	1073 [1005, 1172]	175
Brain volume [%ICV]	67.3 [64.3, 70.9]	182	67.1 [64.2, 70.5]	175

Periventricular Fazekas score	1 [1, 2]	182	2 [1, 2]	175
Deep WM Fazekas score	1 [1, 2]	182	1 [1, 2]	175
Total Fazekas score	3 [2, 4]	182	3 [2, 4]	175
BG PVS score	2 [1, 3]	182	2 [1, 3]	175
CSO PVS score	2 [2, 3]	182	2 [2, 3]	175
Total PVS score	4 [3, 5]	182	4 [3, 5]	175
BG PVS volume [ml]	2.8 [2.0, 3.8]	176	2.8 [2.0, 3.9]	169
BG PVS volume [%ROIV]	4.9 [3.3, 6.1]	176	5.0 [3.3, 6.1]	169
CSO PVS volume [ml]	11.3 [7.1, 16.2]	176	11.5 [7.2, 16.2]	169
CSO PVS volume [%ROIV]	3.4 [2.1, 5.6]	176	3.4 [2.2, 5.6]	169
Total PVS volume [ml]	14.0 [9.2, 19.6]	176	14.8 [9.3, 19.8]	169
Total PVS volume [%ROIV]	3.7 [2.4, 5.6]	176	3.7 [2.5, 5.7]	169
SVD score	2 [1, 3]	182	2 [1, 3]	175
MoCA	25 [23, 27]	179	25 [23, 27]	173
SGM CVR [%/mmHg]	0.171 [0.135, 0.207]	182	-	-
NAWM CVR [%/mmHg]	0.042 [0.033, 0.054]	182	-	-
WMH CVR [%/mmHg]	-	-	0.040 [0.025, 0.064]	175

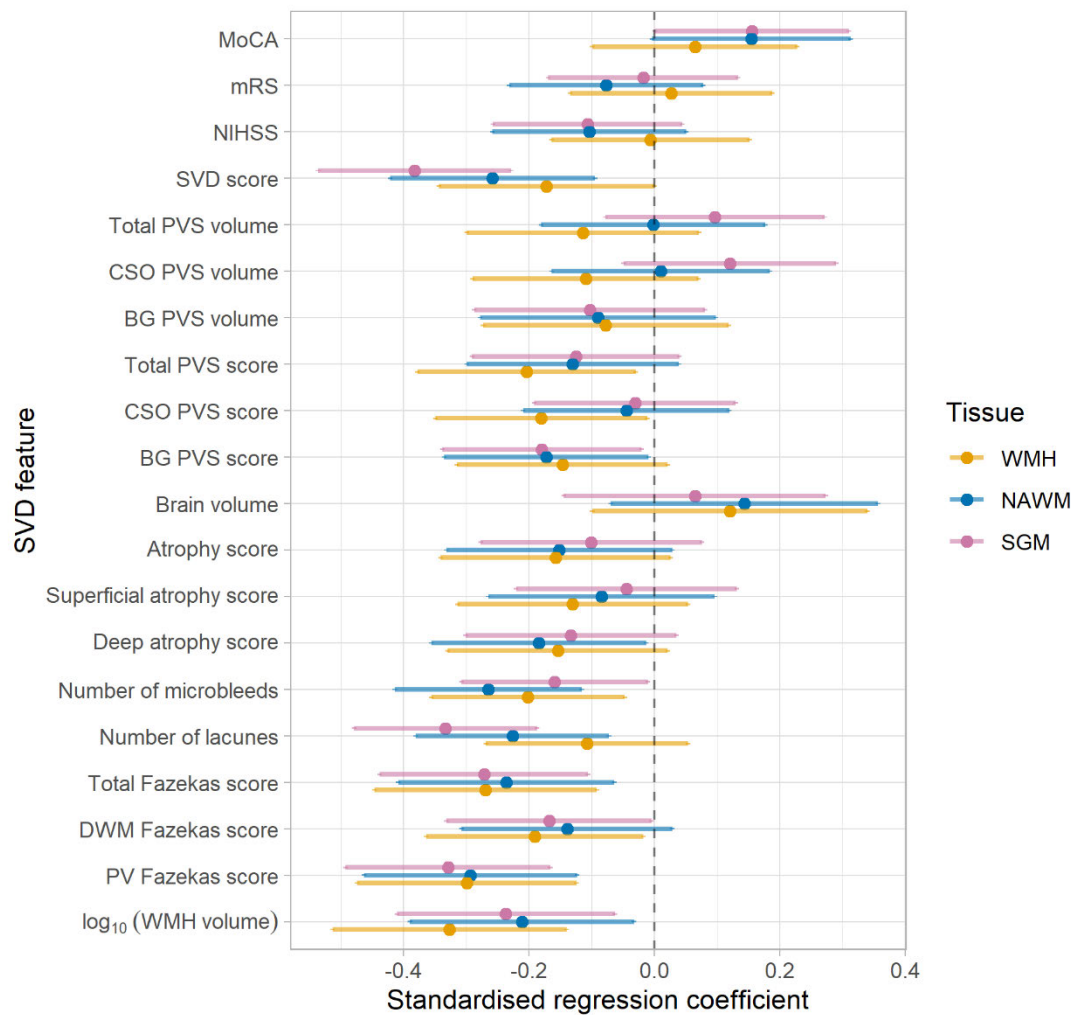


Figure 6-2. Standardised regression coefficients from cross-sectional analysis between SVD features and CVR in SGM (pink), NAWM (blue) and WMH (yellow). The dots represent the mean standardised coefficients and the horizontal lines the associated 95% confidence intervals. The vertical dashed line emphasises a zero-valued coefficient. Coefficients to left of zero line indicate association with lower CVR.

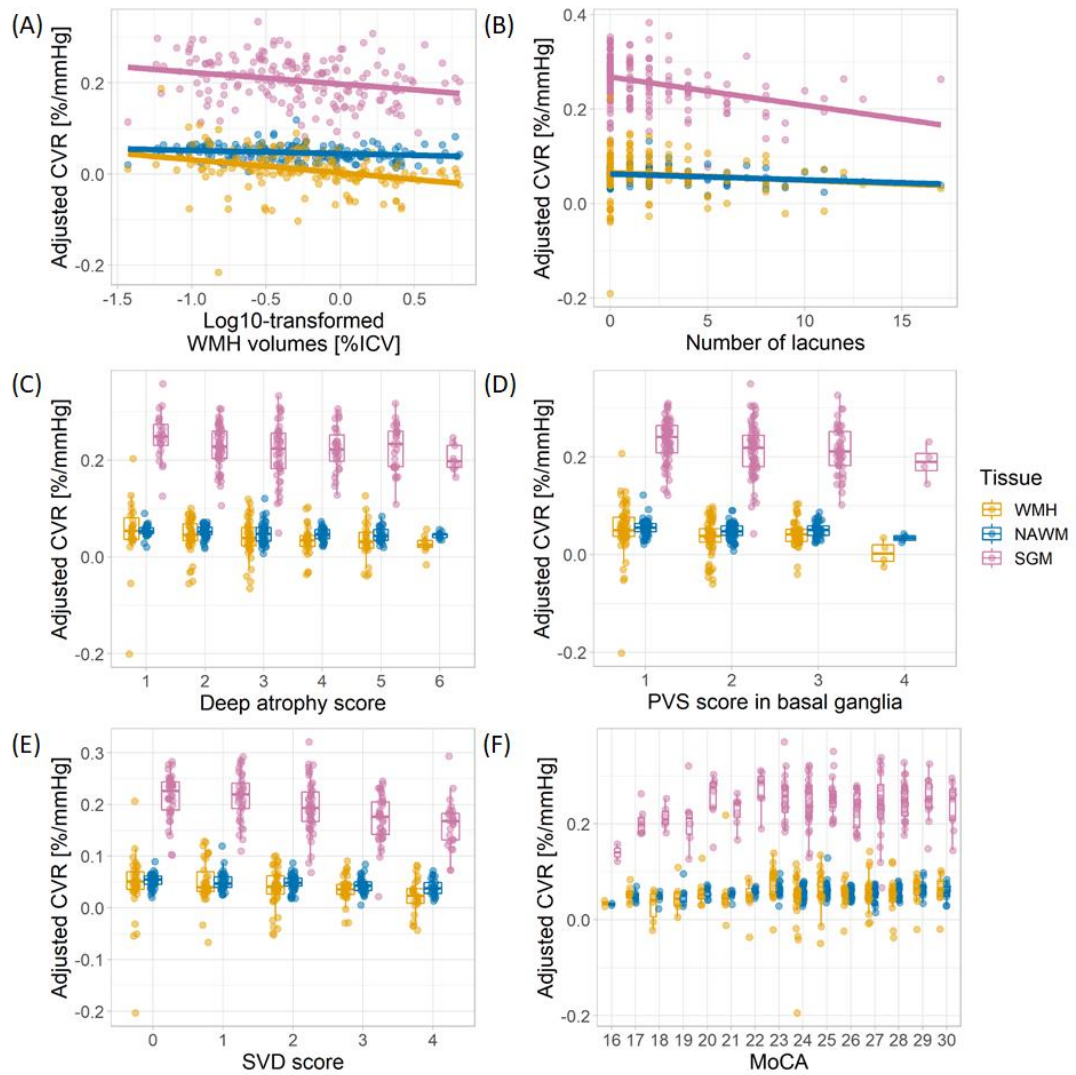


Figure 6-3. Cross-sectional relationships between adjusted CVR, SVD features and cognition. CVR was adjusted for age, sex and vascular risk factors. The results are shown for adjusted CVR in SGM (pink), NAWM (blue) and WMH (yellow). In plots A and B, the regression lines are shown.

Table 6-2: Cross-sectional analyses. Each row represents a different statistical model where the SVD predictor of interest is given in the first column. The associated regression coefficient B , its 95% confidence interval and p -value are given in the columns 2-4. The last column gives the units of B . All models were corrected for age, sex, MAP, diagnosis of diabetes, hypertension, and hypercholesterolaemia and smoking history.

Variables	SGM CVR	NAWM CVR	WMH CVR	Units of B
WMH volume	$B=-0.0256$ [-0.0443, -0.0068] $p=0.008$	$B=-0.00705$ [-0.01302, -0.00108] $p=0.021$	$B=-0.0288$ [-0.0453, -0.0124] $p=0.001$	%BOLD/mmHg per $\log_{10}(\%ICV)$
Periventricular Fazekas score	$B=-0.0203$ [-0.0304, -0.0102] $p<0.001$	$B=-0.00561$ [-0.00885, -0.00237] $p=0.001$	$B=-0.0151$ [-0.0240, -0.0063] $p=0.001$	%BOLD/mmHg per score unit
Deep WM Fazekas score	$B=-0.0110$ [-0.0216, -0.0003] $p=0.044$	$B=-0.00282$ [-0.00621, 0.00058] $p=0.104$	$B=-0.0102$ [-0.0194, -0.0009] $p=0.031$	%BOLD/mmHg per score unit
Total Fazekas score	$B=-0.00909$ [-0.01466, -0.00353] $p=0.002$	$B=-0.00245$ [-0.00423, -0.00067] $p=0.007$	$B=-0.00737$ [-0.01222, -0.00252] $p=0.003$	%BOLD/mmHg per score unit
Number of lacunes	$B=-0.00594$ [-0.00855, -0.00334] $p<0.001$	$B=-0.00125$ [-0.00211, -0.00040] $p=0.004$	$B=-0.00157$ [-0.00392, 0.00077] $p=0.187$	%BOLD/mmHg per lacune
Number of microbleeds	$B=-0.00162$ [-0.00313, -0.00011] $p=0.036$	$B=-0.000835$ [-0.001305, -0.000366] $p=0.001$	$B=-0.00168$ [-0.00296, -0.00040] $p=0.011$	%BOLD/mmHg per microbleed
Deep atrophy score	$B=-0.00496$ [-0.01122, 0.00130] $p=0.120$	$B=-0.00213$ [-0.00411, -0.00016] $p=0.035$	$B=-0.00469$ [-0.01004, 0.00065] $p=0.085$	%BOLD/mmHg per score unit

Chapter 6. MSS3 cross-sectional analysis

Superficial atrophy score	B=-0.00169 [-0.00830, 0.00492] p=0.615	B=-0.000985 [-0.003081, 0.001112] p=0.355	B=-0.00401 [-0.00967, 0.00164] p=0.163	%BOLD/mmHg per score unit
Total atrophy score	B=-0.00200 [-0.00548, 0.00149] p=0.260	B=-0.000929 [-0.002030, 0.000171] p=0.097	B=-0.00255 [-0.00551, 0.00041] p=0.091	%BOLD/mmHg per score unit
Brain volume	B=0.000734 [-0.001655, 0.003122] p=0.545	B=0.000507 [-0.000248, 0.001263] p=0.187	B=0.00113 [-0.00093, 0.00318] p=0.281	%BOLD/mmHg per %ICV
BG PVS score	B=-0.0114 [-0.0213, -0.0013] p=0.027	B=-0.00338 [-0.00657, -0.00019] p=0.038	B=-0.00760 [-0.01628, 0.00108] p=0.086	%BOLD/mmHg per score unit
CSO PVS score	B=-0.00181 [-0.01106, 0.00745] p=0.701	B=-0.000804 [-0.003741, 0.002133] p=0.590	B=-0.00852 [-0.01651, -0.00053] p=0.037	%BOLD/mmHg per score unit
Total PVS score	B=-0.00437 [-0.01012, 0.00137] p=0.135	B=-0.00141 [-0.00323, 0.00042] p=0.130	B=-0.00581 [-0.01077, -0.00086] p=0.022	%BOLD/mmHg per score unit
BG PVS volume	B=-0.00237 [-0.00657, 0.00183] p=0.267	B=-0.000637 [-0.001971, 0.000696] p=0.347	B=-0.00145 [-0.00512, 0.00222] p=0.435	%BOLD/mmHg per %ROIV
CSO PVS volume	B=0.00255 [-0.00105, 0.00615] p=0.163	B=0.000064 [-0.001083, 0.001211] p=0.912	B=-0.00191 [-0.00504, 0.00121] p=0.229	%BOLD/mmHg per %ROIV
Total PVS volume	B=0.00215 [-0.00174, 0.00605] p=0.276	B=-0.000017 [-0.001254, 0.001220] p=0.978	B=-0.00209 [-0.00547, 0.00129] p=0.224	%BOLD/mmHg per %ROIV

SVD score	B=-0.0150 [-0.0211, -0.0090] p<0.001	B=-0.00314 [-0.00514, -0.00115] p=0.002	B=-0.00554 [-0.01106, -0.00002] p=0.049	%BOLD/mmHg per score unit
NIHSS	B=-0.00412 [-0.00994, 0.00171] p=0.165	B=-0.00125 [-0.00310, 0.00060] p=0.185	B=-0.000202 [-0.005188, 0.004784] p=0.936	%BOLD/mmHg per score unit
mRS	B=-0.00144 [-0.01336, 0.01048] p=0.812	B=-0.00188 [-0.00565, 0.00190] p=0.327	B=0.00171 [-0.00863, 0.01205] p=0.744	%BOLD/mmHg per score unit
MoCA	B=0.00231 [0.00001, 0.00462] p=0.049	B=0.000713 [-0.000019, 0.001444] p=0.056	B=0.000783 [-0.001209, 0.002776] p=0.439	%BOLD/mmHg per score unit

6.3.2 WMH

Lower CVR in all ROIs was associated with greater WMH volume ($B_{WMH}=-0.0288$ [-0.0453,-0.0124] %/mmHg per ten-fold increase in %ICV; Table 6-2, Figure 6-2, Figure 6-3) and higher Fazekas score ($B_{WMH}=-0.00737$ [-0.01222,-0.00252] %/mmHg per total Fazekas score point increase; Table 6-2, Figure 6-2).

6.3.3 Lacunes and cerebral microbleeds

Lower CVR in all ROIs was associated with more lacunes ($B_{SGM}=-0.00594$ [-0.00855,-0.00334] %/mmHg per lacune; Table 6-2, Figure 6-2, Figure 6-3). Lower CVR in all ROIs was associated with more microbleeds ($B_{WMH}=-0.00168$ [-0.00296,-0.00040] %/mmHg per microbleed; Table 6-2, Figure 6-2), though weakened after adjusting for WMH burden (Table A3-22).

6.3.4 Brain atrophy

There was a trend of association between lower CVR in all ROIs and higher deep and total atrophy scores ($B_{WMH}=-0.00255$ [-0.00551,0.00041] %/mmHg

per total atrophy score point increase; Table 6-2, Figure 6-2, Figure 6-3). A similar trend was observed with brain volumes (Table 6-2, Figure 6-2).

6.3.5 PVS

Lower CVR in all ROIs was associated with higher PVS score in BG ($B_{SGM} = -0.0114$ [-0.0213, -0.0013] %/mmHg per PVS score point increase) and total PVS scores ($B_{WMH} = -0.00581$ [-0.01077, -0.00086] %/mmHg per score PVS point increase; Table 6-2, Figure 6-2). However, only lower CVR in WMH was associated with higher CSO PVS score ($B_{WMH} = -0.00852$ [-0.01651, -0.00053] %/mmHg per PVS score point increase; Table 6-2, Figure 6-2). There were no associations between CVR and PVS volumes (Table 6-2, Figure 6-2).

6.3.6 SVD burden

Lower CVR in all ROIs was associated with higher SVD score ($B_{SGM} = -0.0150$ [-0.0211, -0.0090] %/mmHg per SVD score point increase; Table 6-2, Figure 6-2, Figure 6-3).

6.3.7 NIHSS, mRS and cognition

There was a negative tendency between CVR in SGM and NAWM with NIHSS ($B_{SGM} = -0.00412$ [-0.00994, 0.00171] %/mmHg per NIHSS score point increase), but not for WMH CVR (Table 6-2, Figure 6-2). There were no associations between CVR and mRS (Table 6-2, Figure 6-2). Lower CVR in SGM and NAWM was associated with lower MoCA score ($B_{SGM} = 0.00231$ [0.00001, 0.00462] %/mmHg per point MoCA score increase; Table 6-2, Figure 6-2, Figure 6-3). Overall, those associations became weaker when further adjusting for WMH burden (Table A3-22).

6.4 Discussion

We investigated how CVR relates to a comprehensive set of SVD features and cognitive impairment. In this largest study of CVR in SVD to date, CVR was lower in patients with more severe SVD even in normal-appearing tissues, and

in association with different SVD features, although the strength of association varied across tissue and lesion types. Lower CVR in normal-appearing tissues was also associated with lower MoCA scores. These associations were independent of age, sex and VRFs, although they were weaker when further adjusting for WMH burden. As SVD-related tissue damage accumulates over time,³² regions with low CVR could be at risk of deteriorating. Indeed, a previous study (N=45) found that CVR in NAWM that progressed into WMH after one year was lower than in contralateral NAWM.⁷⁶ Future studies should confirm this.

The relationship between lower CVR and higher WMH burden is consistent between WMH volumes and visual scores. Such relationships have been found in previous studies in older subjects with WMH,^{76,210,364,365,368} patients with Alzheimer's disease⁷⁴ and SVD patients with mild stroke.⁷² However, the sample size of the current study is larger (N=182 versus N=10-75), thereby making the finding more robust.

Lower CVR in SGM, NAWM and WMH was associated with more lacunes and microbleeds. Two previous studies also investigated these relationships, but found no associations between CVR and number of lacunes.^{72,357} Results for number of microbleeds were divided: one study found CVR impairment related to more microbleeds³⁵⁷ and the other found no associations.⁷² However, the two studies had much smaller sample sizes (N=49-53) and data were acquired at different field strengths (1.5 and 7T). Furthermore, other brain regions were considered for CVR computation: whole brain³⁵⁷ or whole WM region including WMH.⁷²

Higher visually assessed brain atrophy was associated with lower CVR in all ROIs. Relationships were similar but weaker when using brain volumes. A previous study⁷² did not find any association between CVR and atrophy, possibly due to smaller sample size (N=53).

We found an association between lower CVR in all ROIs and higher PVS scores, though the association did not hold between CVR in normal-appearing

tissues and CSO PVS score. Different relationships with CVR were found when using PVS scores and volumes: whereas scores reflect only a count, volumes will also be influenced by PVS size. Moreover, scores could be limited by floor and ceiling effects.³⁶⁹ Previous studies have found that lower CVR^{72,370} and higher vascular pulsatility⁷⁵ are associated with enlarged PVS. Although currently under debate, lower CVR and higher vascular pulsatility could be linked to vascular stiffness, which itself could induce stagnation of interstitial fluid, thereby providing a link between the brain's waste clearance and vascular systems.^{2,53}

There was also an association between CVR impairment in SGM, NAWM and WMH and higher SVD score in agreement with a previous study.⁷² Therefore, CVR could be a marker reflecting overall SVD severity and should be considered for future clinical studies of SVD.

CVR impairment in normal-appearing tissues was associated with worse cognitive function, but not stroke outcome or severity, although the severities were very mild in this cohort. However, this did not hold when further adjusting for WMH burden, known to be negatively associated with cognitive function.³⁷¹ One study previously reported no associations between CVR and stroke severity or dependency, though its sample size was smaller.⁷² Previous studies on Alzheimer's disease have found lower CVR compared to healthy volunteers, but did not report on the relationship between CVR and cognition directly.^{74,198}

This work has multiple strengths. A reproducible CVR experiment optimised for SVD research was used.¹¹⁴ Visual assessments of SVD features were systematic, comprehensive and conducted under the supervision of expert neuroradiologists, and statistical analyses were verified by an experienced statistician. Image analysis used pipelines designed and tested in cerebrovascular disease. Finally, this is the largest study to date to have assessed CVR impairment in SVD.

There are also some limitations. More males were recruited than females, reflecting male excess in small vessel stroke.²⁸ The population had mild stroke, but patients with more severe stroke would not be able to tolerate long scanning sessions. Moreover, only MoCA was used to assess cognition whereas other metrics could be investigated, e.g. Trail making A and B test.³⁷² Another potential limitation is the fact that this is a cross-sectional analysis; therefore the relationships found are not necessarily causal.

In conclusion, CVR impairment in WMH, NAWM and SGM was associated with SVD burden in patients with mild ischaemic stroke and SVD. The strength of association depended on the tissue in which CVR was measured and SVD feature type. Chapter 7 aims to understand how baseline CVR impairment relates to the longitudinal progression of SVD lesions.

7 Cerebrovascular reactivity in patients with small vessel disease: longitudinal analysis

The content of this chapter is included in a manuscript currently in preparation for submission to a peer-reviewed journal and part of it was/will be presented at conferences (ESOC 2021, ISMRM 2023).

7.1 Introduction

As discussed in Chapter 5, the MSS3 study is a prospective longitudinal study designed to deepen our knowledge regarding the link between vascular dysfunction and SVD features and identify potential biomarkers of disease progression.³⁴¹ As shown in Chapter 6 and previous studies, CVR impairment is associated with higher WMH burden,^{72,129,304,373} higher PVS scores,⁷² more microbleeds^{72,357} and more lacunes. However, how impaired CVR relates to the longitudinal evolution of SVD burden has not yet been extensively investigated. One study reported that NAWM tissues that progressed into WMH initially had reduced CVR magnitude and longer CVR delay than contralateral NAWM.²¹⁰

Therefore, the aim of this chapter was to assess baseline CVR in deep brain structures in relation to changes in SVD neuroimaging features after one year using the MSS3 data. We hypothesised that reduced CVR at baseline would be associated with an increase in SVD severity at one year follow-up.

7.2 Methods

The recruitment of participants and the data acquisition and data processing methods of the study have been described in Chapter 5. Here the statistical models used for the analyses presented in this chapter are described. Analyses were conducted using R (version 3.6.1; cran.r-project.org/) with the additional packages: tidyverse, ggplot2, insight, sjPlot and car.

Associations with CVR were modelled separately for each tissue. We used multivariable linear regressions for analyses related to quantitative neuroimaging features and multivariable ordinal logistic regressions for analyses related to visual scores. For all regressions, the feature/score of interest at one-year follow-up was defined as the outcome, whereas CVR and the feature/score of interest at baseline were independent variables. All models were adjusted for age, sex, MAP, smoking history (current or recent versus ex-smoker for more than one year versus never), hypertension diagnosis, diabetes diagnosis and hypercholesterolaemia diagnosis.

For each model, model assumptions were checked (e.g. normality of residuals and heteroscedasticity), as well as the absence of collinearity between independent variables (defined by variable inflation factor < 2). To ensure normality of residuals, the WMH and PVS volumes were transformed using the logarithm to the base-10 function.

Coefficients of the regressions and odds ratios (OR) were reported along with 95% confidence intervals and p-values.

As in Chapter 6, several sensitivity analyses were conducted (see Appendix A4.3): 1) adjusting for baseline WMH volume; 2) adjusting for EtCO₂ baseline in all models; 3) excluding datasets where the mean or standard deviation of the framewise displacement during the BOLD-CVR scan were upper outliers of their respective distribution; 4) excluding datasets where the CVR scan was stopped before the end of the first CO₂ block; 5) excluding CVR data where the masks in mean BOLD space had fewer than 10 voxels.

7.3 Results

7.3.1 Population characteristics

As described in Chapter 5, 182/207 patients had useable baseline CVR data in SGM and NAWM while 175/207 patients had useable baseline CVR data in WMH. Of the 182 patients with useable baseline CVR, 163 completed their

one-year follow-up with MRI scans to assess the evolution of SVD neuroimaging features (median age at baseline: 68.0 years old, 68% male; Figure 7-1, Table 7-1). Due to missing sequences or poor quality T2W images, a few datasets were excluded from specific analyses (3/163 excluded from analysis with PVS volumes, 1/163 excluded from analysis with PVS scores, 1/163 excluded from analysis with microbleeds, 2/163 excluded from analysis with SVD scores; Figure 7-1).

After one year, the cohort had a median increase in WMH volume of 0.32 [-0.48,1.78] ml with 60% of patients having new WMH at follow-up (Table 7-1). The median change in number of lacunes and microbleeds was of 0 [0,0] (Table 7-1); 8% and 10% of patients had new lacunes and microbleeds respectively, whereas 2 and 1% had less of them after one year. 83% participants had a lower brain volume at follow-up with a median cohort change of -0.97 [-1.60,-0.34] ml (Table 7-1). The median changes in BG, CSO and total PVS volume were of 0.24 [-0.34,0.95], 0.32 [-0.12,1.18], 0.36 [-0.12,1.15] %ROIV respectively (Table 7-1). 60%, 70% and 68% of patients had increased BG, CSO and total PVS volume after one year respectively. There were minimal changes in visual scores (Table 7-1).

7.3.2 WMH

Lower baseline CVR in normal-appearing tissues was associated with increasing WMH volume over one year ($B_{NAWM} = -1.14 [-2.13, -0.14] \log_{10}(\%ICV)$ per %/mmHg; Table 7-2, Figure 7-2, Figure 7-3, Figure 7-4). A similar tendency was observed between lower WMH CVR and increased WMH volume after one year ($B_{WMH} = -0.251 [-0.635, 0.133] \log_{10}(\%ICV)$ per %/mmHg; Table 7-2, Figure 7-2, Figure 7-3, Figure 7-4).

7.3.3 Lacunes and cerebral microbleeds

There were no associations between baseline CVR and number of lacunes or microbleeds after one year (Table 7-2, Figure 7-2, Figure 7-3). This was still the case in the sensitivity analyses (see Appendix A4.3).

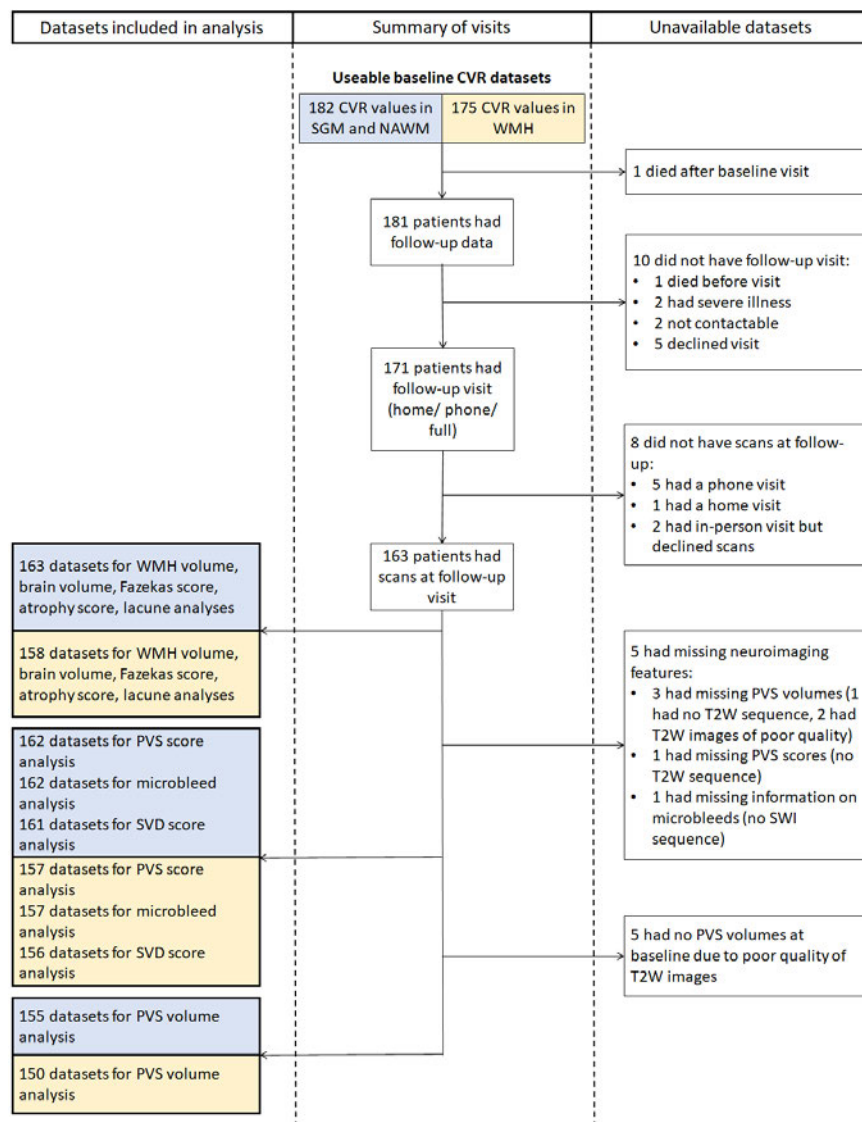


Figure 7-1: Flow diagram showing the dataset exclusion process for the longitudinal analysis. Blue squares contain number of datasets for analyses related to SGM and NAWM CVR, whereas yellow squares contain number of datasets for analyses related to WMH CVR.

Table 7-1: Population characteristics of longitudinal analysis. Non-binary variables are reported as median [IQR] and binary and smoking variables as number (%). Baseline values and, where relevant, change after one year are reported for the various parameters.

Variables	Baseline values for CVR	N	Baseline values for CVR	N	Change after one year
-----------	-------------------------	---	-------------------------	---	-----------------------

	analysis in SGM and NAWM		analysis in WMH		
Age [years]	68.0 [56.2, 74.4]	163	68.1 [56.3, 75.2]	158	-
Sex (male, female)	111 (68), 52 (32)	163	106 (67), 52 (33)	158	-
MAP [mmHg]	105 [98, 115]	163	105 [98, 114]	158	-
Diabetes diagnosis	32 (20)	163	31 (20)	158	-
Hypertension diagnosis	118 (72)	163	115 (73)	158	-
Hypercholesterolaemia diagnosis	118 (72)	163	114 (72)	158	-
Smoker (current, ever, never)	26 (16), 63 (39), 74 (45)	163	25 (16), 63 (40), 70 (44)	158	-
Stroke type (lacunar, cortical)	66 (40), 97 (60)	163	66 (42), 92 (58)	158	-
WMH volume [ml]	8.04 [3.90, 18.89]	163	8.36 [4.21, 19.13]	158	0.32 [-0.48, 1.78]
WMH volume [%ICV]	0.506 [0.242, 1.140]	163	0.518 [0.279, 1.187]	158	0.019 [-0.029, 0.117]
Number of lacunes	1 [0, 3]	163	1 [0, 3]	158	0 [0, 0]
Number of microbleeds	0 [0, 0]	162	0 [0, 0]	157	0 [0, 0]
Total atrophy score	6 [4, 8]	163	6 [4, 8]	158	0 [0, 0]
Brain volume [ml]	1089 [1009, 1179]	163	1081 [1006, 1176]	158	-15 [-27, -5]
Brain volume [%ICV]	67.6 [64.5, 71.1]	163	67.3 [64.4, 71.0]	158	-1.0 [-1.6, -0.3]
Total Fazekas score	3 [2, 4]	163	3 [2, 4]	158	0 [0, 0]
Total PVS score	4 [3, 5]	162	4 [3, 5]	157	0 [0, 0]
BG PVS volume [%ROIV]	4.89 [3.33, 6.07]	155	4.93 [3.34, 6.07]	150	0.24 [-0.34, 0.95]
CSO PVS volume [%ROIV]	3.31 [2.18, 5.22]	155	3.34 [2.21, 5.23]	150	0.32 [-0.12, 1.18]
Total PVS volume [%ROIV]	3.66 [2.47, 5.41]	155	3.70 [2.51, 5.41]	150	0.36 [-0.12, 1.15]
SVD score	2 [1, 3]	161	2 [1, 3]	156	0 [0, 0]
CVR in SGM [%/mmHg]	0.171 [0.135, 0.207]	163	-	-	-
CVR in NAWM [%/mmHg]	0.042 [0.033, 0.054]	163	-	-	-

Chapter 7. MSS3 longitudinal analysis

CVR in WMH [%/mmHg]	-	-	0.040 [0.025, 0.065]	158	-
---------------------	---	---	----------------------------	-----	---

Table 7-2: Longitudinal analyses with quantitative SVD features. Each row represents a different statistical model where the SVD feature of interest after one year is given in the first column. The associated regression coefficient *B*, its 95% confidence interval and *p*-value are given in columns 2-4. The last column gives the units of *B*. All models were corrected for the SVD feature of interest at baseline, age, sex, MAP, diagnosis of diabetes, hypertension, and hypercholesterolaemia and smoking history.

Variables after one year	SGM CVR	NAWM CVR	WMH CVR	Units of <i>B</i>
WMH volume	<i>B</i> =-0.325 [-0.652, 0.002] <i>p</i> =0.052	<i>B</i> =-1.14 [-2.13, -0.14] <i>p</i> =0.026	<i>B</i> =-0.251 [-0.635, 0.133] <i>p</i> =0.199	log ₁₀ (%ICV) per %/mmHg
Number of lacunes	<i>B</i> =-0.809 [-2.591, 0.974] <i>p</i> =0.371	<i>B</i> =0.454 [-4.852, 5.761] <i>p</i> =0.866	<i>B</i> =-0.932 [-2.929, 1.065] <i>p</i> =0.358	lacunes per %/mmHg
Number of microbleeds	<i>B</i> =-0.946 [-5.121, 3.230] <i>p</i> =0.655	<i>B</i> =-4.35 [-17.48, 8.79] <i>p</i> =0.514	<i>B</i> =-2.01 [-7.85, 3.82] <i>p</i> =0.496	microbleeds per %/mmHg
Brain volume	<i>B</i> =0.128 [-5.028, 5.283] <i>p</i> =0.961	<i>B</i> =9.85 [-6.00, 25.70] <i>p</i> =0.221	<i>B</i> =-0.241 [-6.320, 5.839] <i>p</i> =0.938	%ICV per %/mmHg
BG PVS volume	<i>B</i> =-0.446 [-0.814, -0.078] <i>p</i> =0.018	<i>B</i> =-2.12 [-3.23, -1.01] <i>p</i> <0.001	<i>B</i> =-0.607 [-1.010, -0.203] <i>p</i> =0.003	log ₁₀ (%ROIV) per %/mmHg
CSO PVS volume	<i>B</i> =-0.143 [-0.620, 0.334] <i>p</i> =0.554	<i>B</i> =-1.93 [-3.37, -0.48] <i>p</i> =0.009	<i>B</i> =-0.163 [-0.714, 0.388] <i>p</i> =0.560	log ₁₀ (%ROIV) per %/mmHg
Total PVS volume	<i>B</i> =-0.207 [-0.637, 0.223] <i>p</i> =0.343	<i>B</i> =-1.90 [-3.21, -0.60] <i>p</i> =0.005	<i>B</i> =-0.366 [-0.858, 0.126] <i>p</i> =0.144	log ₁₀ (%ROIV) per %/mmHg

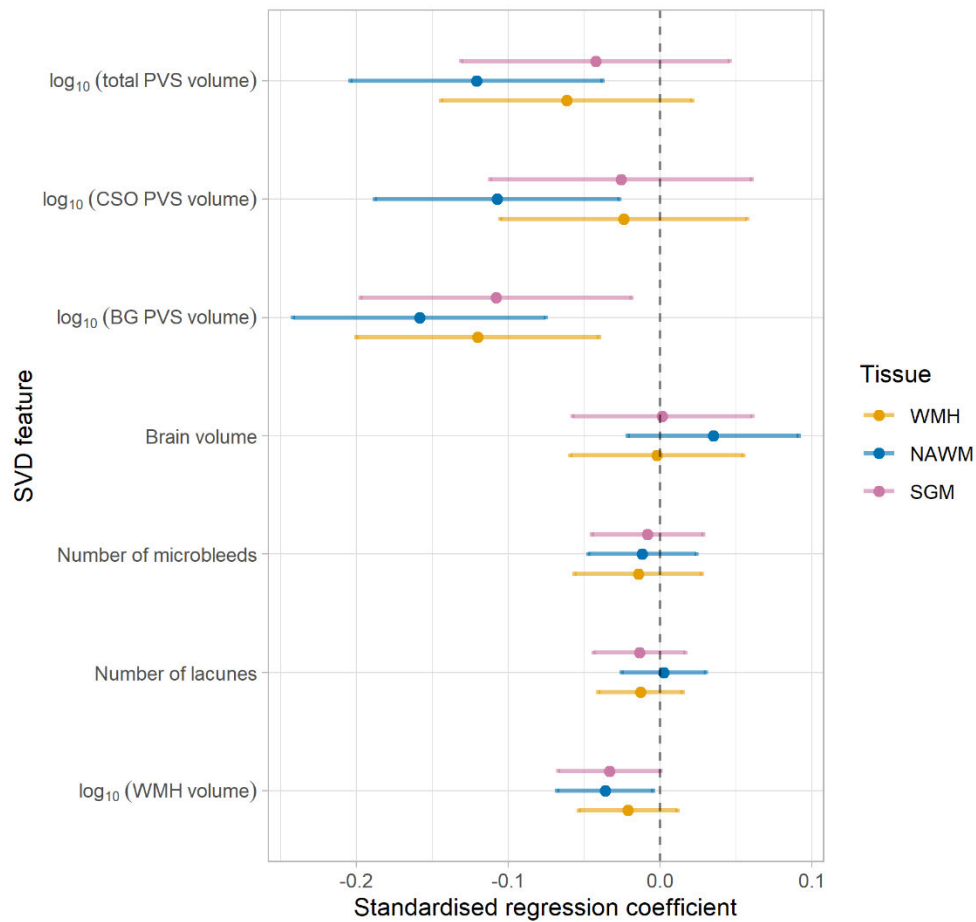


Figure 7-2: Standardised regression coefficients from longitudinal analysis between SVD quantitative features after one year (corrected for values at baseline) and baseline CVR in SGM (pink), NAWM (blue) and WMH (yellow). The dots represent the mean standardised coefficients and the horizontal lines the associated 95% confidence intervals. The vertical dashed line emphasises a zero-valued coefficient. Coefficients to left of zero line indicate association with lower CVR.

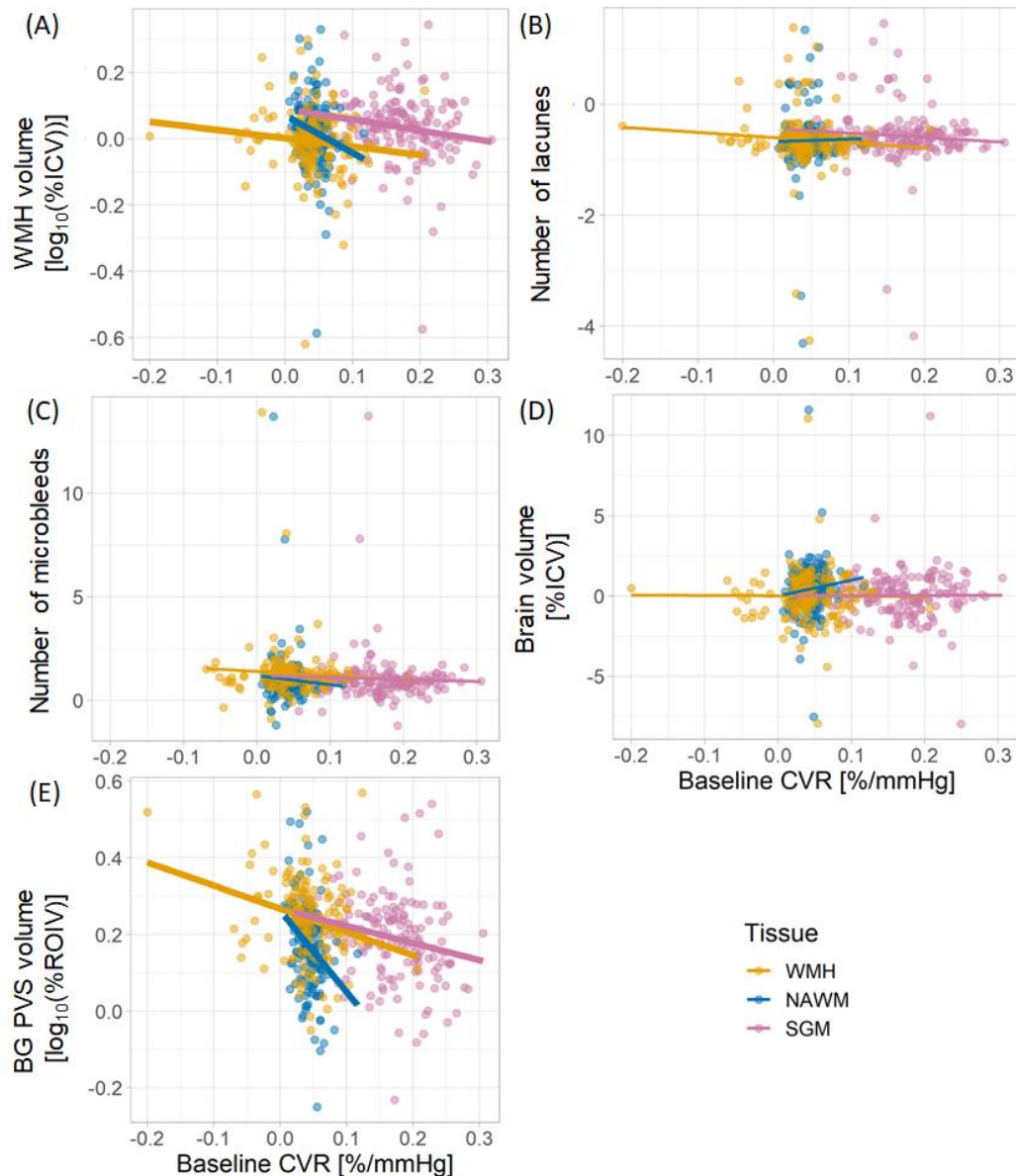


Figure 7-3: Longitudinal relationships between baseline CVR and adjusted SVD quantitative features after one year. Each SVD feature was adjusted for the SVD feature at baseline, age, sex and vascular risk factors. The results are shown for CVR in SGM (pink), NAWM (blue) and WMH (yellow). The regression lines are shown in all plots.

7.3.4 Brain volume

There was no association between baseline CVR and evolution of brain volume after one year (Table 7-2, Figure 7-2, Figure 7-3).

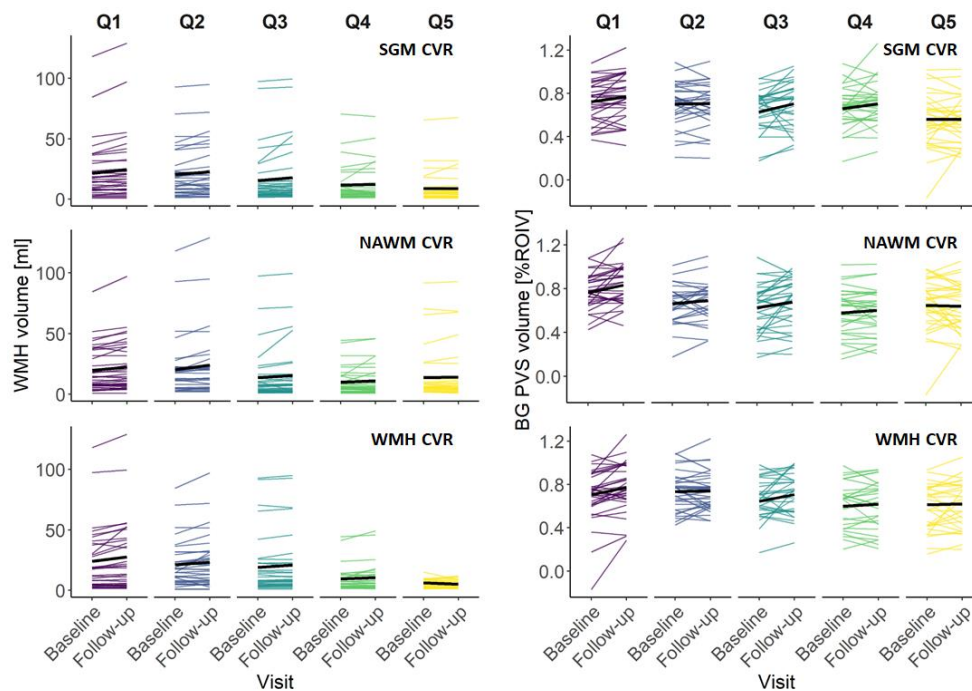


Figure 7-4: One year change in WMH (1st column) and BG PVS volumes (2nd column) as a function of CVR quintile. CVR in SGM (1st row), NAWM (2nd row) and WMH (3rd row) were split into quintiles (Q1–Q5) and color-coded accordingly. The lines represent individual change in WMH or BG PVS volume from baseline to one-year follow-up. The mean one-year change across individuals for each quintile is emphasised in bold.

7.3.5 PVS volumes

Lower baseline CVR in all ROIs was associated with increased PVS volume in BG after one year ($B_{NAWM} = -2.12 [-3.23, -1.01] \log_{10}(\%ROIV)$ per $\%/mmHg$; Table 7-2, Figure 7-2, Figure 7-3). Only lower baseline CVR in NAWM was associated with increased CSO ($B_{NAWM} = -1.93 [-3.37, -0.48] \log_{10}(\%ROIV)$ per $\%/mmHg$) and total PVS volume after one year ($B_{NAWM} = -1.90 [-3.21, -0.60] \log_{10}(\%ROIV)$ per $\%/mmHg$; Table 7-2, Figure 7-2). There was a tendency to lower baseline WMH CVR in patients with higher total PVS volume after one year ($B_{WMH} = -0.366 [-0.858, 0.126] \log_{10}(\%ROIV)$ per $\%/mmHg$; Table 7-2, Figure 7-2). Those associations held after further adjusting for WMH burden at baseline (Table A4-9).

7.3.6 Visual scores

The regression coefficients between baseline CVR and visual scores after one year are summarised in Table 7-3 for total Fazekas, total atrophy, total PVS and SVD scores. The 95% confidence intervals related to the regression coefficients are large (e.g., $OR_{NAWM}=15.8$ [0.0, 5.1×10^{16}]). Figure 7-5 shows that most total Fazekas scores were stable over one year (in agreement with Table 7-1) and that, for most datasets, the total Fazekas score was an “ideal” predictor for the total Fazekas scores after one year – also known as a quasi-separation situation. While Figure 7-5 shows only total Fazekas scores, similar observations were made for all the visual scores.

Table 7-3: Longitudinal analyses with SVD visual ratings. Each row represents a different statistical model where the SVD score of interest after one year is given in the first column. The associated odds ratio, 95% confidence interval and p-value are given in the other columns for SGM, NAWM and WMH respectively. All models were corrected for the SVD score of interest at baseline, age, sex, MAP, diagnosis of diabetes, hypertension, and hypercholesterolaemia and smoking history.

Variables after one year	SGM CVR	NAWM CVR	WMH CVR
Total Fazekas score	OR=0.00 [0.00, 119.64] p=0.269	OR=15.8 [0.0, 5.1×10^{16}] p=0.883	OR=0.00 [0.00, 1.80] p=0.060
Total atrophy score	OR=4.84 [0.00, 2.86×10^4] p=0.718	OR=0.00 [0.00, 5.12×10^8] p=0.648	OR=2.91 [0.00, 1.83×10^5] p=0.845
Total PVS score	OR=0.19 [0.00, 413.49] p=0.674	OR= 6.53×10^5 [0.00, 9.64×10^{15}] p=0.264	OR=151 [0, 5×10^6] p=0.332
SVD score	OR=88.9 [0.0, 2.5×10^5] p=0.266	OR= 5.78×10^8 [0.04, 8.65×10^{18}] p=0.089	OR=0.06 [0.00, 2.4×10^3] p=0.598

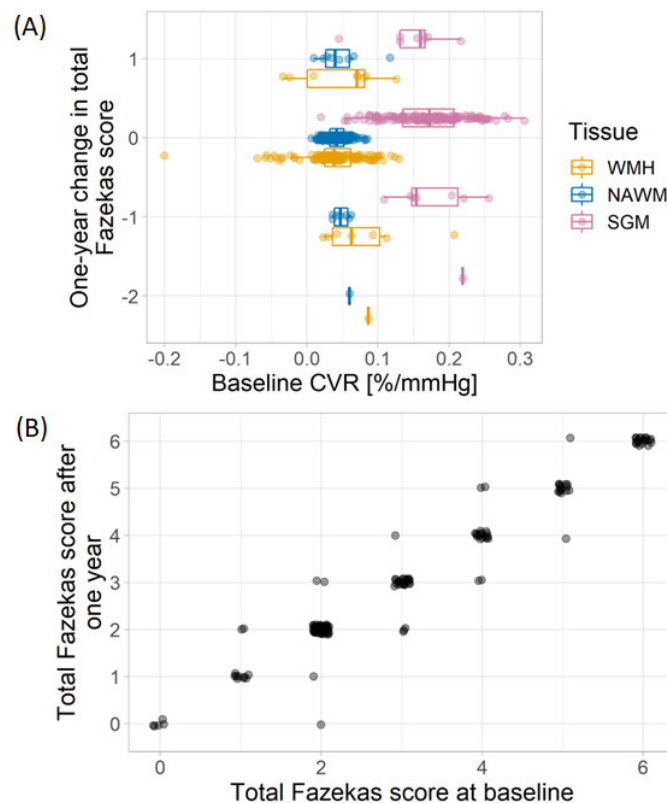


Figure 7-5 : Change in total Fazekas scores after one year. (A) Change in total Fazekas scores after one year as a function of baseline CVR in SGM (pink), NAWM (green) and WMH (blue). (B) Total Fazekas scores after one year as a function of total Fazekas scores at baseline.

7.4 Discussion

This work investigated the relationships between baseline CVR impairment and evolution of SVD features after one year. Results showed that impaired CVR at baseline predicted increased WMH and PVS volumes after one year, although the latter depended on the tissue types from which CVR impairment and PVS volume were extracted. These associations were independent of age, sex and key VRFs.

The progression of SVD features in this cohort was limited as it was measured over a period of one year only, although it was consistent with previous studies.^{32,374}

More severe CVR impairment in all ROIs at baseline predicted increased WMH volume after one year. Although this has not been investigated previously, one study observed that CVR in NAWM that progressed into WMH after one year was lower than CVR in contralateral NAWM.²¹⁰ This would support our finding that CVR impairment predicts WMH progression.

There were no relationships between impaired baseline CVR and evolution of lacunes, microbleeds or brain volumes. This could reflect the early stages of the disease where disease progression is slow.³² Indeed, most patients did not have new lacunes or microbleeds after one year and had a median decrease in brain volume of only 1%.

CVR impairment in all ROIs at baseline was associated with increased PVS volume in BG after one year. Baseline CVR impairment in NAWM could also predict one-year increase in CSO and total PVS volumes. As found in previous studies^{72,370} and the cross-sectional analysis in Chapter 6, there seems to be a link between vascular dysfunction and impairment of the drainage system in the brains of SVD patients, presumably mediated by other SVD features. This longitudinal analysis provided additional validation of this hypothesis and further suggested that CVR impairment predicts increased presence of interstitial fluid around the blood vessels. However, those findings need to be replicated in future research.

This work showed that the evolution of visual ratings of SVD features over one year was minimal. This resulted in poor modelling of the relationships between baseline CVR impairment and SVD progression as quasi-separation in the models arose when predicting visual scores after one year using baseline visual scores. Therefore, the regression coefficient associated with baseline CVR could not be used and findings from visual ratings and quantitative features could not be compared.

The analysis conducted in this chapter shared similar strengths to the cross-sectional analysis reported in Chapter 6, namely: a reproducible CVR experiment optimised for SVD research,^{114,319} systematic and comprehensive

rating of SVD visual features, image analysis pipelines designed and tested in cerebrovascular disease. Moreover, at the time of writing this thesis, this cohort study was the first to investigate how CVR impairment relates to the evolution of SVD features.

Aside from the limitations stated in Chapter 6, there were further limitations related to the longitudinal aspect of the study. CVR was only measured during the baseline and not the follow-up visit. Therefore, it was not possible to observe how CVR impairment changed over one year in parallel to the evolution of SVD features nor if SVD burden at baseline could predict further CVR impairment. Furthermore, only one time point was used to inform on the evolution of SVD features. However, patients had additional visits between baseline and one-year follow-up where scanning sessions took place, as described in Chapter 5. Those time points could also have been used in this longitudinal analysis; though the number of visits was patient-dependent and the use of more complex models would be required (e.g., linear mixed models). Finally, the evolution of SVD features was limited to one year. As shown in this work, the changes in SVD features over this period were relatively small, especially when considering SVD visual ratings. Fortunately, at the time of writing this thesis, the MSS3 study was still on-going. Approvals were obtained to carry out an in-person third-year follow-up visit, which has been added to the initial study design. Those additional datasets will be useful to investigate longitudinal relationships over longer periods of time and understand if CVR reduction precedes or predicts SVD progression.

In conclusion, CVR impairment at baseline predicted an increase in WMH volume and PVS volume after one year in SVD patients with mild ischaemic stroke. Future research is needed to understand if these findings still hold when considering SVD progression over longer periods.

8 Discussion and conclusion

There is a growing interest in developing in vivo techniques to assess vascular properties in cerebrovascular diseases. Measuring CVR using MRI is a way to assess the health of cerebral blood vessels by probing their ability to dilate in response to a vasodilatory stimulus. It has been used in numerous studies, however, further validation and harmonisation of the technique is needed. This thesis aimed to investigate the accuracy and repeatability of the technique and apply it in clinical research to study the role of CVR impairment in SVD. This chapter is divided into two main parts: CVR MRI methodology and CVR measurements in SVD patients. In both parts, the main findings are summarised, followed by discussions on the contributions that this work makes to the CVR MRI and clinical SVD fields respectively. The limitations of the thesis are also reviewed and future directions of research are proposed.

8.1 CVR MRI methodology

8.1.1 Summary of findings

A systematic review of the CVR MRI experiment in humans was carried out in Chapter 2 and revealed the progress of the technique towards clinical translation. The experiment showed good repeatability and was validated against other imaging modalities such as TCD, SPECT, PET, though this was mostly confined to small healthy populations. CVR MRI was also used in pathologies to detect CVR impairment and to detect disease progression or response to intervention/treatment, showing the biological validity of the technique. However, the review revealed a variety of methodologies across the literature. Despite emerging consensus in the use of the BOLD MRI technique to measure CVR, the accompanying vasodilatory stimulus was more variable with the most common stimuli being fixed inhaled CO₂ and EtCO₂ targeting. Furthermore, most studies did not justify the use of a specific processing method (e.g. ROI- versus voxel-based analysis, correction for CVR

delay, use of specific HRF) and comparisons between methods are lacking. There is also a need for open-source softwares to promote reproducibility and harmonisation.

In Chapter 3, the reliability of ROI- against voxel-based processing method was investigated using simulations and a test-retest experiment in healthy volunteers. Simulations showed that voxel-based analysis was accurate and precise in experiments where the noise level is low, but showed a delay constraint dependency as the noise level increased. Dependent on the noise level in real data, tissues such as NAWM are prone to this bias, which was verified in the data acquired in the study. Alternatively, ROI-based analysis could be used as it was robust against noise and gave estimates of CVR magnitude with similar precision, though CVR magnitude was consistently underestimated with respect to the ground-truth mean due to signal averaging over voxels with a distribution of CVR delays. Using a fixed delay resulted in comparable estimates of CVR magnitude between methods, but estimation errors increased with respect to using variable CVR delay in NAWM. The test-retest experiment showed that the repeatability for both processing methods was similar. However, the EtCO₂ change induced by the fixed inhaled CO₂ concentration stimulus differed slightly between the two scans, which could have come from a habituation effect of the gas challenge from the participants, thereby resulting in a small bias in CVR estimates.

Chapter 4 detailed a feasibility study to extract cerebral pulsatility from BOLD-CVR data. The processing method was optimised and showed low to moderate strength of associations with pulsatility measurements from PC MRI. To an extent, the technique allowed extraction of cerebral pulsatility from BOLD-CVR in brain regions further downstream in both healthy volunteers and patients with SVD. However, further optimisation and validation mentioned in the related chapter could increase the correlation with pulsatility measurements from PC MRI, thereby improving the technique for future clinical uses.

8.1.2 Contributions to the CVR MRI field

While previous reviews have focused on the numerous types of stimulus,^{84,122} CVR MRI experiments with breath-hold challenge,^{86,121} CVR data and interpretation¹²³ or common aspects of CVR methodology,⁸³ this systematic review is the first to give a detailed description of the CVR MRI experiments used in the literature.¹⁰¹ One of its main contributions to the field is that it identifies areas of consensus in the methodology and highlights different aspects that still need to be validated and/or harmonised. For example, the review revealed the need for better reporting CVR studies and differing data processing and delay correction methods.

Findings from Chapter 3 imply that the use of fixed CVR delay results in poor accuracy of CVR magnitude and a variable CVR delay bounded to realistic values should be favoured instead. The choice of voxel- versus ROI-based analyses should consider the noise level in tissues where CVR is being investigated and ROI-based analysis should be used in case of high noise levels. This is especially relevant for SVD research where deep brain structures and WMH, which have with lower tCNR, are of interest.^{72,114,304}

The within-day test-retest repeatability experiment with fixed inhaled CO₂ stimulus conducted in Chapter 3 showed that the experiment is repeatable and well-tolerated and the inter-scan coefficients of variation were similar to those reported in other studies,^{114,263,271} validating its use in clinical research. Familiarising participants with gas challenge prior to CVR scans is necessary to avoid anxiety and mitigate habituation effects, which is especially relevant for longitudinal studies. As suggested in the associated chapter, an indication of the extent of those effects can be provided by measuring and reporting physiological parameters such as blood pressure, heart and respiration rates.

Lastly, the extraction of cerebral pulsatility in various brain tissues from CVR data was tested in Chapter 4 and promising pulsatile waveforms were obtained. Though the technique is still premature, it is of interest in the community^{129,334} as it would have multiple benefits, e.g. reducing scan time,

measuring cerebral pulsatility in tissues further away from large blood vessels. Furthermore, measuring cerebral pulsatility under hypercapnia could give complementary information about vascular health.

8.1.3 Limitations

The systematic review in Chapter 2 was restricted to human studies, thereby excluding any pre-clinical work.¹⁰¹ Although processing methods are similar between the two fields of research,²⁹⁴ preclinical studies contribute to the biological validation of the CVR MRI experiment, which is consequently under-represented in the review.

One limitation of the comparison of CVR data processing strategies in Chapter 3 is that the work did not investigate the use of various HRFs in the model of the BOLD signal,^{91,100} although the accuracy and precision of estimating CVR parameters when including such functions in the processing strategy could be affected by noise. Another limitation is that some pre-processing steps were not included in the analysis, though methods like spatial smoothing could affect CVR estimates.

The design of the test-retest study in Chapter 3 did not allow for the duration of the habituation effect to be investigated and further work is needed to understand whether it is a short- or long-term effect. Another limitation that should be mentioned concerning the use of a gas challenge as a vasoactive stimulus is the assumption that the associated MRI response is linear. Previous studies using an EtCO₂ targeting stimulus with ramp paradigm explored the MRI response to multiple EtCO₂ values and described the response shape as sigmoidal^{94,268} - with horizontal asymptotes at low and high EtCO₂ levels and a linear range of response in-between. This finding implies that using an EtCO₂ change overlapping with the nonlinear part of the MRI response could result in the assumption being incorrect. This is a limitation generalisable to any breathing challenges where the linear range of the response to the stimulus is unknown, with the latter potentially varying across cohorts and individuals.

8.2 Cerebrovascular reactivity in patients with small vessel disease

8.2.1 Summary of findings

Chapter 5 gave an overview of the MSS3 study, a prospective clinical study of SVD patients with mild ischaemic stroke. CVR data collected in this study were analysed in Chapters 6 and 7. Chapter 6 investigated cross-sectional relationships between CVR and SVD neuroimaging features, cognition, stroke severity and outcome. Results showed that SVD patients with lower CVR in normal-appearing and damaged tissues had higher WMH burden, more lacunes, more microbleeds, higher atrophy and PVS scores and cognition deficit. There was also an association between lower CVR in normal-appearing and damaged tissues and higher SVD score implying that lower CVR could be a marker of overall SVD severity and could precede visible tissue damage. Chapter 7 focused on longitudinal relationships between CVR and SVD features. SVD patients with lower baseline CVR had increased WMH and PVS volumes after one year implying that lower CVR can predict worsening of those SVD features.

8.2.2 Contributions to the SVD clinical field

According to previous studies in humans and pre-clinical models, BBB dysfunction could be a mechanism responsible for SVD.^{2,45,55,58–61,63–69} This would affect vascular properties, such as CVR, BBB permeability and cerebral pulsatility.² To advance knowledge on SVD pathogenesis, the MSS3 study aimed to explore the role of vascular dysfunction in relation to visible tissue damage and other medical assessments such as cognitive function.³⁴¹

Currently, this is the largest study to report on CVR measurements in different deep brain structures in a cohort of SVD patients. Whereas other studies focused on WMH burden,^{76,210,365} this study benefited from detailed radiological MRI assessments in addition to visually rated WMHs, e.g. lacunes, microbleeds, atrophy, PVS,³¹ which were also investigated as a function of

CVR impairment. Moreover, this is one of the few and the largest study to analyse relationships between CVR and computational measurements of SVD neuroimaging features such as WMH and PVS volumes.^{362,363,375} Those computational measurements can:

- detect small changes in SVD features, which are not perceived when using categorical variables such as visual scores, e.g. longitudinal analyses in Chapter 7 were only possible with computational measurements, but not with visual ratings which had limited evolution over one year
- confirm associations found with visual ratings, e.g. similar cross-sectional associations found between CVR, WMH volumes and Fazekas scores
- give additional information on the relationships with the features of interest, e.g. the difference between PVS scores and volumes was reflected in cross-sectional relationships with CVR, where higher PVS scores were associated with lower CVR, but no associations were found between CVR and PVS volumes.

The MSS3 confirmed cross-sectional associations between impaired CVR and higher WMH burden previously found.^{72,76,210,364,365,368} Moreover, the study revealed further associations between impaired CVR, increased presence of other SVD neuroimaging features, higher SVD score and lower cognitive function. Future directions would include comparing CVR impairment in relation to other vascular damages such as BBB permeability, increased cerebral pulsatility or markers of endothelial dysfunction.

The MSS3 was the first study to investigate relationships between baseline CVR and evolution of SVD features over one year. As suggested by a previous study,²¹⁰ CVR impairment predicted progression of WMH burden. Moreover, CVR impairment predicted increased PVS volumes after one year - a new finding that needs to be confirmed by future studies. Future work could also

measure CVR longitudinally and investigate whether baseline SVD burden can predict deterioration of CVR.

Overall, findings from the study suggest that CVR is associated with SVD severity and can predict worsening of several SVD features. This emphasises the importance of including CVR measurements in future SVD studies³⁷⁶ and trials.³⁷⁷

8.2.3 Limitations

When investigating CVR in relation to cognition in patients with SVD, the MoCA score was used as an indicator of cognitive function. However, there exist other tests that could also be considered to confirm the findings, such as Trail making A and B test³⁷² or the informant questionnaire on cognitive decline in the elderly.³⁷⁸ Moreover, due to the study design at the time of writing this thesis, longitudinal analyses were restricted to the comparison of baseline CVR and other evolving SVD features. As this work showed that baseline CVR impairment could predict the progression of certain features such as WMH and PVS volumes, future studies should investigate whether CVR reduction precedes or predicts SVD progression.

8.3 Conclusion

As a final conclusion, this thesis demonstrated that it is possible to measure CVR in the deep brain structures of healthy volunteers and SVD patients using MRI. This does, however, require optimisation of processing strategy in order to provide CVR estimates that are robust against noise and comparable across studies. The technique was applied in an SVD population as part of a large observational study. Findings showed that CVR impairment was related to SVD severity and predicted progression of several SVD features after one year.

Bibliography

1. Regenhardt RW, Das AS, Lo EH, Caplan LR. Advances in Lacunar Stroke Pathophysiology: A Review. *JAMA Neurol.* 2018;75:1273–1281.
2. Wardlaw JM, Smith C, Dichgans M. Small vessel disease: mechanisms and clinical implications. *The Lancet Neurology.* 2019;18:684–696.
3. Wardlaw JM, DeBette S, Jokinen H, De Leeuw F-E, Pantoni L, Chabriat H, Staals J, Doubal F, Rudilosso S, Eppinger S, et al. ESO Guideline on covert cerebral small vessel disease. *European Stroke Journal.* 2021;6:CXI–CLXII.
4. Kalaria RN. Small Vessel Disease and Alzheimer's Dementia: Pathological Considerations. *CED.* 2002;13:48–52.
5. Sweeney MD, Montagne A, Sagare AP, Nation DA, Schneider LS, Chui HC, Harrington MG, Pa J, Law M, Wang DJJ, et al. Vascular dysfunction—The disregarded partner of Alzheimer's disease. *Alzheimer's & Dementia.* 2019;15:158–167.
6. DeBette S, Markus HS. The clinical importance of white matter hyperintensities on brain magnetic resonance imaging: systematic review and meta-analysis. *BMJ.* 2010;341:c3666.
7. Clancy U, Appleton JP, Arteaga C, Doubal FN, Bath PM, Wardlaw JM. Clinical management of cerebral small vessel disease: a call for a holistic approach. *Chinese Medical Journal.* 2021;134:127–142.
8. Wittenberg R, Knapp M, Hu B, Comas-Herrera A, King D, Rehill A, Shi C, Banerjee S, Patel A, Jagger C, et al. The costs of dementia in England. *Int J Geriatr Psychiatry.* 2019;34:1095–1103.
9. Gorelick PB, Scuteri A, Black SE, DeCarli C, Greenberg SM, Iadecola C, Launer LJ, Laurent S, Lopez OL, Nyenhuis D, et al. Vascular Contributions to Cognitive Impairment and Dementia. *Stroke.* 2011;42:2672–2713.
10. Xu X-M, Vestesson E, Paley L, Desikan A, Wonderling D, Hoffman A, Wolfe CD, Rudd AG, Bray BD. The economic burden of stroke care in England, Wales and Northern Ireland: Using a national stroke register to estimate and report patient-level health economic outcomes in stroke. *European Stroke Journal.* 2018;3:82–91.
11. Pantoni L. Cerebral small vessel disease: from pathogenesis and clinical characteristics to therapeutic challenges. *Lancet Neurol.* 2010;9:689–701.

12. Clancy U, Gilmartin D, Jochems ACC, Knox L, Doubal FN, Wardlaw JM. Neuropsychiatric symptoms associated with cerebral small vessel disease: a systematic review and meta-analysis. *The Lancet Psychiatry*. 2021;8:225–236.
13. de Laat KF, van Norden AGW, Gons RAR, van Oudheusden LJB, van Uden IWM, Bloem BR, Zwiers MP, de Leeuw F-E. Gait in Elderly With Cerebral Small Vessel Disease. *Stroke*. 2010;41:1652–1658.
14. Callisaya ML, Beare R, Phan T, Blizzard L, Thrift AG, Chen J, Srikanth VK. Progression of White Matter Hyperintensities of Presumed Vascular Origin Increases the Risk of Falls in Older People. *The Journals of Gerontology: Series A*. 2015;70:360–366.
15. Poggesi A, Pracucci G, Chabriot H, Erkinjuntti T, Fazekas F, Verdelho A, Hennerici M, Langhorne P, O'Brien J, Scheltens P, et al. Urinary complaints in nondisabled elderly people with age-related white matter changes: the Leukoaraiosis And DISability (LADIS) Study. *J Am Geriatr Soc*. 2008;56:1638–1643.
16. Kuchel GA, Moscufo N, Guttmann CR, Zeevi N, Wakefield D, Schmidt J, DuBeau CE, Wolfson L. Localization of Brain White Matter Hyperintensities and Urinary Incontinence in Community-Dwelling Older Adults. *J Gerontol A Biol Sci Med Sci*. 2009;64A:902–909.
17. Saini M, Ikram K, Hilal S, Qiu A, Venketasubramanian N, Chen C. Silent Stroke. *Stroke*. 2012;43:3102–3104.
18. Staals J, Makin SDJ, Doubal FN, Dennis MS, Wardlaw JM. Stroke subtype, vascular risk factors, and total MRI brain small-vessel disease burden. *Neurology*. 2014;83:1228–1234.
19. Hilal S, Mok V, Youn YC, Wong A, Ikram MK, Chen CL-H. Prevalence, risk factors and consequences of cerebral small vessel diseases: data from three Asian countries. *J Neurol Neurosurg Psychiatry*. 2017;88:669–674.
20. Dickie DA, Ritchie SJ, Cox SR, Sakka E, Royle NA, Aribisala BS, Valdés Hernández M del C, Maniega SM, Pattie A, Corley J, et al. Vascular risk factors and progression of white matter hyperintensities in the Lothian Birth Cohort 1936. *Neurobiol Aging*. 2016;42:116–123.
21. Shi Y, Wardlaw JM. Update on cerebral small vessel disease: a dynamic whole-brain disease. *Stroke Vasc Neurol*. 2016;1.
22. Chauhan G, Adams HHH, Satizabal CL, Bis JC, Teumer A, Sargurupremraj M, Hofer E, Trompet S, Hilal S, Smith AV, et al. Genetic

- and lifestyle risk factors for MRI-defined brain infarcts in a population-based setting. *Neurology*. 2019;92:486–503.
23. Geijselaers SLC, Sep SJS, Stehouwer CDA, Biessels GJ. Glucose regulation, cognition, and brain MRI in type 2 diabetes: a systematic review. *The Lancet Diabetes & Endocrinology*. 2015;3:75–89.
 24. Heye AK, Thrippleton MJ, Chappell FM, Valdés Hernández M del C, Armitage PA, Makin SD, Muñoz Maniega S, Sakka E, Flatman PW, Dennis MS, et al. Blood pressure and sodium: Association with MRI markers in cerebral small vessel disease. *J Cereb Blood Flow Metab*. 2016;36:264–274.
 25. Hankey GJ. The Role of Nutrition in the Risk and Burden of Stroke. *Stroke*. 2017;48:3168–3174.
 26. Lakka TA, Laaksonen DE. Physical activity in prevention and treatment of the metabolic syndrome. *Appl. Physiol. Nutr. Metab*. 2007;32:76–88.
 27. Makin SD, Doubal FN, Shuler K, Chappell FM, Staals J, Dennis MS, Wardlaw JM. The impact of early-life intelligence quotient on post stroke cognitive impairment. *Eur Stroke J*. 2018;3:145–156.
 28. Jiménez-Sánchez L, Hamilton OKL, Clancy U, Backhouse EV, Stewart CR, Stringer MS, Doubal FN, Wardlaw JM. Sex Differences in Cerebral Small Vessel Disease: A Systematic Review and Meta-Analysis. *Front Neurol*. 2021;12:756887.
 29. Huang Y, Yang C, Yuan R, Liu M, Hao Z. Association of obstructive sleep apnea and cerebral small vessel disease: a systematic review and meta-analysis. *Sleep*. 2020;43:zsz264.
 30. Marini S, Anderson CD, Rosand J. Genetics of Cerebral Small Vessel Disease. *Stroke*. 2020;51:12–20.
 31. Wardlaw JM, Smith EE, Biessels GJ, Cordonnier C, Fazekas F, Frayne R, Lindley RI, O'Brien JT, Barkhof F, Benavente OR, et al. Neuroimaging standards for research into small vessel disease and its contribution to ageing and neurodegeneration. *The Lancet Neurology*. 2013;12:822–838.
 32. Leijssen EMC van, Uden IWM van, Ghafoorian M, Bergkamp MI, Lohner V, Kooijmans ECM, Holst HM van der, Tuladhar AM, Norris DG, Dijk EJ van, et al. Nonlinear temporal dynamics of cerebral small vessel disease: The RUN DMC study. *Neurology*. 2017;89:1569–1577.
 33. Wardlaw JM, Chappell FM, Valdés Hernández MDC, Makin SDJ, Staals J, Shuler K, Thrippleton MJ, Armitage PA, Muñoz-Maniega S, Heye AK,

- et al. White matter hyperintensity reduction and outcomes after minor stroke. *Neurology*. 2017;89:1003–1010.
34. Snowdon DA, Greiner LH, Mortimer JA, Riley KP, Greiner PA, Markesbery WR. Brain Infarction and the Clinical Expression of Alzheimer Disease: The Nun Study. *JAMA*. 1997;277:813–817.
35. Vermeer SE, Longstreth WT, Koudstaal PJ. Silent brain infarcts: a systematic review. *The Lancet Neurology*. 2007;6:611–619.
36. Choi P, Ren M, Phan TG, Callisaya M, Ly JV, Beare R, Chong W, Srikanth V. Silent Infarcts and Cerebral Microbleeds Modify the Associations of White Matter Lesions With Gait and Postural Stability. *Stroke*. 2012;43:1505–1510.
37. Werring DJ, Frazer DW, Coward LJ, Losseff NA, Watt H, Cipolotti L, Brown MM, Jäger HR. Cognitive dysfunction in patients with cerebral microbleeds on T2*-weighted gradient-echo MRI. *Brain*. 2004;127:2265–2275.
38. Groeschel S, Chong WK, Surtees R, Hanefeld F. Virchow-Robin spaces on magnetic resonance images: normative data, their dilatation, and a review of the literature. *Neuroradiology*. 2006;48:745–754.
39. Doubal FN, MacLulich AMJ, Ferguson KJ, Dennis MS, Wardlaw JM. Enlarged Perivascular Spaces on MRI Are a Feature of Cerebral Small Vessel Disease. *Stroke*. 2010;41:450–454.
40. Kwee RM, Kwee TC. Virchow-Robin Spaces at MR Imaging. *RadioGraphics*. 2007;27:1071–1086.
41. MacLulich A, Wardlaw J, Ferguson K, Starr J, Seckl J, Deary I. Enlarged perivascular spaces are associated with cognitive function in healthy elderly men. *J Neurol Neurosurg Psychiatry*. 2004;75:1519–1523.
42. ter Telgte A, van Leijsen EMC, Wiegertjes K, Klijn CJM, Tuladhar AM, de Leeuw F-E. Cerebral small vessel disease: from a focal to a global perspective. *Nat Rev Neurol*. 2018;14:387–398.
43. Fisher CM. Lacunar strokes and infarcts: A review. *Neurology*. 1982;32:871–871.
44. Lammie GA. Pathology of small vessel stroke. *British Medical Bulletin*. 2000;56:296–306.
45. Wardlaw, Sandercock P a. g., Dennis M s., Starr J. Is Breakdown of the Blood-Brain Barrier Responsible for Lacunar Stroke, Leukoaraiosis, and Dementia? *Stroke*. 2003;34:806–812.

46. Wardlaw JM, Smith C, Dichgans M. Mechanisms of sporadic cerebral small vessel disease: insights from neuroimaging. *The Lancet Neurology*. 2013;12:483–497.
47. Bouvy WH, Biessels GJ, Kuijf HJ, Kappelle LJ, Luijten PR, Zwanenburg JJM. Visualization of perivascular spaces and perforating arteries with 7 T magnetic resonance imaging. *Invest Radiol*. 2014;49:307–313.
48. De Guio F, Jouvent E, Biessels GJ, Black SE, Brayne C, Chen C, Cordonnier C, De Leeuw F-E, Dichgans M, Doubal F, et al. Reproducibility and variability of quantitative magnetic resonance imaging markers in cerebral small vessel disease. *J Cereb Blood Flow Metab*. 2016;36:1319–1337.
49. Rosenberg GA. Inflammation and White Matter Damage in Vascular Cognitive Impairment. 2009;40:S20–S23.
50. Brown WR, Moody DM, Thore CR, Challa VR. Apoptosis in Leukoaraiosis. *American Journal of Neuroradiology*. 2000;21:79–82.
51. Markus HS. Genes, endothelial function and cerebral small vessel disease in man. *Experimental Physiology*. 2008;93:121–127.
52. Iadecola C. The Neurovascular Unit Coming of Age: A Journey through Neurovascular Coupling in Health and Disease. *Neuron*. 2017;96:17–42.
53. Brown R, Benveniste H, Black SE, Charpak S, Dichgans M, Joutel A, Nedergaard M, Smith KJ, Zlokovic BV, Wardlaw JM. Understanding the role of the perivascular space in cerebral small vessel disease. *Cardiovasc Res*. 2018;114:1462–1473.
54. Mooradian AD. Effect of aging on the blood-brain barrier. *Neurobiology of Aging*. 1988;9:31–39.
55. Farrall AJ, Wardlaw JM. Blood–brain barrier: Ageing and microvascular disease – systematic review and meta-analysis. *Neurobiology of Aging*. 2009;30:337–352.
56. Wallin A, Sjögren M. Cerebrospinal fluid cytoskeleton proteins in patients with subcortical white-matter dementia. *Mechanisms of Ageing and Development*. 2001;122:1937–1949.
57. Lehmann M, Regland B, Blennow K, Gottfries CG. Vitamin B12-B6-Folate Treatment Improves Blood-Brain Barrier Function in Patients with Hyperhomocysteinaemia and Mild Cognitive Impairment. *DEM*. 2003;16:145–150.

58. Wallin A, Sjögren M, Edman Å, Blennow K, Regland B. Symptoms, Vascular Risk Factors and Blood-Brain Barrier Function in Relation to CT White-Matter Changes in Dementia. *ENE*. 2000;44:229–235.
59. Hanyu H, Asano T, Tanaka Y, Iwamoto T, Takasaki M, Abe K. Increased Blood-Brain Barrier Permeability in White Matter Lesions of Binswanger's Disease Evaluated by Contrast-Enhanced MRI. *DEM*. 2002;14:1–6.
60. Starr JM, Wardlaw J, Ferguson K, MacLulich A, Deary IJ, Marshall I. Increased blood–brain barrier permeability in type II diabetes demonstrated by gadolinium magnetic resonance imaging. *Journal of Neurology, Neurosurgery & Psychiatry*. 2003;74:70–76.
61. Wardlaw JM, Farrall A, Armitage PA, Carpenter T, Chappell F, Doubal F, Chowdhury D, Cvorovic V, Dennis MS. Changes in Background Blood–Brain Barrier Integrity Between Lacunar and Cortical Ischemic Stroke Subtypes. *Stroke*. 2008;39:1327–1332.
62. Wardlaw JM, Doubal F, Armitage P, Chappell F, Carpenter T, Muñoz Maniega S, Farrall A, Sudlow C, Dennis M, Dhillon B. Lacunar stroke is associated with diffuse blood-brain barrier dysfunction. *Ann Neurol*. 2009;65:194–202.
63. Akiguchi I, Tomimoto H, Suenaga T, Wakita H, Budka H. Blood-brain barrier dysfunction in Binswanger's disease; an immunohistochemical study. *Acta Neuropathol*. 1997;95:78–84.
64. Fredriksson K, Kalimo H, Nordborg C, Olsson Y, Johansson BB. Cyst formation and glial response in the brain lesions of stroke-prone spontaneously hypertensive rats. *Acta Neuropathol*. 1988;76:441–450.
65. Armao D, Kornfeld M, Estrada EY, Grossetete M, Rosenberg GA. Neutral proteases and disruption of the blood–brain barrier in rat. *Brain Research*. 1997;767:259–264.
66. Rajani RM, Quick S, Ruigrok SR, Graham D, Harris SE, Verhaaren BFJ, Fornage M, Seshadri S, Atanur SS, Dominiczak AF, et al. Reversal of endothelial dysfunction reduces white matter vulnerability in cerebral small vessel disease in rats. *Sci Transl Med*. 2018;10:eaam9507.
67. Huisa BN, Caprihan A, Thompson J, Prestopnik J, Qualls CR, Rosenberg GA. Long-Term Blood–Brain Barrier Permeability Changes in Binswanger Disease. *Stroke*. 2015;46:2413–2418.
68. Muñoz Maniega S, Chappell FM, Valdés Hernández MC, Armitage PA, Makin SD, Heye AK, Thrippleton MJ, Sakka E, Shuler K, Dennis MS, et al. Integrity of normal-appearing white matter: Influence of age, visible

- lesion burden and hypertension in patients with small-vessel disease. *J Cereb Blood Flow Metab.* 2017;37:644–656.
69. Wardlaw JM, Makin SJ, Valdés Hernández MC, Armitage PA, Heye AK, Chappell FM, Muñoz-Maniega S, Sakka E, Shuler K, Dennis MS, et al. Blood-brain barrier failure as a core mechanism in cerebral small vessel disease and dementia: evidence from a cohort study. *Alzheimers Dement.* 2017;13:634–643.
 70. Conijn M.M.A., Hoogduin J.M., van der Graaf Y., Hendrikse J., Luijten P.R., Geerlings M.I. Microbleeds, lacunar infarcts, white matter lesions and cerebrovascular reactivity - A 7T study. *NeuroImage.* 2012;59:950–956.
 71. Thomas BP, Liu P, Park DC, van Osch MJ, Lu H. Cerebrovascular Reactivity in the Brain White Matter: Magnitude, Temporal Characteristics, and Age Effects. *J Cereb Blood Flow Metab.* 2014;34:242–247.
 72. Blair GW, Thrippleton MJ, Shi Y, Hamilton I, Stringer M, Chappell F, Dickie DA, Andrews P, Marshall I, Doubal FN, et al. Intracranial hemodynamic relationships in patients with cerebral small vessel disease. *Neurology.* 2020;94:e2258–e2269.
 73. Hund-Georgiadis M, Zysset S, Naganawa S, Norris DG, Cramon DY von. Determination of Cerebrovascular Reactivity by Means of fMRI Signal Changes in Cerebral Microangiopathy: A Correlation with Morphological Abnormalities. *CED.* 2003;16:158–165.
 74. Yezhuvath US, Uh J, Cheng Y, Martin-Cook K, Weiner M, Diaz-Arrastia R, van Osch M, Lu H. Forebrain-dominant deficit in cerebrovascular reactivity in Alzheimer's disease. *Neurobiol Aging.* 2012;33:75–82.
 75. Shi Y, Thrippleton MJ, Blair GW, Dickie DA, Marshall I, Hamilton I, Doubal FN, Chappell F, Wardlaw JM. Small vessel disease is associated with altered cerebrovascular pulsatility but not resting cerebral blood flow. *J Cereb Blood Flow Metab.* 2020;40:85–99.
 76. Sam K, Conklin J, Poubanc J, Crawley AP, Sobczyk O, Mandell DM, Mikulis DJ, Venkatraghavan L, Duffin J, Fisher JA, et al. Development of White Matter Hyperintensity Is Preceded by Reduced Cerebrovascular Reactivity. *Ann. Neurol.* 2016;80:277–285.
 77. Davis TL, Kwong KK, Weisskoff RM, Rosen BR. Calibrated functional MRI: Mapping the dynamics of oxidative metabolism. 1998;95:1834–9.
 78. Hoge RD, Atkinson J, Gill B, Crelier GR, Marrett S, Pike GB. Investigation of BOLD signal dependence on cerebral blood flow and

- oxygen consumption: The deoxyhemoglobin dilution model. *Magnetic Resonance in Medicine*. 1999;42:849–863.
79. Grubb RL, Raichle ME, Eichling JO, Ter-Pogossian MM. The Effects of Changes in PaCO₂ Cerebral Blood Volume, Blood Flow, and Vascular Mean Transit Time. *Stroke*. 1974;5:630–639.
80. Gauthier C.J., Desjardins-Crepeau L., Madjar C., Bherer L., Hoge R.D. Absolute quantification of resting oxygen metabolism and metabolic reactivity during functional activation using QUO₂ MRI. *NeuroImage*. 2012;63:1353–1363.
81. van der Zwaag W, Francis S, Head K, Peters A, Gowland P, Morris P, Bowtell R. fMRI at 1.5, 3 and 7 T: Characterising BOLD signal changes. *NeuroImage*. 2009;47:1425–1434.
82. Liu P., Li Y., Pinho M., Park D.C., Welch B.G., Lu H. Cerebrovascular reactivity mapping without gas challenges. *NeuroImage*. 2017;146:320–326.
83. Liu P, De Vis JB, Lu H. Cerebrovascular reactivity (CVR) MRI with CO₂ challenge: A technical review. *NeuroImage*. 2019;187:104–115.
84. Fierstra J, Sobczyk O, Battisti-Charbonney A, Mandell DM, Poublanc J, Crawley AP, Mikulis DJ, Duffin J, Fisher JA. Measuring cerebrovascular reactivity: what stimulus to use? *J Physiol*. 2013;591:5809–5821.
85. Petersson J, Glenny RW. Gas exchange and ventilation–perfusion relationships in the lung. *European Respiratory Journal*. 2014;44:1023–1041.
86. Urback AL, MacIntosh BJ, Goldstein BI. Cerebrovascular reactivity measured by functional magnetic resonance imaging during breath-hold challenge: A systematic review. *Neuroscience & Biobehavioral Reviews*. 2017;79:27–47.
87. Slessarev M, Han J, Mardimae A, Prisman E, Preiss D, Volgyesi G, Ansel C, Duffin J, Fisher JA. Prospective targeting and control of end-tidal CO₂ and O₂ concentrations. *The Journal of Physiology*. 2007;581:1207–1219.
88. Vagal AS, Leach JL, Fernandez-Ulloa M, Zuccarello M. The Acetazolamide Challenge: Techniques and Applications in the Evaluation of Chronic Cerebral Ischemia. *American Journal of Neuroradiology*. 2009;30:876–884.
89. Siero J.C.W., Hartkamp N.S., Donahue M.J., Harteveld A.A., Compter A., Petersen E.T., Hendrikse J. Neuronal activation induced BOLD and

- CBF responses upon acetazolamide administration in patients with steno-occlusive artery disease. *NeuroImage*. 2015;105:276–285.
90. Tong Y., Bergethon P.R., Frederick B.D. An improved method for mapping cerebrovascular reserve using concurrent fMRI and near-infrared spectroscopy with Regressor Interpolation at Progressive Time Delays (RIPTiDe). *NeuroImage*. 2011;56:2047–2057.
 91. Poubanc J., Crawley A.P., Sobczyk O., Montandon G., Sam K., Mandell D.M., Duffin J., Venkatraghavan L., Mikulis D.J., et al. Measuring cerebrovascular reactivity: The dynamic response to a step hypercapnic stimulus. *J. Cereb. Blood Flow Metab.* 2015;35:1746–1756.
 92. Bhogal A.A., Philippens M.E.P., Siero J.C.W., Fisher J.A., Petersen E.T., Luijten P.R., Hoogduin H. Examining the regional and cerebral depth-dependent BOLD cerebrovascular reactivity response at 7T. *NeuroImage*. 2015;114:239–248.
 93. Blockley NP, Driver ID, Francis ST, Fisher JA, Gowland PA. An improved method for acquiring cerebrovascular reactivity maps. *Magnetic Resonance in Medicine*. 2011;65:1278–1286.
 94. Bhogal A.A., Siero J.C.W., Fisher J.A., Froeling M., Luijten P., Philippens M., Hoogduin H. Investigating the non-linearity of the BOLD cerebrovascular reactivity response to targeted hypo/hypercapnia at 7T. *NeuroImage*. 2014;98:296–305.
 95. Bhogal A.A., De Vis J.B., Siero J.C.W., Petersen E.T., Luijten P.R., Hendrikse J., Philippens M.E.P., Hoogduin H. The BOLD cerebrovascular reactivity response to progressive hypercapnia in young and elderly. *NeuroImage*. 2016;139:94–102.
 96. Bhogal AA, Sayin ES, Poubanc J, Duffin J, Fisher JA, Sobczyk O, Mikulis DJ. Quantifying cerebral blood arrival times using hypoxia-mediated arterial BOLD contrast [Internet]. 2022 [cited 2022 Jul 28];2022.03.27.485933. Available from: <https://www.biorxiv.org/content/10.1101/2022.03.27.485933v1>
 97. Champagne A.A., Bhogal A.A., Coverdale N.S., Mark C.I., Cook D.J. A novel perspective to calibrate temporal delays in cerebrovascular reactivity using hypercapnic and hyperoxic respiratory challenges. *NeuroImage*. 2019;187:154–165.
 98. Duffin J., Sobczyk O., McKetton L., Crawley A., Poubanc J., Venkatraghavan L., Sam K., Alan Mutch W., Mikulis D., Fisher J.A. Cerebrovascular resistance: The basis of cerebrovascular reactivity. *Front. Neurosci.* 2018;12:409.

99. McKetton L., Cohn M., Tang-Wai D.F., Sobczyk O., Duffin J., Holmes K.R., Poubanc J., Sam K., Crawley A.P., Venkatraghavan L., et al. Cerebrovascular resistance in healthy aging and mild cognitive impairment. *Front. Aging Neurosci.* 2019;11:79.
100. Yao J (Fiona), Yang H-C (Shawn), Wang JH, Liang Z, Talavage TM, Tamer GG, Jang I, Tong Y. A novel method of quantifying hemodynamic delays to improve hemodynamic response, and CVR estimates in CO₂ challenge fMRI. *J Cereb Blood Flow Metab.* 2021;0271678X20978582.
101. Sleight E, Stringer MS, Marshall I, Wardlaw JM, Thrippleton MJ. Cerebrovascular Reactivity Measurement Using Magnetic Resonance Imaging: A Systematic Review. *Front. Physiol.* 2021;12:643468.
102. Mandell D.M., Han J.S., Poubanc J., Crawley A.P., Stainsby J.A., Fisher J.A., Mikulis D.J. Mapping cerebrovascular reactivity using blood oxygen level-dependent MRI in patients with arterial steno-occlusive disease: Comparison with arterial spin labeling MRI. *Stroke.* 2008;39:2021–2028.
103. Chen JJ. Cerebrovascular-Reactivity Mapping Using MRI: Considerations for Alzheimer's Disease. *Front. Aging Neurosci.* 2018;10:170.
104. Ogasawara K, Ito H, Sasoh M, Okuguchi T, Kobayashi M, Yukawa H, Terasaki K, Ogawa A. Quantitative Measurement of Regional Cerebrovascular Reactivity to Acetazolamide Using 123I-N-Isopropyl-p-Iodoamphetamine Autoradiography with SPECT: Validation Study Using H215O with PET. *J Nucl Med.* 2003;44:520–525.
105. Marion D, Bouma G. The Use of Stable Xenon-Enhanced Computed Tomographic Studies of Cerebral Blood Flow to Define Changes in Cerebral Carbon Dioxide Vasoresponsivity Caused by a Severe Head Injury. *Neurosurgery.* 1991;29:869–873.
106. Purkayastha S, Sorond F. Transcranial Doppler Ultrasound: Technique and Application. *Semin Neurol.* 2012;32:411–420.
107. McDonnell MN, Berry NM, Cutting MA, Keage HA, Buckley JD, Howe PRC. Transcranial Doppler ultrasound to assess cerebrovascular reactivity: reliability, reproducibility and effect of posture. *Peerj.* 2013;1:65.
108. Valdueza JM, Balzer JO, Villringer A, Vogl TJ, Kutter R, Einhaupl KM. Changes in blood flow velocity and diameter of the middle cerebral artery during hyperventilation: assessment with MR and transcranial Doppler sonography. *AJNR Am J Neuroradiol.* 1997;18:1929–34.

109. Noth U, Kotajima F, Deichmann R, Turner R, Corfield DR. Mapping of the cerebral vascular response to hypoxia and hypercapnia using quantitative perfusion MRI at 3 T. *NMR Biomed.* 2008;21:464–72.
110. Donahue MJ, van Laar PJ, van Zijl PCM, Stevens RD, Hendrikse J. Vascular space occupancy (VASO) cerebral blood volume-weighted MRI identifies hemodynamic impairment in patients with carotid artery disease. *J Magn Reson Imaging.* 2009;29:718–24.
111. Taneja K., Lu H., Welch B.G., Thomas B.P., Pinho M., Lin D., Hillis A.E., Liu P. Evaluation of cerebrovascular reserve in patients with cerebrovascular diseases using resting-state MRI: A feasibility study. *Magn. Reson. Imaging.* 2019;59:46–52.
112. Donahue MJ, Ayad M, Moore R, van Osch M, Singer R, Clemmons P, Strother M. Relationships between hypercarbic reactivity, cerebral blood flow, and arterial circulation times in patients with moyamoya disease. *J Magn Reson Imaging.* 2013;38:1129–39.
113. Wu J., Dehkharghani S., Nahab F., Qiu D. Acetazolamide-augmented dynamic BOLD (aczBOLD) imaging for assessing cerebrovascular reactivity in chronic steno-occlusive disease of the anterior circulation: An initial experience. *NeuroImage Clin.* 2017;13:116–122.
114. Thrippleton M.J., Shi Y., Blair G., Hamilton I., Waiter G., Schwarzbauer C., Pernet C., Andrews P.J.D., Marshall I., Doubal F., et al. Cerebrovascular reactivity measurement in cerebral small vessel disease: Rationale and reproducibility of a protocol for MRI acquisition and image processing. *Int. J. Stroke.* 2018;13:195–206.
115. Donahue M.J., Strother M.K., Lindsey K.P., Hocke L.M., Tong Y., Frederick B.D.B. Time delay processing of hypercapnic fMRI allows quantitative parameterization of cerebrovascular reactivity and blood flow delays. *J. Cereb. Blood Flow Metab.* 2016;36:1767–1779.
116. Ziyeh S., Rick J., Reinhard M., Hetzel A., Mader I., Speck O. Blood oxygen level-dependent MRI of cerebral CO₂ reactivity in severe carotid stenosis and occlusion. *Stroke.* 2005;36:751–756.
117. Germuska M., Chandler H.L., Stickland R.C., Foster C., Fasano F., Okell T.W., Steventon J., Tomassini V., Murphy K., Wise R.G. Dual-calibrated fMRI measurement of absolute cerebral metabolic rate of oxygen consumption and effective oxygen diffusivity. *NeuroImage.* 2019;184:717–728.
118. Duffin J., Sobczyk O., Crawley A.P., Poublanc J., Mikulis D.J., Fisher J.A. The dynamics of cerebrovascular reactivity shown with transfer function analysis. *NeuroImage.* 2015;114:207–16.

119. Kannurpatti SS, Motes MA, Biswal BB, Rypma B. Assessment of unconstrained cerebrovascular reactivity marker for large age-range fMRI studies. *PLoS ONE*. 2014;9:e88751.
120. Jahanian H, Christen T, Moseley ME, Pajewski NM, Wright CB, Tamura MK, Zaharchuk G, SPRINT Study Research Group. Measuring vascular reactivity with resting-state blood oxygenation level-dependent (BOLD) signal fluctuations: A potential alternative to the breath-holding challenge?. *J Cereb Blood Flow Metab*. 2017;37:2526–2538.
121. Pillai JJ, Mikulis DJ. Cerebrovascular Reactivity Mapping: An Evolving Standard for Clinical Functional Imaging. *American Journal of Neuroradiology*. 2015;36:7–13.
122. Moreton FC, Dani KA, Goutcher C, O'Hare K, Muir KW. Respiratory challenge MRI: Practical aspects. *Neuroimage Clin*. 2016;11:667–677.
123. Fisher Joseph A., Venkatraghavan Lashmi, Mikulis David J. Magnetic Resonance Imaging–Based Cerebrovascular Reactivity and Hemodynamic Reserve. *Stroke*. 2018;49:2011–2018.
124. Spano VR, Mandell DM, Poubanc J, Sam K, Battisti-Charbonney A, Pucci O, Han JS, Crawley AP, Fisher JA, Mikulis DJ. CO₂ blood oxygen level-dependent MR mapping of cerebrovascular reserve in a clinical population: safety, tolerability, and technical feasibility. *Radiology*. 2013;266:592–598.
125. Krainik A., Hund-Georgiadis M., Zysset S., Von Cramon D.Y. Regional impairment of cerebrovascular reactivity and BOLD signal in adults after stroke. *Stroke*. 2005;36:1146–1152.
126. da Costa L, van Niftrik CB, Crane D, Fierstra J, Bethune A. Temporal Profile of Cerebrovascular Reactivity Impairment, Gray Matter Volumes, and Persistent Symptoms after Mild Traumatic Head Injury. *Front Neurol*. 2016;7:70.
127. Hartkamp N.S., Petersen E.T., Chappell M.A., Okell T.W., Uyttenboogaart M., Zeebregts C.J., Bokkers R.P.H. Relationship between haemodynamic impairment and collateral blood flow in carotid artery disease. *J. Cereb. Blood Flow Metab*. 2018;38:2021–2032.
128. Hartkamp NS, Hendrikse J, van der Worp HB, de Borst GJ, Bokkers RPH. Time course of vascular reactivity using repeated phase-contrast MR angiography in patients with carotid artery stenosis. *Stroke*. 2012;43:553–6.
129. Atwi S., Shao H., Crane D.E., da Costa L., Aviv R.I., Mikulis D.J., Black S.E., MacIntosh B.J. BOLD-based cerebrovascular reactivity vascular

- transfer function isolates amplitude and timing responses to better characterize cerebral small vessel disease. *NMR Biomed.* 2019;32:e4064.
130. Holmes K.R., Tang-Wai D., Sam K., Mcketton L., Poubanc J., Crawley A.P., Sobczyk O., Cohn M., Duffin J., Tartaglia M.C., et al. Slowed Temporal and Parietal Cerebrovascular Response in Patients with Alzheimer's Disease. *Can. J. Neurol. Sci.* 2020;47:366–373.
 131. Driver I., Blockley N., Fisher J., Francis S., Gowland P. The change in cerebrovascular reactivity between 3 T and 7 T measured using graded hypercapnia. *NeuroImage.* 2010;51:274–279.
 132. Triantafyllou C., Wald L.L., Hoge R.D. Echo-time and field strength dependence of BOLD reactivity in veins and parenchyma using flow-normalized hypercapnic manipulation. *PLoS ONE.* 2011;6:e24519.
 133. Peng S.-L., Yang H.-C., Chen C.-M., Shih C.-T. Short- and long-term reproducibility of BOLD signal change induced by breath-holding at 1.5 and 3 T. *NMR Biomed.* 2020;33:e4195.
 134. Noth U, Meadows GE, Kotajima F, Deichmann R, Corfield DR, Turner R. Cerebral vascular response to hypercapnia: determination with perfusion MRI at 1.5 and 3.0 Tesla using a pulsed arterial spin labeling technique. *J Magn Reson Imaging.* 2006;24:1229–35.
 135. Inoue Y., Tanaka Y., Hata H., Hara T. Arterial spin-labeling evaluation of cerebrovascular reactivity to acetazolamide in healthy subjects. *Am. J. Neuroradiol.* 2014;35:1111–1116.
 136. Winter J.D., Poubanc J., Crawley A.P., Kassner A. Comparison of Spiral Imaging and SENSE-EPI at 1.5 and 3.0 T Using a Controlled Cerebrovascular Challenge. *J. Magn. Reson. Imaging.* 2009;29:1206–1210.
 137. Ravi H., Liu P., Peng S.-L., Liu H., Lu H. Simultaneous multi-slice (SMS) acquisition enhances the sensitivity of hemodynamic mapping using gas challenges. *NMR Biomed.* 2016;29:1511–1518.
 138. Cohen A.D., Wang Y. Improving the Assessment of Breath-Holding Induced Cerebral Vascular Reactivity Using a Multiband Multi-echo ASL/BOLD Sequence. *Sci Rep.* 2019;9:5079.
 139. Sobczyk O., Battisti-Charbonney A., Fierstra J., Mandell D.M., Poubanc J., Crawley A.P., Mikulis D.J., Duffin J., Fisher J.A. A conceptual model for CO₂-induced redistribution of cerebral blood flow with experimental confirmation using BOLD MRI. *NeuroImage.* 2014;92:56–68.

140. Mutch W.A.C., Mandell D.M., Fisher J.A., Mikulis D.J., Crawley A.P., Pucci O., Duffin J. Approaches to Brain Stress Testing: BOLD Magnetic Resonance Imaging with Computer-Controlled Delivery of Carbon Dioxide. *PLoS ONE*. 2012;7:e47443.
141. Sobczyk O., Battisti-Charbonney A., Poublanc J., Crawley A.P., Sam K., Fierstra J., Mandell D.M., Mikulis D.J., Duffin J., Fisher J.A. Assessing cerebrovascular reactivity abnormality by comparison to a reference atlas. *J. Cereb. Blood Flow Metab.* 2015;35:213–220.
142. Fisher J.A., Sobczyk O., Crawley A., Poublanc J., Dufort P., Venkatraghavan L., Sam K., Mikulis D., Duffin J. Assessing cerebrovascular reactivity by the pattern of response to progressive hypercapnia. *Hum. Brain Mapp.* 2017;38:3415–3427.
143. Sam K., Poublanc J., Sobczyk O., Han J.S., Battisti-Charbonney A., Mandell D.M., Tymianski M., Crawley A.P., Fisher J.A., Mikulis D.J. Assessing the effect of unilateral cerebral revascularisation on the vascular reactivity of the non-intervened hemisphere: A retrospective observational study. *BMJ Open*. 2015;5:e006014.
144. Thomas B, Logan W, Donner EJ, Shroff M. Assessment of cerebrovascular reactivity using real-time BOLD fMRI in children with moyamoya disease: a pilot study. *Childs Nerv Syst.* 2013;29:457–463.
145. Dlamini N., Shah-Basak P., Leung J., Kirkham F., Shroff M., Kassner A., Robertson A., Dirks P., Westmacott R., De Veber G., et al. Breath-hold blood oxygen level-dependent MRI: A tool for the assessment of cerebrovascular reserve in children with moyamoya disease. *Am. J. Neuroradiol.* 2018;39:1717–1723.
146. De Vis J.B., Petersen E.T., Bhogal A., Hartkamp N.S., Klijn C.J.M., Kappelle L.J., Hendrikse J. Calibrated MRI to evaluate cerebral hemodynamics in patients with an internal carotid artery occlusion. *J. Cereb. Blood Flow Metab.* 2015;35:1015–1023.
147. Goode S.D., Altaf N., Auer D.P., MacSweeney S.T.R. Carotid Endarterectomy Improves Cerebrovascular Reserve Capacity Preferentially in Patients with Preoperative Impairment as Indicated by Asymmetric BOLD Response to Hypercapnia. *Eur. J. Vasc. Endovasc. Surg.* 2009;38:546–551.
148. Federau C., Christensen S., Zun Z., Park S.-W., Ni W., Moseley M., Zaharchuk G. Cerebral blood flow, transit time, and apparent diffusion coefficient in moyamoya disease before and after acetazolamide. *Neuroradiology*. 2017;59:5–12.

149. Herrera CRC, Beltramini GC, Avelar WM, Lima FO, Li LM. Cerebral vasomotor reactivity assessment using Transcranial Doppler and MRI with apnea test. *Braz. J. Med. Biol. Res.* 2016;49.
150. Hartkamp N.S., Bokkers R.P.H., van Osch M.J.P., de Borst G.J., Hendrikse J. Cerebrovascular reactivity in the caudate nucleus, lentiform nucleus and thalamus in patients with carotid artery disease. *J. Neuroradiol.* 2017;44:143–150.
151. Dlamini N, Yau I, Westmacott R, Shroff M, Armstrong D, Logan W, Mikulis D, deVeber G, Kassner A. Cerebrovascular Reactivity and Intellectual Outcome in Childhood Stroke With Transient Cerebral Arteriopathy. *Pediatr Neurol.* 2017;69:71–78.
152. Bokkers R.P.H., Van Osch M.J.P., Klijn C.J.M., Kappelle L.J., Hendrikse J. Cerebrovascular reactivity within perfusion territories in patients with an internal carotid artery occlusion. *J. Neurol. Neurosurg. Psychiatry.* 2011;82:1011–1016.
153. Uchihashi Y., Hosoda K., Zimine I., Fujita A., Fujii M., Sugimura K., Kohmura E. Clinical application of arterial spin-labeling MR imaging in patients with carotid stenosis: Quantitative comparative study with single-photon emission CT. *Am. J. Neuroradiol.* 2011;32:1545–1551.
154. Calviere L., Catalaa I., Marlats F., Viguier A., Bonneville F., Cognard C., Larrue V. Correlation between cognitive impairment and cerebral hemodynamic disturbances on perfusion magnetic resonance imaging in European adults with moyamoya disease: Clinical article. *J. Neurosurg.* 2010;113:753–759.
155. Chang T-Y, Liu H-L, Lee T-H, Kuan W-C, Chang C-H, Wu H-C, Wu T-C, Chang Y-J. Change in Cerebral Perfusion after Carotid Angioplasty with Stenting Is Related to Cerebral Vasoreactivity: A Study Using Dynamic Susceptibility-Weighted Contrast-Enhanced MR Imaging and Functional MR Imaging with a Breath-Holding Paradigm. *AJNR Am J Neuroradiol.* 2009;30:1330–1336.
156. Waddle S.L., Juttukonda M.R., Lants S.K., Davis L.T., Chitale R., Fusco M.R., Jordan L.C., Donahue M.J. Classifying intracranial stenosis disease severity from functional MRI data using machine learning. *J. Cereb. Blood Flow Metab.* 2019;40:705–719.
157. Watchmaker J.M., Frederick B.D., Fusco M.R., Davis L.T., Juttukonda M.R., Lants S.K., Kirshner H.S., Donahue M.J. Clinical use of cerebrovascular compliance imaging to evaluate revascularization in patients with moyamoya. *Clin. Neurosurgery.* 2019;84:261–271.

158. Faraco C.C., Strother M.K., Dethrage L.M., Jordan L., Singer R., Clemmons P.F., Donahue M.J. Dual echo vessel-encoded ASL for simultaneous BOLD and CBF reactivity assessment in patients with ischemic cerebrovascular disease. *Magn. Reson. Med.* 2015;73:1579–1592.
159. Strother M.K., Buckingham C., Faraco C.C., Arteaga D.F., Lu P., Xu Y., Donahue M.J. Crossed cerebellar diaschisis after stroke identified noninvasively with cerebral blood flow-weighted arterial spin labeling MRI. *Eur. J. Radiol.* 2016;85:136–142.
160. Kim H.J., Kim T.W., Ryu S.-Y., Yang P.S., Kwon M.J., Kim J.C., Lee Y.S., Lee H.J., Yang J.H., Kim J.K., et al. Acetazolamide-challenged perfusion magnetic resonance imaging for assessment of cerebrovascular reserve capacity in patients with symptomatic middle cerebral artery stenosis: Comparison with technetium-99m-hexamethylpropyleneamine oxime single-photon emission computed tomography. *Clin. Imaging.* 2011;35:413–420.
161. Hu H.H., Li Z., Pokorney A.L., Chia J.M., Stefani N., Pipe J.G., Miller J.H. Assessment of cerebral blood perfusion reserve with acetazolamide using 3D spiral ASL MRI: Preliminary experience in pediatric patients. *Magn. Reson. Imaging.* 2017;35:132–140.
162. Griffiths P.D., Gaines P., Cleveland T., Beard J., Venables G., Wilkinson I.D. Assessment of cerebral haemodynamics and vascular reserve in patients with symptomatic carotid artery occlusion: An integrated MR method. *Neuroradiology.* 2005;47:175–182.
163. Sebok M., Van Niftrik C.H.B., Piccirelli M., Bozinov O., Wegener S., Esposito G., Pangalu A., Valavanis A., Buck A., Luft A.R., et al. Bold cerebrovascular reactivity as a novel marker for crossed cerebellar diaschisis. *Neurology.* 2018;91:E1328–E1337.
164. Schreiber WG, Guckel F, Stritzke P, Schmiedek P, Schwartz A, Brix G. Cerebral blood flow and cerebrovascular reserve capacity: estimation by dynamic magnetic resonance imaging. *J Cereb Blood Flow Metab.* 1998;18:1143–56.
165. De Vis J.B., Bhogal A.A., Hendrikse J., Petersen E.T., Siero J.C.W. Effect sizes of BOLD CVR, resting-state signal fluctuations and time delay measures for the assessment of hemodynamic impairment in carotid occlusion patients. *NeuroImage.* 2018;179:530–539.
166. Shiino A., Morita Y., Tsuji A., Maeda K., Ito R., Furukawa A., Matsuda M., Inubushi T. Estimation of cerebral perfusion reserve by blood oxygenation level-dependent imaging: Comparison with single-photon

- emission computed tomography. *J. Cereb. Blood Flow Metab.* 2003;23:121–135.
167. van Niftrik CHB, Piccirelli M, Bozinov O, Pangalu A, Valavanis A, Regli L, Fierstra J. Fine tuning breath-hold-based cerebrovascular reactivity analysis models. *Brain Behav.* 2016;6:e00426.
168. Chang T-Y, Kuan W-C, Huang K-L, Chang C-H, Chang Y-J, Wong H-F, Lee T-H, Liu H-L. Heterogeneous cerebral vasoreactivity dynamics in patients with carotid stenosis. *PLoS ONE.* 2013;8:e76072.
169. Hauser T-K, Seeger A, Bender B, Klose U, Thurow J, Ernemann U, Tatagiba M, Meyer PT, Khan N, Roder C. Hypercapnic BOLD MRI compared to H215O PET/CT for the hemodynamic evaluation of patients with Moyamoya Disease. *Neuroimage (Amst).* 2019;22:101713.
170. Han J.S., Abou-Hamden A., Mandell D.M., Poublanc J., Crawley A.P., Fisher J.A., Mikulis D.J., Tymianski M. Impact of extracranial-intracranial bypass on cerebrovascular reactivity and clinical outcome in patients with symptomatic moyamoya vasculopathy. *Stroke.* 2011;42:3047–3054.
171. Papassin J., Heck O., Condamine E., Pietras J., Detante O., Krainik A. Impaired cerebrovascular reactivity is associated with recurrent stroke in patients with severe intracranial arterial stenosis: A CO₂ BOLD fMRI study. *J. Neuroradiol.* 2020;48:339–345.
172. Goode S.D., Altaf N., Munshi S., MacSweeney S.T.R., Auer D.P. Impaired cerebrovascular reactivity predicts recurrent symptoms in patients with carotid artery occlusion: A hypercapnia BOLD fMRI study. *Am. J. Neuroradiol.* 2016;37:904–909.
173. Hartkamp N.S., Hendrikse J., de Borst G.J., Kappelle L.J., Bokkers R.P.H. Intracerebral steal phenomenon in symptomatic carotid artery disease. *J. Neuroradiol.* 2019;46:173–178.
174. Para A.E., Sam K., Poublanc J., Fisher J.A., Crawley A.P., Mikulis D.J. Invalidation of fMRI experiments secondary to neurovascular uncoupling in patients with cerebrovascular disease. *J. Magn. Reson. Imaging.* 2017;46:1448–1455.
175. Rosen C, McKetton L, Russell J, Sam K, Poublanc J, Crawley A, Han JS, Sobczyk O, Duffin J, Mandell DM, et al. Long-term changes in cerebrovascular reactivity following EC-IC bypass for intracranial stenocclusive disease. *J Clin Neurosci.* 2018;54:77–82.
176. Conklin J., Fierstra J., Crawley A.P., Han J.S., Poublanc J., Silver F.L., Tymianski M., Fisher J.A., Mandell D.M., Mikulis D.J. Mapping white

- matter diffusion and cerebrovascular reactivity in carotid occlusive disease. *Neurology*. 2011;77:431–438.
177. Venkatraghavan L., Poubanc J., Han J.S., Sobczyk O., Rozen C., Sam K., Duffin J., Mikulis D.J., Fisher J.A. Measurement of Cerebrovascular Reactivity as Blood Oxygen Level-Dependent Magnetic Resonance Imaging Signal Response to a Hypercapnic Stimulus in Mechanically Ventilated Patients. *J. Stroke Cerebrovasc. Dis.* 2018;27:301–308.
178. Han J.S., Mikulis D.J., Mardimae A., Kassner A., Poubanc J., Crawley A.P., Deveber G.A., Fisher J.A., Logan W.J. Measurement of cerebrovascular reactivity in pediatric patients with cerebral vasculopathy using blood oxygen level-dependent MRI. *Stroke*. 2011;42:1261–1269.
179. Liu P., Welch B.G., Li Y., Gu H., King D., Yang Y., Pinho M., Lu H. Multiparametric imaging of brain hemodynamics and function using gas-inhalation MRI. *NeuroImage*. 2017;146:715–723.
180. Noguchi T, Kawashima M, Nishihara M, Egashira Y, Azama S, Irie H. Noninvasive method for mapping CVR in moyamoya disease using ASL-MRI. *Eur J Radiol*. 2015;84:1137–43.
181. Ma J., Mehrkens J.H., Holtmannspoetter M., Linke R., Schmid-Elsaesser R., Steiger H.-J., Brueckmann H., Bruening R. Perfusion MRI before and after acetazolamide administration for assessment of cerebrovascular reserve capacity in patients with symptomatic internal carotid artery (ICA) occlusion: Comparison with 99mTc-ECD SPECT. *Neuroradiology*. 2007;49:317–326.
182. Ladner T.R., Donahue M.J., Arteaga D.F., Faraco C.C., Roach B.A., Davis L.T., Jordan L.C., Froehler M.T., Strother M.K. Prior Infarcts, Reactivity, and Angiography in Moyamoya Disease (PIRAMD): A scoring system for moyamoya severity based on multimodal hemodynamic imaging. *J. Neurosurg*. 2017;126:495–503.
183. Mandell DM, Han JS, Poubanc J, Crawley AP, Fierstra J, Tymianski M, Fisher JA, Mikulis DJ. Quantitative measurement of cerebrovascular reactivity by blood oxygen level-dependent MR imaging in patients with intracranial stenosis: preoperative cerebrovascular reactivity predicts the effect of extracranial-intracranial bypass surgery. *AJNR Am J Neuroradiol*. 2011;32:721–7.
184. Haller S., Bonati L.H., Rick J., Klarhofer M., Speck O., Lyrer P.A., Bilecen D., Engelter S.T., Wetzel S.G. Reduced cerebrovascular reserve at CO₂ BOLD MR imaging is associated with increased risk of periinterventional ischemic lesions during carotid endarterectomy or stent placement: Preliminary results. *Radiology*. 2008;249:251–258.

185. Bouvier J., Detante O., Tahon F., Attye A., Perret T., Chechin D., Barbieux M., Boubagra K., Garambois K., Tropres I., et al. Reduced CMRO₂ and cerebrovascular reserve in patients with severe intracranial arterial stenosis: A combined multiparametric qBOLD oxygenation and BOLD fMRI study. *Hum. Brain Mapp.* 2015;36:695–706.
186. Sam K., Small E., Poubanc J., Han J.S., Mandell D.M., Fisher J.A., Crawley A.P., Mikulis D.J. Reduced contralateral cerebrovascular reserve in patients with unilateral steno-occlusive disease. *Cerebrovasc. Dis.* 2014;38:94–100.
187. Fierstra J, van Niftrik C, Warnock G, Wegener S, Piccirelli M, Pangalu A, Esposito G, Valavanis A, Buck A, Luft A, et al. Staging Hemodynamic Failure With Blood Oxygen-Level-Dependent Functional Magnetic Resonance Imaging Cerebrovascular Reactivity: A Comparison Versus Gold Standard (15O-)H₂O-Positron Emission Tomography. *Stroke.* 2018;49:621–629.
188. Ohnishi T., Nakano S., Yano T., Hoshi H., Jinnouchi S., Nagamachi S., Flores II L., Watanabe K., Yokogami K., Ohta H. Susceptibility-weighted MR for evaluation of vasodilatory capacity with acetazolamide challenge. *AM. J. NEURORADIOL.* 1996;17:631–637.
189. Hamzei F., Knab R., Weiller C., Rother J. The influence of extra- and intracranial artery disease on the BOLD signal in FMRI. *NeuroImage.* 2003;20:1393–1399.
190. Duffin J, Sobczyk O, Crawley A, Poubanc J, Venkatraghavan L, Sam K, Mutch A, Mikulis D, Fisher J. The role of vascular resistance in BOLD responses to progressive hypercapnia. *Hum Brain Mapp.* 2017;38:5590–5602.
191. Donahue MJ, Dethrage LM, Faraco CC, Jordan LC, Clemmons P, Singer R, Mocco J, Shyr Y, Desai A, O'Duffy A, et al. Routine Clinical Evaluation of Cerebrovascular Reserve Capacity Using Carbogen in Patients With Intracranial Stenosis. *Stroke.* 2014;45:2335–2341.
192. Poubanc J, Han JS, Mandell DM, Conklin J, Stainsby JA, Fisher JA, Mikulis DJ, Crawley AP. Vascular Steal Explains Early Paradoxical Blood Oxygen Level-Dependent Cerebrovascular Response in Brain Regions with Delayed Arterial Transit Times. *Cerebrovasc Dis Extra.* 2013;3:55–64.
193. Guckel F., Brix G., Schmiedek P., Piepgras A., Rempp K., Kopke J., Lammler B., Georgi M. Noninvasive quantification of regional cerebral blood flow and blood volume with dynamic MR-imaging. Preliminary results in volunteers and patients with cerebrovascular disorders. *RADIOLOGE.* 1995;35:791–800.

194. Piepgras A, Guckel F, Lammler B, Weigel R, Schmiedek P. [Noninvasive diagnosis of cerebral ischemia with nuclear magnetic resonance tomography and near infrared spectroscopy]. *Radiologe*. 1994;34:627–31.
195. Sobczyk O., Crawley A.P., Poubanc J., Sam K., Mandell D.M., Mikulis D.J., Duffin J., Fisher J.A. Identifying significant changes in cerebrovascular reactivity to carbon dioxide. *Am. J. Neuroradiol*. 2016;37:818–824.
196. Richiardi J., Monsch A.U., Haas T., Barkhof F., Van de Ville D., Radu E.W., Kressig R.W., Haller S. Altered cerebrovascular reactivity velocity in mild cognitive impairment and Alzheimer's disease. *Neurobiol. Aging*. 2015;36:33–41.
197. Lajoie I., Nugent S., Debacker C., Dyson K., Tancredi F.B., Badhwar A., Belleville S., Deschaintre Y., Bellec P., Doyon J., et al. Application of calibrated fMRI in Alzheimer's disease. *NeuroImage Clin*. 2017;15:348–358.
198. Cantin S, Villien M, Moreaud O, Tropres I, Keignart S, Chipon E, Le Bas J-F, Warnking J, Krainik A. Impaired cerebral vasoreactivity to CO₂ in Alzheimer's disease using BOLD fMRI. *Neuroimage*. 2011;58:579–87.
199. Suri S, Mackay CE, Kelly ME, Germuska M, Tunbridge EM, Frisoni GB, Matthews PM, Ebmeier KP, Bulte DP, Filippini N. Reduced cerebrovascular reactivity in young adults carrying the APOE epsilon4 allele. *Alzheimer's dement*. 2015;11:648–57.e1.
200. Gao Y-Z, Zhang J-J, Liu H, Wu G-Y, Xiong L, Shu M. Regional cerebral blood flow and cerebrovascular reactivity in Alzheimer's disease and vascular dementia assessed by arterial spinlabeling magnetic resonance imaging. *Curr Neurovasc Res*. 2013;10:49–53.
201. Haight TJ, Bryan RN, Erus G, Davatzikos C, Jacobs DR, D'Esposito M, Lewis CE, Launer LJ. Vascular risk factors, cerebrovascular reactivity, and the default-mode brain network. *Neuroimage*. 2015;115:7–16.
202. De Vis J.B., Hendrikse J., Bhogal A., Adams A., Kappelle L.J., Petersen E.T. Age-related changes in brain hemodynamics; A calibrated MRI study. *Hum. Brain Mapp*. 2015;36:3973–3987.
203. Liu P, Hebrank AC, Rodrigue KM, Kennedy KM, Section J, Park DC, Lu H. Age-related differences in memory-encoding fMRI responses after accounting for decline in vascular reactivity. *Neuroimage*. 2013;78:415–425.

204. Leoni R.F., Oliveira I.A.F., Pontes-Neto O.M., Santos A.C., Leite J.P. Cerebral blood flow and vasoreactivity in aging: An arterial spin labeling study. *Braz. J. Med. Biol. Res.* 2017;50:e5670.
205. Catchlove S.J., Parrish T.B., Chen Y., Macpherson H., Hughes M.E., Pipingas A. Regional Cerebrovascular Reactivity and Cognitive Performance in Healthy Aging. *J. Exp. Neurosci.* [Internet]. 2018;12. Available from: <http://www.la-press.com/journal-of-experimental-neuroscience-j131>
206. Riecker A., Grodd W., Klose U., Schulz J.B., Groschel K., Erb M., Ackermann H., Kastrup A. Relation between regional functional MRI activation and vascular reactivity to carbon dioxide during normal aging. *J. Cereb. Blood Flow Metab.* 2003;23:565–573.
207. Miller KB, Howery AJ, Rivera-Rivera LA, Johnson SC, Rowley HA, Wieben O, Barnes JN. Age-Related Reductions in Cerebrovascular Reactivity Using 4D Flow MRI. *Front. Aging Neurosci.* 2019;11:281.
208. Liem M.K., Lesnik Oberstein S.A.J., Haan J., Boom R.V.D., Ferrari M.D., Buchem M.A.V., Grond J.V.D. Cerebrovascular reactivity is a main determinant of white matter hyperintensity progression in CADASIL. *Am. J. Neuroradiol.* 2009;30:1244–1247.
209. Tchistiakova E., Crane D.E., Mikulis D.J., Anderson N.D., Greenwood C.E., Black S.E., MacIntosh B.J. Vascular risk factor burden correlates with cerebrovascular reactivity but not resting state coactivation in the default mode network. *J. Magn. Reson. Imaging.* 2015;42:1369–1376.
210. Sam K., Conklin J., Holmes K.R., Sobczyk O., Poublanc J., Crawley A.P., Mandell D.M., Venkatraghavan L., Duffin J., Fisher J.A., et al. Impaired dynamic cerebrovascular response to hypercapnia predicts development of white matter hyperintensities. *NeuroImage Clin.* 2016;11:796–801.
211. Sam K., Peltenburg B., Conklin J., Sobczyk O., Poublanc J., Crawley A.P., Mandell D.M., Venkatraghavan L., Duffin J., Fisher J.A., et al. Cerebrovascular reactivity and white matter integrity. *Neurology.* 2016;87:2333–2339.
212. Coverdale N.S., Fernandez-Ruiz J., Champagne A.A., Mark C.I., Cook D.J. Co-localized impaired regional cerebrovascular reactivity in chronic concussion is associated with BOLD activation differences during a working memory task. *Brain Imaging Behav.* 2020;14:2438–2449.
213. Champagne A.A., Coverdale N.S., Fernandez-Ruiz J., Mark C.I., Cook D.J. Compromised resting cerebral metabolism after sport-related

- p>concussion: A calibrated MRI study.
- Brain Imaging Behav.*
- 2020;15:133–146.
214. Svaldi D.O., Joshi C., McCuen E.C., Music J.P., Hannemann R., Leverenz L.J., Nauman E.A., Talavage T.M. Accumulation of high magnitude acceleration events predicts cerebrovascular reactivity changes in female high school soccer athletes. *Brain Imaging Behav.* 2020;14:164–174.
 215. Mutch W.A.C., Ellis M.J., Ryner L.N., Morissette M.P., Pries P.J., Dufault B., Essig M., Mikulis D.J., Duffin J., Fisher J.A. Longitudinal brain magnetic resonance imaging CO2 stress testing in individual adolescent sports-related concussion patients: A pilot study. *Front. Neurol.* 2016;7:107.
 216. Champagne A.A., Coverdale N.S., Germuska M., Cook D.J. Multi-parametric analysis reveals metabolic and vascular effects driving differences in BOLD-based cerebrovascular reactivity associated with a history of sport concussion. *Brain Inj.* 2019;33:1479–1489.
 217. Mutch W.A.C., Ellis M.J., Ryner L.N., McDonald P.J., Morissette M.P., Pries P., Essig M., Mikulis D.J., Duffin J., Fisher J.A. Patient-specific alterations in CO2 cerebrovascular responsiveness in acute and sub-acute sports-related concussion. *Front. Neurol.* 2018;9:23.
 218. Champagne AA, Coverdale NS, Nashed JY, Fernandez-Ruiz J, Cook DJ. Resting CMRO2 fluctuations show persistent network hyper-connectivity following exposure to sub-concussive collisions. *Neuroimage (Amst).* 2019;22:101753.
 219. Buterbaugh J, Wynstra C, Provencio N, Combs D, Gilbert M, Parthasarathy S. Cerebrovascular reactivity in young subjects with sleep apnea. *Sleep.* 2015;38:241–250.
 220. Thiel S., Lettau F., Rejmer P., Rossi C., Haile S.R., Schwarz E.I., Stoberl A.S., Sievi N.A., Boss A., Becker A.S., et al. Effects of short-term continuous positive airway pressure withdrawal on cerebral vascular reactivity measured by blood oxygen level-dependent magnetic resonance imaging in obstructive sleep apnoea: a randomised controlled trial. *Eur. Respir. J.* 2019;53.
 221. Ryan C.M., Battisti-Charbonney A., Sobczyk O., Mikulis D.J., Duffin J., Fisher J.A., Venkatraghavan L. Evaluation of Cerebrovascular Reactivity in Subjects with and without Obstructive Sleep Apnea. *J. Stroke Cerebrovasc. Dis.* 2018;27:162–168.

222. Ponsaing L.B., Lindberg U., Rostrup E., Iversen H.K., Larsson H.B.W., Jennum P. Impaired cerebrovascular reactivity in obstructive sleep apnea: a case-control study. *Sleep Med.* 2018;43:7–13.
223. Wu P.-H., Rodriguez-Soto A.E., Rodgers Z.B., Englund E.K., Wiemken A., Langham M.C., Detre J.A., Schwab R.J., Guo W., Wehrli F.W. MRI evaluation of cerebrovascular reactivity in obstructive sleep apnea. *J. Cereb. Blood Flow Metab.* 2020;40:1328–1337.
224. Raut R.V., Nair V.A., Sattin J.A., Prabhakaran V. Hypercapnic evaluation of vascular reactivity in healthy aging and acute stroke via functional MRI. *NeuroImage Clin.* 2016;12:173–179.
225. Geranmayeh F., Wise R.J.S., Leech R., Murphy K. Measuring vascular reactivity with breath-holds after stroke: A method to aid interpretation of group-level BOLD signal changes in longitudinal fMRI studies. *Hum. Brain Mapp.* 2015;36:1755–1771.
226. Zhao P., Alsop D.C., Abduljalil A., Selim M., Lipsitz L., Novak P., Caplan L., Hu K., Novak V. Vasoreactivity and peri-infarct hyperintensities in stroke. *Neurology.* 2009;72:643–649.
227. Mutch WAC, Ellis MJ, Ryner LN, Graham MR, Dufault B, Gregson B, Hall T, Bunge M, Essig M, Fisher JA, et al. Brain magnetic resonance imaging CO2 stress testing in adolescent postconcussion syndrome. *J Neurosurg.* 2016;125:648–60.
228. Amyot F, Kenney K, Moore C, Haber M, Turtzo LC, Shenouda C, Silverman E, Gong Y, Qu B-X, Harburg L, et al. Imaging of Cerebrovascular Function in Chronic Traumatic Brain Injury. *J. Neurotrauma.* 2018;35:1116–1123.
229. Champagne A.A., Coverdale N.S., Ross A., Chen Y., Murray C.I., Dubowitz D., Cook D.J. Multi-modal normalization of resting-state using local physiology reduces changes in functional connectivity patterns observed in mTBI patients. *NeuroImage Clin.* 2020;26:102204.
230. Zaca D., Jovicich J., Nadar S.R., Voyvodic J.T., Pillai J.J. Cerebrovascular reactivity mapping in patients with low grade gliomas undergoing presurgical sensorimotor mapping with BOLD fMRI. *J. Magn. Reson. Imaging.* 2014;40:383–390.
231. Fierstra J., van Niftrik C., Piccirelli M., Bozinov O., Pangalu A., Kraysenbuhl N., Valavanis A., Weller M., Regli L. Diffuse gliomas exhibit whole brain impaired cerebrovascular reactivity. *Magn. Reson. Imaging.* 2018;45:78–83.

232. Pillai J.J., Zaca D. Comparison of BOLD cerebrovascular reactivity mapping and DSC MR perfusion imaging for prediction of neurovascular uncoupling potential in brain tumors. *Technol. Cancer Res. Treat.* 2012;11:361–374.
233. Hsu Y.-Y., Chang C.-N., Jung S.-M., Lim K.-E., Huang J.-C., Fang S.-Y., Liu H.-L. Blood Oxygenation Level-Dependent MRI of Cerebral Gliomas during Breath Holding. *J. Magn. Reson. Imaging.* 2004;19:160–167.
234. Kario K, Ishikawa J, Hoshida S, Matsui Y, Morinari M, Eguchi K, Ishikawa S, Shimada K. Diabetic brain damage in hypertension: role of renin-angiotensin system. *Hypertension.* 2005;45:887–93.
235. Tchistiakova E, Anderson ND, Greenwood CE, MacIntosh BJ. Combined effects of type 2 diabetes and hypertension associated with cortical thinning and impaired cerebrovascular reactivity relative to hypertension alone in older adults. *Neuroimage (Amst).* 2014;5:36–41.
236. Zhou X.-H., Li W., Zhang Y., Lu S., Ni C.-L., Song W.-Y., Zhang Q. Breath holding fMRI evaluation of cerebrovascular reactivity in patients with type 2 diabetes mellitus. *Chin. J. Med. Imaging Technol.* 2015;31:688–692.
237. Anazodo U.C., Shoemaker J.K., Suskin N., Ssali T., Wang D.J.J., St. Lawrence K.S. Impaired cerebrovascular function in coronary artery disease patients and recovery following cardiac rehabilitation. *Front. Aging Neurosci.* 2016;7:224.
238. Jefferson AL, Liu D, Gupta DK, Pechman KR, Watchmaker JM, Gordon EA, Rane S, Bell SP, Mendes LA, Davis LT, et al. Lower cardiac index levels relate to lower cerebral blood flow in older adults. *Neurology.* 2017;89:2327–2334.
239. Leung J., Duffin J., Fisher J.A., Kassner A. MRI-based cerebrovascular reactivity using transfer function analysis reveals temporal group differences between patients with sickle cell disease and healthy controls. *NeuroImage Clin.* 2016;12:624–630.
240. Kosinski PD, Croal PL, Leung J, Williams S, Odame I, Hare GMT, Shroff M, Kassner A. The severity of anaemia depletes cerebrovascular dilatory reserve in children with sickle cell disease: a quantitative magnetic resonance imaging study. *British Journal of Haematology.* 2017;176:280–287.
241. Metzger A, Le Bars E, Deverdun J, Molino F, Marechal B, Picot M-C, Ayrignac X, Carra C, Bauchet L, Krainik A, et al. Is impaired cerebral vasoreactivity an early marker of cognitive decline in multiple sclerosis patients?. *Eur Radiol.* 2018;28:1204–1214.

242. Sivakolundu D.K., West K.L., Maruthy G.B., Zuppichini M., Turner M.P., Abdelkarim D., Zhao Y., Nguyen D., Spence J.S., Lu H., et al. Reduced arterial compliance along the cerebrovascular tree predicts cognitive slowing in multiple sclerosis: Evidence for a neurovascular uncoupling hypothesis. *Mult. Scler. J.* 2019;26:1486–1496.
243. Tucker W.J., Thomas B.P., Puzziferri N., Samuel T.J., Zaha V.G., Lingvay I., Almandoz J., Wang J., Gonzales E.A., Brothers R.M., et al. Impact of bariatric surgery on cerebral vascular reactivity and cognitive function: A non-randomized pilot study. *Pilot Feasibility Stud.* 2020;6:21.
244. Frosch OH, Yau PL, Osorio RS, Rusinek H, Storey P, Convit A. Insulin resistance among obese middle-aged is associated with decreased cerebrovascular reactivity. *Neurology.* 2017;89:249–255.
245. Fierstra J., Conklin J., Krings T., Slessarev M., Han J.S., Fisher J.A., Terbrugge K., Wallace M.C., Tymianski M., Mikulis D.J. Impaired perinidal cerebrovascular reserve in seizure patients with brain arteriovenous malformations. *Brain.* 2011;134:100–109.
246. Fierstra J, Spieth S, Tran L, Conklin J, Tymianski M, ter Brugge KG, Fisher JA, Mikulis DJ, Krings T. Severely impaired cerebrovascular reserve in patients with cerebral proliferative angiopathy. *J Neurosurg Pediatrics.* 2011;8:310–5.
247. Al-Bachari S., Parkes L.M., Vidyasagar R., Hanby M.F., Tharaken V., Leroi I., Emsley H.C.A. Arterial spin labelling reveals prolonged arterial arrival time in idiopathic Parkinson's disease. *NeuroImage Clin.* 2014;6:1–8.
248. Pelizzari L., Lagana M.M., Rossetto F., Bergsland N., Galli M., Baselli G., Clerici M., Nemni R., Baglio F. Cerebral blood flow and cerebrovascular reactivity correlate with severity of motor symptoms in Parkinson's disease. *Ther. Adv. Neurol. Disord.* 2019;12:1756286419838354.
249. Zheng G., Wen J., Yu W., Li X., Chen H., Kong X., Luo S., Jiang X., Liu Y., Zhang Z., et al. Anemia rather than hypertension contributes to cerebral hyperperfusion in young adults undergoing hemodialysis: A phase contrast MRI study. *Sci Rep.* 2016;6:22346.
250. Urback AL, Metcalfe AW, Korczak DJ, MacIntosh BJ, Goldstein BI. Reduced cerebrovascular reactivity among adolescents with bipolar disorder. *Bipolar Disord.* 2019;21:124–131.
251. Abi Zeid Daou M, Boyd BD, Donahue MJ, Albert K, Taylor WD. Frontocingulate cerebral blood flow and cerebrovascular reactivity

- associated with antidepressant response in late-life depression. *Journal of Affective Disorders*. 2017;215:103–110.
252. Hanby M.F., Al-Bachari S., Makin F., Vidyasagar R., Parkes L.M., Emsley H.C.A. Structural and physiological MRI correlates of occult cerebrovascular disease in late-onset epilepsy. *NeuroImage Clin*. 2015;9:128–133.
 253. Callen A.L., Dupont S.M., Pyne J., Talbott J., Tien P., Calabrese E., Saloner D., Chow F.C., Narvid J. The regional pattern of abnormal cerebrovascular reactivity in HIV-infected, virally suppressed women. *J. Neurovirol*. 2020;26:734–742.
 254. Da Costa L., Fierstra J., Fisher J.A., Mikulis D.J., Han J.S., Tymianski M. BOLD MRI and early impairment of cerebrovascular reserve after aneurysmal subarachnoid hemorrhage. *J. Magn. Reson. Imaging*. 2014;40:972–979.
 255. Rodan LH, Poubanc J, Fisher JA, Sobczyk O, Wong T, Hlasny E, Mikulis D, Tein I. Cerebral hyperperfusion and decreased cerebrovascular reactivity correlate with neurologic disease severity in MELAS. *Mitochondrion*. 2015;22:66–74.
 256. Prisman E., Slessarev M., Han J., Poubanc J., Mardimae A., Crawley A., Fisher J., Mikulis D. Comparison of the effects of independently-controlled end-tidal PCO₂ and PO₂ on Blood Oxygen Level-Dependent (BOLD) MRI. *J. Magn. Reson. Imaging*. 2008;27:185–191.
 257. Hare HV, Germuska M, Kelly ME, Bulte DP. Comparison of CO₂ in air versus carbogen for the measurement of cerebrovascular reactivity with magnetic resonance imaging. *J Cereb Blood Flow Metab*. 2013;33:1799–805.
 258. Golestani A.M., Wei L.L., Chen J.J. Quantitative mapping of cerebrovascular reactivity using resting-state BOLD fMRI: Validation in healthy adults. *NeuroImage*. 2016;138:147–163.
 259. Leoni R.F., Mazzeto-Betti K.C., Andrade K.C., de Araujo D.B. Quantitative evaluation of hemodynamic response after hypercapnia among different brain territories by fMRI. *NeuroImage*. 2008;41:1192–1198.
 260. Liu H.-L., Huang J.-C., Wu C.-T., Hsu Y.-Y. Detectability of blood oxygenation level-dependent signal changes during short breath hold duration. *Magn. Reson. Imaging*. 2002;20:643–648.

261. Siero J.C.W., Strother M.K., Faraco C.C., Hoogduin H., Hendrikse J., Donahue M.J. In vivo quantification of hyperoxic arterial blood water T1. *NMR Biomed.* 2015;28:1518–1525.
262. Lu H., Liu P., Yezhuvath U., Cheng Y., Marshall O., Ge Y. MRI mapping of cerebrovascular reactivity via gas inhalation challenges. *J Vis Exp.* 2014;
263. Kassner A., Winter J.D., Poubanc J., Mikulis D.J., Crawley A.P. Blood-oxygen level dependent MRI measures of cerebrovascular reactivity using a controlled respiratory challenge: Reproducibility and gender differences. *J. Magn. Reson. Imaging.* 2010;31:298–304.
264. Dengel D.R., Evanoff N.G., Marlatt K.L., Geijer J.R., Mueller B.A., Lim K.O. Reproducibility of blood oxygen level-dependent signal changes with end-tidal carbon dioxide alterations. *Clin. Physiol. Funct. Imaging.* 2017;37:794–798.
265. Zhou Y., Rodgers Z.B., Kuo A.H. Cerebrovascular reactivity measured with arterial spin labeling and blood oxygen level dependent techniques. *Magn. Reson. Imaging.* 2015;33:566–576.
266. Zande FH, Hofman PA, Backes WH. Mapping hypercapnia-induced cerebrovascular reactivity using BOLD MRI. *Neuroradiology.* 2005;47:114–120.
267. Spilt A., Van Den Boom R., Kamper A.M., Blauw G.J., Bollen E.L.E.M., Van Buchem M.A. MR assessment of cerebral vascular response: A comparison of two methods. *J. Magn. Reson. Imaging.* 2002;16:610–616.
268. Tancredi FB, Hoge RD. Comparison of cerebral vascular reactivity measures obtained using breath-holding and CO₂ inhalation. *J Cereb Blood Flow Metab.* 2013;33:1066–74.
269. Heijtel DFR, Mutsaerts HJMM, Bakker E, Schober P, Stevens MF, Petersen ET, van Berckel BNM, Majoie CBLM, Booi J, van Osch MJP, et al. Accuracy and precision of pseudo-continuous arterial spin labeling perfusion during baseline and hypercapnia: a head-to-head comparison with ¹⁵O H₂O positron emission tomography. *Neuroimage.* 2014;92:182–92.
270. Grandin CB, Bol A, Smith AM, Michel C, Cosnard G. Absolute CBF and CBV Measurements by MRI Bolus Tracking before and after Acetazolamide Challenge: Repeatability and Comparison with PET in Humans. *Neuroimage.* 2005;26:525–35.

271. Leung J., Kim J.A., Kassner A. Reproducibility of cerebrovascular reactivity measures in children using BOLD MRI. *J. Magn. Reson. Imaging*. 2016;43:1191–1195.
272. Bright M.G., Murphy K. Reliable quantification of BOLD fMRI cerebrovascular reactivity despite poor breath-hold performance. *NeuroImage*. 2013;83:559–568.
273. Sousa I., Vilela P., Figueiredo P. Reproducibility of hypocapnic cerebrovascular reactivity measurements using BOLD fMRI in combination with a paced deep breathing task. *NeuroImage*. 2014;98:31–41.
274. Merola A., Germuska M.A., Murphy K., Wise R.G. Assessing the repeatability of absolute CMRO₂, OEF and haemodynamic measurements from calibrated fMRI. *NeuroImage*. 2018;173:113–126.
275. Mandell D.M., Han J.S., Poublanc J., Crawley A.P., Kassner A., Fisher J.A., Mikulis D.J. Selective reduction of blood flow to white matter during hypercapnia corresponds with leukoaraiosis. *Stroke*. 2008;39:1993–1998.
276. Halani S., Kwinta J.B., Golestani A.M., Khatamian Y.B., Chen J.J. Comparing cerebrovascular reactivity measured using BOLD and cerebral blood flow MRI: The effect of basal vascular tension on vasodilatory and vasoconstrictive reactivity. *NeuroImage*. 2015;110:110–123.
277. van Niftrik C.H.B., Piccirelli M., Bozinov O., Maldaner N., Strittmatter C., Pangalu A., Valavanis A., Regli L., Fierstra J. Impact of baseline CO₂ on Blood-Oxygenation-Level-Dependent MRI measurements of cerebrovascular reactivity and task-evoked signal activation. *Magn. Reson. Imaging*. 2018;49:123–130.
278. Hou X., Liu P., Li Y., Jiang D., De Vis J.B., Lin Z., Sur S., Baker Z., Mao D., Ravi H., et al. The association between BOLD-based cerebrovascular reactivity (CVR) and end-tidal CO₂ in healthy subjects. *Neuroimage*. 2019;116:365.
279. Petrella J.R., DeCarli C., Dagli M., Grandin C.B., Duyn J.H., Frank J.A., Hoffman E.A., Theodore W.H. Age-related vasodilatory response to acetazolamide challenge in healthy adults: A dynamic contrast-enhanced MR study. *Am. J. Neuroradiol*. 1998;19:39–44.
280. McKetton L., Sobczyk O., Duffin J., Poublanc J., Sam K., Crawley A.P., Venkatraghavan L., Fisher J.A., Mikulis D.J. The aging brain and cerebrovascular reactivity. *NeuroImage*. 2018;181:132–141.

281. Thomas B.P., Liu P., Aslan S., King K.S., van Osch M.J.P., Lu H. Physiologic underpinnings of negative BOLD cerebrovascular reactivity in brain ventricles. *NeuroImage*. 2013;83:505–512.
282. Bright M.G., Bianciardi M., de Zwart J.A., Murphy K., Duyn J.H. Early anti-correlated BOLD signal changes of physiologic origin. *NeuroImage*. 2014;87:287–296.
283. Ravi H, Thomas BP, Peng S-L, Liu H, Lu H. On the optimization of imaging protocol for the mapping of cerebrovascular reactivity. *J Magn Reson Imaging*. 2016;43:661–8.
284. Chen JJ, Pike GB. MRI measurement of the BOLD-specific flow–volume relationship during hypercapnia and hypocapnia in humans. *NeuroImage*. 2010;53:383–391.
285. Hoge RD. Calibrated fMRI. *NeuroImage*. 2012;62:930–937.
286. Germuska M, Merola A, Murphy K, Babic A, Richmond L, Khot S, Hall JE, Wise RG. A forward modelling approach for the estimation of oxygen extraction fraction by calibrated fMRI. *NeuroImage*. 2016;139:313–323.
287. Merola A., Germuska M.A., Warnert E.A., Richmond L., Helme D., Khot S., Murphy K., Rogers P.J., Hall J.E., Wise R.G. Mapping the pharmacological modulation of brain oxygen metabolism: The effects of caffeine on absolute CMRO₂ measured using dual calibrated fMRI. *NeuroImage*. 2017;155:331–343.
288. Germuska M, Wise RG. Calibrated fMRI for mapping absolute CMRO₂: Practicalities and prospects. *NeuroImage*. 2019;187:145–153.
289. Morgan AG, Thrippleton MJ, Wardlaw JM, Marshall I. 4D flow MRI for non-invasive measurement of blood flow in the brain: A systematic review. *J Cereb Blood Flow Metab*. 2020;0271678X20952014.
290. Bright MG, Mazerolle EL, Sobczyk O, Fan AP, van Osch MJ, Mark CI, Huber L, Berman AJ, Bulte DP, Pike BG, et al. Clinical mapping of cerebrovascular reactivity using MRI: a framework for reaching consensus. Honolulu, Hawaii: 2017.
291. Wells JA, Holmes HE, O’Callaghan JM, Colgan N, Ismail O, Fisher EM, Siow B, Murray TK, Schwarz AJ, O’Neill MJ, et al. Increased Cerebral Vascular Reactivity in the Tau Expressing rTg4510 Mouse: Evidence against the Role of Tau Pathology to Impair Vascular Health in Alzheimer’s Disease. *J Cereb Blood Flow Metab*. 2015;35:359–362.
292. Lake EMR, Bazzigaluppi P, Stefanovic B. Functional magnetic resonance imaging in chronic ischaemic stroke. *Philosophical*

- Transactions of the Royal Society B: Biological Sciences.* 2016;371:20150353.
293. Gonçalves MR, Johnson SP, Ramasawmy R, Lythgoe MF, Pedley RB, Walker-Samuel S. The effect of imatinib therapy on tumour cycling hypoxia, tissue oxygenation and vascular reactivity. *Wellcome Open Res.* 2017;2:38.
294. Stringer MS, Lee H, Huuskonen MT, MacIntosh BJ, Brown R, Montagne A, Atwi S, Ramirez J, Jansen MA, Marshall I, et al. A Review of Translational Magnetic Resonance Imaging in Human and Rodent Experimental Models of Small Vessel Disease. *Transl. Stroke Res.* 2021;12:15–30.
295. Seitz I, Dirnagl U, Lindauer U. Impaired Vascular Reactivity of Isolated Rat Middle Cerebral Artery after Cortical Spreading Depression in Vivo. *J Cereb Blood Flow Metab.* 2004;24:526–530.
296. Joutel A, Monet-Leprêtre M, Gosele C, Baron-Menguy C, Hammes A, Schmidt S, Lemaire-Carrette B, Domenga V, Schedl A, Lacombe P, et al. Cerebrovascular dysfunction and microcirculation rarefaction precede white matter lesions in a mouse genetic model of cerebral ischemic small vessel disease. *J Clin Invest.* 2010;120:433–445.
297. Lynch CE, Eisenbaum M, Algamal M, Balbi M, Ferguson S, Mouzon B, Saltiel N, Ojo J, Diaz-Arrastia R, Mullan M, et al. Impairment of cerebrovascular reactivity in response to hypercapnic challenge in a mouse model of repetitive mild traumatic brain injury. *J Cereb Blood Flow Metab.* 2020;0271678X20954015.
298. Joo IL, Lai AY, Bazzigaluppi P, Koletar MM, Dorr A, Brown ME, Thomason LAM, Sled JG, McLaurin J, Stefanovic B. Early neurovascular dysfunction in a transgenic rat model of Alzheimer's disease. *Scientific Reports.* 2017;7:46427.
299. Kisler K, Nelson AR, Rege SV, Ramanathan A, Wang Y, Ahuja A, Lazic D, Tsai PS, Zhao Z, Zhou Y, et al. Pericyte degeneration leads to neurovascular uncoupling and limits oxygen supply to brain. *Nature Neuroscience.* 2017;20:406–416.
300. Leung J, Kosinski PD, Croal PL, Kassner A. Developmental trajectories of cerebrovascular reactivity in healthy children and young adults assessed with magnetic resonance imaging. *The Journal of Physiology.* 2016;594:2681–2689.
301. Sobczyk O, Sam K, Mandell DM, Crawley AP, McKetton L, Poublanc J, Mikulis DJ, Venkatraghavan L, Duffin J, Fisher JA. Cerebrovascular

- Reactivity Assays Collateral Function in Carotid Stenosis. *Front. Physiol.* 2020;11:1031.
302. Sebök M, Esposito G, Niftrik CHB van, Fierstra J, Schubert T, Wegener S, Held J, Kulcsár Z, Luft AR, Regli L. Flow augmentation STA-MCA bypass evaluation for patients with acute stroke and unilateral large vessel occlusion: a proposal for an urgent bypass flowchart. *Journal of Neurosurgery.* 2022;1:1–9.
303. Waddle SL, Garza M, Davis LT, V. Chitale R, R. Fusco M, A. Lee C, Patel NJ, Kang H, Jordan LC, Donahue MJ. Presurgical Magnetic Resonance Imaging Indicators of Revascularization Response in Adults With Moyamoya Vasculopathy. *Journal of Magnetic Resonance Imaging.* 2022;56:983–994.
304. Stringer MS, Blair GW, Hamilton I, Doubal FN, Marshall IM, Thrippleton MJ, Wardlaw JM, Shi Y, Dickie DA. A Comparison of CVR Magnitude and Delay Assessed at 1.5 and 3T in Patients With Cerebral Small Vessel Disease. *Front. Physiol.* 2021;12:644837.
305. Rudilosso S, Chui E, Stringer MS, Thrippleton M, Chappell F, Blair GW, Garcia DJ, Doubal F, Hamilton I, Kopczak A, et al. Prevalence and Significance of the Vessel-Cluster Sign on Susceptibility-Weighted Imaging in Patients With Severe Small Vessel Disease. *Neurology.* 2022;99:e440–e452.
306. Kim D, Bobinski M, Hughes TM, Craft S, Baker LD, Lockhart SN, Okonmah-Obazee SE, Hugenschmidt CE, Lipford ME, Whitlow CT, et al. Relationship Between Cerebrovascular Reactivity and Cognition Among People With Risk of Cognitive Decline. *Front. Physiol.* 2021;12:645342.
307. Amyot F, Lynch CE, Ollinger J, Werner JK, Silverman E, Moore C, Davis C, Turtzo LC, Diaz-Arrastia R, Kenney K. Cerebrovascular Reactivity Measures Are Associated With Post-traumatic Headache Severity in Chronic TBI; A Retrospective Analysis. *Frontiers in Physiology.* 2021;12:649901.
308. Afzali-Hashemi L, Baas KPA, Schrantee A, Coolen BF, van Osch MJP, Spann SM, Nur E, Wood JC, Biemond BJ, Nederveen AJ. Impairment of Cerebrovascular Hemodynamics in Patients With Severe and Milder Forms of Sickle Cell Disease. *Frontiers in Physiology.* 2021;12:645205.
309. Chan ST, Mercaldo ND, Kwong KK, Hersch SM, Rosas HD. Impaired Cerebrovascular Reactivity in Huntington's Disease. *Frontiers in Physiology.* 2021;12:663898.

310. Pinto J, Bright MG, Bulte DP, Figueiredo P. Cerebrovascular Reactivity Mapping Without Gas Challenges: A Methodological Guide. *Frontiers in Physiology*. 2021;11:608475.
311. Solis-Barquero SM, Echeverria-Chasco R, Calvo-Imirizaldu M, Cacho-Asenjo E, Martinez-Simon A, Vidorreta M, Dominguez PD, García de Eulate R, Fernandez-Martinez M, Fernández-Seara MA. Breath-Hold Induced Cerebrovascular Reactivity Measurements Using Optimized Pseudocontinuous Arterial Spin Labeling. *Frontiers in Physiology*. 2021;12:621720.
312. Stickland RC, Zvolanek KM, Moia S, Caballero-Gaudes C, Bright MG. Lag-Optimized Blood Oxygenation Level Dependent Cerebrovascular Reactivity Estimates Derived From Breathing Task Data Have a Stronger Relationship With Baseline Cerebral Blood Flow. *Frontiers in Neuroscience*. 2022;16:910025.
313. Poublanc J, Shafi R, Sobczyk O, Sam K, Mandell DM, Venkatraghavan L, Duffin J, Fisher JA, Mikulis DJ. Normal BOLD Response to a Step CO₂ Stimulus After Correction for Partial Volume Averaging. *Frontiers in Physiology*. 2021;12:639360.
314. Bhogal AA. Medullary vein architecture modulates the white matter BOLD cerebrovascular reactivity signal response to CO₂: Observations from high-resolution T2* weighted imaging at 7T. *NeuroImage*. 2021;245:118771.
315. Turner R. How Much Cortex Can a Vein Drain? Downstream Dilution of Activation-Related Cerebral Blood Oxygenation Changes. *NeuroImage*. 2002;16:1062–1067.
316. Liu P, Jiang D, Albert M, Bauer CE, Caprihan A, Gold BT, Greenberg SM, Helmer KG, Jann K, Jicha G, et al. Multi-vendor and multisite evaluation of cerebrovascular reactivity mapping using hypercapnia challenge. *NeuroImage*. 2021;245:118754.
317. Sobczyk O, Sayin ES, Sam K, Poublanc J, Duffin J, Fisher JA, Mikulis DJ. The Reproducibility of Cerebrovascular Reactivity Across MRI Scanners. *Frontiers in Physiology*. 2021;12:668662.
318. Sobczyk O, Fierstra J, Venkatraghavan L, Poublanc J, Duffin J, Fisher JA, Mikulis DJ. Measuring Cerebrovascular Reactivity: Sixteen Avoidable Pitfalls. *Frontiers in Physiology*. 2021;12:665049.
319. Sleight E, Stringer MS, Mitchell I, Murphy M, Marshall I, Wardlaw JM, Thrippleton MJ. Cerebrovascular reactivity measurements using 3T BOLD MRI and a fixed inhaled CO₂ gas challenge: Repeatability and

- impact of processing strategy. *Frontiers in Physiology*. 2023;14:1070233.
320. Ogawa S, Lee TM, Kay AR, Tank DW. Brain magnetic resonance imaging with contrast dependent on blood oxygenation. *Proc Natl Acad Sci U S A*. 1990;87:9868–9872.
321. Rostrup E, Larsson HBW, Toft PB, Garde K, Thomsen C, Ring P, Søndergaard L, Henriksen O. Functional MRI of CO₂ induced increase in cerebral perfusion. *NMR in Biomedicine*. 1994;7:29–34.
322. Lipp A, Schmelzer JD, Low PA, Johnson BD, Benarroch EE. Ventilatory and Cardiovascular Responses to Hypercapnia and Hypoxia in Multiple-System Atrophy. *Archives of Neurology*. 2010;67:211–216.
323. Li X, Morgan PS, Ashburner J, Smith J, Rorden C. The first step for neuroimaging data analysis: DICOM to NIfTI conversion. *Journal of Neuroscience Methods*. 2016;264:47–56.
324. Friston KJ, editor. Statistical parametric mapping. In: Statistical parametric mapping: the analysis of functional brain images. Amsterdam ; Boston: Elsevier/Academic Press; 2007. p. 10–31.
325. Zhang Y, Brady M, Smith S. Segmentation of brain MR images through a hidden Markov random field model and the expectation-maximization algorithm. *IEEE Transactions on Medical Imaging*. 2001;20:45–57.
326. Patenaude B, Smith SM, Kennedy DN, Jenkinson M. A Bayesian model of shape and appearance for subcortical brain segmentation. *Neuroimage*. 2011;56:907–922.
327. Fonov V, Evans AC, Botteron K, Almli CR, McKinstry RC, Collins DL. Unbiased average age-appropriate atlases for pediatric studies. *NeuroImage*. 2011;54:313–327.
328. Fonov V, Evans A, McKinstry R, Almli C, Collins D. Unbiased nonlinear average age-appropriate brain templates from birth to adulthood. *NeuroImage*. 2009;47:S102.
329. Jenkinson M, Smith S. A global optimisation method for robust affine registration of brain images. *Medical Image Analysis*. 2001;5:143–156.
330. Jenkinson M, Bannister P, Brady M, Smith S. Improved Optimization for the Robust and Accurate Linear Registration and Motion Correction of Brain Images. *NeuroImage*. 2002;17:825–841.

331. Blockley N.P., Harkin J.W., Bulte D.P. Rapid cerebrovascular reactivity mapping: Enabling vascular reactivity information to be routinely acquired. *NeuroImage*. 2017;159:214–223.
332. Press WH. Numerical Recipes 3rd Edition: The Art of Scientific Computing. Cambridge University Press; 2007.
333. Gudbjartsson H, Patz S. The Rician Distribution of Noisy MRI Data. *Magn Reson Med*. 1995;34:910–914.
334. Theyers AE, Goldstein BI, Metcalfe AW, Robertson AD, MacIntosh BJ. Cerebrovascular blood oxygenation level dependent pulsatility at baseline and following acute exercise among healthy adolescents. *J Cereb Blood Flow Metab*. 2019;39:1737–1749.
335. Atwi S, Robertson AD, Theyers AE, Ramirez J, Swartz RH, Marzolini S, MacIntosh BJ. Cardiac-Related Pulsatility in the Insula Is Directly Associated With Middle Cerebral Artery Pulsatility Index. *Journal of Magnetic Resonance Imaging*. 2019;51:1454–1462.
336. Benetos A, Waeber B, Izzo J, Mitchell G, Resnick L, Asmar R, Safar M. Influence of age, risk factors, and cardiovascular and renal disease on arterial stiffness: clinical applications. *Am J Hypertens*. 2002;15:1101–1108.
337. Chung C-P, Lee H-Y, Lin P-C, Wang P-N. Cerebral Artery Pulsatility is Associated with Cognitive Impairment and Predicts Dementia in Individuals with Subjective Memory Decline or Mild Cognitive Impairment. *J Alzheimers Dis*. 2017;60:625–632.
338. Shi Y, Thrippleton MJ, Marshall I, Wardlaw JM. Intracranial pulsatility in patients with cerebral small vessel disease: a systematic review. *Clinical Science*. 2018;132:157–171.
339. Webb AJS, Simoni M, Mazzucco S, Kuker W, Schulz U, Rothwell PM. Increased cerebral arterial pulsatility in patients with leukoaraiosis: arterial stiffness enhances transmission of aortic pulsatility. *Stroke*. 2012;43:2631–2636.
340. Vikner T, Karalija N, Eklund A, Malm J, Lundquist A, Gallewicz N, Dahlin M, Lindenberger U, Riklund K, Bäckman L, et al. 5-Year Associations among Cerebral Arterial Pulsatility, Perivascular Space Dilation, and White Matter Lesions. *Annals of Neurology*. 2022;92:871–881.
341. Clancy U, Garcia DJ, Stringer MS, Thrippleton MJ, Valdés-Hernández MC, Wiseman S, Hamilton OK, Chappell FM, Brown R, Blair GW, et al. Rationale and design of a longitudinal study of cerebral small vessel diseases, clinical and imaging outcomes in patients presenting with mild

- ischaemic stroke: Mild Stroke Study 3. *European Stroke Journal*. 2020;2396987320929617.
342. Glover GH, Li T-Q, Ress D. Image-based method for retrospective correction of physiological motion effects in fMRI: RETROICOR. *Magnetic Resonance in Medicine*. 2000;44:162–167.
343. Fazekas F, Chawluk J, Alavi A, Hurtig H, Zimmerman R. MR signal abnormalities at 1.5 T in Alzheimer's dementia and normal aging. *American Journal of Roentgenology*. 1987;149:351–356.
344. Rivera-Rivera LA, Schubert T, Turski P, Johnson KM, Berman SE, Rowley HA, Carlsson CM, Johnson SC, Wieben O. Changes in intracranial venous blood flow and pulsatility in Alzheimer's disease: A 4D flow MRI study. *J Cereb Blood Flow Metab*. 2017;37:2149–2158.
345. Valsamis J, Luciw N, Schwardfager W, Lim A, Ramirez J, Black S, MacIntosh BJ. Estimating cerebrovascular compliance from normocapnia and hypercapnia BOLD pulsatility mapping. In: Proceedings of ISMRM 2022. 2022.
346. Czosnyka M, Richards HK, Whitehouse HE, Pickard JD. Relationship between transcranial Doppler-determined pulsatility index and cerebrovascular resistance: an experimental study. *Journal of Neurosurgery*. 1996;84:79–84.
347. Geurts LJ, Zwanenburg JJM, Klijn CJM, Luijten PR, Biessels GJ. Higher Pulsatility in Cerebral Perforating Arteries in Patients With Small Vessel Disease Related Stroke, a 7T MRI Study. *Stroke*. 2019;50:62–68.
348. O'Rourke MF, Hashimoto J. Mechanical factors in arterial aging: a clinical perspective. *J Am Coll Cardiol*. 2007;50:1–13.
349. Kaufman FL, Hughson RL, Schaman JP. Effect of exercise on recovery blood pressure in normotensive and hypertensive subjects. *Med Sci Sports Exerc*. 1987;19:17–20.
350. Bärtsch P, Gibbs JSR. Effect of Altitude on the Heart and the Lungs. *Circulation*. 2007;116:2191–2202.
351. Makedonov I, Black SE, MacIntosh BJ. BOLD fMRI in the White Matter as a Marker of Aging and Small Vessel Disease. *PLoS One*. 2013;8:e67652.
352. Wardlaw JM, Doubal FN, Valdes-Hernandez M, Wang X, Chappell FM, Shuler K, Armitage PA, Carpenter TC, Dennis MS. Blood-brain barrier permeability and long-term clinical and imaging outcomes in cerebral small vessel disease. *Stroke*. 2013;44:525–527.

353. Montagne A, Barnes SR, Sweeney MD, Halliday MR, Sagare AP, Zhao Z, Toga AW, Jacobs RE, Liu CY, Amezcua L, et al. Blood-Brain Barrier Breakdown in the Aging Human Hippocampus. *Neuron*. 2015;85:296–302.
354. Nation DA, Sweeney MD, Montagne A, Sagare AP, D’Orazio LM, Pachicano M, Seppehrband F, Nelson AR, Buennagel DP, Harrington MG, et al. Blood–brain barrier breakdown is an early biomarker of human cognitive dysfunction. *Nat Med*. 2019;25:270–276.
355. Kerkhofs D, Wong SM, Zhang E, Uiterwijk R, Hoff EI, Jansen JFA, Staals J, Backes WH, van Oostenbrugge RJ. Blood–brain barrier leakage at baseline and cognitive decline in cerebral small vessel disease: a 2-year follow-up study. *GeroScience*. 2021;43:1643–1652.
356. Birnefeld J, Wählin A, Eklund A, Malm J. Cerebral arterial pulsatility is associated with features of small vessel disease in patients with acute stroke and TIA: a 4D flow MRI study. *J Neurol*. 2020;267:721–730.
357. Hoogduin JM, Hendrikse J, Conijn MMA, van der Graaf Y, Geerlings MI, Luijten PR. Microbleeds, lacunar infarcts, white matter lesions and cerebrovascular reactivity - A 7T study. *NeuroImage*. 2012;59:950–956.
358. Potter GM, Chappell FM, Morris Z, Wardlaw JM. Cerebral Perivascular Spaces Visible on Magnetic Resonance Imaging: Development of a Qualitative Rating Scale and its Observer Reliability. *Cerebrovasc Dis*. 2015;39:224–231.
359. Farrell C, Chappell F, Armitage PA, Keston P, MacLulich A, Shenkin S, Wardlaw JM. Development and initial testing of normal reference MR images for the brain at ages 65-70 and 75-80 years. *Eur Radiol*. 2009;19:177–183.
360. Fischl B, Salat DH, Busa E, Albert M, Dieterich M, Haselgrove C, van der Kouwe A, Killiany R, Kennedy D, Klaveness S, et al. Whole Brain Segmentation: Automated Labeling of Neuroanatomical Structures in the Human Brain. *Neuron*. 2002;33:341–355.
361. Fischl B, Salat DH, van der Kouwe AJW, Makris N, Ségonne F, Quinn BT, Dale AM. Sequence-independent segmentation of magnetic resonance images. *NeuroImage*. 2004;23:S69–S84.
362. Ballerini L, Lovreglio R, Valdés Hernández M del C, Ramirez J, MacIntosh BJ, Black SE, Wardlaw JM. Perivascular Spaces Segmentation in Brain MRI Using Optimal 3D Filtering. *Sci Rep*. 2018;8:2132.

-
363. Ballerini L, Booth T, Valdés Hernández M del C, Wiseman S, Lovreglio R, Muñoz Maniega S, Morris Z, Pattie A, Corley J, Gow A, et al. Computational quantification of brain perivascular space morphologies: Associations with vascular risk factors and white matter hyperintensities. A study in the Lothian Birth Cohort 1936. *NeuroImage: Clinical*. 2020;25:102120.
364. Sam K, Crawley AP, Poubanc J, Conklin J, Sobczyk O, Mandell DM, Mikulis DJ, Duffin J, Venkatraghavan L, Fisher JA, et al. Vascular dysfunction in leukoaraiosis. *Am. J. Neuroradiol*. 2016;37:2258–2264.
365. Uh J, Yezhuvath U, Cheng Y, Lu H. In vivo vascular hallmarks of diffuse leukoaraiosis. *J Magn Reson Imaging*. 2010;32:184–190.
366. Georgakis MK, Duering M, Wardlaw JM, Dichgans M. WMH and long-term outcomes in ischemic stroke: A systematic review and meta-analysis. *Neurology*. 2019;92:e1298–e1308.
367. Bath PM, Wardlaw JM. Pharmacological Treatment and Prevention of Cerebral Small Vessel Disease: A Review of Potential Interventions. *International Journal of Stroke*. 2015;10:469–478.
368. Sam K, Conklin J, Sobczyk O, Poubanc J, Crawley AP, Mandell DM, Mikulis DJ, Venkatraghavan L, Duffin J, Fisher JA, et al. Cerebrovascular reactivity and white matter integrity. *Neurology*. 2016;87:2333–2339.
369. Wardlaw JM, Benveniste H, Nedergaard M, Zlokovic BV, Mestre H, Lee H, Doubal FN, Brown R, Ramirez J, MacIntosh BJ, et al. Perivascular spaces in the brain: anatomy, physiology and pathology. *Nat Rev Neurol*. 2020;16:137–153.
370. Kapoor A, Yew B, Jang JY, Dutt S, Li Y, Alitin JPM, Gaubert A, Ho JK, Blanken AE, Sible IJ, et al. Older adults with perivascular spaces exhibit cerebrovascular reactivity deficits. *NeuroImage*. 2022;264:119746.
371. Haley AP, Hoth KF, Gunstad J, Paul RH, Jefferson AL, Tate DF, Ono M, Jerskey BA, Poppas A, Sweet LH, et al. Subjective cognitive complaints relate to white matter hyperintensities and future cognitive decline in patients with cardiovascular disease. *Am J Geriatr Psychiatry*. 2009;17:976–985.
372. Tombaugh TN. Trail Making Test A and B: Normative data stratified by age and education. *Archives of Clinical Neuropsychology*. 2004;19:203–214.
373. Yang D, Qin R, Xu H, Ma J, Shao P, Xu Y, Ni L, Zhang B. Lower Cerebrovascular Reactivity Contributed to White Matter Hyperintensity-

- Related Cognitive Impairment: A Resting-State Functional MRI Study. *J. Magn. Reson. Imaging*. 2021;53:703–711.
374. Cai M, Jacob MA, van Loenen MR, Bergkamp M, Marques J, Norris DG, Duering M, Tuladhar AM, de Leeuw F-E. Determinants and Temporal Dynamics of Cerebral Small Vessel Disease: 14-Year Follow-Up. *Stroke*. 2022;53:2789–2798.
375. Valdés Hernández M del C, Ferguson KJ, Chappell FM, Wardlaw JM. New multispectral MRI data fusion technique for white matter lesion segmentation: method and comparison with thresholding in FLAIR images. *Eur Radiol*. 2010;20:1684–1691.
376. Blair G, Doubal F, Thrippleton M, Stringer M, Hamilton I, Wardlaw J, Kopczak A, Dichgans M, Staals J, Kerkhofs D, et al. Imaging neurovascular, endothelial and structural integrity in preparation to treat small vessel diseases. the investigate@svds study. part of the svds@target project. *European Stroke Journal*. 2017;2:328.
377. Kopczak A, S Stringer M, van den Brink H, Kerkhofs D, W Blair G, van Dinther M, Onkenhout L, A Wartolowska K, Thrippleton MJ, Duering M, et al. The EffectS of Amlodipine and other Blood PREssure Lowering Agents on Microvascular FuncTion in Small Vessel Diseases (TREAT-SVDs) trial: Study protocol for a randomised crossover trial. *European Stroke Journal*. 2022;23969873221143570.
378. Jorm AF, Jacomb PA. The Informant Questionnaire on Cognitive Decline in the Elderly (IQCODE): socio-demographic correlates, reliability, validity and some norms. *Psychol Med*. 1989;19:1015–1022.

Appendix

A1 Supplementary material of Chapter 2

Below are the full details of the search strategy for the systematic review:

1. magnetic resonance/ or MR.mp. [mp=ti, ab, ot, nm, hw, fx, kf, ox, px, rx, ui, sy, tn, dm, mf, dv, kw, dq]
2. Blood*oxygen*level*dependent/ or BOLD.mp. [mp=ti, ab, ot, nm, hw, fx, kf, ox, px, rx, ui, sy, tn, dm, mf, dv, kw, dq]
3. susceptibility weight*/ or T2.mp. [mp=ti, ab, ot, nm, hw, fx, kf, ox, px, rx, ui, sy, tn, dm, mf, dv, kw, dq]
4. diffusion imaging/ or perfusion imaging.mp. [mp=ti, ab, ot, nm, hw, fx, kf, ox, px, rx, ui, sy, tn, dm, mf, dv, kw, dq]
5. ASL/ or arterial spin labelling.mp. [mp=ti, ab, ot, nm, hw, fx, kf, ox, px, rx, ui, sy, tn, dm, mf, dv, kw, dq]
6. phase-contrast MRI.mp. [mp=ti, ab, ot, nm, hw, fx, kf, ox, px, rx, ui, sy, tn, dm, mf, dv, kw, dq]
7. dual-echo imaging/ or dual-echo MRI.mp. [mp=ti, ab, ot, nm, hw, fx, kf, ox, px, rx, ui, sy, tn, dm, mf, dv, kw, dq]
8. functional magnetic resonance/ or fMRI.mp. [mp=ti, ab, ot, nm, hw, fx, kf, ox, px, rx, ui, sy, tn, dm, mf, dv, kw, dq]
9. 1 or 2 or 3 or 4 or 5 or 6 or 7 or 8
10. cerebrovascular reactivity/ or CVR.mp. [mp=ti, ab, ot, nm, hw, fx, kf, ox, px, rx, ui, sy, tn, dm, mf, dv, kw, dq]
11. cerebrovascular capacity/ or CVC.mp. [mp=ti, ab, ot, nm, hw, fx, kf, ox, px, rx, ui, sy, tn, dm, mf, dv, kw, dq]

12. vasodilation/ or vasoconstriction.mp. [mp=ti, ab, ot, nm, hw, fx, kf, ox, px, rx, ui, sy, tn, dm, mf, dv, kw, dq]
13. vascular resistance/ or cerebrovascular reserve.mp. [mp=ti, ab, ot, nm, hw, fx, kf, ox, px, rx, ui, sy, tn, dm, mf, dv, kw, dq]
14. 10 or 11 or 12 or 13
15. carbon dioxide/ or CO2/ or carbogen.mp. [mp=ti, ab, ot, nm, hw, fx, kf, ox, px, rx, ui, sy, tn, dm, mf, dv, kw, dq]
16. hypercapnia/ or hypercapnic.mp. [mp=ti, ab, ot, nm, hw, fx, kf, ox, px, rx, ui, sy, tn, dm, mf, dv, kw, dq]
17. hyperoxia/ or hypoxia.mp. [mp=ti, ab, ot, nm, hw, fx, kf, ox, px, rx, ui, sy, tn, dm, mf, dv, kw, dq]
18. breath-hold*/ or breath hold*/ or BH.mp. [mp=ti, ab, ot, nm, hw, fx, kf, ox, px, rx, ui, sy, tn, dm, mf, dv, kw, dq]
19. hyperventilation.mp. [mp=ti, ab, ot, nm, hw, fx, kf, ox, px, rx, ui, sy, tn, dm, mf, dv, kw, dq]
20. respiract.mp. [mp=ti, ab, ot, nm, hw, fx, kf, ox, px, rx, ui, sy, tn, dm, mf, dv, kw, dq]
21. end-tidal CO2/ or end-tidal carbon dioxide.mp. [mp=ti, ab, ot, nm, hw, fx, kf, ox, px, rx, ui, sy, tn, dm, mf, dv, kw, dq]
22. end-tidal O2/ or end-tidal oxygen.mp. [mp=ti, ab, ot, nm, hw, fx, kf, ox, px, rx, ui, sy, tn, dm, mf, dv, kw, dq]
23. resting state/ or resting-state.mp. [mp=ti, ab, ot, nm, hw, fx, kf, ox, px, rx, ui, sy, tn, dm, mf, dv, kw, dq]
24. acetazolamide.mp
25. 15 or 16 or 17 or 18 or 19 or 20 or 21 or 22 or 23 or 24
26. 9 and 14 and 25

27. limit 26 to human

28. remove duplicates from 27

A2 Supplementary material of Chapter 3

A2.1 CVR magnitudes and delays used for simulations

The mean and standard deviation of CVR magnitudes and delays used in the simulations were extracted from the healthy volunteer data acquired for this study. For each participant, only one of the two scans was used and was chosen visually as the one with highest quality. The CVR and delay maps were then registered to the MNI template and averaged across participants. From the averaged maps, we extracted the distributions of CVR magnitudes and delays in NAWM (Figure A2-1), SGM and CGM using the MATLAB 'fitdist' function with a kernel distribution, excluding negative delays. We then generated ground-truth CVR magnitude and delay values for each simulated voxel by sampling the probability density functions; the true mean, median and standard deviation were calculated from the ground-truth data.

A2.2 Supplementary Figures

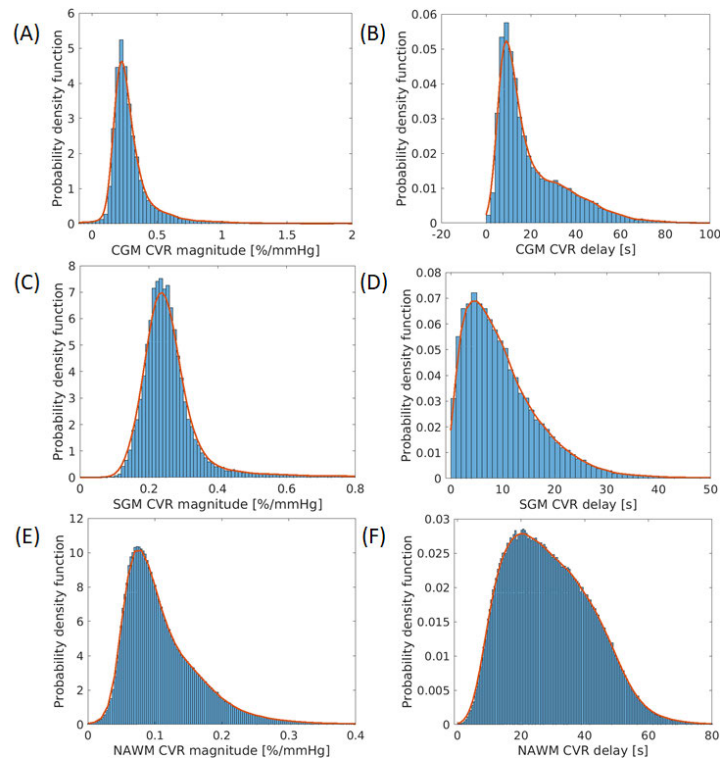


Figure A2-1: Distributions of CVR magnitudes (1st column) and delays (2nd column) in CGM (A, B), CGM (C, D) and NAWM (E, F) in the cohort-averaged parameter map. The orange curve represents the extracted distribution.

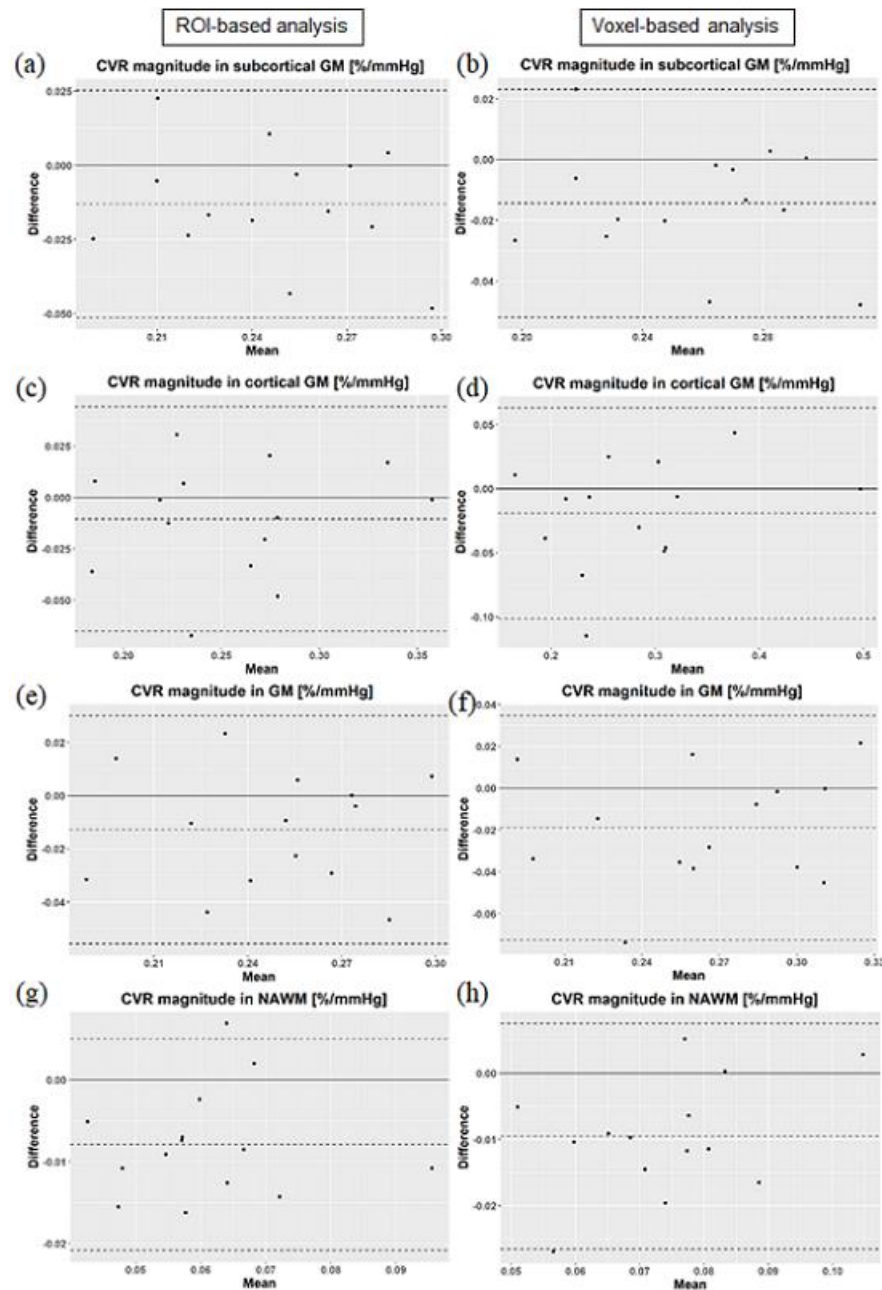


Figure A2-2: Comparison of CVR magnitudes between scans using Bland-Altman plots in subcortical GM (a, b), cortical GM (c, d), GM (e, f) and NAWM (g, h). CVR magnitudes were computed with the ROI-based (first column) and voxel-based analysis (second column). The dashed lines represent the mean inter-scan differences and the limits of agreement.

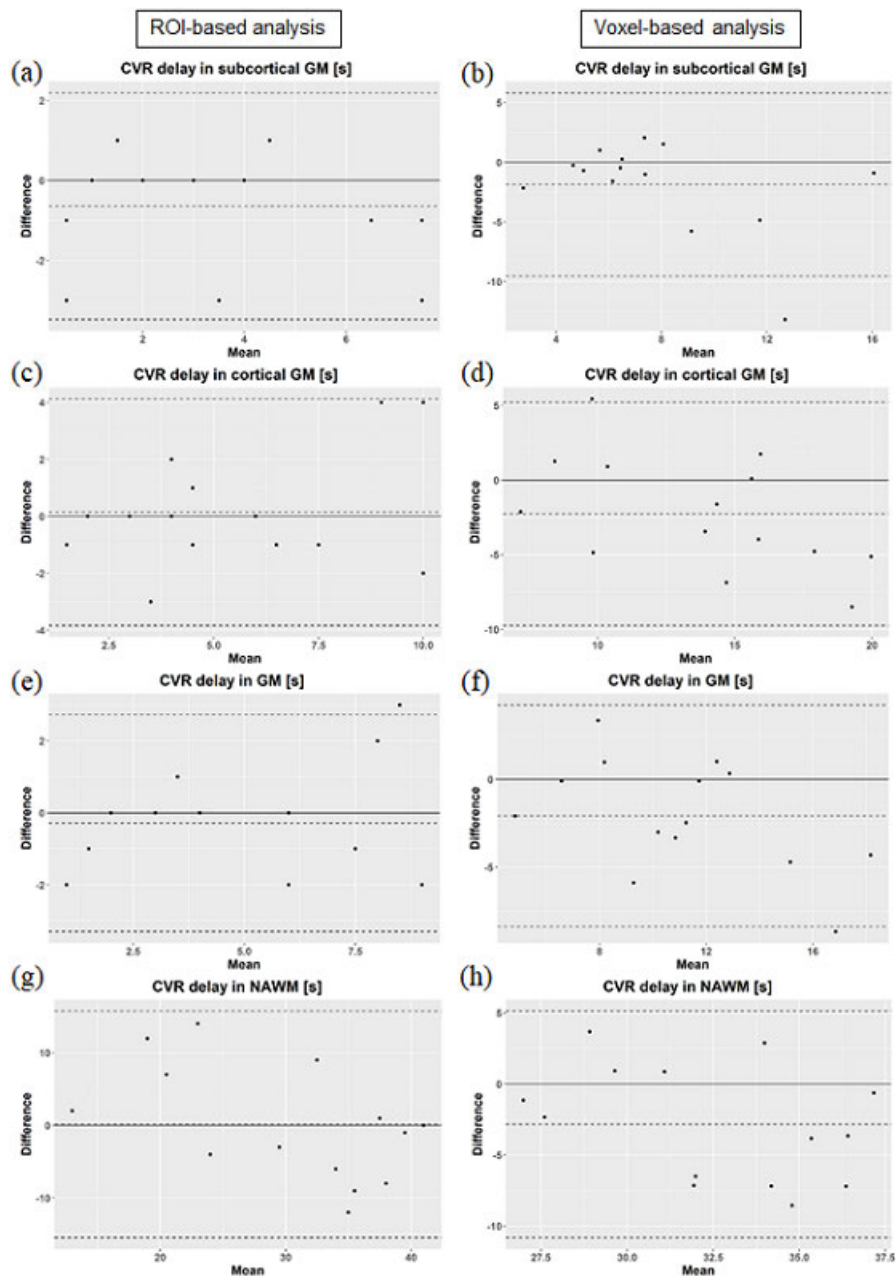


Figure A2-3: Comparison of CVR delays between scans using Bland-Altman statistics in subcortical GM (a, b), cortical GM (c, d), GM (e, f) and NAWM (g, h). CVR delays were computed with the ROI-based (first column) and voxel-based analysis (second column). The dashed lines represent the mean inter-scan differences and the limits of agreement.

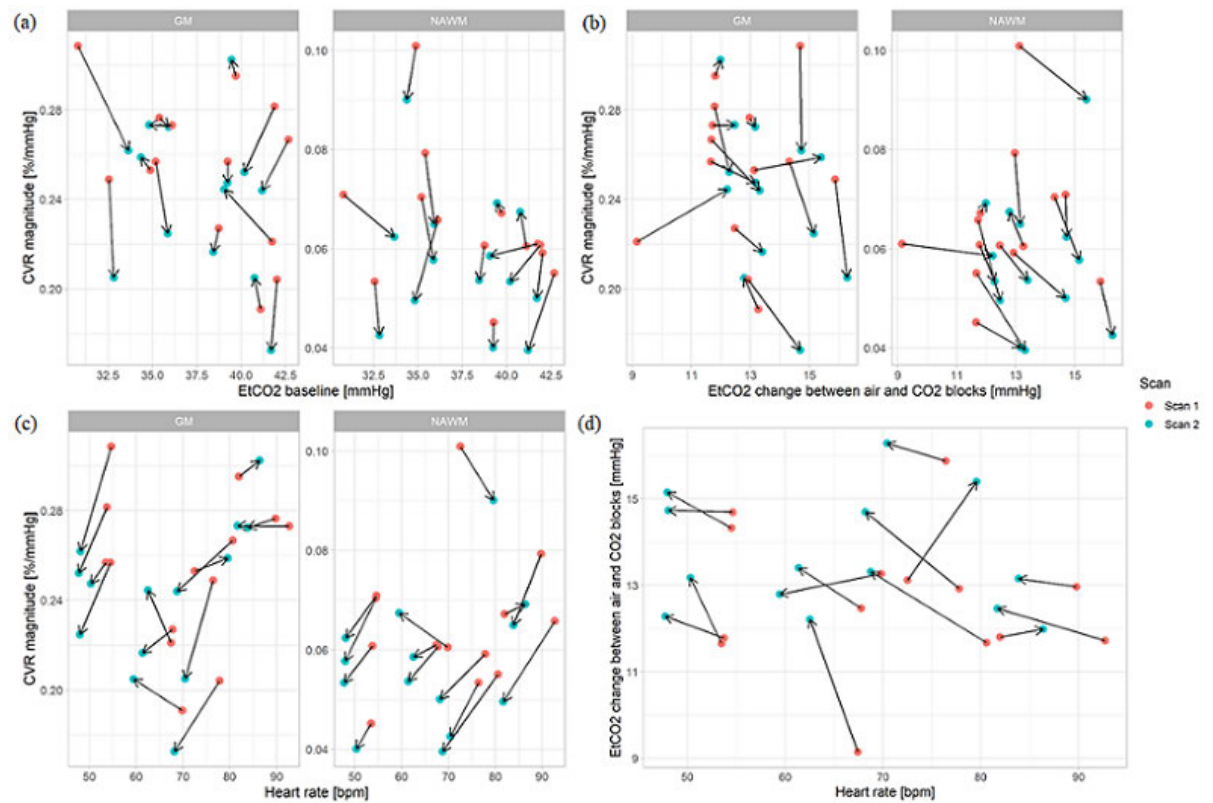


Figure A2-4: Difference in CVR magnitude and in physiological parameters between scans. Difference in CVR magnitude in GM and NAWM versus (a) the difference in EtCO₂ baseline, (b) the difference in EtCO₂ baseline, (c) the difference in heart rate. (d) Difference in EtCO₂ change versus the difference in heart rate.

A2.3 Supplementary table

Table A2-1: Mean and standard deviation across subjects of CVR magnitudes and delays in SGM, CGM, GM and NAWM computed for each delay constraint and each scan with ROI- and voxel-based processing. Mean and standard deviation of the inter-constraint differences are reported, with 95% confidence intervals for the mean given in square brackets.

Analysis type	ROI	Scan number	Delay constraint 1: -31 to 93 s (centre: 31 s)		Delay constraint 2: -31 to 124 s (centre: 46.5 s)		Inter-constraint difference (constraint 2 – constraint 1)	
			Voxel	ROI	Voxel	ROI	Voxel	ROI
CVR magnitude [%/mmHg]	SGM	1	0.26 ± 0.04	0.25 ± 0.04	0.26 ± 0.03	0.25 ± 0.04	-0.008 ± 0.015 [-0.017, 0.001]	-0.006 ± 0.023 [-0.019, 0.007]
		2	0.25 ± 0.03	0.24 ± 0.03	0.25 ± 0.03	0.24 ± 0.03	-0.003 ± 0.003 [-0.005, -0.002]	-
	CGM	1	0.29 ± 0.08	0.26 ± 0.05	0.27 ± 0.09	0.25 ± 0.06	-0.020 ± 0.026 [-0.034, -0.005]	-0.007 ± 0.026 [-0.022, 0.008]
		2	0.27 ± 0.09	0.25 ± 0.05	0.26 ± 0.10	0.25 ± 0.05	-0.011 ± 0.013 [-0.018, -0.004]	-
	GM	1	0.27 ± 0.04	0.25 ± 0.03	0.26 ± 0.05	0.25 ± 0.04	-0.015 ± 0.021 [-0.027, -0.003]	-0.007 ± 0.025 [-0.021, 0.008]
		2	0.26 ± 0.05	0.24 ± 0.03	0.25 ± 0.05	0.24 ± 0.03	-0.007 ± 0.008 [-0.012, -0.003]	-

CVR delay [s]	NAWM	1	0.08 ± 0.01	0.07 ± 0.01	0.08 ± 0.01	0.06 ± 0.01	-0.001 ± 0.013	-0.002 ± 0.008	
							[-0.009, 0.006]	[-0.006, 0.002]	
		2	0.07 ± 0.02	0.06 ± 0.01	0.07 ± 0.01	0.06 ± 0.01	0.002 ± 0.003	-	
							[-0.000, 0.004]		
	SGM	1	8.8 ± 4.8	3.9 ± 2.6	11.8 ± 6.9	3.9 ± 2.6	3.0 ± 2.6	-	
							[1.5, 4.5]		
		2	6.9 ± 3.2	3.2 ± 2.4	9.2 ± 4.0	3.2 ± 2.4	2.3 ± 1.2	-	
							[1.6, 3.1]		
		CGM	1	14.9 ± 5.3	5.4 ± 2.6	19.8 ± 6.7	5.4 ± 2.6	4.9 ± 2.4	-
								[3.5, 6.3]	
			2	12.7 ± 3.4	5.5 ± 3.3	18.2 ± 6.0	5.5 ± 3.3	5.6 ± 3.3	-
								[3.6, 7.5]	
GM	1	12.2 ± 4.8	4.8 ± 2.7	16.4 ± 6.1	4.8 ± 2.7	4.2 ± 1.9	-		
						[3.1, 5.2]			
	2	10.1 ± 3.3	4.5 ± 3.2	14.2 ± 5.1	4.5 ± 3.2	4.1 ± 2.3	-		
						[2.7, 5.4]			
NAWM	1	34.0 ± 4.6	30.1 ± 11.4	41.7 ± 5.1	29.5 ± 12.5	7.7 ± 1.9	-0.6 ± 2.1		
						[6.6, 8.8]	[-1.8, 0.7]		
		2	31.2 ± 3.2	30.2 ± 7.4	39.3 ± 3.9	30.2 ± 7.4	8.1 ± 1.5	-	
							[7.2, 9.0]		

A3 Supplementary material of Chapter 6

A3.1 Univariate analyses

Table A3-1: Regression coefficients from univariate cross-sectional analysis.

Each row represents a different statistical model where the SVD predictor of interest is given in the first column. The associated regression coefficient B , its 95% confidence interval and p -value are given in columns 2-4. The last column gives the units of B .

Variables	SGM CVR	NAWM CVR	WMH CVR	Units of B
WMH volume	$B=-0.0323$ [-0.0474, -0.0172] $p<0.001$	$B=-0.00733$ [-0.01212, -0.00254] $p=0.003$	$B=-0.0241$ [-0.0372, -0.0110] $p<0.001$	%/mmHg per $\log_{10}(\%ICV)$
Periventricular Fazekas score	$B=-0.0222$ [-0.0307, -0.0138] $p<0.001$	$B=-0.00522$ [-0.00792, -0.00251] $p<0.001$	$B=-0.0131$ [-0.0203, -0.0058] $p<0.001$	%/mmHg per score point
Deep white matter Fazekas score	$B=-0.0162$ [-0.0255, -0.0069] $p=0.001$	$B=-0.00354$ [-0.00647, -0.00062] $p=0.018$	$B=-0.0104$ [-0.0182, -0.0026] $p=0.009$	%/mmHg per score point
Total Fazekas score	$B=-0.0108$ [-0.0154, -0.0061] $p<0.001$	$B=-0.00246$ [-0.00394, -0.00098] $p=0.001$	$B=-0.00658$ [-0.01053, -0.00262] $p=0.001$	%/mmHg per score point
Number of lacunes	$B=-0.00564$ [-0.00813, -0.00315] $p<0.001$	$B=-0.00112$ [-0.00192, -0.00033] $p=0.006$	$B=-0.00148$ [-0.00363, 0.00068] $p=0.179$	%/mmHg per lacune
Number of microbleeds	$B=-0.00122$ [-0.00270, 0.00027] $p=0.108$	$B=-0.000666$ [-0.001119, -0.000213] $p=0.004$	$B=-0.00133$ [-0.00255, -0.00012] $p=0.032$	%/mmHg per microbleed
Deep atrophy score	$B=-0.00624$ [-0.01164, -0.00085] $p=0.024$	$B=-0.00202$ [-0.00369, -0.00035] $p=0.018$	$B=-0.00470$ [-0.00920, -0.00020] $p=0.041$	%/mmHg per score point
Superficial atrophy score	$B=-0.00483$ [-0.01031, 0.00065] $p=0.084$	$B=-0.00134$ [-0.00304, 0.00036] $p=0.122$	$B=-0.00429$ [-0.00884, 0.00027] $p=0.065$	%/mmHg per score point
Total atrophy score	$B=-0.00310$ [-0.00597, -0.00023] $p=0.001$	$B=-0.00094$ [-0.00183, -0.00005] $p=0.001$	$B=-0.00251$ [-0.00490, -0.00012] $p=0.001$	%/mmHg per score point

	-0.00023] p=0.035	-0.00005] p=0.039	-0.00012] p=0.040	
Brain volume	B=0.00185 [0.00019, 0.00351] p=0.029	B=0.000523 [0.000007, 0.001038] p=0.047	B=0.00119 [-0.00021, 0.00259] p=0.094	%/mmHg per %ICV
BG PVS score	B=-0.01303 [-0.02213, -0.00393] p=0.005	B=-0.00337 [-0.00621, -0.00054] p=0.020	B=-0.00738 [-0.01509, 0.00032] p=0.060	%/mmHg per score point
CSO PVS score	B=-0.00580 [-0.01425, 0.00264] p=0.177	B=-0.00151 [-0.00413, 0.00111] p=0.256	B=-0.00820 [-0.01529, -0.00111] p=0.024	%/mmHg per score point
Total PVS score	B=-0.00604 [-0.01108, -0.00101] p=0.019	B=-0.00157 [-0.00314, -0.00000] p=0.050	B=-0.00526 [-0.00952, -0.00100] p=0.016	%/mmHg per score point
BG PVS volume	B=-0.00410 [-0.00750, -0.00071] p=0.018	B=-0.000834 [-0.001889, 0.000222] p=0.121	B=-0.00178 [-0.00463, 0.00106] p=0.218	%/mmHg per %ROIV
CSO PVS volume	B=-0.000639 [-0.003846, 0.002569] p=0.695	B=-0.000410 [-0.001396, 0.000576] p=0.413	B=-0.00227 [-0.00490, 0.00036] p=0.090	%/mmHg per %ROIV
Total PVS volume	B=-0.00125 [-0.00461, 0.00212] p=0.466	B=-0.000503 [-0.001538, 0.000532] p=0.339	B=-0.00239 [-0.00516, 0.00037] p=0.090	%/mmHg per %ROIV
SVD score	B=-0.0156 [-0.0209, -0.0103] p<0.001	B=-0.00312 [-0.00485, -0.00139] p<0.001	B=-0.00551 [-0.01025, -0.00076] p=0.023	%/mmHg per score point
NIHSS	B=-0.00577 [-0.01139, -0.00016] p=0.044	B=-0.00145 [-0.00320, 0.00029] p=0.102	B=-0.000675 [-0.005355, 0.004004] p=0.776	%/mmHg per score point
mRS	B=-0.00446 [-0.01600, 0.00708] p=0.447	B=-0.00232 [-0.00589, 0.00124] p=0.200	B=0.000040 [-0.009663, 0.009743] p=0.994	%/mmHg per score point
MoCA	B=0.00325 [0.00108, 0.00541] p=0.003	B=0.000821 [0.000147, 0.001496] p=0.017	B=0.00111 [-0.00070, 0.00292] p=0.226	%/mmHg per score point

A3.2 Adjusted analyses

Table A3-2: Cross-sectional linear regression between CVR and WMH volume, adjusted for age, sex and vascular risk factors. Columns 2 to 4 contain the regression coefficients, 95% confidence intervals and p-values. The last column gives the units of the regression coefficient.

Variables	SGM CVR	NAWM CVR	WMH CVR	Units of B
WMH volume	B=-0.0256 [-0.0443, -0.0068] p=0.008	B=-0.00705 [-0.01302, -0.00108] p=0.021	B=-0.0288 [-0.0453, -0.0124] p=0.001	%/mmHg per log ₁₀ (%ICV)
Age	B=-0.000533 [-0.001325, 0.000258] p=0.185	B=-0.000083 [-0.000335, 0.000170] p=0.519	B=0.000077 [-0.000614, 0.000769] p=0.825	%/mmHg per year
Sex [Male]	B=0.0104 [-0.0062, 0.0270] p=0.218	B=0.00218 [-0.00311, 0.00748] p=0.417	B=0.000601 [-0.013438, 0.014641] p=0.933	%/mmHg
MAP	B=-0.000055 [-0.000657, 0.000547] p=0.857	B=-0.000027 [-0.000219, 0.000165] p=0.782	B=0.000173 [-0.000343, 0.000690] p=0.509	%/mmHg per mmHg
Diabetes	B=-0.00191 [-0.02143, 0.01761] p=0.847	B=-0.00167 [-0.00790, 0.00456] p=0.598	B=-0.00205 [-0.01874, 0.01464] p=0.809	%/mmHg
Smoker [Ever]	B=-0.0116 [-0.0282, 0.0049] p=0.168	B=-0.00193 [-0.00722, 0.00335] p=0.471	B=-0.00272 [-0.01681, 0.01136] p=0.703	%/mmHg
Smoker [Current]	B=-0.0195 [-0.0420, 0.0030] p=0.088	B=-0.00349 [-0.01067, 0.00368] p=0.338	B=-0.00259 [-0.02179, 0.01661] p=0.790	%/mmHg
Hypertension	B=0.00869 [-0.00936, 0.02673] p=0.343	B=0.00466 [-0.00110, 0.01042] p=0.112	B=0.0128 [-0.0028, 0.0284] p=0.107	%/mmHg
Hypercholesterolaemia	B=0.00255 [-0.01455, 0.01965] p=0.769	B=0.00166 [-0.00380, 0.00712] p=0.549	B=-0.000728 [-0.015344, 0.013888] p=0.922	%/mmHg

Table A3-3: Cross-sectional linear regression between CVR and periventricular Fazekas score, adjusted for age, sex and vascular risk factors. Columns 2 to 4 contain the regression coefficients, 95% confidence intervals and p-values. The last column gives the units of the regression coefficient.

Variables	SGM CVR	NAWM CVR	WMH CVR	Units of B
Periventricular Fazekas score	B=-0.0203 [-0.0304, -0.0102] p<0.001	B=-0.00561 [-0.00885, -0.00237] p=0.001	B=-0.0151 [-0.0240, -0.0063] p=0.001	%/mmHg per score point
Age	B=-0.000418 [-0.001170, 0.000334] p=0.274	B=-0.000051 [-0.000292, 0.000191] p=0.678	B=0.000009 [-0.000668, 0.000687] p=0.978	%/mmHg per year
Sex [Male]	B=0.00835 [-0.00791, 0.02461] p=0.312	B=0.00162 [-0.00360, 0.00684] p=0.541	B=-0.000112 [-0.014228, 0.014005] p=0.988	%/mmHg
MAP	B=-0.000086 [-0.000673, 0.000501] p=0.772	B=-0.000036 [-0.000224, 0.000153] p=0.710	B=0.000121 [-0.000395, 0.000636] p=0.645	%/mmHg per mmHg
Diabetes	B=-0.00478 [-0.02375, 0.01419] p=0.619	B=-0.00246 [-0.00855, 0.00363] p=0.427	B=-0.00542 [-0.02204, 0.01120] p=0.520	%/mmHg
Smoker [Ever]	B=-0.0120 [-0.0281, 0.0042] p=0.146	B=-0.00203 [-0.00722, 0.00317] p=0.442	B=-0.00250 [-0.01660, 0.01161] p=0.727	%/mmHg
Smoker [Current]	B=-0.0195 [-0.0411, 0.0021] p=0.077	B=-0.00348 [-0.01042, 0.00346] p=0.323	B=-0.00456 [-0.02357, 0.01444] p=0.636	%/mmHg
Hypertension	B=0.0124 [-0.0053, 0.0301] p=0.167	B=0.00569 [0.00001, 0.01138] p=0.050	B=0.0126 [-0.0030, 0.0282] p=0.113	%/mmHg
Hypercholesterolaemia	B=0.00304 [-0.01365, 0.01973] p=0.720	B=0.00180 [-0.00356, 0.00715] p=0.509	B=-0.000087 [-0.014711, 0.014538] p=0.991	%/mmHg

Table A3-4: Cross-sectional linear regression between CVR and deep white matter Fazekas score, adjusted for age, sex and vascular risk factors. Columns 2 to 4 contain the regression coefficients, 95% confidence intervals and p-values *f*. The last column gives the units of the regression coefficient.

Variables	SGM CVR	NAWM CVR	WMH CVR	Units of B
Deep white matter	B=-0.0110	B=-0.00282	B=-0.0102	%mmHg per score point
Fazekas score	[-0.0216, -0.0003]	[-0.00621, 0.00058]	[-0.0194, -0.0009]	
	p=0.044	p=0.104	p=0.031	
Age	B=-0.000713	B=-0.000138	B=-0.000152	%mmHg per year
	[-0.001487, 0.000061]	[-0.000385, 0.000109]	[-0.000844, 0.000540]	
	p=0.071	p=0.270	p=0.665	
Sex [Male]	B=0.0111	B=0.00242	B=0.00172	%mmHg
	[-0.0056, 0.0278]	[-0.00291, 0.00775]	[-0.01261, 0.01604]	
	p=0.191	p=0.372	p=0.813	
MAP	B=-0.000087	B=-0.000036	B=0.000127	%mmHg per mmHg
	[-0.000693, 0.000519]	[-0.000229, 0.000157]	[-0.000399, 0.000654]	
	p=0.777	p=0.713	p=0.634	
Diabetes	B=-0.00328	B=-0.00207	B=-0.00399	%mmHg
	[-0.02292, 0.01635]	[-0.00833, 0.00419]	[-0.02097, 0.01299]	
	p=0.742	p=0.515	p=0.643	
Smoker [Ever]	B=-0.0128	B=-0.00224	B=-0.00339	%mmHg
	[-0.0295, 0.0039]	[-0.00758, 0.00309]	[-0.01779, 0.01102]	
	p=0.133	p=0.408	p=0.643	
Smoker [Current]	B=-0.0230	B=-0.00453	B=-0.00654	%mmHg
	[-0.0453, -0.0007]	[-0.01165, 0.00259]	[-0.02593, 0.01285]	
	p=0.044	p=0.211	p=0.506	
Hypertension	B=0.00526	B=0.00364	B=0.00775	%mmHg
	[-0.01253, 0.02305]	[-0.00204, 0.00931]	[-0.00772, 0.02322]	
	p=0.560	p=0.208	p=0.324	
Hypercholesterolaemia	B=0.00319	B=0.00185	B=-0.000022	%mmHg
	[-0.01405, 0.02043]	[-0.00365, 0.00734]	[-0.014936, 0.014893]	
	p=0.715	p=0.509	p=0.998	

Table A3-5: Cross-sectional linear regression between CVR and total Fazekas score, adjusted for age, sex and vascular risk factors. Columns 2 to 4 contain the regression coefficients, 95% confidence intervals and p-values. The last column gives the units of the regression coefficient.

Variables	SGM CVR	NAWM CVR	WMH CVR	Units of B
Total Fazekas score	B=-0.00909 [-0.01466, -0.00353] p=0.002	B=-0.00245 [-0.00423, -0.00067] p=0.007	B=-0.00737 [-0.01222, -0.00252] p=0.003	%/mmHg per score point
Age	B=-0.000494 [-0.001265, 0.000277] p=0.207	B=-0.000075 [-0.000322, 0.000172] p=0.548	B=-0.000007 [-0.000699, 0.000685] p=0.984	%/mmHg per year
Sex [Male]	B=0.00939 [-0.00709, 0.02586] p=0.262	B=0.00193 [-0.00335, 0.00721] p=0.471	B=0.000471 [-0.013725, 0.014667] p=0.948	%/mmHg
MAP	B=-0.000082 [-0.000678, 0.000514] p=0.786	B=-0.000035 [-0.000225, 0.000156] p=0.721	B=0.000130 [-0.000389, 0.000650] p=0.621	%/mmHg per mmHg
Diabetes	B=-0.00357 [-0.02283, 0.01569] p=0.715	B=-0.00213 [-0.00830, 0.00404] p=0.496	B=-0.00444 [-0.02118, 0.01231] p=0.602	%/mmHg
Smoker [Ever]	B=-0.0127 [-0.0291, 0.0037] p=0.129	B=-0.00222 [-0.00748, 0.00304] p=0.406	B=-0.00314 [-0.01735, 0.01107] p=0.663	%/mmHg
Smoker [Current]	B=-0.0203 [-0.0422, 0.0017] p=0.071	B=-0.00374 [-0.01078, 0.00330] p=0.296	B=-0.00473 [-0.02393, 0.01447] p=0.627	%/mmHg
Hypertension	B=0.00958 [-0.00822, 0.02739] p=0.290	B=0.00485 [-0.00085, 0.01055] p=0.095	B=0.0110 [-0.0046, 0.0266] p=0.165	%/mmHg
Hypercholesterolaemia	B=0.00301 [-0.01393, 0.01995] p=0.726	B=0.00179 [-0.00363, 0.00721] p=0.515	B=-0.000153 [-0.014882, 0.014575] p=0.984	%/mmHg

Table A3-6: Cross-sectional linear regression between CVR and number of lacunes, adjusted for age, sex and vascular risk factors. Columns 2 to 4 contain the regression coefficients, 95% confidence intervals and p-values. The last column gives the units of the regression coefficient.

Variables	SGM CVR	NAWM CVR	WMH CVR	Units of B
Number of lacunes	B=-0.00594 [-0.00855, -0.00334] p<0.001	B=-0.00125 [-0.00211, -0.00040] p=0.004	B=-0.00157 [-0.00392, 0.00077] p=0.187	%/mmHg per lacune
Age	B=-0.00114 [-0.00182, -0.00046] p=0.001	B=-0.000242 [-0.000466, -0.000018] p=0.034	B=-0.000495 [-0.001133, 0.000143] p=0.128	%/mmHg per year
Sex [Male]	B=0.0102 [-0.0057, 0.0262] p=0.208	B=0.00231 [-0.00292, 0.00754] p=0.385	B=0.00265 [-0.01177, 0.01706] p=0.717	%/mmHg
MAP	B=-0.000168 [-0.000749, 0.000412] p=0.568	B=-0.000054 [-0.000244, 0.000136] p=0.576	B=0.000081 [-0.000449, 0.000612] p=0.762	%/mmHg per mmHg
Diabetes	B=-0.00316 [-0.02192, 0.01560] p=0.740	B=-0.00211 [-0.00826, 0.00404] p=0.499	B=-0.00465 [-0.02177, 0.01246] p=0.592	%/mmHg
Smoker [Ever]	B=-0.0134 [-0.0294, 0.0026] p=0.101	B=-0.00232 [-0.00756, 0.002923] p=0.384	B=-0.00295 [-0.01747, 0.01158] p=0.689	%/mmHg
Smoker [Current]	B=-0.0165 [-0.0381, 0.0050] p=0.132	B=-0.00336 [-0.01042, 0.00370] p=0.349	B=-0.00791 [-0.02752, 0.01170] p=0.427	%/mmHg
Hypertension	B=0.0118 [-0.0055, 0.0290] p=0.179	B=0.00483 [-0.00083, 0.01048] p=0.094	B=0.00639 [-0.00931, 0.02209] p=0.423	%/mmHg
Hypercholesterolaemia	B=0.00128 [-0.01524, 0.01781] p=0.879	B=0.00146 [-0.00396, 0.00688] p=0.595	B=-0.000238 [-0.015313, 0.014837] p=0.975	%/mmHg

Table A3-7: Cross-sectional linear regression between CVR and number of microbleeds, adjusted for age, sex and vascular risk factors. Columns 2 to 4 contain the regression coefficients, 95% confidence intervals and p-values. The last column gives the units of the regression coefficient.

Variables	SGM CVR	NAWM CVR	WMH CVR	Units of B
Number of microbleeds	B=-0.00162 [-0.00313, -0.00011] p=0.036	B=-0.000835 [-0.001305, -0.000366] p=0.001	B=-0.00168 [-0.00296, -0.00040] p=0.011	%/mmHg per microbleed
Age	B=-0.00118 [-0.00191, -0.00046] p=0.002	B=-0.000298 [-0.000523, -0.000073] p=0.010	B=-0.000630 [-0.001270, 0.000010] p=0.054	%/mmHg per year
Sex [Male]	B=0.0104 [-0.0064, 0.0272] p=0.222	B=0.00160 [-0.00361, 0.00681] p=0.545	B=0.000820 [-0.013475, 0.015115] p=0.910	%/mmHg
MAP	B=-0.000081 [-0.000687, 0.000525] p=0.792	B=-0.000029 [-0.000217, 0.000159] p=0.763	B=0.000126 [-0.000397, 0.000649] p=0.635	%/mmHg per mmHg
Diabetes	B=-0.00583 [-0.02542, 0.01377] p=0.558	B=-0.00302 [-0.00911, 0.00307] p=0.329	B=-0.00629 [-0.02316, 0.01058] p=0.463	%/mmHg
Smoker [Ever]	B=-0.0131 [-0.0299, 0.0036] p=0.123	B=-0.00265 [-0.00784, 0.00255] p=0.316	B=-0.00396 [-0.01830, 0.01038] p=0.587	%/mmHg
Smoker [Current]	B=-0.0273 [-0.0492, -0.0053] p=0.015	B=-0.00566 [-0.01248, 0.00115] p=0.103	B=-0.01115 [-0.03009, 0.00780] p=0.247	%/mmHg
Hypertension	B=0.00461 [-0.01301, 0.02223] p=0.606	B=0.00434 [-0.00114, 0.00981] p=0.120	B=0.00693 [-0.00820, 0.02205] p=0.367	%/mmHg
Hypercholesterolaemia	B=0.00480 [-0.01245, 0.02206] p=0.583	B=0.00257 [-0.00279, 0.00793] p=0.345	B=0.00177 [-0.01309, 0.01662] p=0.815	%/mmHg

Table A3-8: Cross-sectional linear regression between CVR and deep atrophy score, adjusted for age, sex and vascular risk factors. Columns 2 to 4 contain the regression coefficients, 95% confidence intervals and p-values. The last column gives the units of the regression coefficient.

Variables	SGM CVR	NAWM CVR	WMH CVR	Units of B
Deep atrophy score	B=-0.00496 [-0.01122, 0.00130] p=0.120	B=-0.00213 [-0.00411, -0.00016] p=0.035	B=-0.00469 [-0.01004, 0.00065] p=0.085	%/mmHg per score point
Age	B=-0.000708 [-0.001528, 0.000111] p=0.090	B=-0.000082 [-0.000341, 0.000177] p=0.533	B=-0.000166 [-0.000886, 0.000553] p=0.649	%/mmHg per year
Sex [Male]	B=0.0163 [-0.0010, 0.0335] p=0.065	B=0.00432 [-0.00112, 0.00977] p=0.119	B=0.00654 [-0.00822, 0.02130] p=0.383	%/mmHg
MAP	B=-0.000124 [-0.000733, 0.000486] p=0.689	B=-0.000049 [-0.000241, 0.000143] p=0.616	B=0.000074 [-0.000455, 0.000603] p=0.784	%/mmHg per mmHg
Diabetes	B=-0.00413 [-0.02382, 0.01556] p=0.679	B=-0.00219 [-0.00841, 0.00402] p=0.487	B=-0.00448 [-0.02153, 0.01257] p=0.605	%/mmHg
Smoker [Ever]	B=-0.0131 [-0.0299, 0.0038] p=0.127	B=-0.00252 [-0.00784, 0.00280] p=0.350	B=-0.00358 [-0.01809, 0.01092] p=0.626	%/mmHg
Smoker [Current]	B=-0.0269 [-0.0490, -0.0048] p=0.017	B=-0.00549 [-0.01246, 0.00147] p=0.121	B=-0.0103 [-0.0295, 0.0088] p=0.289	%/mmHg
Hypertension	B=0.00252 [-0.01499, 0.02004] p=0.777	B=0.00315 [-0.00238, 0.00868] p=0.262	B=0.00472 [-0.01041, 0.01985] p=0.538	%/mmHg
Hypercholesterolaemia	B=0.00424 [-0.01310, 0.02157] p=0.630	B=0.00223 [-0.00325, 0.00770] p=0.423	B=0.000927 [-0.014067, 0.015920] p=0.903	%/mmHg

Table A3-9: Cross-sectional linear regression between CVR and superficial atrophy score, adjusted for age, sex and vascular risk factors. Columns 2 to 4 contain the regression coefficients, 95% confidence intervals and p-values. The last column gives the units of the regression coefficient.

Variables	SGM CVR	NAWM CVR	WMH CVR	Units of B
Superficial atrophy score	B=-0.00169 [-0.00830, 0.00492] p=0.615	B=-0.000985 [-0.003081, 0.001112] p=0.355	B=-0.00401 [-0.00967, 0.00164] p=0.163	%/mmHg per score point
Age	B=-0.000906 [-0.001766, -0.000047] p=0.039	B=-0.000149 [-0.000421, 0.000124] p=0.283	B=-0.000177 [-0.000931, 0.000576] p=0.643	%/mmHg per year
Sex [Male]	B=0.0139 [-0.0034, 0.0312] p=0.114	B=0.00347 [-0.00201, 0.00895] p=0.213	B=0.00583 [-0.00894, 0.02060] p=0.437	%/mmHg
MAP	B=-0.000118 [-0.000733, 0.000497] p=0.705	B=-0.000049 [-0.000244, 0.000146] p=0.623	B=0.000067 [-0.000465, 0.000599] p=0.804	%/mmHg per mmHg
Diabetes	B=-0.00469 [-0.02449, 0.01512] p=0.641	B=-0.00243 [-0.00871, 0.00385] p=0.445	B=-0.00498 [-0.02206, 0.01211] p=0.566	%/mmHg
Smoker [Ever]	B=-0.0123 [-0.0293, 0.0047] p=0.154	B=-0.00224 [-0.00762, 0.00314] p=0.412	B=-0.00358 [-0.01816, 0.01099] p=0.628	%/mmHg
Smoker [Current]	B=-0.0266 [-0.0489, -0.0042] p=0.020	B=-0.00525 [-0.01233, 0.00183] p=0.145	B=-0.00939 [-0.02866, 0.00989] p=0.338	%/mmHg
Hypertension	B=0.00196 [-0.01581, 0.01973] p=0.828	B=0.00302 [-0.00262, 0.00865] p=0.292	B=0.00526 [-0.01004, 0.02057] p=0.498	%/mmHg
Hypercholesterolaemia	B=0.00344 [-0.01400, 0.02088] p=0.698	B=0.00186 [-0.00367, 0.00738] p=0.508	B=-0.000081 [-0.015130, 0.014968] p=0.992	%/mmHg

Table A3-10: Cross-sectional linear regression between CVR and total atrophy score, adjusted for age, sex and vascular risk factors. Columns 2 to 4 contain the regression coefficients, 95% confidence intervals and p-values. The last column gives the units of the regression coefficient.

Variables	SGM CVR	NAWM CVR	WMH CVR	Units of B
Total atrophy score	B=-0.00200 [-0.00548, 0.00149] p=0.260	B=-0.000929 [-0.002030, 0.000171] p=0.097	B=-0.00255 [-0.00551, 0.00041] p=0.091	%/mmHg per score point
Age	B=-0.000757 [-0.001614, 0.000101] p=0.084	B=-0.000093 [-0.000364, 0.000178] p=0.500	B=-0.000120 [-0.000870, 0.000630] p=0.753	%/mmHg per year
Sex [Male]	B=0.0154 [-0.0019, 0.0328] p=0.081	B=0.00407 [-0.00142, 0.00955] p=0.145	B=0.00666 [-0.00816, 0.02147] p=0.376	%/mmHg
MAP	B=-0.000129 [-0.000741, 0.000484] p=0.679	B=-0.000052 [-0.000246, 0.000142] p=0.597	B=0.000065 [-0.000465, 0.000595] p=0.809	%/mmHg per mmHg
Diabetes	B=-0.00446 [-0.02422, 0.01529] p=0.656	B=-0.00233 [-0.00857, 0.00392] p=0.463	B=-0.00467 [-0.02172, 0.01238] p=0.589	%/mmHg
Smoker [Ever]	B=-0.0128 [-0.0298, 0.0041] p=0.136	B=-0.00245 [-0.00780, 0.00290] p=0.367	B=-0.00378 [-0.01831, 0.01076] p=0.609	%/mmHg
Smoker [Current]	B=-0.0263 [-0.0485, -0.0042] p=0.020	B=-0.00522 [-0.01223, 0.00179] p=0.144	B=-0.00969 [-0.02886, 0.00949] p=0.320	%/mmHg
Hypertension	B=0.00259 [-0.01506, 0.02025] p=0.772	B=0.00323 [-0.00235, 0.00881] p=0.255	B=0.00527 [-0.00993, 0.02048] p=0.495	%/mmHg
Hypercholesterolaemia	B=0.00367 [-0.01371, 0.02104] p=0.678	B=0.00198 [-0.00351, 0.00747] p=0.478	B=0.000372 [-0.014618, 0.015361] p=0.961	%/mmHg

Table A3-11: Cross-sectional linear regression between CVR and brain volume, adjusted for age, sex and vascular risk factors. Columns 2 to 4 contain the regression coefficients, 95% confidence intervals and p-values. The last column gives the units of the regression coefficient.

Variables	SGM CVR	NAWM CVR	WMH CVR	Units of B
Brain volume	B=0.000443 [-0.001371, 0.002256] p=0.631	B=0.000177 [-0.000398, 0.000753] p=0.544	B=0.00346 [0.00199, 0.00492] p<0.001	%/mmHg per %ICV
Age	B=-0.000927 [-0.001754, -0.000100] p=0.028	B=-0.000179 [-0.000441, 0.000084] p=0.180	B=0.000297 [-0.000386, 0.000979] p=0.392	%/mmHg per year
Sex [Male]	B=0.0136 [-0.0035, 0.0307] p=0.118	B=0.00316 [-0.00226, 0.00858] p=0.251	B=0.00929 [-0.00452, 0.02310] p=0.186	%/mmHg
MAP	B=-0.000121 [-0.000737, 0.000496] p=0.700	B=-0.000047 [-0.000243, 0.000149] p=0.635	B=-0.000023 [-0.000527, 0.000481] p=0.928	%/mmHg per mmHg
Diabetes	B=-0.00437 [-0.02422, 0.01548] p=0.665	B=-0.00230 [-0.00860, 0.00400] p=0.471	B=-0.00212 [-0.01833, 0.01409] p=0.796	%/mmHg
Smoker [Ever]	B=-0.0116 [-0.0286, 0.0053] p=0.176	B=-0.00191 [-0.00728, 0.00346] p=0.484	B=-0.00114 [-0.01486, 0.01258] p=0.870	%/mmHg
Smoker [Current]	B=-0.0270 [-0.0492, -0.0048] p=0.018	B=-0.00554 [-0.01259, 0.00152] p=0.123	B=-0.0101 [-0.0282, 0.0081] p=0.275	%/mmHg
Hypertension	B=0.00125 [-0.01631, 0.01880] p=0.888	B=0.00261 [-0.00297, 0.00818] p=0.357	B=0.00370 [-0.01060, 0.01799] p=0.610	%/mmHg
Hypercholesterolaemia	B=0.00335 [-0.01410, 0.02081] p=0.705	B=0.00185 [-0.00369, 0.00739] p=0.511	B=-0.00183 [-0.01607, 0.01242] p=0.800	%/mmHg

Table A3-12: Cross-sectional linear regression between CVR and BG PVS score, adjusted for age, sex and vascular risk factors. Columns 2 to 4 contain the regression coefficients, 95% confidence intervals and p-values. The last column gives the units of the regression coefficient.

Variables	SGM CVR	NAWM CVR	WMH CVR	Units of B
BG PVS score	B=-0.0114 [-0.0214, -0.0013] p=0.027	B=-0.00338 [-0.00657, -0.00019] p=0.038	B=-0.00760 [-0.01628, 0.00108] p=0.086	%/mmHg per score point
Age	B=-0.000763 [-0.001510, -0.000017] p=0.045	B=-0.000140 [-0.000378, 0.000097] p=0.245	B=-0.000297 [-0.000959, 0.000366] p=0.378	%/mmHg per year
Sex [Male]	B=0.0139 [-0.0027, 0.0305] p=0.101	B=0.00317 [-0.00212, 0.00845] p=0.238	B=0.00403 [-0.01030, 0.01837] p=0.579	%/mmHg
MAP	B=-0.000026 [-0.000634, 0.000582] p=0.933	B=-0.000017 [-0.000211, 0.000176] p=0.860	B=0.000142 [-0.000389, 0.000673] p=0.598	%/mmHg per mmHg
Diabetes	B=-0.00323 [-0.02282, 0.01635] p=0.745	B=-0.00200 [-0.00823, 0.00423] p=0.527	B=-0.00428 [-0.02135, 0.01278] p=0.621	%/mmHg
Smoker [Ever]	B=-0.0150 [-0.0319, 0.0019] p=0.082	B=-0.00293 [-0.00830, 0.00244] p=0.284	B=-0.00454 [-0.01917, 0.01010] p=0.542	%/mmHg
Smoker [Current]	B=-0.0253 [-0.0472, -0.0033] p=0.024	B=-0.00504 [-0.01202, 0.00195] p=0.157	B=-0.00919 [-0.02840, 0.01002] p=0.346	%/mmHg
Hypertension	B=0.00669 [-0.01128, 0.02466] p=0.463	B=0.00422 [-0.00149, 0.00994] p=0.146	B=0.00737 [-0.00831, 0.02306] p=0.355	%/mmHg
Hypercholesterolaemia	B=0.00116 [-0.01616, 0.01849] p=0.895	B=0.00123 [-0.00429, 0.00674] p=0.661	B=-0.00112 [-0.01621, 0.01397] p=0.884	%/mmHg

Table A3-13: Cross-sectional linear regression between CVR and CSO PVS score, adjusted for age, sex and vascular risk factors. Columns 2 to 4 contain the regression coefficients, 95% confidence intervals and p-values. The last column gives the units of the regression coefficient.

Variables	SGM CVR	NAWM CVR	WMH CVR	Units of B
CSO PVS score	B=-0.00181 [-0.01106, 0.00745] p=0.701	B=-0.000804 [-0.003741, 0.002133] p=0.590	B=-0.00852 [-0.01651, -0.00053] p=0.037	%/mmHg per score point
Age	B=-0.000980 [-0.001738, -0.000222] p=0.012	B=-0.000198 [-0.000439, 0.000043] p=0.106	B=-0.000248 [-0.000911, 0.000416] p=0.462	%/mmHg per year
Sex [Male]	B=0.0127 [-0.0042, 0.0295] p=0.139	B=0.00278 [-0.00256, 0.00813] p=0.305	B=0.00226 [-0.01204, 0.01655] p=0.756	%/mmHg
MAP	B=-0.000084 [-0.000706, 0.000537] p=0.789	B=-0.000032 [-0.000229, 0.000165] p=0.751	B=0.000183 [-0.000349, 0.000716] p=0.497	%/mmHg per mmHg
Diabetes	B=-0.00485 [-0.02469, 0.01498] p=0.630	B=-0.00251 [-0.00880, 0.00379] p=0.433	B=-0.00585 [-0.02282, 0.01112] p=0.497	%/mmHg
Smoker [Ever]	B=-0.0125 [-0.0296, 0.0047] p=0.153	B=-0.00227 [-0.00772, 0.00318] p=0.412	B=-0.00519 [-0.01980, 0.00942] p=0.484	%/mmHg
Smoker [Current]	B=-0.0266 [-0.0490, -0.0043] p=0.020	B=-0.00537 [-0.01247, 0.00174] p=0.138	B=-0.00850 [-0.02766, 0.01066] p=0.382	%/mmHg
Hypertension	B=0.00194 [-0.01597, 0.01984] p=0.831	B=0.00291 [-0.00277, 0.00859] p=0.314	B=0.00665 [-0.00863, 0.02193] p=0.391	%/mmHg
Hypercholesterolaemia	B=0.00301 [-0.01469, 0.02070] p=0.738	B=0.00169 [-0.00393, 0.00730] p=0.554	B=-0.00239 [-0.01754, 0.01277] p=0.756	%/mmHg

Table A3-14: Cross-sectional linear regression between CVR and total PVS score, adjusted for age, sex and vascular risk factors. Columns 2 to 4 contain the regression coefficients, 95% confidence intervals and p-values. The last column gives the units of the regression coefficient.

Variables	SGM CVR	NAWM CVR	WMH CVR	Units of B
Total PVS score	B=-0.00437 [-0.01012, 0.00137] p=0.135	B=-0.00141 [-0.00323, 0.00042] p=0.130	B=-0.00581 [-0.01077, -0.00086] p=0.022	%/mmHg per score point
Age	B=-0.000812 [-0.001581, -0.000044] p=0.038	B=-0.000150 [-0.000394, 0.000094] p=0.227	B=-0.000188 [-0.000861, 0.000484] p=0.581	%/mmHg per year
Sex [Male]	B=0.0128 [-0.0039, 0.0295] p=0.133	B=0.00285 [-0.00246, 0.00815] p=0.292	B=0.00311 [-0.01111, 0.01733] p=0.666	%/mmHg
MAP	B=-0.000027 [-0.000644, 0.000591] p=0.933	B=-0.000016 [-0.000212, 0.000181] p=0.875	B=0.000190 [-0.000341, 0.000721] p=0.480	%/mmHg per mmHg
Diabetes	B=-0.00454 [-0.02423, 0.01515] p=0.650	B=-0.00239 [-0.00864, 0.00387] p=0.452	B=-0.00496 [-0.02188, 0.01196] p=0.563	%/mmHg
Smoker [Ever]	B=-0.0145 [-0.0316, 0.0026] p=0.097	B=-0.00285 [-0.00829, 0.00259] p=0.303	B=-0.00589 [-0.02053, 0.00875] p=0.428	%/mmHg
Smoker [Current]	B=-0.02515 [-0.04739, -0.00292] p=0.027	B=-0.00495 [-0.01201, 0.00211] p=0.168	B=-0.00813 [-0.02725, 0.01100] p=0.403	%/mmHg
Hypertension	B=0.00500 [-0.01313, 0.02314] p=0.587	B=0.00381 [-0.00195, 0.00957] p=0.193	B=0.00858 [-0.00699, 0.02414] p=0.278	%/mmHg
Hypercholesterolaemia	B=0.00122 [-0.01638, 0.01883] p=0.891	B=0.00119 [-0.00440, 0.00678] p=0.676	B=-0.00268 [-0.01780, 0.01244] p=0.727	%/mmHg

Table A3-15: Cross-sectional linear regression between CVR and BG PVS volume, adjusted for age, sex and vascular risk factors. Columns 2 to 4 contain the regression coefficients, 95% confidence intervals and p-values. The last column gives the units of the regression coefficient.

Variables	SGM CVR	NAWM CVR	WMH CVR	Units of B
BG PVS volume	B=-0.00237 [-0.00657, 0.00183] p=0.267	B=-0.000637 [-0.001971, 0.000696] p=0.347	B=-0.00145 [-0.00512, 0.00222] p=0.435	%/mmHg per %ROIV
Age	B=-0.000898 [-0.001744, -0.000053] p=0.037	B=-0.000174 [-0.000442, 0.000094] p=0.202	B=-0.000286 [-0.001052, 0.000480] p=0.462	%/mmHg per year
Sex [Male]	B=0.0159 [-0.0012, 0.0331] p=0.069	B=0.00358 [-0.00188, 0.00903] p=0.197	B=0.00597 [-0.00888, 0.02083] p=0.428	%/mmHg
MAP	B=-0.000134 [-0.000756, 0.000487] p=0.670	B=-0.000037 [-0.000234, 0.000160] p=0.709	B=0.000029 [-0.000516, 0.000574] p=0.917	%/mmHg per mmHg
Diabetes	B=0.000196 [-0.020622, 0.021013] p=0.985	B=-0.00103 [-0.00764, 0.00557] p=0.758	B=-0.00698 [-0.02519, 0.01124] p=0.451	%/mmHg
Smoker [Ever]	B=-0.0135 [-0.0308, 0.0037] p=0.124	B=-0.00246 [-0.00793, 0.00302] p=0.377	B=-0.00124 [-0.01627, 0.01379] p=0.871	%/mmHg
Smoker [Current]	B=-0.0270 [-0.0497, -0.0043] p=0.020	B=-0.00566 [-0.01287, 0.00155] p=0.123	B=-0.00744 [-0.02735, 0.01247] p=0.461	%/mmHg
Hypertension	B=0.00453 [-0.01480, 0.02386] p=0.644	B=0.00320 [-0.00293, 0.00934] p=0.304	B=0.00655 [-0.01042, 0.02351] p=0.447	%/mmHg
Hypercholesterolaemia	B=0.00543 [-0.01228, 0.02314] p=0.545	B=0.00233 [-0.00329, 0.00795] p=0.414	B=0.00154 [-0.01393, 0.01701] p=0.844	%/mmHg

Table A3-16: Cross-sectional linear regression between CVR and CSO PVS volume, adjusted for age, sex and vascular risk factors. Columns 2 to 4 contain the regression coefficients, 95% confidence intervals and p-values. The last column gives the units of the regression coefficient.

Variables	SGM CVR	NAWM CVR	WMH CVR	Units of B
CSO PVS volume	B=0.00255 [-0.00105, 0.00615] p=0.163	B=0.000064 [-0.001083, 0.001211] p=0.912	B=-0.00191 [-0.00504, 0.00121] p=0.229	%/mmHg per %ROIV
Age	B=-0.00140 [-0.00222, -0.00058] p=0.001	B=-0.000244 [-0.000506, 0.000018] p=0.068	B=-0.000229 [-0.000973, 0.000514] p=0.543	%/mmHg per year
Sex [Male]	B=0.0139 [-0.0031, 0.0310] p=0.109	B=0.00323 [-0.00221, 0.00866] p=0.243	B=0.00575 [-0.00897, 0.02048] p=0.442	%/mmHg
MAP	B=-0.000153 [-0.000774, 0.000468] p=0.626	B=-0.000037 [-0.000235, 0.000161] p=0.711	B=0.000049 [-0.000495, 0.000594] p=0.858	%/mmHg per mmHg
Diabetes	B=-0.000980 [-0.021733, 0.019774] p=0.926	B=-0.00122 [-0.00784, 0.00540] p=0.716	B=-0.00681 [-0.02498, 0.01136] p=0.460	%/mmHg
Smoker [Ever]	B=-0.0122 [-0.0293, 0.0050] p=0.163	B=-0.00219 [-0.00765, 0.00328] p=0.430	B=-0.000908 [-0.015825, 0.014010] p=0.905	%/mmHg
Smoker [Current]	B=-0.0317 [-0.0544, -0.0090] p=0.007	B=-0.00627 [-0.01351, 0.00097] p=0.089	B=-0.00680 [-0.02666, 0.01307] p=0.500	%/mmHg
Hypertension	B=-0.00241 [-0.02063, 0.01580] p=0.794	B=0.00200 [-0.00380, 0.00781] p=0.496	B=0.00597 [-0.00993, 0.02187] p=0.459	%/mmHg
Hypercholesterolaemia	B=0.00672 [-0.01089, 0.02433] p=0.452	B=0.00258 [-0.00303, 0.00819] p=0.365	B=0.00166 [-0.01373, 0.01704] p=0.832	%/mmHg

Table A3-17: Cross-sectional linear regression between CVR and total PVS volume, adjusted for age, sex and vascular risk factors. Columns 2 to 4 contain the regression coefficients, 95% confidence intervals and p-values. The last column gives the units of the regression coefficient.

Variables	SGM CVR	NAWM CVR	WMH CVR	Units of B
Total PVS volume	B=0.00215 [-0.00174, 0.00605] p=0.276	B=-0.000017 [-0.001254, 0.001220] p=0.978	B=-0.00209 [-0.00547, 0.00129] p=0.224	%/mmHg per %ROIV
Age	B=-0.00136 [-0.00220, -0.00052] p=0.002	B=-0.000236 [-0.000502, 0.000031] p=0.083	B=-0.000211 [-0.000967, 0.000545] p=0.583	%/mmHg per year
Sex [Male]	B=0.0140 [-0.0031, 0.0311] p=0.108	B=0.00325 [-0.00219, 0.00869] p=0.239	B=0.00586 [-0.00888, 0.02059] p=0.434	%/mmHg
MAP	B=-0.000147 [-0.000769, 0.000475] p=0.642	B=-0.000036 [-0.000234, 0.000161] p=0.716	B=0.000048 [-0.000496, 0.000592] p=0.862	%/mmHg per mmHg
Diabetes	B=-0.000919 [-0.021724, 0.019886] p=0.931	B=-0.00120 [-0.00782, 0.00541] p=0.720	B=-0.00677 [-0.02494, 0.01140] p=0.463	%/mmHg
Smoker [Ever]	B=-0.0121 [-0.0293, 0.0051] p=0.166	B=-0.00220 [-0.00767, 0.00327] p=0.428	B=-0.00104 [-0.01597, 0.01388] p=0.891	%/mmHg
Smoker [Current]	B=-0.0312 [-0.0539, -0.0084] p=0.008	B=-0.00619 [-0.01343, 0.00106] p=0.094	B=-0.00671 [-0.02659, 0.01318] p=0.506	%/mmHg
Hypertension	B=-0.00226 [-0.02070, 0.01618] p=0.809	B=0.00209 [-0.00377, 0.00796] p=0.482	B=0.00644 [-0.00963, 0.02251] p=0.430	%/mmHg
Hypercholesterolaemia	B=0.00672 [-0.01094, 0.02437] p=0.454	B=0.00257 [-0.00305, 0.00818] p=0.368	B=0.00159 [-0.01380, 0.01697] p=0.839	%/mmHg

Table A3-18: Cross-sectional linear regression between CVR and SVD score, adjusted for age, sex and vascular risk factors. Columns 2 to 4 contain the regression coefficients, 95% confidence intervals and p-values. The last column gives the units of the regression coefficient.

Variables	SGM CVR	NAWM CVR	WMH CVR	Units of B
SVD score	B=-0.0150 [-0.0211, -0.0090] p<0.001	B=-0.00314 [-0.00514, -0.00115] p=0.002	B=-0.00554 [-0.01106, -0.00002] p=0.049	%/mmHg per score point
Age	B=-0.000425 [-0.001141, 0.000291] p=0.243	B=-0.000093 [-0.000329, 0.000143] p=0.439	B=-0.000236 [-0.000908, 0.000437] p=0.490	%/mmHg per year
Sex [Male]	B=0.00898 [-0.00685, 0.02482] p=0.264	B=0.00206 [-0.00317, 0.00728] p=0.439	B=0.00182 [-0.01254, 0.01618] p=0.803	%/mmHg
MAP	B=0.000004 [-0.000572, 0.000580] p=0.989	B=-0.000018 [-0.000208, 0.000172] p=0.853	B=0.000137 [-0.000391, 0.000666] p=0.609	%/mmHg per mmHg
Diabetes	B=-0.00564 [-0.02421, 0.01292] p=0.549	B=-0.00263 [-0.00876, 0.00349] p=0.398	B=-0.00555 [-0.02254, 0.01144] p=0.520	%/mmHg
Smoker [Ever]	B=-0.0151 [-0.0310, 0.0008] p=0.062	B=-0.00268 [-0.00792, 0.00256] p=0.313	B=-0.00368 [-0.01814, 0.01078] p=0.616	%/mmHg
Smoker [Current]	B=-0.0170 [-0.0382, 0.0042] p=0.116	B=-0.00347 [-0.01046, 0.00353] p=0.329	B=-0.00693 [-0.02636, 0.01249] p=0.482	%/mmHg
Hypertension	B=0.0136 [-0.0036, 0.0308] p=0.120	B=0.00519 [-0.00048, 0.01086] p=0.072	B=0.00839 [-0.00739, 0.02416] p=0.296	%/mmHg
Hypercholesterolaemia	B=-0.00186 [-0.01833, 0.01462] p=0.824	B=0.000808 [-0.004628, 0.006243] p=0.770	B=-0.00161 [-0.01669, 0.01347] p=0.833	%/mmHg

Table A3-19: Cross-sectional linear regression between CVR and NIHSS, adjusted for age, sex and vascular risk factors. Columns 2 to 4 contain the regression coefficients, 95% confidence intervals and p-values. The last column gives the units of the regression coefficient.

Variables	SGM CVR	NAWM CVR	WMH CVR	Units of B
NIHSS	B=-0.00412 [-0.00994, 0.00171] p=0.165	B=-0.00125 [-0.00310, 0.00060] p=0.185	B=-0.000202 [-0.005188, 0.004784] p=0.936	%/mmHg per score point
Age	B=-0.000962 [-0.001683, -0.000241] p=0.009	B=-0.000199 [-0.000428, 0.000030] p=0.088	B=-0.000462 [-0.001106, 0.000182] p=0.159	%/mmHg per year
Sex [Male]	B=0.0133 [-0.0035, 0.0300] p=0.119	B=0.00299 [-0.00233, 0.00831] p=0.268	B=0.00340 [-0.01105, 0.01786] p=0.643	%/mmHg
MAP	B=-0.000036 [-0.000653, 0.000582] p=0.909	B=-0.000020 [-0.000216, 0.000176] p=0.842	B=0.000101 [-0.000439, 0.000641] p=0.712	%/mmHg per mmHg
Diabetes	B=-0.00424 [-0.02396, 0.01548] p=0.672	B=-0.00230 [-0.00856, 0.00397] p=0.470	B=-0.00514 [-0.02234, 0.01206] p=0.556	%/mmHg
Smoker [Ever]	B=-0.0114 [-0.0282, 0.0054] p=0.183	B=-0.00186 [-0.00720, 0.00349] p=0.493	B=-0.00248 [-0.01708, 0.01212] p=0.738	%/mmHg
Smoker [Current]	B=-0.0235 [-0.0462, -0.0008] p=0.043	B=-0.00448 [-0.01170, 0.00273] p=0.222	B=-0.0104 [-0.0301, 0.0094] p=0.303	%/mmHg
Hypertension	B=0.00300 [-0.01464, 0.02065] p=0.737	B=0.00314 [-0.00247, 0.00874] p=0.271	B=0.00365 [-0.01169, 0.01899] p=0.639	%/mmHg
Hypercholesterolaemia	B=0.00385 [-0.01350, 0.02119] p=0.662	B=0.00202 [-0.00349, 0.00753] p=0.469	B=0.000462 [-0.014661, 0.015584] p=0.952	%/mmHg

Table A3-20: Cross-sectional linear regression between CVR and mRS, adjusted for age, sex and vascular risk factors. Columns 2 to 4 contain the regression coefficients, 95% confidence intervals and p-values. The last column gives the units of the regression coefficient.

Variables	SGM CVR	NAWM CVR	WMH CVR	Units of B
mRS	B=-0.00144 [-0.01336, 0.01048] p=0.812	B=-0.00188 [-0.00565, 0.00190] p=0.327	B=0.00171 [-0.00863, 0.01205] p=0.744	%/mmHg per score point
Age	B=-0.00103 [-0.00174, -0.00031] p=0.006	B=-0.000216 [-0.000444, 0.000011] p=0.062	B=-0.000467 [-0.001107, 0.000173] p=0.152	%/mmHg per year
Sex [Male]	B=0.0129 [-0.0040, 0.0297] p=0.133	B=0.00284 [-0.00249, 0.00817] p=0.294	B=0.00347 [-0.01098, 0.01792] p=0.636	%/mmHg
MAP	B=-0.000105 [-0.000718, 0.000508] p=0.736	B=-0.000042 [-0.000236, 0.000153] p=0.673	B=0.000096 [-0.000437, 0.000629] p=0.722	%/mmHg per mmHg
Diabetes	B=-0.00448 [-0.02437, 0.01540] p=0.657	B=-0.00217 [-0.00847, 0.00413] p=0.497	B=-0.00543 [-0.02269, 0.01182] p=0.535	%/mmHg
Smoker [Ever]	B=-0.0120 [-0.0289, 0.0049] p=0.164	B=-0.00212 [-0.00747, 0.00324] p=0.437	B=-0.00245 [-0.01703, 0.01213] p=0.741	%/mmHg
Smoker [Current]	B=-0.0264 [-0.0495, -0.0033] p=0.025	B=-0.00462 [-0.01193, 0.00269] p=0.214	B=-0.0114 [-0.0314, 0.0086] p=0.263	%/mmHg
Hypertension	B=0.00146 [-0.01619, 0.01910] p=0.871	B=0.00288 [-0.00271, 0.00846] p=0.311	B=0.00337 [-0.01188, 0.01862] p=0.663	%/mmHg
Hypercholesterolaemia	B=0.00357 [-0.01387, 0.02101] p=0.687	B=0.00191 [-0.00361, 0.00743] p=0.495	B=0.000498 [-0.014620, 0.015615] p=0.948	%/mmHg

Table A3-21: Cross-sectional linear regression between CVR and MoCA, adjusted for age, sex and vascular risk factors. Columns 2 to 4 contain the regression coefficients, 95% confidence intervals and p-values. The last column gives the units of the regression coefficient.

Variables	SGM CVR	NAWM CVR	WMH CVR	Units of B
MoCA	B=0.00231 [0.00001, 0.00462] p=0.049	B=0.000713 [-0.000019, 0.001444] p=0.056	B=0.000783 [-0.001209, 0.002776] p=0.439	%/mmHg per score point
Age	B=-0.000871 [-0.001610, -0.000132] p=0.021	B=-0.000172 [-0.000406, 0.000062] p=0.149	B=-0.000404 [-0.001067, 0.000259] p=0.231	%/mmHg per year
Sex [Male]	B=0.0111 [-0.0057, 0.0279] p=0.195	B=0.00226 [-0.00307, 0.00758] p=0.404	B=0.00219 [-0.01231, 0.01668] p=0.766	%/mmHg
MAP	B=-0.000162 [-0.000777, 0.000452] p=0.602	B=-0.000062 [-0.000256, 0.000133] p=0.533	B=0.000094 [-0.000439, 0.000626] p=0.729	%/mmHg per mmHg
Diabetes	B=-0.00225 [-0.02205, 0.01755] p=0.823	B=-0.00163 [-0.00790, 0.00465] p=0.610	B=-0.00399 [-0.02124, 0.01325] p=0.648	%/mmHg
Smoker [Ever]	B=-0.00980 [-0.02693, 0.00733] p=0.260	B=-0.00133 [-0.00676, 0.00411] p=0.631	B=-0.00178 [-0.01661, 0.01304] p=0.813	%/mmHg
Smoker [Current]	B=-0.0259 [-0.0481, -0.0038] p=0.022	B=-0.00517 [-0.01219, 0.00184] p=0.147	B=-0.00981 [-0.02912, 0.00950] p=0.317	%/mmHg
Hypertension	B=0.00355 [-0.01422, 0.02132] p=0.694	B=0.00329 [-0.00235, 0.00892] p=0.251	B=0.00416 [-0.01129, 0.01960] p=0.596	%/mmHg
Hypercholesterolaemia	B=0.00410 [-0.01348, 0.02168] p=0.646	B=0.00215 [-0.00342, 0.00773] p=0.447	B=0.00220 [-0.01310, 0.01751] p=0.777	%/mmHg

A3.3 Sensitivity analyses

Table A3-22: Regression coefficients from cross-sectional analysis after adjusting for WMH volume. Each row represents a different statistical model where the SVD predictor of interest is given in the first column. The associated regression coefficient *B*, its 95% confidence interval and *p*-value are given in columns 2-4. The last column gives the units of *B*. All models were corrected for WMH volume, age, sex, MAP, diagnosis of diabetes, hypertension, and hypercholesterolaemia and history of smoking.

Variables	SGM CVR	NAWM CVR	WMH CVR	Units of B
Number of lacunes	B=-0.00535 [-0.00825, -0.00246] p<0.001	B=-0.00100 [-0.00195, -0.00005] p=0.039	B=0.000191 [-0.002343, 0.002725] p=0.882	%BOLD/mmHg per lacune
Number of microbleeds	B=-0.00101 [-0.00262, 0.00059] p=0.214	B=-0.000726 [-0.001229, -0.000223] p=0.005	B=-0.00101 [-0.00236, 0.00034] p=0.141	%BOLD/mmHg per microbleed
Deep atrophy score	B=-0.00308 [-0.00945, 0.00330] p=0.342	B=-0.00166 [-0.00369, 0.00036] p=0.107	B=-0.00242 [-0.00783, 0.00299] p=0.379	%BOLD/mmHg per score unit
Superficial atrophy score	B=-0.000470 [-0.007035, 0.006095] p=0.888	B=-0.000658 [-0.002751, 0.001435] p=0.536	B=-0.00287 [-0.00840, 0.00266] p=0.307	%BOLD/mmHg per score unit
Total atrophy score	B=-0.00106 [-0.00457, 0.00244] p=0.550	B=-0.000690 [-0.001806, 0.000426] p=0.224	B=-0.00154 [-0.00449, 0.00141] p=0.305	%BOLD/mmHg per score unit
Brain volume	B=0.000011 [-0.002400, 0.002422] p=0.993	B=0.000324 [-0.000444, 0.001092] p=0.406	B=0.000399 [-0.001643, 0.002441] p=0.700	%BOLD/mmHg per %ICV
BG PVS score	B=-0.00694 [-0.01785, 0.00396] p=0.211	B=-0.00221 [-0.00569, 0.00127] p=0.211	B=-0.00185 [-0.01115, 0.00745] p=0.695	%BOLD/mmHg per score unit
CSO PVS score	B=0.00169 [-0.00776, 0.01114] p=0.724	B=0.000137 [-0.002880, 0.003154] p=0.929	B=-0.00521 [-0.01331, 0.00289] p=0.206	%BOLD/mmHg per score unit
Total PVS score	B=-0.00150 [-0.00770, 0.00470] p=0.634	B=-0.000651 [-0.002630, 0.001327] p=0.517	B=-0.00284 [-0.00815, 0.00247] p=0.293	%BOLD/mmHg per score unit

BG PVS volume	B=-0.000202 [-0.004823, 0.004418] p=0.931	B=0.000094 [-0.001369, 0.001557] p=0.899	B=0.00151 [-0.00241, 0.00543] p=0.447	%BOLD/mmHg per %ROIV
CSO PVS volume	B=0.00413 [0.00046, 0.00780] p=0.028	B=0.000507 [-0.000669, 0.001683] p=0.396	B=-0.000455 [-0.003614, 0.002703] p=0.776	%BOLD/mmHg per %ROIV
Total PVS volume	B=0.00412 [0.00010, 0.00814] p=0.045	B=0.000534 [-0.000753, 0.001820] p=0.414	B=-0.000270 [-0.003729, 0.003189] p=0.878	%BOLD/mmHg per %ROIV
NIHSS	B=-0.00311 [-0.00890, 0.00268] p=0.291	B=-0.000970 [-0.002819, 0.000878] p=0.302	B=0.000972 [-0.003901, 0.005846] p=0.694	%BOLD/mmHg per score unit
mRS	B=-0.000139 [-0.011888, 0.011610] p=0.981	B=-0.00153 [-0.00527, 0.00221] p=0.420	B=0.00320 [-0.00684, 0.01324] p=0.530	%BOLD/mmHg per score unit
MoCA	B=0.00192 [-0.00038, 0.00422] p=0.100	B=0.000609 [-0.000124, 0.001341] p=0.103	B=0.000341 [-0.001607, 0.002288] p=0.730	%BOLD/mmHg per score unit

Table A3-23: Regression coefficients from cross-sectional analysis after adjusting for EtCO₂ baseline. Each row represents a different statistical model where the SVD predictor of interest is given in the first column. The associated regression coefficient *B*, its 95% confidence interval and *p*-value are given in columns 2-4. The last column gives the units of *B*. All models were corrected for EtCO₂ baseline, age, sex, MAP, diagnosis of diabetes, hypertension, and hypercholesterolaemia and history of smoking.

Variables	SGM CVR	NAWM CVR	WMH CVR	Units of B
WMH volume	B=-0.0220 [-0.0398, -0.0042] p=0.016	B=-0.00614 [-0.01198, -0.00029] p=0.040	B=-0.0278 [-0.0445, -0.0110] p=0.001	%BOLD/mmHg per log ₁₀ (%ICV)
Periventricular Fazekas score	B=-0.0173 [-0.0269, -0.0076] p=0.001	B=-0.00485 [-0.00804, -0.00167] p=0.003	B=-0.0142 [-0.0232, -0.0053] p=0.002	%BOLD/mmHg per score unit
Deep white matter Fazekas score	B=-0.00879 [-0.01892, 0.00134] p=0.089	B=-0.00225 [-0.00557, 0.00106] p=0.182	B=-0.00936 [-0.01871, -0.00001] p=0.050	%BOLD/mmHg per score unit
Total Fazekas score	B=-0.00759 [-0.01290, -0.00228] p=0.005	B=-0.00207 [-0.00382, -0.00033] p=0.020	B=-0.00689 [-0.01181, -0.00196] p=0.006	%BOLD/mmHg per score unit
Number of lacunes	B=-0.00531 [-0.00778, -0.00284] p<0.001	B=-0.00109 [-0.00193, -0.00026] p=0.010	B=-0.00135 [-0.00371, 0.00101] p=0.260	%BOLD/mmHg per lacune
Number of microbleeds	B=-0.00172 [-0.00313, -0.00030] p=0.018	B=-0.000859 [-0.001310, -0.000408] p<0.001	B=-0.00170 [-0.00298, -0.00041] p=0.010	%BOLD/mmHg per microbleed
Deep atrophy score	B=-0.00421 [-0.01010, 0.00169] p=0.161	B=-0.00195 [-0.00386, -0.00003] p=0.046	B=-0.00442 [-0.00976, 0.00093] p=0.104	%BOLD/mmHg per score unit
Superficial atrophy score	B=-0.00124 [-0.00745, 0.00497] p=0.694	B=-0.000878 [-0.002903, 0.001147] p=0.393	B=-0.00387 [-0.00951, 0.00177] p=0.177	%BOLD/mmHg per score unit
Total atrophy score	B=-0.00164 [-0.00491, 0.00164] p=0.325	B=-0.000841 [-0.001905, 0.000223] p=0.120	B=-0.00243 [-0.00539, 0.00053] p=0.107	%BOLD/mmHg per score unit
Brain volume	B=0.00103	B=0.000582	B=0.00120	%BOLD/mmHg per %ICV

	[-0.00121, 0.00328] p=0.364	[-0.000147, 0.001311] p=0.117	[-0.00085, 0.00326] p=0.248	
BG PVS score	B=-0.0109 [-0.0203, -0.0015] p=0.023	B=-0.00327 [-0.00634, -0.00019] p=0.038	B=-0.00740 [-0.01606, 0.00126] p=0.093	%BOLD/mmHg per score unit
CSO PVS score	B=-0.000484 [-0.009197, 0.008230] p=0.913	B=-0.000486 [-0.003330, 0.002359] p=0.736	B=-0.00803 [-0.01603, -0.00002] p=0.049	%BOLD/mmHg per score unit
Total PVS score	B=-0.00372 [-0.00913, 0.00169] p=0.176	B=-0.00125 [-0.00301, 0.00052] p=0.165	B=-0.00555 [-0.01051, -0.00060] p=0.028	%BOLD/mmHg per score unit
BG PVS volume	B=-0.00216 [-0.00611, 0.00180] p=0.283	B=-0.000564 [-0.001846, 0.000718] p=0.386	B=-0.00129 [-0.00497, 0.00239] p=0.489	%BOLD/mmHg per %ROIV
CSO PVS volume	B=0.00301 [-0.00038, 0.00640] p=0.081	B=0.000203 [-0.000904, 0.001309] p=0.718	B=-0.00170 [-0.00486, 0.00145] p=0.288	%BOLD/mmHg per %ROIV
Total PVS volume	B=0.00263 [-0.00104, 0.00629] p=0.159	B=0.000127 [-0.001067, 0.001321] p=0.834	B=-0.00186 [-0.00527, 0.00155] p=0.282	%BOLD/mmHg per %ROIV
SVD score	B=-0.0134 [-0.0192, -0.0077] p<0.001	B=-0.00274 [-0.00468, -0.00079] p=0.006	B=-0.00496 [-0.01053, 0.00061] p=0.081	%BOLD/mmHg per score unit
NIHSS	B=-0.00208 [-0.00766, 0.00350] p=0.463	B=-0.000735 [-0.002557, 0.001086] p=0.426	B=0.000585 [-0.004473, 0.005644] p=0.820	%BOLD/mmHg per score unit
mRS	B=0.000476 [-0.010757, 0.011708] p=0.933	B=-0.00140 [-0.00506, 0.00226] p=0.451	B=0.00265 [-0.00772, 0.01302] p=0.615	%BOLD/mmHg per score unit
MoCA	B=0.00202 [-0.00017, 0.00421] p=0.071	B=0.000639 [-0.000075, 0.001353] p=0.079	B=0.000631 [-0.001382, 0.002644] p=0.537	%BOLD/mmHg per score unit

Table A3-24: Regression coefficients from cross-sectional analysis after excluding datasets with high motion during BOLD-CVR scan. Each row represents a different statistical model where the SVD predictor of interest is given in the first column. The associated regression coefficient *B*, its 95% confidence interval and *p*-value are given in columns 2-4. The last column gives the units of *B*. All models were corrected for age, sex, MAP, diagnosis of diabetes, hypertension, and hypercholesterolaemia and history of smoking. A total of 12 datasets was removed.

Variables	SGM CVR	NAWM CVR	WMH CVR	Units of B
WMH volume	B=-0.0195 [-0.0392, 0.0002] p=0.052	B=-0.00599 [-0.01219, 0.00021] p=0.058	B=-0.0267 [-0.0440, -0.0093] p=0.003	%BOLD/mmHg per log ₁₀ (%ICV)
Periventricular Fazekas score	B=-0.0176 [-0.0284, -0.0068] p=0.002	B=-0.00500 [-0.00843, -0.00158] p=0.004	B=-0.0138 [-0.0233, -0.0044] p=0.004	%BOLD/mmHg per score unit
Deep white matter Fazekas score	B=-0.00845 [-0.01941, 0.00251] p=0.130	B=-0.00224 [-0.00570, 0.00122] p=0.202	B=-0.00879 [-0.01830, 0.00072] p=0.070	%BOLD/mmHg per score unit
Total Fazekas score	B=-0.00747 [-0.01331, -0.00163] p=0.012	B=-0.00208 [-0.00393, -0.00023] p=0.028	B=-0.00654 [-0.01162, -0.00146] p=0.012	%BOLD/mmHg per score unit
Number of lacunes	B=-0.00534 [-0.00819, -0.00249] p<0.001	B=-0.00120 [-0.00212, -0.00028] p=0.011	B=-0.00142 [-0.00396, 0.00111] p=0.269	%BOLD/mmHg per lacune
Number of microbleeds	B=-0.00140 [-0.00296, 0.00015] p=0.076	B=-0.000813 [-0.001291, -0.000336] p=0.001	B=-0.00144 [-0.00277, -0.00012] p=0.033	%BOLD/mmHg per microbleed
Deep atrophy score	B=-0.00381 [-0.01031, 0.00269] p=0.249	B=-0.00210 [-0.00413, -0.00007] p=0.042	B=-0.00443 [-0.00997, 0.00112] p=0.117	%BOLD/mmHg per score unit
Superficial atrophy score	B=-0.00124 [-0.00813, 0.00565] p=0.722	B=-0.000962 [-0.003128, 0.001203] p=0.381	B=-0.00358 [-0.00947, 0.00238] p=0.232	%BOLD/mmHg per score unit
Total atrophy score	B=-0.00152 [-0.00513, 0.00210] p=0.409	B=-0.000912 [-0.002043, 0.000219] p=0.113	B=-0.00234 [-0.00541, 0.00074] p=0.135	%BOLD/mmHg per score unit
Brain volume	B=-0.000163	B=0.000722	B=0.00119	%BOLD/mmHg per %ICV

	[-0.002843, 0.002518] p=0.905	[-0.000115, 0.001558] p=0.090	[-0.00112, 0.00350] p=0.309	
BG PVS score	B=-0.0101 [-0.0204, 0.0001] p=0.052	B=-0.00292 [-0.00615, 0.00032] p=0.077	B=-0.00740 [-0.01626, 0.00147] p=0.101	%BOLD/mmHg per score unit
CSO PVS score	B=0.000783 [-0.008831, 0.010396] p=0.872	B=-0.000179 [-0.003206, 0.002849] p=0.907	B=-0.00656 [-0.01494, 0.00181] p=0.124	%BOLD/mmHg per score unit
Total PVS score	B=-0.00299 [-0.00888, 0.00290] p=0.317	B=-0.00101 [-0.00286, 0.00084] p=0.283	B=-0.00490 [-0.00999, 0.00019] p=0.059	%BOLD/mmHg per score unit
BG PVS volume	B=-0.00131 [-0.00569, 0.00307] p=0.557	B=-0.000376 [-0.001747, 0.000996] p=0.589	B=-0.00141 [-0.00521, 0.00239] p=0.465	%BOLD/mmHg per %ROIV
CSO PVS volume	B=0.00387 [0.00011, 0.00763] p=0.044	B=0.000539 [-0.000652, 0.001730] p=0.373	B=-0.00148 [-0.00477, 0.00181] p=0.376	%BOLD/mmHg per %ROIV
Total PVS volume	B=0.00359 [-0.00049, 0.00766] p=0.084	B=0.00048 [-0.00080, 0.00177] p=0.461	B=-0.00167 [-0.00523, 0.00189] p=0.355	%BOLD/mmHg per %ROIV
SVD score	B=-0.0141 [-0.0205, -0.0076] p<0.001	B=-0.00301 [-0.00511, -0.00091] p=0.005	B=-0.00533 [-0.01121, 0.00055] p=0.075	%BOLD/mmHg per score unit
NIHSS	B=-0.00467 [-0.01105, 0.00171] p=0.150	B=-0.00234 [-0.00433, -0.00035] p=0.021	B=-0.00156 [-0.00702, 0.00391] p=0.575	%BOLD/mmHg per score unit
mRS	B=0.00109 [-0.01146, 0.01365] p=0.864	B=-0.00149 [-0.00543, 0.00246] p=0.458	B=0.00316 [-0.00776, 0.01407] p=0.568	%BOLD/mmHg per score unit
MoCA	B=0.00240 [-0.00002, 0.00483] p=0.052	B=0.000934 [0.000177, 0.001690] p=0.016	B=0.000932 [-0.001167, 0.003031] p=0.382	%BOLD/mmHg per score unit

Table A3-25: Regression coefficients from cross-sectional analysis after excluding datasets with short hypercapnic paradigm. Each row represents a different statistical model where the SVD predictor of interest is given in the first column. The associated regression coefficient *B*, its 95% confidence interval and *p*-value are given in columns 2-4. The last column gives the units of *B*. All models were corrected for age, sex, MAP, diagnosis of diabetes, hypertension, and hypercholesterolaemia and history of smoking. A total of 15 datasets (15/182 for SGM, NAWM CVR analyses and 15/175 for WMH CVR) was removed.

Variables	SGM CVR	NAWM CVR	WMH CVR	Units of B
WMH volume	B=-0.0305 [-0.0504, -0.0107] p=0.003	B=-0.00678 [-0.01275, -0.00081] p=0.026	B=-0.0210 [-0.0355, -0.0065] p=0.005	%BOLD/mmHg per log ₁₀ (%ICV)
Periventricular Fazekas score	B=-0.0230 [-0.0337, -0.0123] p<0.001	B=-0.00501 [-0.00826, -0.00177] p=0.003	B=-0.00935 [-0.01712, -0.00158] p=0.019	%BOLD/mmHg per score unit
Deep white matter Fazekas score	B=-0.0110 [-0.0222, 0.0001] p=0.053	B=-0.00241 [-0.00574, 0.00092] p=0.155	B=-0.00934 [-0.01716, -0.00152] p=0.020	%BOLD/mmHg per score unit
Total Fazekas score	B=-0.00983 [-0.01569, -0.00396] p=0.001	B=-0.00214 [-0.00391, -0.00038] p=0.018	B=-0.00541 [-0.00959, -0.00123] p=0.012	%BOLD/mmHg per score unit
Number of lacunes	B=-0.00618 [-0.00888, -0.00349] p<0.001	B=-0.00126 [-0.00208, -0.00043] p=0.003	B=-0.00203 [-0.00399, -0.00007] p=0.043	%BOLD/mmHg per lacune
Number of microbleeds	B=-0.00163 [-0.00319, -0.00007] p=0.040	B=-0.000756 [-0.001210, -0.000303] p=0.001	B=-0.00181 [-0.00286, -0.00076] p=0.001	%BOLD/mmHg per microbleed
Deep atrophy score	B=-0.00546 [-0.01218, 0.00126] p=0.111	B=-0.00259 [-0.00455, -0.00062] p=0.010	B=-0.00540 [-0.01001, -0.00079] p=0.022	%BOLD/mmHg per score unit
Superficial atrophy score	B=-0.00221 [-0.00914, 0.00472] p=0.529	B=-0.00158 [-0.00362, 0.00046] p=0.128	B=-0.00376 [-0.00855, 0.00103] p=0.123	%BOLD/mmHg per score unit
Total atrophy score	B=-0.00226 [-0.00595, 0.00143] p=0.227	B=-0.00123 [-0.00231, -0.00014] p=0.027	B=-0.00268 [-0.00521, -0.00015] p=0.038	%BOLD/mmHg per score unit
Brain volume	B=0.00118	B=0.000573	B=0.000758	%BOLD/mmHg per %ICV

	[-0.00133, 0.00369] p=0.354	[-0.000167, 0.001314] p=0.128	[-0.000994, 0.002510] p=0.394	
BG PVS score	B=-0.0146 [-0.0252, -0.0040] p=0.007	B=-0.00317 [-0.00634, 0.00000] p=0.050	B=-0.00764 [-0.01510, -0.00018] p=0.045	%BOLD/mmHg per score unit
CSO PVS score	B=-0.00220 [-0.01191, 0.00752] p=0.656	B=-0.000100 [-0.002983, 0.002783] p=0.946	B=-0.00909 [-0.01582, -0.00236] p=0.008	%BOLD/mmHg per score unit
Total PVS score	B=-0.00548 [-0.01151, 0.00055] p=0.075	B=-0.00104 [-0.00284, 0.00076] p=0.254	B=-0.00602 [-0.01021, -0.00183] p=0.005	%BOLD/mmHg per score unit
BG PVS volume	B=-0.00336 [-0.00785, 0.00114] p=0.142	B=-0.00104 [-0.00237, 0.00028] p=0.122	B=-0.00165 [-0.00482, 0.00153] p=0.307	%BOLD/mmHg per %ROIV
CSO PVS volume	B=0.00225 [-0.00152, 0.00603] p=0.240	B=0.000045 [-0.001075, 0.001166] p=0.936	B=-0.00119 [-0.00384, 0.00146] p=0.377	%BOLD/mmHg per %ROIV
Total PVS volume	B=0.00174 [-0.00236, 0.00584] p=0.402	B=-0.000082 [-0.001295, 0.001131] p=0.894	B=-0.00140 [-0.00427, 0.00148] p=0.338	%BOLD/mmHg per %ROIV
SVD score	B=-0.0168 [-0.0231, -0.0105] p<0.001	B=-0.00297 [-0.00494, -0.00100] p=0.003	B=-0.00531 [-0.01003, -0.00058] p=0.028	%BOLD/mmHg per score unit
NIHSS	B=-0.00531 [-0.01142, 0.00080] p=0.088	B=-0.000935 [-0.002758, 0.000888] p=0.313	B=-0.000392 [-0.004640, 0.003857] p=0.856	%BOLD/mmHg per score unit
mRS	B=-0.00244 [-0.01521, 0.01033] p=0.706	B=-0.000281 [-0.004068, 0.003507] p=0.884	B=-0.00195 [-0.01093, 0.00703] p=0.669	%BOLD/mmHg per score unit
MoCA	B=0.00292 [0.00048, 0.00537] p=0.019	B=0.000665 [-0.000061, 0.001392] p=0.072	B=-0.000021 [-0.001741, 0.001698] p=0.981	%BOLD/mmHg per score unit

Table A3-26: Regression coefficients from cross-sectional analysis after excluding datasets where masks contain low number of voxels in mean BOLD space. Each row represents a different statistical model where the SVD predictor of interest is given in the first column. The associated regression coefficient B , its 95% confidence interval and p -value are given in the second column. The third column gives the units of B . All models were corrected for age, sex, MAP, diagnosis of diabetes, hypertension, and hypercholesterolaemia and history of smoking. Only WMH CVR analysis was affected by this sensitivity analysis where 34 datasets were removed.

Variables	WMH CVR	Units of B
WMH volume	$B=-0.0233$ [-0.0395, -0.0071] $p=0.005$	%BOLD/mmHg per $\log_{10}(\%ICV)$
Periventricular Fazekas score	$B=-0.0143$ [-0.0220, -0.0066] $p<0.001$	%BOLD/mmHg per score unit
Deep white matter Fazekas score	$B=-0.00864$ [-0.01651, -0.00076] $p=0.032$	%BOLD/mmHg per score unit
Total Fazekas score	$B=-0.00673$ [-0.01094, -0.00253] $p=0.002$	%BOLD/mmHg per score unit
Number of lacunes	$B=-0.00193$ [-0.00383, -0.00002] $p=0.047$	%BOLD/mmHg per lacune
Number of microbleeds	$B=-0.00190$ [-0.00289, -0.00090] $p<0.001$	%BOLD/mmHg per microbleed
Deep atrophy score	$B=-0.00348$ [-0.00811, 0.00116] $p=0.140$	%BOLD/mmHg per score unit
Superficial atrophy score	$B=-0.00176$ [-0.00655, 0.00303] $p=0.468$	%BOLD/mmHg per score unit
Total atrophy score	$B=-0.00153$ [-0.00407, 0.00100] $p=0.234$	%BOLD/mmHg per score unit
Brain volume	$B=0.00101$ [-0.00073, 0.00275] $p=0.253$	%BOLD/mmHg per %ICV
BG PVS score	$B=-0.00377$ [-0.01128, 0.00374] $p=0.322$	%BOLD/mmHg per score unit
CSO PVS score	$B=-0.00303$ [-0.01037, 0.00432] $p=0.416$	%BOLD/mmHg per score unit

Total PVS score	B=-0.00256 [-0.00711, 0.00200] p=0.268	%BOLD/mmHg per score unit
BG PVS volume	B=-0.000677 [-0.003754, 0.002400] p=0.664	%BOLD/mmHg per %ROIV
CSO PVS volume	B=-0.000272 [-0.002899, 0.002355] p=0.838	%BOLD/mmHg per %ROIV
Total PVS volume	B=-0.000354 [-0.003198, 0.002489] p=0.806	%BOLD/mmHg per %ROIV
SVD score	B=-0.00395 [-0.00878, 0.00089] p=0.109	%BOLD/mmHg per score unit
NIHSS	B=-0.000376 [-0.004591, 0.003838] p=0.860	%BOLD/mmHg per score unit
mRS	B=0.000292 [-0.008773, 0.009357] p=0.949	%BOLD/mmHg per score unit
MoCA	B=0.000891 [-0.000828, 0.002611] p=0.307	%BOLD/mmHg per score unit

A4 Supplementary material of Chapter 7

A4.1 Univariate analyses

Table A4-1: Regression coefficients from univariate longitudinal analysis. Each row represents a different statistical model where the SVD predictor of interest is given in the first column. The associated regression coefficient B , its 95% confidence interval and p -value are given in columns 2-4. The last column gives the units of B .

Variables	SGM CVR	NAWM CVR	WMH CVR	Units of B
WMH volume	$B=-0.425$ [-0.752, -0.097] $p=0.011$	$B=-1.37$ [-2.38, -0.36] $p=0.008$	$B=-0.301$ [-0.693, 0.090] $p=0.131$	$\log_{10}(\%ICV)$ per %/mmHg
Number of lacunes	$B=-0.701$ [-2.426, 1.024] $p=0.423$	$B=0.764$ [-4.549, 6.078] $p=0.777$	$B=-0.811$ [-2.839, 1.217] $p=0.431$	lacunes per %/mmHg
Number of microbleeds	$B=-0.330$ [-4.310, 3.650] $p=0.870$	$B=-3.04$ [-15.92, 9.84] $p=0.642$	$B=-0.386$ [-5.915, 5.142] $p=0.890$	microbleeds per %/mmHg
Brain volume	$B=-12.0$ [-29.5, 5.4] $p=0.175$	$B=10.5$ [-45.3, 66.3] $p=0.711$	$B=12.6$ [-8.5, 33.8] $p=0.239$	%ICV per %/mmHg
BG PVS volume	$B=-0.430$ [-0.789, -0.072] $p=0.019$	$B=-2.01847$ [-3.13216, -0.90478] $p<0.001$	$B=-0.616$ [-1.026, -0.205] $p=0.004$	$\log_{10}(\%ROIV)$ per %/mmHg
CSO PVS volume	$B=-0.286$ [-0.744, 0.172] $p=0.219$	$B=-2.01$ [-3.46, -0.56] $p=0.007$	$B=-0.233$ [-0.790, 0.323] $p=0.408$	$\log_{10}(\%ROIV)$ per %/mmHg
Total PVS volume	$B=-0.310$ [-0.724, 0.105] $p=0.142$	$B=-1.94$ [-3.25, -0.64] $p=0.004$	$B=-0.423$ [-0.918, 0.073] $p=0.094$	$\log_{10}(\%ROIV)$ per %/mmHg

A4.2 Adjusted analyses

Table A4-2: Longitudinal linear regression between WMH volume at one-year follow-up and baseline CVR, adjusted for WMH volume at baseline, age, sex and vascular risk factors. Columns 2 to 4 contain the regression coefficients, 95% confidence intervals and p-values. The last column gives the units of the regression coefficient.

Variables	SGM CVR	NAWM CVR	WMH CVR	Units of B
CVR	B=-0.325 [-0.653, 0.002] p=0.052	B=-1.14 [-2.13, -0.14] p=0.026	B=-0.251 [-0.635, 0.133] p=0.199	log ₁₀ (%ICV) per %/mmHg
Baseline WMH volume	B=0.996 [0.955, 1.037] p<0.001	B=0.997 [0.956, 1.038] p<0.001	B=0.995 [0.952, 1.037] p<0.001	
Age	B=0.00146 [-0.00023, 0.00315] p=0.089	B=0.00158 [-0.00010, 0.00325] p=0.064	B=0.00177 [0.00003, 0.00351] p=0.046	log ₁₀ (%ICV) per year
Sex [Male]	B=-0.0224 [-0.0582, 0.0134] p=0.218	B=-0.0230 [-0.0586, 0.0126] p=0.204	B=-0.0241 [-0.0598, 0.0115] p=0.183	log ₁₀ (%ICV)
MAP	B=-0.000789 [-0.002068, 0.000490] p=0.225	B=-0.000761 [-0.002035, 0.000513] p=0.240	B=-0.000575 [-0.001877, 0.000726] p=0.384	log ₁₀ (%ICV) per mmHg
Diabetes	B=0.0411 [-0.0014, 0.0837] p=0.058	B=0.0414 [-0.0009, 0.0837] p=0.055	B=0.0381 [-0.0051, 0.0813] p=0.083	log ₁₀ (%ICV)
Smoker [Ever]	B=0.0123 [-0.0235, 0.0482] p=0.498	B=0.0136 [-0.0220, 0.0492] p=0.452	B=0.0116 [-0.0243, 0.0475] p=0.524	log ₁₀ (%ICV)
Smoker [Current]	B=0.00163 [-0.04777, 0.05104] p=0.948	B=0.00437 [-0.04437, 0.05311] p=0.860	B=0.00523 [-0.04435, 0.05481] p=0.835	log ₁₀ (%ICV)
Hypertension	B=-0.0543 [-0.0951, -0.0136] p=0.009	B=-0.0533 [-0.0940, -0.0127] p=0.010	B=-0.0566 [-0.0982, -0.0150] p=0.008	log ₁₀ (%ICV)
Hypercholesterolaemia	B=0.00676	B=0.00782	B=0.0131	log ₁₀ (%ICV)

Appendix

[-0.02948, 0.04301] p=0.713	[-0.02830, 0.04394] p=0.669	[-0.0238, 0.0500] p=0.484
-----------------------------------	-----------------------------------	---------------------------------

Table A4-3: Longitudinal linear regression between number of lacunes at one-year follow-up and baseline CVR, adjusted for number of lacunes at baseline, age, sex and vascular risk factors. Columns 2 to 4 contain the regression coefficients, 95% confidence intervals and p-values. The last column gives the units of the regression coefficient.

Variables	SGM CVR	NAWM CVR	WMH CVR	Units of B
CVR	B=-0.809 [-2.591, 0.974] p=0.371	B=0.454 [-4.852, 5.761] p=0.866	B=-0.932 [-2.929, 1.065] p=0.358	lacunes per %/mmHg
Baseline number of lacunes	B=0.991 [0.959, 1.022] p<0.001	B=0.996 [0.966, 1.027] p<0.001	B=0.994 [0.963, 1.024] p<0.001	
Age	B=-0.000176 [-0.008457, 0.008104] p=0.966	B=0.000847 [-0.007264, 0.008958] p=0.837	B=-0.000019 [-0.008591, 0.008552] p=0.996	lacunes per year
Sex [Male]	B=0.0253 [-0.1623, 0.2129] p=0.790	B=0.0167 [-0.1710, 0.2044] p=0.861	B=0.0216 [-0.1688, 0.2120] p=0.823	lacunes
MAP	B=0.00456 [-0.00219, 0.01131] p=0.184	B=0.00466 [-0.00210, 0.01143] p=0.175	B=0.00514 [-0.00183, 0.01212] p=0.147	lacunes per mmHg
Diabetes	B=0.244 [0.021, 0.466] p=0.032	B=0.253 [0.030, 0.476] p=0.026	B=0.257 [0.027, 0.486] p=0.029	lacunes
Smoker [Ever]	B=-0.137 [-0.326, 0.053] p=0.156	B=-0.126 [-0.314, 0.063] p=0.191	B=-0.139 [-0.332, 0.053] p=0.155	lacunes
Smoker [Current]	B=-0.144 [-0.402, 0.114] p=0.273	B=-0.123 [-0.380, 0.133] p=0.344	B=-0.150 [-0.415, 0.115] p=0.265	lacunes
Hypertension	B=0.0162 [-0.1993, 0.2317] p=0.882	B=0.000620 [-0.214889, 0.216129] p=0.995	B=0.00681 [-0.21361, 0.22723] p=0.951	lacunes
Hypercholesterolaemia	B=0.227 [0.036, 0.418] p=0.020	B=0.228 [0.036, 0.419] p=0.020	B=0.227 [0.029, 0.424] p=0.025	lacunes

Table A4-4: Longitudinal linear regression between number of microbleeds at one-year follow-up and baseline CVR, adjusted for number of microbleeds at baseline, age, sex and vascular risk factors. Columns 2 to 4 contain the regression coefficients, 95% confidence intervals and p-values. The last column gives the units of the regression coefficient.

Variables	SGM CVR	NAWM CVR	WMH CVR	Units of B
CVR	B=-0.946 [-5.121, 3.230] p=0.655	B=-4.35 [-17.48, 8.79] p=0.514	B=-2.01 [-7.85, 3.82] p=0.496	microbleeds per %/mmHg
Baseline number of microbleeds	B=1.08 [1.04, 1.12] p<0.001	B=1.08 [1.04, 1.12] p<0.001	B=1.08 [1.03, 1.12] p<0.001	
Age	B=-0.0214 [-0.0427, -0.0001] p=0.049	B=-0.0213 [-0.0423, -0.0003] p=0.046	B=-0.0245 [-0.0479, -0.0012] p=0.040	microbleeds per year
Sex [Male]	B=-0.136 [-0.603, 0.332] p=0.567	B=-0.137 [-0.603, 0.329] p=0.563	B=-0.151 [-0.626, 0.324] p=0.530	microbleeds
MAP	B=0.00565 [-0.01109, 0.02239] p=0.506	B=0.00580 [-0.01093, 0.02254] p=0.494	B=0.00529 [-0.01200, 0.02258] p=0.546	microbleeds per mmHg
Diabetes	B=0.636 [0.090, 1.183] p=0.023	B=0.632 [0.087, 1.178] p=0.023	B=0.674 [0.114, 1.234] p=0.019	microbleeds
Smoker [Ever]	B=0.207 [-0.257, 0.671] p=0.379	B=0.207 [-0.255, 0.669] p=0.377	B=0.190 [-0.283, 0.664] p=0.428	microbleeds
Smoker [Current]	B=-0.355 [-0.980, 0.271] p=0.264	B=-0.353 [-0.968, 0.263] p=0.259	B=-0.361 [-1.008, 0.287] p=0.273	microbleeds
Hypertension	B=0.107 [-0.404, 0.617] p=0.681	B=0.118 [-0.394, 0.630] p=0.651	B=0.136 [-0.388, 0.660] p=0.608	microbleeds
Hypercholesterolaemia	B=-0.239 [-0.709, 0.231] p=0.317	B=-0.232 [-0.703, 0.238] p=0.331	B=-0.273 [-0.758, 0.212] p=0.267	microbleeds

Table A4-5: Longitudinal linear regression between brain volume at one-year follow-up and baseline CVR, adjusted for brain volume at baseline, age, sex and vascular risk factors. Columns 2 to 4 contain the regression coefficients, 95% confidence intervals and p-values. The last column gives the units of the regression coefficient.

Variables	SGM CVR	NAWM CVR	WMH CVR	Units of B
CVR	B=0.128 [-5.0, 5.3] p=0.961	B=9.85 [-6.00, 25.70] p=0.221	B=-0.241 [-6.320, 5.839] p=0.938	%ICV per %/mmHg
Baseline brain volume	B=0.819 [0.739, 0.900] p<0.001	B=0.815 [0.735, 0.896] p<0.001	B=0.814 [0.732, 0.896] p<0.001	
Age	B=-0.0631 [-0.0968, -0.0294] p<0.001	B=-0.0628 [-0.095981, -0.029470] p<0.001	B=-0.0639 [-0.0989, -0.0290] p<0.001	%ICV per year
Sex [Male]	B=-0.479 [-1.096, 0.138] p=0.127	B=-0.515 [-1.128, 0.099] p=0.099	B=-0.498 [-1.121, 0.125] p=0.116	%ICV
MAP	B=-0.00342 [-0.02422, 0.01738] p=0.746	B=-0.00346 [-0.02416, 0.01724] p=0.742	B=-0.00466 [-0.02601, 0.01669] p=0.667	%ICV per mmHg
Diabetes	B=-0.0409 [-0.6438, 0.7256] p=0.906	B=0.0677 [-0.6125, 0.7480] p=0.844	B=-0.0306 [-0.7341, 0.6730] p=0.932	%ICV
Smoker [Ever]	B=-0.0420 [-0.6227, 0.5387] p=0.887	B=-0.0266 [-0.6026, 0.5494] p=0.927	B=-0.0308 [0.6199, 0.5583] p=0.918	%ICV
Smoker [Current]	B=-0.394 [-1.180, 0.391] p=0.323	B=-0.332 [-1.101, 0.437] p=0.396	B=-0.419 [-1.213, 0.375] p=0.299	%ICV
Hypertension	B=-0.306 [-0.935, 0.322] p=0.337	B=-0.330 [-0.956, 0.296] p=0.299	B=-0.359 [-1.004, 0.287] p=0.274	%ICV
Hypercholesterolaemia	B=-0.157 [-0.429, 0.742] p=0.597	B=0.147 [-0.436, 0.730] p=0.620	B=0.218 [-0.385, 0.822] p=0.476	%ICV

Table A4-6: Longitudinal linear regression between BG PVS volume at one-year follow-up and baseline CVR, adjusted for BG PVS volume at baseline, age, sex and vascular risk factors. Columns 2 to 4 contain the regression coefficients, 95% confidence intervals and p-values. The last column gives the units of the regression coefficient.

Variables	SGM CVR	NAWM CVR	WMH CVR	Units of B
CVR	B=-0.446 [-0.814, -0.078] p=0.018	B=-2.12 [-3.23, -1.01] p<0.001	B=-0.607 [-1.010, -0.203] p=0.003	log ₁₀ (%ROIV) per %/mmHg
Baseline BG PVS volume	B=0.856 [0.739, 0.974] p<0.001	B=0.850 [0.737, 0.964] p<0.001	B=0.912 [0.801, 1.023] p<0.001	
Age	B=-0.00100 [-0.00311, 0.00110] p=0.347	B=-0.000920 [-0.002954, 0.001115] p=0.373	B=-0.00226 [-0.00437, -0.00016] p=0.035	log ₁₀ (%ROIV) per year
Sex [Male]	B=-0.0373 [-0.0793, 0.0048] p=0.082	B=-0.0380 [-0.0787, 0.0026] p=0.067	B=-0.0360 [-0.0756, 0.0036] p=0.074	log ₁₀ (%ROIV)
MAP	B=0.000028 [-0.001460, 0.001515] p=0.971	B=0.000166 [-0.001282, 0.001614] p=0.821	B=-0.000042 [-0.001476, 0.001391] p=0.953	log ₁₀ (%ROIV) per mmHg
Diabetes	B=0.0575 [0.0051, 0.1099] p=0.032	B=0.0594 [0.0085, 0.1103] p=0.023	B=0.0520 [0.0012, 0.1029] p=0.045	log ₁₀ (%ROIV)
Smoker [Ever]	B=-0.0242 [-0.0661, 0.0177] p=0.255	B=-0.0239 [-0.0645, 0.0167] p=0.247	B=-0.0201 [-0.0599, 0.0196] p=0.318	log ₁₀ (%ROIV)
Smoker [Current]	B=-0.0450 [-0.1015, 0.0115] p=0.118	B=-0.0432 [-0.0974, 0.0109] p=0.117	B=-0.0312 [-0.0849, 0.0224] p=0.252	log ₁₀ (%ROIV)
Hypertension	B=-0.0135 [-0.0632, 0.0363] p=0.593	B=-0.0105 [-0.0589, 0.0379] p=0.669	B=-0.0182 [-0.0658, 0.0294] p=0.450	log ₁₀ (%ROIV)
Hypercholesterolaemia	B=0.0475 [0.0060, 0.0891] p=0.025	B=0.0497 [0.0092, 0.0901] p=0.016	B=0.0569 [0.0168, 0.0970] p=0.006	log ₁₀ (%ROIV)

Table A4-7: Longitudinal linear regression between CSO PVS volume at one-year follow-up and baseline CVR, adjusted for CSO PVS volume at baseline, age, sex and vascular risk factors. Columns 2 to 4 contain the regression coefficients, 95% confidence intervals and p-values. The last column gives the units of the regression coefficient.

Variables	SGM CVR	NAWM CVR	WMH CVR	Units of B
CVR	B=2.21 [-7.54, 12.07] p=0.658	B=22.0 [-7.8, 50.9] p=0.139	B=7.10 [-6.11, 20.75] p=0.308	log ₁₀ (%ROIV) per %/mmHg
Baseline CSO PVS volume	B=0.771 [0.671, 0.871] p<0.001	B=0.767 [0.669, 0.865] p<0.001	B=0.790 [0.689, 0.891] p<0.001	
Age	B=0.00189 [-0.00083, 0.00462] p=0.172	B=0.00170 [-0.00092, 0.00431] p=0.202	B=0.000820 [-0.001984, 0.003624] p=0.564	log ₁₀ (%ROIV) per year
Sex [Male]	B=-0.0350 [-0.0896, 0.0196] p=0.207	B=-0.0322 [-0.0853, 0.0210] p=0.234	B=-0.0320 [-0.0859, 0.0219] p=0.242	log ₁₀ (%ROIV)
MAP	B=0.00114 [-0.00081, 0.00309] p=0.248	B=0.00125 [-0.00065, 0.00315] p=0.197	B=0.00102 [-0.00094, 0.00299] p=0.306	log ₁₀ (%ROIV) per mmHg
Diabetes	B=0.0666 [-0.0018, 0.1350] p=0.056	B=0.0662 [-0.0006, 0.1330] p=0.052	B=0.0620 [-0.0075, 0.1314] p=0.080	log ₁₀ (%ROIV)
Smoker [Ever]	B=-0.00238 [-0.05652, 0.05176] p=0.931	B=-0.00492 [-0.05770, 0.04787] p=0.854	B=-0.00431 [-0.05823, 0.04962] p=0.875	log ₁₀ (%ROIV)
Smoker [Current]	B=0.00789 [-0.06588, 0.08165] p=0.833	B=-0.000263 [-0.070871, 0.070345] p=0.994	B=0.0141 [-0.0584, 0.0866] p=0.702	log ₁₀ (%ROIV)
Hypertension	B=-0.0283 [-0.0889, 0.0323] p=0.358	B=-0.0249 [-0.0843, 0.0344] p=0.407	B=-0.0306 [-0.0916, 0.0303] p=0.322	log ₁₀ (%ROIV)
Hypercholesterolaemia	B=0.0671 [0.0128, 0.1214] p=0.016	B=0.0697 [0.0166, 0.1228] p=0.010	B=0.0783 [0.0234, 0.1333] p=0.005	log ₁₀ (%ROIV)

Table A4-8: Longitudinal linear regression between total PVS volume at one-year follow-up and baseline CVR, adjusted for total PVS volume at baseline, age, sex and vascular risk factors. Columns 2 to 4 contain the regression coefficients, 95% confidence intervals and p-values. The last column gives the units of the regression coefficient.

Variables	SGM CVR	NAWM CVR	WMH CVR	Units of B
CVR	B=-0.207 [-0.637, 0.223] p=0.343	B=-1.90 [-3.21, -0.60] p=0.005	B=-0.366 [-0.858, 0.126] p=0.144	log ₁₀ (%ROIV) per %/mmHg
Baseline total PVS volume	B=0.752 [0.648, 0.856] p<0.001	B=0.745 [0.644, 0.847] p<0.001	B=0.775 [0.671, 0.879] p<0.001	
Age	B=0.00140 [-0.00110, 0.00390] p=0.271	B=0.00129 [-0.00111, 0.00369] p=0.288	B=0.000274 [-0.002275, 0.002823] p=0.832	log ₁₀ (%ROIV) per year
Sex [Male]	B=-0.0363 [-0.0857, 0.0130] p=0.148	B=-0.0343 [-0.0822, 0.0136] p=0.159	B=-0.0328 [-0.0809, 0.0153] p=0.180	log ₁₀ (%ROIV)
MAP	B=0.000758 [-0.001000, 0.002516] p=0.396	B=0.000872 [-0.000844, 0.002587] p=0.317	B=0.000655 [-0.001099, 0.002409] p=0.462	log ₁₀ (%ROIV) per mmHg
Diabetes	B=0.0632 [0.0014, 0.1250] p=0.045	B=0.0633 [0.0031, 0.1235] p=0.039	B=0.0574 [-0.0046, 0.1194] p=0.069	log ₁₀ (%ROIV)
Smoker [Ever]	B=-0.0110 [-0.0600, 0.0380] p=0.659	B=-0.0128 [-0.0604, 0.0348] p=0.596	B=-0.0119 [-0.0601, 0.0363] p=0.626	log ₁₀ (%ROIV)
Smoker [Current]	B=-0.00586 [-0.07271, 0.06098] p=0.863	B=-0.0113 [-0.0751, 0.0526] p=0.728	B=0.000474 [-0.064498, 0.065446] p=0.989	log ₁₀ (%ROIV)
Hypertension	B=-0.0178 [-0.0734, 0.0379] p=0.529	B=-0.0143 [-0.0686, 0.0400] p=0.603	B=-0.0199 [-0.0752, 0.0353] p=0.476	log ₁₀ (%ROIV)
Hypercholesterolaemia	B=0.0594 [0.0103, 0.1085] p=0.018	B=0.0618 [0.0138, 0.1097] p=0.012	B=0.0704 [0.0214, 0.1195] p=0.005	log ₁₀ (%ROIV)

A4.3 Sensitivity analyses

Table A4-9: Regression coefficients after adjusting for WMH volume at baseline.

Each row represents a different statistical model where the SVD quantitative feature of interest after one year is given in the first column. The associated regression coefficient *B*, its 95% confidence interval and *p*-value are given in columns 2-4. The last column gives the units of *B*. All models were corrected for WMH volume at baseline, the SVD feature of interest at baseline, age, sex, MAP, diagnosis of diabetes, hypertension, and hypercholesterolaemia and history of smoking.

Variables after one year	SGM CVR	NAWM CVR	WMH CVR	Units of B
Number of lacunes	B=-0.617 [-2.388, 1.153] p=0.492	B=1.08 [-4.18, 6.35] p=0.685	B=-0.448 [-2.488, 1.591] p=0.665	lacunes per %mmHg
Number of microbleeds	B=0.139 [-4.010, 4.288] p=0.947	B=-2.45 [-15.35, 10.46] p=0.709	B=-0.578 [-6.389, 5.234] p=0.844	microbleeds per %mmHg
Brain volume	B=-22.3 [-39.4, -5.3] p=0.011	B=-4.32 [-57.43, 48.79] p=0.873	B=-9.03 [-30.60, 12.55] p=0.410	%ICV per %mmHg
BG PVS volume	B=-0.337 [-0.698, 0.026] p=0.068	B=-1.81 [-2.90, -0.71] p=0.001	B=-0.441 [-0.852, -0.031] p=0.035	log ₁₀ (%ROIV) per %mmHg
CSO PVS volume	B=-0.00706 [-0.49133, 0.47722] p=0.977	B=-1.63 [-3.10, -0.17] p=0.029	B=-0.00451 [-0.56750, 0.55847] p=0.987	log ₁₀ (%ROIV) per %mmHg
Total PVS volume	B=-0.0547 [-0.4865, 0.3772] p=0.803	B=-1.55 [-2.86, -0.25] p=0.020	B=-0.193 [-0.692, 0.307] p=0.447	log ₁₀ (%ROIV) per %mmHg

Table A4-10: Regression coefficients after adjusting for EtCO₂ baseline. Each row represents a different statistical model where the SVD quantitative feature of interest after one year is given in the first column. The associated regression coefficient *B*, its 95% confidence interval and *p*-value are given in columns 2-4. The last column gives the units of *B*. All models were corrected for EtCO₂ baseline, the SVD feature of interest at baseline, age, sex, MAP, diagnosis of diabetes, hypertension, and hypercholesterolaemia and history of smoking.

Variables after one year	SGM CVR	NAWM CVR	WMH CVR	Units of B
WMH volume	B=-0.321 [-0.676, 0.034] p=0.076	B=-1.11 [-2.15, -0.07] p=0.037	B=-0.238 [-0.626, 0.151] p=0.229	log ₁₀ (%ICV) per %/mmHg
Number of lacunes	B=-1.16 [-3.09, 0.76] p=0.235	B=0.0302 [-5.5206, 5.5811] p=0.991	B=-1.05 [-3.07, 0.98] p=0.309	lacunes per %mmHg
Number of microbleeds	B=-1.60 [-6.19, 2.98] p=0.491	B=-5.91 [-19.82, 8.00] p=0.402	B=-2.25 [-8.18, 3.68] p=0.454	microbleeds per %/mmHg
Brain volume	B=-0.866 [-6.494, 4.761] p=0.761	B=8.62 [-8.09, 25.32] p=0.310	B=-0.577 [-6.759, 5.605] p=0.854	%ICV per %/mmHg
BG PVS volume	B=-0.341 [-0.739, 0.0571] p=0.093	B=-1.90 [-3.06, -0.73] p=0.002	B=-0.559 [-0.967, -0.152] p=0.007	log ₁₀ (%ROIV) per %/mmHg
CSO PVS volume	B=0.0368 [-0.4798, 0.5535] p=0.888	B=-1.67 [-3.19, -0.14] p=0.033	B=-0.109 [-0.666, 0.447] p=0.698	log ₁₀ (%ROIV) per %/mmHg
Total PVS volume	B=-0.0345 [-0.4999, 0.4309] p=0.884	B=-1.62 [-3.00, -0.25] p=0.021	B=-0.311 [-0.808, 0.186] p=0.218	log ₁₀ (%ROIV) per %/mmHg

Table A4-11: Regression coefficients after excluding datasets with high motion during BOLD-CVR scan. Each row represents a different statistical model where the SVD quantitative feature of interest after one year is given in the first column. The associated regression coefficient *B*, its 95% confidence interval and *p*-value are given in columns 2-4. The last column gives the units of *B*. All models were corrected for EtCO₂ baseline, the SVD feature of interest at baseline, age, sex, MAP, diagnosis of diabetes, hypertension, and hypercholesterolaemia and history of smoking. A total of 10 datasets was removed.

Variables after one year	SGM CVR	NAWM CVR	WMH CVR	Units of B
WMH volume	B=-0.321 [-0.660, 0.018] p=0.063	B=-1.31 [-2.35, -0.27] p=0.014	B=-0.268 [-0.666, 0.130] p=0.185	log ₁₀ (%ICV) per %/mmHg
Number of lacunes	B=-0.675 [-2.369, 1.019] p=0.432	B=-0.0539 [-5.1986, 5.0907] p=0.983	B=-0.547 [-2.475, 1.380] p=0.575	lacunes per %mmHg
Number of microbleeds	B=-0.0387 [-2.4956, 2.4181] p=0.975	B=1.44 [-6.40, 9.28] p=0.716	B=0.794 [-2.665, 4.252] p=0.651	microbleeds per %/mmHg
Brain volume	B=0.467 [-4.684, 5.618] p=0.858	B=5.57 [-10.55, 21.69] p=0.496	B=-0.700 [-6.798, 5.398] p=0.821	%ICV per %/mmHg
BG PVS volume	B=-0.429 [-0.808, -0.050] p=0.027	B=-2.17 [-3.32, -1.01] p<0.001	B=-0.634 [-1.052, -0.216] p=0.003	log ₁₀ (%ROIV) per %/mmHg
CSO PVS volume	B=-0.0517 [-0.5376, 0.4341] p=0.833	B=-1.79 [-3.29, -0.30] p=0.019	B=-0.163 [-0.728, 0.403] p=0.570	log ₁₀ (%ROIV) per %/mmHg
Total PVS volume	B=-0.138 [-0.577, 0.301] p=0.536	B=-1.82 [-3.17, -0.47] p=0.009	B=-0.377 [-0.882, 0.128] p=0.142	log ₁₀ (%ROIV) per %/mmHg

Table A4-12: Regression coefficients after excluding datasets with short hypercapnic paradigm. Each row represents a different statistical model where the SVD quantitative feature of interest after one year is given in the first column. The associated regression coefficient B , its 95% confidence interval and p -value are given in columns 2-4. The last column gives the units of B . All models were corrected for $EtCO_2$ baseline, the SVD feature of interest at baseline, age, sex, MAP, diagnosis of diabetes, hypertension, and hypercholesterolaemia and history of smoking. A total of 14 datasets (14/163 for SGM, NAWM CVR analyses and 14/158 for WMH CVR) was removed.

Variables after one year	SGM CVR	NAWM CVR	WMH CVR	Units of B
WMH volume	$B=-0.396$ [-0.739, -0.052] $p=0.024$	$B=-1.21$ [-2.33, -0.09] $p=0.034$	$B=-0.327$ [-0.828, 0.175] $p=0.200$	$\log_{10}(\%ICV)$ per %/mmHg
Number of lacunes	$B=-0.925$ [-2.751, 0.901] $p=0.318$	$B=0.133$ [-5.721, 5.987] $p=0.964$	$B=-1.05$ [-3.64, 1.55] $p=0.427$	lacunes per %/mmHg
Number of microbleeds	$B=-1.23$ [-5.70, 3.25] $p=0.588$	$B=-4.45$ [-19.56, 10.66] $p=0.561$	$B=-2.09$ [-8.92, 4.74] $p=0.546$	microbleeds per %/mmHg
Brain volume	$B=0.109$ [-5.378, 5.597] $p=0.969$	$B=11.1$ [-7.0, 29.2] $p=0.229$	$B=0.107$ [-8.022, 8.237] $p=0.979$	%ICV per %/mmHg
BG PVS volume	$B=-0.492$ [-0.875, -0.110] $p=0.012$	$B=-2.78$ [-4.00, -1.55] $p<0.001$	$B=-0.517$ [-1.055, 0.021] $p=0.059$	$\log_{10}(\%ROIV)$ per %/mmHg
CSO PVS volume	$B=-0.157$ [-0.659, 0.345] $p=0.537$	$B=-2.22$ [-3.86, -0.58] $p=0.008$	$B=-0.677$ [-1.402, 0.048] $p=0.067$	$\log_{10}(\%ROIV)$ per %/mmHg
Total PVS volume	$B=-0.250$ [-0.705, 0.205] $p=0.279$	$B=-2.35$ [-3.83, -0.87] $p=0.002$	$B=-0.651$ [-1.307, 0.005] $p=0.052$	$\log_{10}(\%ROIV)$ per %/mmHg

Table A4-13: Regression coefficients after excluding datasets where masks contain low number of voxels in mean BOLD space. Each row represents a different statistical model where the SVD quantitative feature of interest after one year is given in the first column. The associated regression coefficient B , its 95% confidence interval and p -value are given in the second column. The third column gives the units of B . All models were corrected for EtCO_2 baseline, the SVD feature of interest at baseline, age, sex, MAP, diagnosis of diabetes, hypertension, and hypercholesterolaemia and history of smoking. Only WMH CVR analysis was affected by this sensitivity analysis where 31 datasets were removed.

Variables after one year	WMH CVR	Units of B
WMH volume	$B=-0.445$ [-0.999, 0.108] $p=0.114$	$\log_{10}(\% \text{ICV})$ per %/mmHg
Number of lacunes	$B=-1.25$ [-4.51, 2.00] $p=0.448$	lacunes per %/mmHg
Number of microbleeds	$B=-4.37$ [-12.85, 4.11] $p=0.310$	microbleeds per %/mmHg
Brain volume	$B=1.97$ [-5.95, 9.89] $p=0.623$	%ICV per %/mmHg
BG PVS volume	$B=-0.536192$ [-1.068318, -0.004066] $p=0.048$	$\log_{10}(\% \text{ROIV})$ per %/mmHg
CSO PVS volume	$B=-0.487548$ [-1.167949, 0.192854] $p=0.158$	$\log_{10}(\% \text{ROIV})$ per %/mmHg
Total PVS volume	$B=-0.474122$ [-1.093485, 0.145241] $p=0.132$	$\log_{10}(\% \text{ROIV})$ per %/mmHg